

Examining Peptide and Protein Structure and Dynamics with Two-Dimensional Infrared Spectroscopy

By

Kelsey Webb

Dissertation

Submitted to the Faculty of the

Graduate School of Vanderbilt University

in partial fulfillment of the requirements

for the degree of

DOCTOR OF PHILOSOPHY

in

Chemistry

May 31, 2022

Nashville, Tennessee

Approved:

Dr. Lauren Buchanan (Advisor)

Dr. Craig Duvall

Dr. John McLean

Dr. Lars Plate

Copyright © 2022 Kelsey Webb

All Rights Reserved

ACKNOWLEDGEMENTS

During my time at Vanderbilt, I was fortunate to receive a great deal of financial support for my scientific research. Funding for my first summer of research at Vanderbilt University was provided by a Warren Fellowship, generously granted by the Department of Chemistry. Additionally, three years of financial assistance for my graduate education and research was provided through a National Science Foundation Graduate Research Fellowship. I am also very grateful for the financial aid endowed by Vanderbilt's Chemistry Department that allowed me to share my work at conferences throughout my graduate career.

There are several individuals I would like to acknowledge for supporting my graduate education, research, and ultimately this dissertation. First, I would like to thank my advisor, Dr. Lauren Buchanan, for allowing me work in her lab and her guidance throughout the years. The collective scientific and leadership skills I've developed in this setting has prepared me well for my future endeavors. I would also like to thank Dr. Lars Plate, Dr. John McLean, and Dr. Craig Duvall, for serving on my committee and providing insight and advice on these projects. Thank you to the wonderful research scientists at Vanderbilt's Mass Spectrometry Research Center (MSRC), especially Brian and Wade, who were exceptionally kind and helpful with sample characterization. I am extraordinarily grateful for my undergraduate advisor, Dr. Floyd Beckford, and my REU advisor, Dr. Bhavya Sharma, who collectively introduced me to the world of scientific research and inspired me to pursue chemistry.

Most importantly, I wouldn't be anywhere without the love, support, and encouragement of my family and friends. I have made wonderful friends in the chemistry department at Vanderbilt who have shared dinners, holidays, coffee trips, concerts, and many more experiences with me

over the past five years. Finally, to Caleb—thank you for your unconditional love and support.
Thank you all for your support!

TABLE OF CONTENTS

Acknowledgements.....	iii
List of Tables.....	viii
List of Figures.....	ix
List of Abbreviations.....	xi
Chapter 1: Introduction.....	1
1.1 Overview.....	1
1.2 Introduction.....	1
1.3 Nanoparticles can impact protein structure.....	6
1.4 Infrared spectroscopy is useful for probing protein structure.....	7
1.5 Two-dimensional infrared spectroscopy can provide more insight into protein structure and dynamics.....	10
1.6 Isotopes can be implemented as site-specific probes for protein IR studies.....	13
1.7 Outline.....	14
1.8 References.....	15
Chapter 2: Experimental Methods.....	20
2.1 Introduction.....	20
2.2 Preparation of peptide samples.....	20
2.2.1 Isotope labeling.....	20
2.2.1.1 Fmoc protection of the N-terminal amino group.....	22
2.2.1.2 ¹⁸ O-exchange with an Fmoc-protected ¹³ C-C _α amino acid.....	24
2.2.2 Fmoc solid-phase peptide synthesis.....	28
2.2.3 Peptide cleavage from resin and precipitation with ether.....	32
2.2.4 High-performance liquid chromatography peptide purification.....	34
2.2.5 Electrospray-ionization mass spectrometry peptide characterization.....	36
2.3 Preparation of peptide samples for CD and 2D IR measurements.....	37
2.4 Experimental setup for 2D IR spectroscopy.....	39
2.5 References.....	44
Chapter 3: Structural differences in a short α-helix revealed by two-dimensional infrared spectroscopy and isotope labeling.....	46
3.1 Abstract.....	46
3.2 Introduction.....	47
3.3 Materials and Methods.....	51
3.4 Results and Discussion.....	56
3.4.1 Peptide α-helicity is controlled through solvent conditions.....	56
3.4.2 TFE enhances peptide α-helicity and blueshifts frequencies in 2D IR....	60
3.4.3 Dual ¹³ C ¹⁸ O probes detect α-helix formation spanning central residues..	62
3.4.4 Double ¹³ C ¹⁸ O labeling suggests terminal conformational differences...66	
3.4.5 Semi-quantitative intensity ratio comparison of sidechain and isotopes..	69
3.5 Conclusions.....	74

3.6 References.....	77
Chapter 4: Establishing conditions for structural analysis of nanoparticle-bound peptides and proteins with two-dimensional infrared spectroscopy.....	82
4.1 Abstract.....	82
4.2 Introduction.....	83
4.3 Materials and Methods.....	86
4.4 Results and Discussion.....	90
4.4.1 Citrate does not impact model peptide/protein signal or structure.....	90
4.4.2 Centrifugation/sonication do not alter model peptide/protein structure...94	
4.4.3 Commercial AuNPs remain suspended upon peptide/protein addition...97	
4.4.4 Synthesized AuNPs exhibit opposite affinities for peptide/protein.....	101
4.5 Conclusions.....	104
4.6 References.....	107
Chapter 5: Environmental changes in the Influenza A M2 proton channel revealed by 2D IR spectroscopy.....	114
5.1 Abstract.....	114
5.2 Introduction.....	115
5.3 Materials and Methods.....	117
5.4 Results and Discussion.....	119
5.4.1 AM2TM exhibits unique spectral feature in the inward closed state.....	119
5.4.2 Amantadine induces a conformational change in AM2TM.....	122
5.4.3 Isotopic lineshapes suggest differences in local water environment.....	123
5.5 Conclusions.....	132
5.6 Acknowledgements.....	135
5.7 References.....	135
Chapter 6: Outlook and Future Directions.....	138
6.1 Abstract.....	138
6.2 Investigating α -helical structures with 2D IR and isotope labeling.....	138
6.3 Elucidating nanoparticle-induced structural changes in peptides and proteins with 2D IR spectroscopy.....	142
6.4 Probing local water dynamics in the Influenza A M2 proton channel with 2D IR spectroscopy.....	144
6.5 Acknowledgements.....	144
6.6 References.....	144
Appendix 1: Supporting Information for Chapter 3.....	146
A1.1 Materials and Experimental Methods.....	146
A1.1.1 General Information.....	146
A1.1.2 Peptide synthesis and purification.....	146
A1.1.3 Fmoc protection reaction with ^{13}C -enriched amino acids.....	147
A1.1.4 Acid-catalyzed ^{18}O -exchange with Fmoc protected amino acids.....	148

A1.1.5 Sample preparation for ESI-MS characterization.....	149
A1.1.6 Sample preparation for 2D IR and circular dichroism experiments ...	150
A1.1.7 Peptide quantification.....	151
A1.1.8 2D IR measurements.....	151
A1.1.9 Circular dichroism measurements.....	152
A1.2 Supplementary Data.....	153
A1.3 References.....	171
Curriculum Vitae.....	172

LIST OF TABLES

3.1	Low-frequency to amide I' mode intensity comparison for $^{13}\text{C}^{18}\text{O}$ samples.....	72
4.1	Supplementary information for gold nanoparticles supplied in 0.1 mg/mL sodium citrate from Alfa Aesar.....	89
4.2	Initial solution composition for nanoparticle and model peptide/protein mixtures....	98
4.3	Sample conditions used for troubleshooting nanoparticle isolations.....	100
4.4	Solution composition for synthesized nanoparticle-HEWL mixtures.....	101
4.5	Representative LSPR data for gold nanoparticles with model protein.....	102
4.6	Representative LSPR data for gold nanoparticles with model peptide.....	104
A1.1	Solvatochromatic effects of TFE on model peptide-like compounds.....	157
A1.2	Signal strength comparison of sidechain to amide I' mode for unlabeled MAHP....	166
A1.3	Signal strength comparison of low-frequency to amide I' mode for A5 MAHP.....	167
A1.4	Signal strength comparison of low-frequency to amide I' mode for A3A6 MAHP.....	168
A1.5	Signal strength comparison of low-frequency to amide I' mode for A5A8 MAHP.....	169
A1.6	Signal strength comparison of low-frequency to amide I' mode for A8G11 MAHP.....	170

LIST OF FIGURES

1.1	Chemical makeup of amino acids and peptides.....	3
1.2	Levels of peptide and protein secondary structure.....	5
1.3	Infrared signatures for protein secondary structures.....	10
1.4	2D IR spectrum of a model protein.....	12
2.1	Fmoc protection of $^{13}\text{C}-\text{C}_\alpha$ alanine.....	23
2.2	Mass spectrum of Fmoc $^{13}\text{C}-\text{C}_\alpha$ alanine.....	24
2.3	Reaction scheme and experimental setup for ^{18}O -exchange of Fmoc $^{13}\text{C}-\text{C}_\alpha$ alanine.....	25
2.4	Mass spectrum of ^{18}O -enriched Fmoc $^{13}\text{C}-\text{C}_\alpha$ alanine.....	28
2.5	Schematic of Fmoc solid-phase peptide synthesis.....	30
2.6	Optimized HPLC gradient and chromatogram for MAHP.....	36
2.7	Mass spectrum of pure MAHP.....	37
2.8	Sample composition for MAHP 2D IR and CD experiments.....	38
2.9	Overview of 2D IR process.....	40
2.10	Schematic of experimental 2D IR setup.....	41
3.1	Cartoon depiction of isotope labeling schemes for α -helices and predicted 2D IR spectra.....	51
3.2	Solvent conditions modulate peptide α -helicity.....	59
3.3	Chemical structures of model compounds used for solvatochromism study.....	60
3.4	2D IR spectra of unlabeled MAHP under optimized solvent conditions.....	62
3.5	2D IR spectra of MAHP LS1 as a function of peptide α -helicity.....	63
3.6	Representative 2D IR spectra of MAHP LS2 at varying degrees of α -helicity.....	65
3.7	2D IR spectra of MAHP LS3 as a function of peptide α -helicity.....	66
3.8	N-terminal MAHP LS2 (A3 and A6) 2D IR spectra as a function of peptide α -helicity.....	68
3.9	C-terminal MAHP LS2 (A8 and G11) 2D IR spectra as a function of peptide α -helicity.....	68
3.10	Summary of intensity ratios (low-frequency to amide I' mode) for unlabeled, single, and double $^{13}\text{C}^{18}\text{O}$ -labeled MAHP as a function of α -helicity.....	71
3.11	Representative 2D IR spectra of unlabeled, single, and double $^{13}\text{C}^{18}\text{O}$ -labeled MAHP in the low-frequency spectral window.....	73
4.1	Mass spectrum of EK-helix.....	87
4.2	Citrate does not absorb in amide I' region at relevant concentrations.....	91
4.3	Amide I' frequency of EK-helix is unaffected by citrate.....	92
4.4	Peptide α -helicity remains constant in the presence of citrate.....	94
4.5	Centrifugation retains model peptide and protein secondary structure.....	96
4.6	Sonication does not disrupt HEWL structure.....	97
4.7	2D IR spectra of HEWL with synthesized gold nanoparticles.....	103

4.8	2D IR spectra of EK-helix with synthesized gold nanoparticles.....	104
5.1	AM2TM exhibits prominent spectral signature in DMNG detergent.....	120
5.2	Characteristic M2 feature is not present at low pH in DMNG detergent.....	122
5.3	Amantadine alters AM2TM tetramer conformation.....	123
5.4	Static 2D IR measurements of AM2TM isotopologues.....	125
5.5	Isotopic signatures of AM2TM in the inward closed conformation.....	127
5.6	Isotopic features of AM2TM in the inward open state.....	129
5.7	Sidechain exhibits time-dependent feature in the inward closed state.....	131
5.8	¹³ C is not a feasible vibrational probe for AM2TM.....	132
A1.1	Fmoc protection of a generic ¹³ C-C ₁ -L-amino acid for solid-phase peptide synthesis.....	148
A1.2	HCl-catalyzed ¹⁸ O-exchange with generic Fmoc ¹³ C-C ₁ -L-amino acid.....	149
A1.3	Characterization of ¹³ C and ¹³ C ¹⁸ O ¹⁸ O-labeled alanine.....	153
A1.4	Purification and characterization of the unlabeled model peptide.....	153
A1.5	Purification and characterization of MAHP isotopologues.....	154
A1.6	Supplementary 2D IR spectra for small-molecule solvatochromism study with TFE.....	155
A1.7	FTIR measurements corroborate TFE-induced blueshift in NMA frequency.....	156
A1.8	FTIR measurements verify cosolvent-induced blueshift in NMP frequency.....	156
A1.9	Quantifying peptide α-helicity as a function of solvent conditions.....	158
A1.10	Monitoring structural changes induced by pH and 40% TFE (v/v) through 2D IR frequency shifts.....	159
A1.11	Perpendicular 2D IR spectra of double ¹³ C ¹⁸ O-edited peptides at high helicity condition.....	160
A1.12	Perpendicular 2D IR spectrum of MAHP LS3 (mixed ¹³ C and ¹³ C ¹⁸ O) at intermediate helicity condition.....	160
A1.13	Comprehensive 2D IR spectra of unlabeled MAHP under each solvent condition used for intensity ratio calculations.....	161
A1.14	Comprehensive 2D IR spectra of single-labeled A5 MAHP under each solvent condition used for intensity ratio calculations.....	162
A1.15	2D IR spectra of double ¹³ C ¹⁸ O-labeled A3A6 MAHP under each solvent condition used for intensity ratio calculations.....	163
A1.16	Comprehensive 2D IR spectra of double ¹³ C ¹⁸ O-labeled A5A8 MAHP under optimized solvent conditions used for intensity ratio comparisons.....	164
A1.17	All 2D IR spectra of double ¹³ C ¹⁸ O-labeled A8G11 MAHP under each solvent condition used for intensity ratio calculations.....	165

LIST OF ABBREVIATIONS

2D IR	Two-dimensional infrared
4NBA	4-nitrobenzaldehyde
AgGaS ₂	Silver gallium sulfide
Ala	Alanine
AM2TM	Influenza A matrix 2 transmembrane peptide
Arg	Arginine
Asp	Aspartic acid
BBO	Beta barium borate
CaF ₂	Calcium fluoride
CD	Circular dichroism
CDCl ₃	Deuterated chloroform
CDOD ₃	Deuterated methanol
cm ⁻¹	Wavenumber
Cryo-EM	Cryogenic electron microscopy
C _α	Alpha carbon
D ₂ O	Deuterium oxide
DCl	Deuterium chloride
DFG	Difference frequency generation
DIC	Diisopropylcarbodiimide
DLS	Dynamic light scattering
DMF	Dimethylformamide
DMNG	Decyl maltose neopentyl glycol
DNA	Deoxyribonucleic acid
DPC	Dodecylphosphocholine
ESA	Excited state absorption
ESI-MS	Electrospray ionization mass spectrometry
EtOH	Ethanol
Fmoc	9-Fluorenylmethoxycarbonyl
fs	Femtosecond
FTIR	Fourier transform infrared
g	Gram
Ge AOM	Germanium-based acousto-optic modulator
Glu	Glutamic acid
Gly	Glycine
HCl	Hydrochloric acid
HEWL	Hen egg white lysozyme
HFIP	1,1,1,3,3,3-hexafluoro-2-propanol
His	Histidine
HPLC	High-performance liquid chromatography
IR	Infrared
KHSO ₄	Potassium bisulfate
kHz	Kilohertz
LS	Labeling scheme
LSPR	Localized surface plasmon resonance
M	Molar

M2	Matrix 2
MAHP	Model α -helical peptide
MCT	Mercury cadmium telluride
mL	Milliliter
mm	Millimeter
mmol	Millimole
N ₂	Nitrogen
NaHCO ₃	Sodium bicarbonate
NaOD	Sodium deuterioxide
Nd:YVO ₄	Neodymium-doped yttrium vanadate
nm	Nanometer
NMA	N-methylacetamide
NMP	<i>N</i> -methyl-2-pyrrolidone
NMR	Nuclear magnetic resonance
NP	Nanoparticle
OPA	Optical parametric amplifier
Pbf	2,2,4,6,7-pentamethyldihydrobenzofuran-5-sulfonyl
PEG	Polyethylene glycol
pH	Potential hydrogen
pK _a	Acid dissociation constant
ps	Picosecond
RNA	Ribonucleic acid
RP-HPLC	Reversed-phase high performance liquid chromatography
rpm	Rotations per minute
SC	Sidechain
SPPS	Solid phase peptide synthesis
TFA	Trifluoroacetic acid
TFE	2,2,2-trifluoroethanol
TIPS	Triisopropylsilane
Trp	Tryptophan
UV-Vis	Ultraviolet-visible
Val	Valine
W	Watt
WT	Wild type
α	Alpha
β	Beta
γ	Gamma
μ g	Microgram
μ L	Microliter
μ m	Micrometer
$ \mu $	Transition dipole moment

Chapter 1. Introduction

1.1 Overview

This dissertation will outline how nonlinear vibrational spectroscopy in combination with isotopic labeling can reveal detailed structural and dynamic information within proteins. In particular, my graduate research has focused on characterizing α -helical structures, which are one of the most common secondary structures peptides and proteins adopt. I have employed two-dimensional infrared (2D IR) spectroscopy with isotopic probes to examine a series of model α -helical peptides and proteins, which revealed detailed insights regarding their local structure and dynamics through vibrational coupling interactions. This first chapter will establish a foundational understanding of proteins, including their chemical compositions and how they fold into larger assemblies that impart specific functions involved in nearly every biological process. Additionally, this chapter will describe the fundamentals of 2D IR spectroscopy and isotope labeling methods, and how these techniques provide a powerful toolset to characterize protein structure and folding. Together, these experimental methods enabled us to extract novel information within model polypeptide systems, which improves our understanding of protein structure, folding, and function.

1.2 Introduction

Proteins are large biomolecules that play vital roles in life's chemical processes. Enzymes are proteins that catalyze biochemical reactions, including digestion and muscle contractions, which would otherwise not occur on timescales fast enough to support life.^{1,2} Some proteins aid in transportation, moving nutrients throughout the body and ions across membranes.^{3,4} Other proteins have passive roles, such as providing structural networks for connective tissues.⁵ Although proteins are structurally and functionally diverse, their chemical makeup is relatively simple.

Proteins are biological polymers comprised of linear chains of covalently-linked amino acids. Amino acids consist of a central carbon atom (C_{α}) connected to four functional groups: an amine, a carboxylic acid, a hydrogen atom, and a sidechain (Figure 1.1A). There are twenty amino acids found in nature, which are classified by their characteristic sidechains.

Proteins are formed by linking multiple amino acids through covalent bonds. The condensation reaction between the terminal amine and carboxylic acid of two different amino acids results in amide or “peptide” bond formation with water as a byproduct (Figure 1.1B). When the linear chain consists of ~50 amino acid residues or less, it is called a peptide or polypeptide. Proteins are simply large (>50 residues) polypeptide chains. The repetitive amide bonds make up the peptide backbone, which extends along the entire polypeptide chain. The order of amino acids, conventionally written as the N-terminal amino acid on the left and the C-terminal amino acid on the right, is known as the primary sequence and is the most fundamental descriptor of a polypeptide.

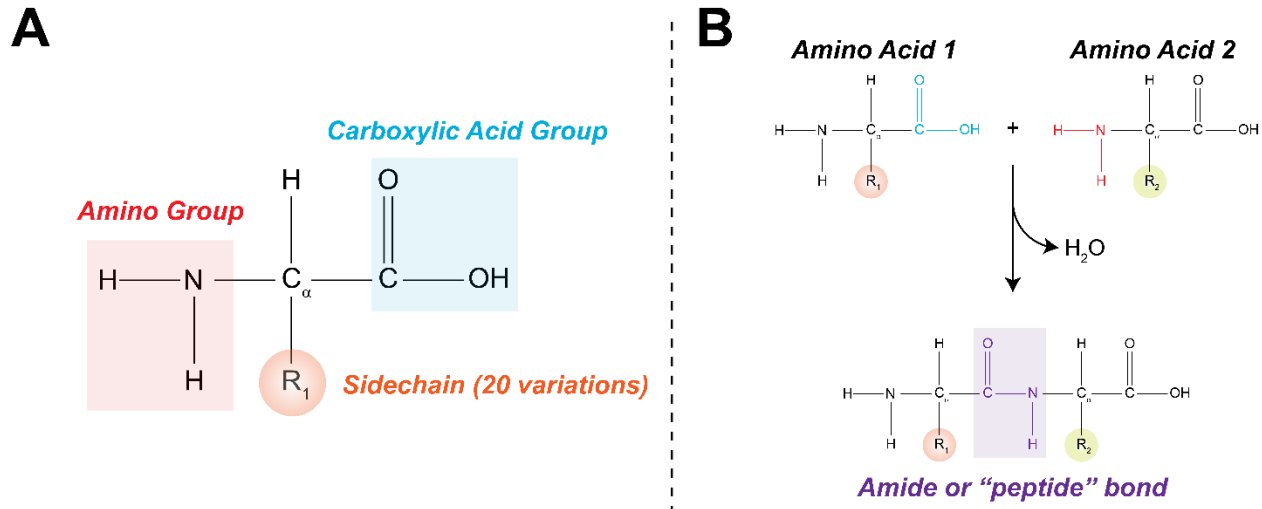


Figure 1.1 Chemical makeup of amino acids and peptides. (A) A central carbon atom (C_{α}) is bound to a hydrogen atom, carboxylic acid (blue), amino group (red), and unique sidechain (R group, orange). At physiological pH, the molecule is zwitterionic. (B) The peptide bond (purple) is formed by the condensation of two amino acids. Molecular geometries are not optimized here for simplicity.

The sidechain chemistry within a polypeptide sequence is a critical determinant for protein folding. One of the most important features of sidechain groups is how they interact with water. Nonpolar sidechains, like alkyl groups, are hydrophobic (“water fearing”) and do not interact favorably with water. Polar sidechains, such as amino and hydroxyl groups, are hydrophilic (“water loving”) and readily form hydrogen bonds with surrounding water molecules. Hydrophobic sidechains cluster together to form a hydrophobic core, where water is excluded, whereas the hydrophilic sidechains remain exposed to water. The formation of a dense hydrophobic core drives protein folding into distinct secondary structures.

Secondary structure describes the local orientation of the polypeptide backbone. To form a hydrophobic core, the peptide backbone must also fold away from the surrounding water molecules. The backbone is hydrophilic, with one hydrogen bond donor (N-H) and one hydrogen bond acceptor (C=O) per residue. There are two main secondary structures that satisfy the hydrogen-bonding requirements for the protein backbone: α -helices and β -sheets. α -helices are

right-handed helical structures stabilized by intramolecular hydrogen bonds between the C=O group of one residue and the N-H group of another residue four positions away. However, the first and last three residues of an α -helix are not hydrogen bonded. α -helices are also characterized by a turn every ~ 3.6 residues. The other common secondary structure found in proteins is the β -sheet. Unlike α -helices, β -sheets are stabilized by intermolecular hydrogen bonds between adjacent strands. The hydrogen bonding patterns can be parallel or antiparallel, where the hydrogen bonds between the C=O and N-H groups are at an angle or aligned, respectively. Many large proteins contain both types of secondary structures with loop regions and disordered segments connecting them.

While secondary structure is commonly used to describe the shape of proteins, there are higher levels of organization. Tertiary structure illustrates the three-dimensional shape of a polypeptide chain. Interactions between different sidechain residues are responsible for stabilizing tertiary structure. A common example is disulfide bond formation between cystine residues. Additionally, some proteins are made up of multiple polypeptide chains, known as subunits. Quaternary structure, the highest level of organization, describes the globular protein structure comprised of multiple subunits. Figure 1.2 summarizes the hierarchy of peptide and protein structure.

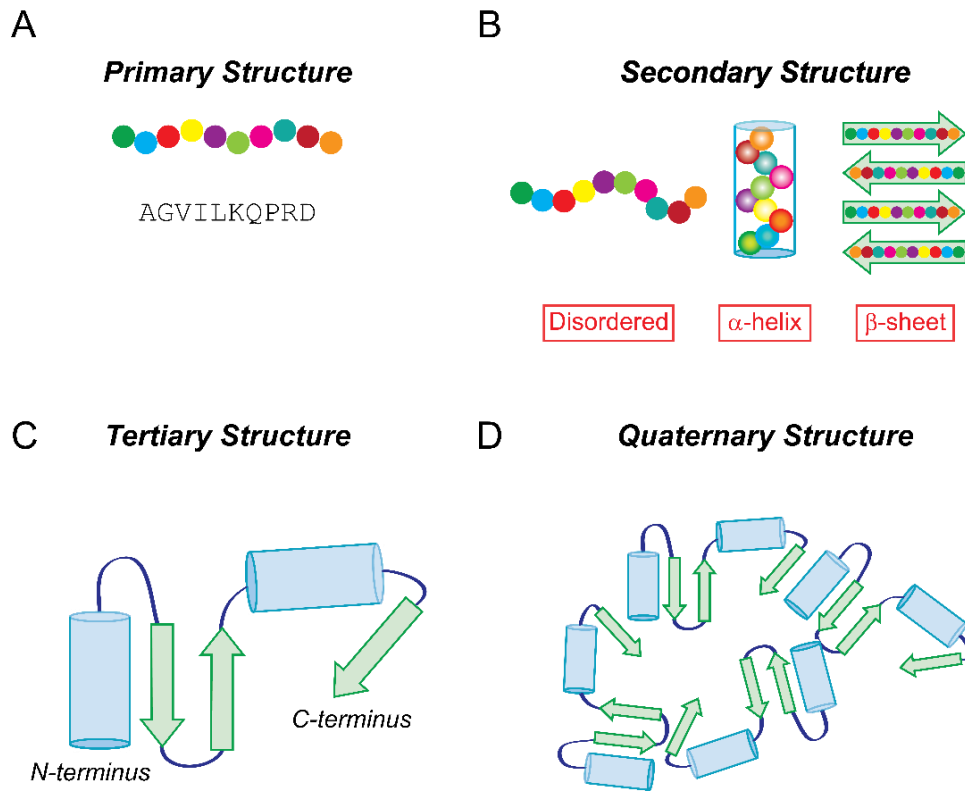


Figure 1.2 Levels of peptide and protein structure. (A) Primary structure lists the order of amino acids (colored circles and 1-letter code) in the polypeptide chain from the N-terminus (green circle, letter “A”) to the C-terminus (orange circle, letter “D”). (B) Secondary structure describes the peptide backbone orientation. The three common secondary structures peptides adopt are disordered, α -helices (blue cylinder), and β -sheets (green arrow). (C) Tertiary structure defines the global peptide/protein structure. (D) Quaternary structure illustrates how multiple peptides/protein units are associated.

The three-dimensional shape a protein adopts is critical for its function.^{6,7,8} However, static snapshots do not fully capture how proteins work. Proteins are dynamic, fluctuating rapidly to perform their biological roles. Therefore, if a protein becomes denatured or improperly folded, it can impact its function and have detrimental consequences. For example, the misfolding of soluble proteins into insoluble amyloid fibrils is implicated in over twenty human diseases, such as Alzheimer’s, type II diabetes, and cataracts.^{9,10,11} Thus, to better understand the link between protein structure and function, both native or toxic, it is ideal to use analytical techniques that can capture both structure and dynamics.

1.3 Nanoparticles can impact protein structure

Nanomaterials are defined as any tangible object with dimensions on the “nano” scale. Specifically, nanoparticles are defined as materials with dimensions less than 100 nanometers (nm), ~1,000 times smaller than the width of a human hair. While nanoscience and nanotechnology are relatively new concepts, nanomaterials have been used by humans for centuries, dating back to Ancient Rome. For example, the brilliant colors of Roman pottery and medieval stained glass have been attributed to the interactions between light and different nanomaterials (gold, silver, and copper).¹²⁻¹⁴ Significant advances in manufacturing and characterization methods have allowed scientists to determine the relationship between nanomaterials’ physical properties (size, shape, composition, etc.) and their unique optical and electronic behaviors.

Over the past few decades, nanomaterials have been extensively researched for a variety of applications, ranging from “smart packaging” in food products to spaceship coatings.^{15,16} Today, nanomaterials are found throughout our daily lives: they are in personal care products, like sunscreen and cosmetics, television displays, and plastic water bottles.¹⁷⁻²⁰ Increasingly, nanomaterials are being explored and integrated in medicine for innovative uses, including drug delivery, therapeutics, and molecular sensing.²¹⁻²³ These materials are attractive for biomedical applications because they are similar in size to many biological macromolecules, like proteins and nucleic acids, which can promote novel interactions.^{24,25}

Despite many advances in nanotechnology and medicine, much remains unknown about the long-term effects of nanoparticle exposure on biological systems. It is well-established that biomacromolecules (DNA, proteins, etc.) can have strong interactions with nanoparticles.²⁶⁻²⁹ When biological molecules associate with nanoparticles, they coat the surface, creating a diverse

and dynamic new identity known as the biomolecular corona.^{30,31} The biomolecular corona, not the bare nanoparticle, is responsible for molecular interactions within biological media. Proteins are abundant in biological fluids. Therefore, it is inevitable that some proteins will associate with nanoparticles and create a new protein corona identity, both *in vitro* and *in vivo*.

Protein coronas can be tailored to have desirable medicinal properties.^{32,33} The protein coverage provides a stealth for the nanoparticle, allowing it to interact with molecules and native cellular receptors.^{34,35} Protein structure is key for the appropriate biological activity of the protein-nanoparticle complex. However, proteins can undergo conformational changes to facilitate favorable interactions with nanoparticles.^{25,36,37} Protein denaturation lends itself to a loss in protein function, rendering the efficacy of the nanoparticle complex. While some proteins may not completely denature, their native structure can be altered by exposing previously buried residues within the hydrophobic core. The exposure of hidden residues, also known as cryptic epitopes, can unlock involuntary biological activities, including autoimmune responses.³⁸ Additionally, nanoparticles can also influence amyloid aggregation, a process linked to many diseases.³⁹⁻⁴¹ Thus, to understand the fundamental mechanisms of nanoparticle exposure in biological systems, it is critical to elucidate their impact on peptide and protein secondary structure.

1.4 Infrared spectroscopy is useful for probing protein structure

Common biophysical techniques to analyze protein structure are X-ray crystallography, cryogenic electron microscopy (cryo-EM), and nuclear magnetic resonance (NMR) spectroscopy.⁴²⁻⁴⁴ X-ray crystallography and cryo-EM provide exquisite structural resolution, but they capture static images of proteins. Additionally, these techniques require great expertise in sample preparation and analysis methods. NMR spectroscopy offers detailed structural

information and is more user friendly, but it is limited to relatively homogeneous samples. While these characterization tools are powerful for probing molecular structure, they have drawbacks: they are expensive, time-consuming, and sometimes lack the ability to monitor the kinetics of the system, although advances in technology are helping overcome this issue.⁴⁵⁻⁴⁷

Key questions in protein science that require knowledge of both structure and dynamics can be challenging to address simultaneously. Optical techniques, such as fluorescence and circular dichroism (CD) spectroscopy, may be more suitable to monitor rapidly evolving structural changes with a tradeoff in resolution.^{48,16} These techniques can capture fluctuations on short timescales (nanoseconds to picoseconds). However, these are bulk spectroscopic techniques that only report global structural information, which neglect critical details about the molecular system. Chemical labels can be synthetically incorporated in proteins, but they can potentially disrupt the native structure and kinetics.⁵⁰ Generally, most characterization methods cannot capture detailed structural changes within unlabeled proteins in real time.

Another useful tool for monitoring protein structure is infrared (IR) spectroscopy.⁵¹⁻⁵³ IR spectroscopy uses light in the mid-IR wavelength spectrum ($\sim 2\text{-}20\ \mu\text{m}$) to excite molecular vibrations within a system. Molecular vibrations are sensitive to both chemical composition and arrangement, making them powerful structural reporters. Native amide group vibrations are commonly examined in protein IR studies because they can report on the local backbone environment (conformation, solvation, etc.). The amide vibrations include the amide I (mostly C=O stretching), amide II (C-N stretch and N-H bending), amide III (C-N stretching, N-H bending, and C=O bending), and amide A (N-H stretching) modes.⁵⁴ Most protein studies focus on the amide I' mode ($\sim 1600\text{-}1700\ \text{cm}^{-1}$, where ' denotes amide deuteration) because it is highly sensitive to secondary structure.^{55,56} The structural sensitivity of the amide I' mode arises from vibrational

coupling (i.e., the interaction between multiple nearby vibrational modes). When several carbonyl groups are located within close proximity, they begin to vibrate together and the modes become delocalized. The delocalization of individual amide I' vibrations (i.e., local modes) result in new normal modes (i.e., the combination of local modes). Vibrational coupling gives rise to characteristic amide I' frequency ranges for different secondary structures.^{54,56}

Figure 1.3 summarizes the characteristic amide I' transitions for the three common secondary structures observed in linear infrared spectra. Disordered structures, also known as random coils, lack in long range ordering. The local amide groups exhibit randomized couplings and hydrogen bonding patterns, which gives rise to a broad amide I' transition between ~ 1645 – 1660 cm^{-1} (Figure 1.3A). In an α -helix, carbonyls experience highly-ordered intramolecular coupling between adjacent residues and turns. The amide I' mode for α -helices is typically observed between ~ 1635 – 1660 cm^{-1} , depending on the helix length and solvent environment (Figure 1.3B).⁵⁷ The amide groups in β -sheet structures experience strong intermolecular coupling between strands, where the strands can be oriented antiparallel or parallel. β -sheets have two IR-active amide I' modes centered at ~ 1620 cm^{-1} and ~ 1680 cm^{-1} (Figure 1.3C).⁵⁶ The intense, low-frequency β -sheet transition arises from in-phase oscillations along adjacent strands perpendicular to the fibril axis (ν_{\perp}). This mode is sensitive to the number of oscillators, and therefore the size of the β -sheet.⁵⁸ For example, the ν_{\perp} mode for amyloid peptides is usually more intense and redshifted.^{59,60} The weak, high-frequency β -sheet mode arises from in-phase oscillations along adjacent strands, but is oriented parallel to the fibril axis (ν_{\parallel}).

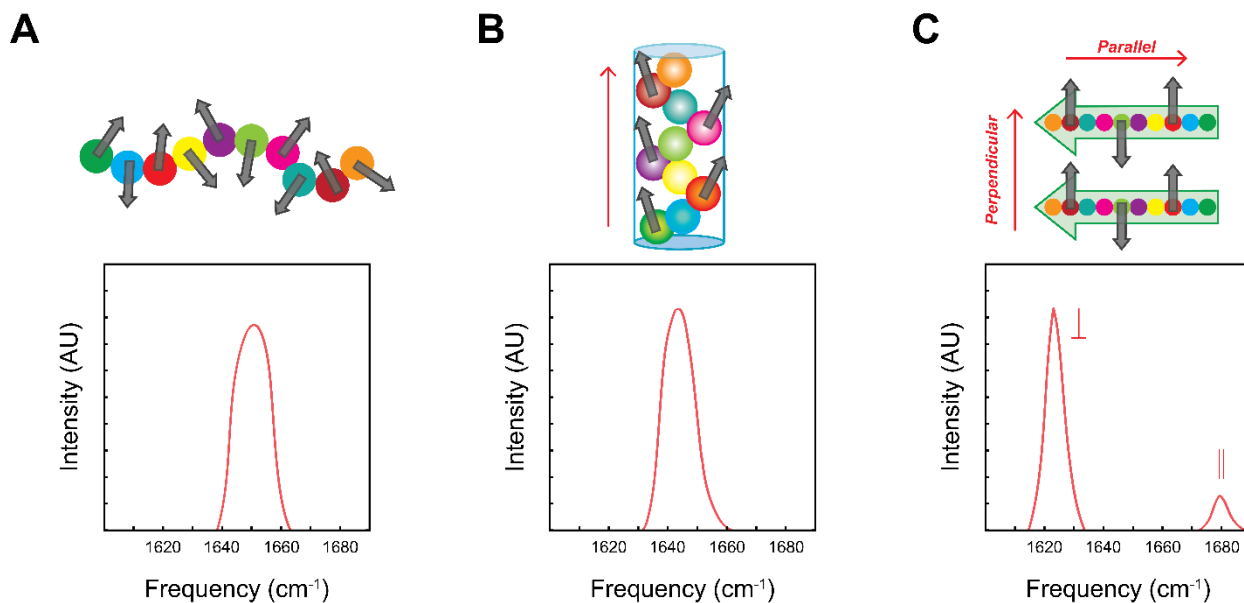


Figure 1.3 Infrared signatures for protein secondary structures. In each cartoon, the black and red arrows represent the local and normal modes, respectively. (A) Disordered structures are characterized by a broad amide I mode centered at $\sim 1650\text{ cm}^{-1}$. (B) The amide I mode for α -helical structures is centered $\sim 1645\text{ cm}^{-1}$. (C) β -sheets have two IR-active modes perpendicular (ν_{\perp} , $\sim 1620\text{ cm}^{-1}$) and parallel (ν_{\parallel} , $\sim 1680\text{ cm}^{-1}$) to the fibril axis.

1.5 Two-dimensional infrared spectroscopy can provide more insight into protein structure and dynamics

Two-dimensional infrared (2D IR) spectroscopy has additional advantages over linear IR methods for protein studies.^{55,61} In 2D IR, the vibrational spectrum is spread over two frequency axes, which can decouple and reveal new features hidden in linear spectra. In this technique, a molecular vibration is first excited and probed after a short waiting time; the resulting 2D spectrum is plotted as a function of excitation (“pump”) and detection (“probe”) frequencies. Spectral features, such as frequencies, intensities, lineshapes, anharmonicities, and crosspeaks, can be examined to better understand the underlying molecular structure and dynamics.^{62–64} Another advantage of 2D IR over linear IR is that an additional vibrational transition is probed. In linear

IR, only the fundamental transition ($0 \rightarrow 1$) is detected. By adding the “detection” pulse, 2D IR also probes the excited state absorption transition (ESA, $1 \rightarrow 2$). The anharmonicity, or energy difference between the fundamental and ESA peak pair, can provide additional molecular information and is directly read from the 2D spectrum.⁶⁵

It is often useful to plot a diagonal trace to examine the intensity amplitude in specific regions of interest in a 2D IR spectrum. When the diagonal line intersects the fundamental transition, the resultant information is comparable to linear IR measurements. However, there are a few critical differences between the diagonal trace of a 2D IR spectrum (plotted along the fundamental transition) and a linear IR spectrum, including spectral resolution and 1D lineshapes.⁵⁶ 2D IR has improved sensitivity compared to linear IR because the signal strength (i.e., transition dipole moment, $|\mu|$) is proportional to the number of light interactions ($|\mu|^4$ in 2D IR versus $|\mu|^2$ in linear IR).⁶⁶ This allows for weaker signals, like sidechains and isotope-labeled residues, to be resolved with 2D IR in the amide I' region.^{66–68} Additionally, lineshapes in the diagonal trace and linear IR spectrum may differ.^{56,69} In contrast to linear IR, 2D IR reveals multidimensional lineshapes, which can decouple homogeneous and inhomogeneous broadening that arise from different molecular interactions.⁶⁹

An example 2D IR spectrum of a model protein, hen egg white lysozyme (HEWL), is shown below in Figure 1.4. HEWL is a relatively small (129 residues, ~14.3 kDa) model protein. Its native secondary structure is predominately helical, with smaller contributions from disordered and β -sheet structures (Figure 1.4A).⁷⁰ The predominant helix/coil character is reflected by the amide I' frequency at ~1660 cm^{-1} . In addition to this intense mode, there are two weaker vibrational signals at ~1580 cm^{-1} and ~1550 cm^{-1} . The ~1580 cm^{-1} mode is characteristic of specific sidechain

(SC) modes, like aspartic/glutamic acid and arginine, all of which are present in lysozyme.⁷⁰ The weak mode at $\sim 1550\text{ cm}^{-1}$ arises from the non-deuterated amide II (A2) mode.

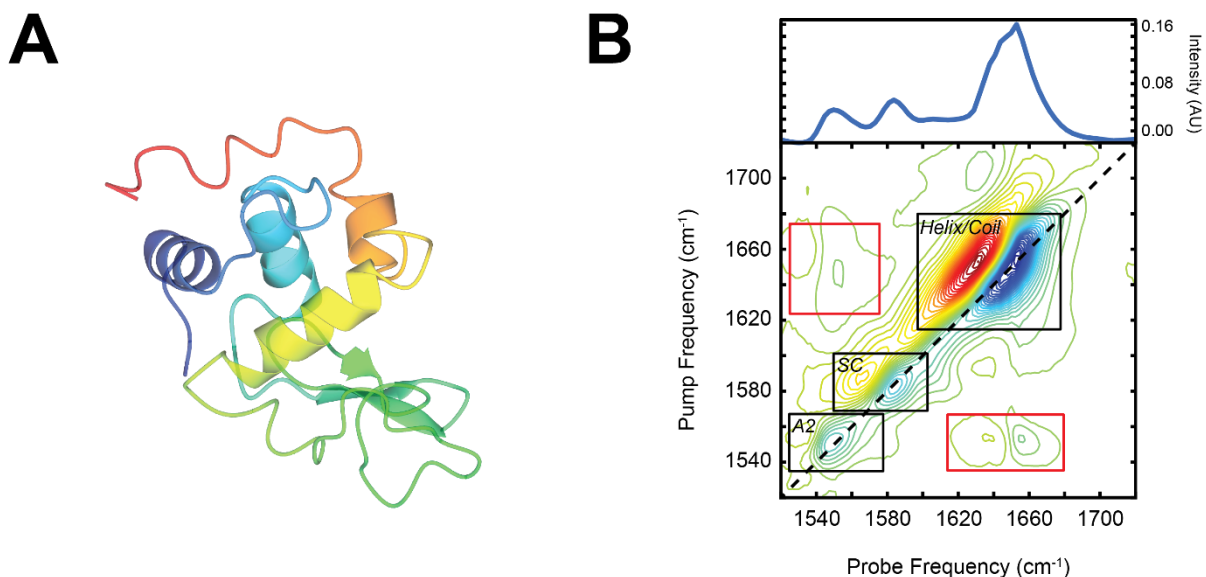


Figure 1.4 2D IR spectrum of a model protein. (A) Protein Data Bank structure for hen egg white lysozyme (HEWL, PDB code: 1DPX). (B) Diagonal trace (above) and 2D spectrum (below) of HEWL. Features along the diagonal are denoted by black boxes. Crosspeaks denoting energy transfer between the amide I' and II modes are highlighted in red boxes.

In addition to structural information, 2D IR can also capture dynamic changes within peptides and proteins. When combined with mid-IR pulse shaping, 2D IR can monitor how protein structures evolve in real time. For example, the union of 2D IR with pulse shaping has captured novel information during the misfolding of polypeptides into amyloid fibrils, which is implicated in diseases like type II diabetes.⁷¹ Revealing local residues and sequences involved in specific pathways of amyloid formation is crucial for a better understanding of protein-misfolding diseases and potential therapeutic solutions. In addition to tracking evolving protein structures, 2D IR can reveal dynamic changes in the water environment surrounding and embedded within proteins.

Water molecules are known to mediate protein stability and binding interactions; thus, revealing water motions is fundamental for a more complete knowledge of protein structure, dynamics, and function.^{72,73} For example, 2D IR waiting studies have uncovered subpicosecond water motions in ion channels.^{74,75} Systematically varying the waiting time between the excitation and detection pulses in the 2D IR pulse sequence reveals dynamical changes on the subpicosecond timescale, which is consistent with hydrogen bond breaking and formation.^{74–76} Thus, 2D IR waiting time measurements are sensitive to hydrogen bonding fluctuations and, in turn, the surrounding water environment. When implemented with isotope labeling, 2D IR can expose local water dynamics near particular residues.^{74,75} Elucidating restricted water motions in proteins is critical for understanding certain functions, as in the case of the influenza A M2 proton channel.^{74–76}

1.6 Isotopes can be implemented as site-specific probes for protein IR studies

Infrared spectroscopy is a bulk technique. Only global changes in protein secondary structure can be examined through the amide I' mode. Even with improved spectral resolution, 2D IR alone cannot resolve individual residues, which could neglect critical details about the system. The structural resolution of IR spectroscopy can be improved when coupled with vibrational probes. Vibrational probes alter the mass of the oscillating atom and thus appear as isolated transitions in IR spectra. Examples of vibrational probes include unnatural azido and cyano groups, which are conveniently located in a biologically-transparent frequency window.^{77–79} While useful, these probes may alter natural protein vibrations, depending on the protein system and placement. Isotopes can be employed as vibrational probes with minimal perturbation to protein structure and dynamics. For short peptides, isotopes, such as ¹³C and ¹³C¹⁸O, can be site-specifically inserted into the peptide backbone or into sidechain groups, although sidechain substitution is less common. Incorporating heavier atoms into the peptide backbone redshifts the amide I' mode,

spectroscopically isolating the residue. Examining spectral changes (frequency shifts, intensity changes, lineshapes, etc.) in the labeled residue can provide additional information about local structure and environment.^{66,80} Isotope labeling can also help distinguish between helical and disordered secondary structures, which is difficult due to the overlapping amide I' frequency ranges (Figure 1.3A and B).

1.7 Outline

This dissertation outlines my graduate research which has focused on (1) monitoring detailed structural changes in a model α -helical peptide (MAHP), (2) establishing conditions to study peptide and protein structural changes in the presence of nanoparticles, specifically gold colloids, and (3) studying conformational and dynamical changes in specific residues within a transmembrane α -helix. For each of these studies, 2D IR spectroscopy was the primary technique used to study molecular changes in these systems. In Chapter 2, I will outline the experimental details for peptide sample preparation and the implementation of 2D IR spectroscopy. Chapter 3 will focus on the structural characterization of MAHP, which also employs isotope labeling, to distinguish between random coil and helical structures. Chapter 4 will discuss the initial sample preparation methods for examining peptide and protein structure in the presence of nanoparticles, specifically gold colloids, with 2D IR spectroscopy. Chapter 5 will outline the initial work to investigate dynamical changes within the transmembrane peptide of the influenza A matrix 2 (AM2TM) proton channel protein, which was in collaboration with the DeGrado Group at the University of California at San Francisco (UCSF). Chapter 6 will summarize my findings and provide an outlook for future 2D IR studies.

1.8 References

- (1) Walmsley, S. J. et al. Comprehensive Analysis of Protein Digestion Using Six Trypsins Reveals the Origin of Trypsin as a Significant Source of Variability in Proteomics. *J. Prot. Res.*, **2013**, 12 (12), 5666–5680.
- (2) Li, M. and Zheng, W. All-Atom Molecular Dynamics Simulations of Actin-Myosin Interactions: A Comparative Study of Cardiac α Myosin, β Myosin, and Fast Skeletal Muscle Myosin. *Biochem.*, **2013**, 52 (47), 8393–8405.
- (3) Perutz, B. M. F. et al. Structure of Haemoglobin: A Three-Dimensional Fourier Synthesis at 5.5-Å Resolution, Obtained by X-Ray Analysis. *Nature*, **1960**, 185, 416–422.
- (4) Doyle, D. A. et al. The Structure of the Potassium Channel: Molecular Basis of K^+ Conduction and Selectivity. *Science*, **1998**, 280 (5360), 69–77.
- (5) Lullo, G. A. Di et al. Mapping the Ligand-Binding Sites and Disease-Associated Mutations on the Most Abundant Protein in the Human, Type I Collagen. *J. Biol. Chem.*, **2002**, 277 (6), 4223–4231.
- (6) Kim, J. M. et al. Structure and Function in Rhodopsin: Rhodopsin Mutants with a Neutral Amino Acid at E134 Have a Partially Activated Conformation in the Dark State. *Proc. Natl. Acad. Sci. U. S. A.*, **1997**, 94 (26), 14273–14278.
- (7) Schnell, H. M. et al. Structures of Chaperone-Associated Assembly Intermediates Reveal Coordinated Mechanisms of Proteasome Biogenesis. *Nat. Struct. Mol. Biol.*, **2021**, 28 (5), 418–425.
- (8) Langan, P. S. et al. Anomalous X-Ray Diffraction Studies of Ion Transport in K^+ Channels. *Nat. Commun.*, **2018**, 9 (1), 1–5.
- (9) Murphy, M. P. and Levine, H. Alzheimer's Disease and the Amyloid- β Peptide. *J. Alz. Dis.*, **2010**, 19 (1), 311–323.
- (10) Chaari, A. and Ladjimi, M. Human Islet Amyloid Polypeptide (HIAPP) Aggregation in Type 2 Diabetes: Correlation between Intrinsic Physicochemical Properties of HIAPP Aggregates and Their Cytotoxicity. *Int. J. Biol. Macromol.*, **2019**, 136, 57–65.
- (11) Meehan, S. et al. Amyloid Fibril Formation by Lens Crystallin Proteins and Its Implications for Cataract Formation. *J. Biol. Chem.*, **2004**, 279 (5), 3413–3419.
- (12) You, A. et al. Copper in Glazes of Renaissance Luster Pottery: Nanoparticles, Ions, and Local Environment. *J. Appl. Phys.*, **2003**, 93 (12), 10058–10063.
- (13) Wagner, F. E. et al. Before Striking Gold in Gold-Ruby Glass. *Nat. Comm.*, **2000**, 407, 691–692.
- (14) Perez-Arantequi, J. et al. Luster Pottery from the Thirteenth Century to the Sixteenth Century: A Nanostructured Thin Metallic Film. *J. Am. Ceram. Soc.*, **2001**, 84 (2), 442–446.
- (15) Siddiqui, J. et al. Nanomaterials in Smart Packaging Applications: A Review. *Small*, **2022**, 18, 1–34.
- (16) Iqbal, A. and Ul, A. A Review Featuring the Fundamentals and Advancements of Polymer/CNT Nanocomposite Application in Aerospace Industry. *Polym. Bull.*, **2021**, 78 (1), 539–557.

- (17) Newman, M. D. et al. The Safety of Nanosized Particles in Titanium Dioxide and Zinc Oxide Based Sunscreens. *J. Am. Derm.*, **2009**, 61 (4), 685–692.
- (18) Katz, L. M. et al. Nanotechnology in Cosmetics. *Food Chem. Toxicol.*, **2015**, 85, 127–137.
- (19) Ko, Y. H. et al. Environmentally Friendly Quantum-Dot Color Filters for Ultra-High-Definition Liquid Crystal Displays. *Sci. Rep.*, **2020**, 1–8.
- (20) Honarvar, Z. et al. Nanocomposites in Food Packaging Applications and Their Risk Assessment for Health. *Electr. Phys.*, **2016**, 8 (6), 2531–2538.
- (21) El-Hamadi, M. and Schätzlein, A. G. Nanoparticles in Medical Imaging. *Fundam. Pharm. Nanosci.*, **2013**, 6 (11), 543–566.
- (22) Jong, W. H. De. Drug Delivery and Nanoparticles: Applications and Hazards. *Int. J. Nanomed.*, **2008**, 3 (2), 133–149.
- (23) Lim, D.; Jeon, K.; Kim, H. M.; Nam, J.; Suh, Y. D. Nanogap-Engineerable Raman-Active Nanodumbbells for Single-Molecule Detection. *Nat. Mater.*, **2010**, 9, 60–67.
- (24) Shao, L. et al. Gold Nanoparticle Wires for Sensing DNA and DNA/Protein Interactions. *Nanoscale*, **2014**, 6, 4089–4095.
- (25) Huang, R. et al. Effects of Surface Compositional and Structural Heterogeneity on Nanoparticle-Protein Interactions: Different Protein Configurations. *ACS Nano*, **2014**, 8 (6), 5402–5412.
- (26) Pershina, A. G. et al. Magnetic Nanoparticles – DNA Interactions: Design and Applications of Nanobiohybrid Systems. *Russ. Chem. Rev.*, **2014**, 83 (4), 299–322.
- (27) He, Q. et al. Interfacing DNA with Nanoparticles: Surface Science and Its Applications in Biosensing. *Int. J. Biol. Macromol.*, **2020**, 151, 757–780.
- (28) Hill, R. A. et al. Protein Interactions with Nanoparticle Surfaces: Highlighting Solution NMR Techniques. *Isr. J. Chem.*, **2019**, 59 (11–12), 962–979.
- (29) Saha, D. et al. Tuning of Silica Nanoparticle – Lysozyme Protein Complexes in the Presence of the SDS Surfactant. *Soft Matter*, **2022**, 18, 434–445.
- (30) Monopoli, M. P. et al. Biomolecular Coronas Provide the Biological Identity of Nanosized Materials. *Nat. Nanotechnol.*, **2012**, 7, 779–786.
- (31) Ju, Y. et al. Person-Specific Biomolecular Coronas Modulate Nanoparticle Interactions with Immune Cells in Human Blood. *ACS Nano*, **2020**, 14, 15723–15737.
- (32) Lu, X. et al. Tailoring the Component of Protein Corona via Simple Chemistry. *Nat. Comm.*, **2019**, 10, 1–14.
- (33) Corbo, C. et al. Unveiling the In Vivo Protein Corona of Circulating Leukocyte-like Carriers. *ACS Nano*, **2017**, 11, 3262–3273.
- (34) Schöttler, S. et al. Protein Adsorption is Required for Stealth Effect of Poly(Ethylene Glycol)- and Poly(Phosphoester)-Coated Nanocarriers. *Nat. Nanotech.*, **2016**, 11, 372–377.
- (35) Rampado, R. et al. Recent Advances in Understanding the Protein Corona of Nanoparticles and in the Formulation of “Stealthy” Nanomaterials. *Front. Bioeng. Biotech.*, **2020**, 8, 1–19.
- (36) Fleischer, C. C. and Payne, C. K. Secondary Structure of Corona Proteins Determines the Cell Surface Receptors Used by Nanoparticles. *J. Phys. Chem. B*, **2014**, 118, 14017–14026.

- (37) Park, S. J. Protein – Nanoparticle Interaction: Corona Formation and Conformational Changes in Proteins on Nanoparticles. *Int. J. Nanomed.*, **2020**, 15, 5783–5802.
- (38) Deng, Z. J. et al. Nanoparticle-Induced Unfolding of Fibrinogen Promotes Mac-1 Receptor Activation and Inflammation. *Nat. Nanotech.*, **2011**, 6, 39–44.
- (39) Kim, Y. et al. How Do the Size, Charge and Shape of Nanoparticles Affect Amyloid β Aggregation on Brain Lipid Bilayer? *Sci. Rep.*, **2016**, 6, 1–14.
- (40) John, T. et al. Impact of Nanoparticles on Amyloid Peptide and Protein Aggregation: A Review with a Focus on Gold Nanoparticles. *Nanoscale*, **2018**, 10 (45), 20894–20913.
- (41) Konar, M. et al. Effect of Silica Nanoparticles on the Amyloid Fibrillation of Lysozyme. *ACS Omega*, **2019**, 4, 1015–1026.
- (42) Yang, J. et al. Cevipabulin-Tubulin Complex Reveals a Novel Agent Binding Site on α -Tubulin with Tubulin Degradation Effect. *Sci. Adv.*, **2021**, 7, 1–12.
- (43) Road, H. et al. Model for the Structure of Bacteriorhodopsin Based on High-Resolution Electron Cryo-Microscopy. *J. Mol. Biol.*, **1990**, 213, 899–929.
- (44) Johnson, C. N. et al. Mechanism of Calmodulin Modulation of the Human Cardiac Sodium Channel. *Struct. Des.*, **2018**, 26 (5), 683–694.
- (45) Kim, J. G. et al. Protein Structural Dynamics Revealed by Time-Resolved X-Ray Solution Scattering. *Acc. Chem. Res.*, **2015**, 48 (8), 2200–2208.
- (46) Dandey, V. P. et al. Time-Resolved Cryo-EM Using Spotiton. *Nat. Methods*, **2020**, 17 (9), 897–900.
- (47) Sun, M. et al. A Time-Resolved Cryo-EM Study of *Saccharomyces Cerevisiae* 80S Ribosome Protein Composition in Response to a Change in Carbon Source. *Proteomics*, **2021**, 21 (2), 1–9.
- (48) Pinotsi, D. et al. Proton Transfer and Structure-Specific Fluorescence in Hydrogen Bond- Rich Protein Structures. *J. Am. Chem. Soc.*, **2016**, 138, 3046–3057.
- (49) Pescitelli, G. et al. Inherent Chirality Dominates the Visible/Near-Ultraviolet CD Spectrum of Rhodopsin. *J. Am. Chem. Soc.*, **2008**, 130, 6170–6181.
- (50) Toseland, C. P. Fluorescent Labeling and Modification of Proteins. *J. Chem. Biol.*, **2013**, 6, 85–95.
- (51) Surewicz, W. K. et al. Determination of Protein Secondary Structure by Fourier Transform Infrared Spectroscopy: A Critical Assessment. *Biochem.*, **1993**, 32 (2), 389–394.
- (52) Kim, S. K. et al. Insulin Dimer Dissociation and Unfolding Revealed by Amide I Two-Dimensional Infrared Spectroscopy. *Phys. Chem. Chem. Phys.*, **2010**, 12, 3579–3588.
- (53) Alperstein, A. M. et al. Amyloid Found in Human Cataracts with Two-Dimensional Infrared Spectroscopy. *Proc. Natl. Acad. Sci. USA*, **2019**, 116 (14), 6602–6607.
- (54) Hayashi, T. and Mukamel, S. Vibrational – Exciton Couplings for the Amide I, II, III, and A Modes of Peptides. *J. Phys. Chem. B*, **2007**, 111, 11032–11046.
- (55) Ghosh, A. et al. Watching Proteins Wiggle: Mapping Structures with Two-Dimensional Infrared Spectroscopy. *Chem. Rev.*, **2017**, 117 (16), 10726–10759.
- (56) Baiz, C. R. et al. An Introduction to Protein 2D IR Spectroscopy. *Ultrafast Infrared Vib. Spectrosc.*, **2013**, 22, 361–403.

- (57) Gnanakaran, S. et al. Nature of Structural Inhomogeneities on Folding a Helix and Their Influence on Spectral Measurements. *Proc. Natl. Acad. Sci. U. S. A.*, **2004**, 101 (25), 9229–9234.
- (58) Cheatum, C. M. et al. Signatures of β -Sheet Secondary Structures in Linear and Two-Dimensional Infrared Spectroscopy. *J. Chem. Phys.*, **2004**, 120 (17), 8201–8215.
- (59) Falvo, C. et al. Frequency Distribution of the Amide-I Vibration Sorted by Residues in Amyloid Fibrils Revealed by 2D-IR Measurements and Simulations. *J. Phys. Chem. B*, **2012**, 116, 3322–3330.
- (60) Phys, J. C. et al. Amide I Two-Dimensional Infrared Spectroscopy of b-Hairpin Peptides. *J. Chem. Phys.*, **2007**, 126, 1–11.
- (61) Thielges, M. C. Transparent Window 2D IR Spectroscopy of Proteins. *J. Chem. Phys.*, **2021**, 155, 1–14.
- (62) Guo, Q. et al. Line Shape Analysis of Two-Dimensional Infrared Spectra. *J. Chem. Phys.*, **2015**, 142, 1–13.
- (63) Price, D. A. et al. Polarization Dependence of 2D IR Cross-Peaks Distinguishes Parallel-Stranded and Antiparallel-Stranded DNA G-Quadruplexes. *Spectrochim. Act. A Mol. Biomol. Spec.*, **2022**, 267 (2), 1–21.
- (64) He, W. et al. Picosecond Dynamics of a Membrane Protein Revealed by 2D IR. *Proc. Natl. Acad. Sci. USA*, **2006**, 103 (10), 13909–13914.
- (65) Meng, K. and Wang, J. Anharmonic Overtone and Combination States of Glycine and Two Model Peptides Examined by Vibrational Self-Consistent Field Theory. *Phys. Chem. Chem. Phys.*, **2011**, 13, 2001–2013.
- (66) Shim, S. et al. Two-Dimensional IR Spectroscopy and Isotope Labeling Defines the Pathway of Amyloid Formation with Residue-Specific Resolution. *Proc. Natl. Acad. Sci.*, **2009**, 106 (16), 6614–6619.
- (67) Ghosh, A. et al. 2D IR Spectroscopy of Histidine: Probing Side-Chain Structure and Dynamics via Backbone Amide Vibrations. *J. Phys. Chem. B*, **2014**, 118 (28), 7799–7805.
- (68) Flanagan, J. C. and Baiz, C. R. Site-Specific Peptide Probes Detect Buried Water in a Lipid Membrane. *Biophys. J.*, **2019**, 116 (9), 1692–1700.
- (69) Tokmakoff, A. Two-Dimensional Line Shapes Derived from Coherent Third-Order Nonlinear Spectroscopy. *J. Phys. Chem. A*, **2000**, 104 (18), 4223–4235.
- (70) Weiss, M. S. et al. Crystallization, Structure Solution and Refinement of Hen Egg-White Lysozyme at pH 8.0 in the Presence of MPD. *Acta Cryst.*, **2000**, 56, 952–958.
- (71) Buchanan, L. E. et al. Mechanism of IAPP Amyloid Fibril Formation Involves an Intermediate with a Transient β -Sheet. *Proc. Natl. Acad. Sci. U. S. A.*, **2013**, 110 (48), 19285–19290.
- (72) Levy, Y. and Onuchic, J. N. Water and Proteins: A Love-Hate Relationship. *Proc. Natl. Acad. Sci. U. S. A.*, **2004**, 101 (10), 3325–3326.
- (73) Levy, Y. and Onuchic, J. N. Water Mediation in Protein Folding and Molecular Recognition. *Annu. Rev. Biophys. Biomol. Struct.*, **2006**, 35 (1), 389–415.
- (74) Ghosh, A. et al. Tidal Surge in the M2 Proton Channel, Sensed by 2D IR Spectroscopy. *Proc. Natl. Acad. Sci.*, **2011**, 108 (15), 6115–6120.

- (75) Ghosh, A. et al. 2D IR Spectroscopy Reveals the Role of Water in the Binding of Channel-Blocking Drugs to the Influenza M2 Channel. *J. Chem. Phys.*, **2014**, 235105 (140), 1–9.
- (76) Ghosh, A. and Hochstrasser, R. M. A Peptide's Perspective of Water Dynamics. *Chem. Phys.*, **2011**, 390 (1), 1–13.
- (77) Schmitz, A. J. et al. Two-Dimensional Infrared Study of Vibrational Coupling between Azide and Nitrile Reporters in a RNA Nucleoside. *J. Phys. Chem. B*, **2016**, 120, 9387–9394.
- (78) Chalyavi, F. et al. Synthesis of 5-Cyano-Tryptophan as a Two-Dimensional Infrared Spectroscopic Reporter of Structure. *Angew. Chem. Int. Ed.*, **2018**, 57, 7528–7532.
- (79) Sueur, A. L. et al. Evaluation of p-(¹³C, ¹⁵N-Cyano)Phenylalanine as an Extended Time Scale 2D IR Probe of Proteins. *Anal. Chem.*, **2017**, 89, 5254–5260.
- (80) Arkin, I. T. Isotope-Edited IR Spectroscopy for the Study of Membrane Proteins. *Curr. Opin. Chem. Bio.*, **2006**, 10, 394–401.

Chapter 2. Experimental Methods

2.1 Introduction

I have learned a broad range of experimental methods throughout graduate school. For example, I have prepared, purified, and characterized countless peptide samples over the past few years. Specifically, I've regularly utilized a Liberty Blue™ Automated Microwave-Assisted peptide synthesizer, high performance liquid chromatography (HPLC) system, and an electrospray-ionization mass spectrometer. I've also explored how to isotope label amino acids and incorporate them into peptides. In addition to these wet lab procedures, I have a great deal of experience operating and troubleshooting an ultrafast 2D IR spectrometer. In this chapter, I have outlined the theoretical and experimental details for these methods.

2.2 Preparation of peptide samples

2.2.1 Isotope labeling

Isotope labeling is a powerful tool to extract detailed information about protein structure and dynamics using vibrational spectroscopies.¹⁻⁴ Specifically, isotope editing the peptide backbone can reveal residue-specific vibrational events.^{5,6} Molecular vibrations are highly dependent upon the oscillator's reduced mass; therefore, isotope-labeled modes appear spectrally isolated from the bulk transition. For infrared protein studies, the amide I' mode (which arises from mostly backbone carbonyl stretching) is often examined because it correlates to secondary structure.⁷ Therefore, both ^{13}C and $^{13}\text{C}^{18}\text{O}$ isotopes alter the amide I' vibrational frequency. However, the $^{13}\text{C}^{18}\text{O}$ isotope is typically more advantageous for single label studies. One advantage is that $^{13}\text{C}^{18}\text{O}$ has a low natural abundance (~1% for ^{13}C and ~0.2% for ^{18}O), making it

unlikely to occur at a random position along the peptide chain. Additionally, incorporating a $^{13}\text{C}^{18}\text{O}$ backbone-labeled residue redshifts the amide I' mode further ($\sim 60\text{ cm}^{-1}$ compared to $\sim 40\text{ cm}^{-1}$ for ^{13}C). Unfortunately, the $^{13}\text{C}^{18}\text{O}$ label is not commercially available and must be synthesized by an ^{18}O -exchange starting with the ^{13}C - C_α amino acid.⁸ It is also critical to note that some sidechains, specifically ones containing carboxylates (aspartic and glutamic acid) and arginine, absorb strongly in this region ($\sim 1570\text{--}1610\text{ cm}^{-1}$).⁹ In this scenario, isotope labeling should be carefully considered.

Amino acids with hydrophobic and unreactive sidechains are often used for isotope labeling the peptide backbone (alanine, glycine, phenylalanine, leucine, isoleucine, and valine). It is possible to label reactive sidechains, but it is more expensive and time consuming.^{10,11} The general process for isotope labeling an amino acid is as follows: (1) N-terminal protection of the ^{13}C - C_α amino acid amino group with a 9-fluorenylmethoxycarbonyl (Fmoc) group; (2) two to three washes with Milli-Q H_2O by vacuum filtration to remove excess salts; (3) characterization with ESI-MS; (4) three rounds of ^{18}O -exchange with the Fmoc-protected ^{13}C - C_α amino acid; (5) centrifugation with cold, dry diethyl ether to remove organic salts; and (6) final ESI-MS characterization. I've found that after the protection and ^{18}O -exchange reactions, it is important to wash the product several times to remove excess salts present (steps 2 and 5) before characterization with mass spectrometry. Undesired Na^+ and K^+ salts reduce the solution's vapor pressure, in turn lowering the analyte signal in the mass spectrum. This results in an incorrect ^{18}O -exchange efficiency value. Salts also artificially inflate the product's mass, which can be detrimental for the coupling reactions during peptide synthesis.

2.2.1.1 Fmoc protection of the N-terminal amino group

It is essential for all amino acids to have an Fmoc protecting group to be compatible with Fmoc solid-phase peptide synthesis (SPPS). Fmoc-protected $^{13}\text{C}-\text{C}_\alpha$ amino acids are commercially available, but they are quite expensive (\$500–600 per gram). Unprotected $^{13}\text{C}-\text{C}_\alpha$ amino acids can be purchased at a lower cost (~\$200–300 per gram) and the Fmoc protecting group can be synthetically added in a simple one pot reaction.¹² The Fmoc protection reaction of a $^{13}\text{C}-\text{C}_\alpha$ amino acid I have used, which was adapted from literature, is shown in Figure 2.1.¹² In this reaction, equimolar amounts of the amino acid, sodium bicarbonate (NaHCO_3), and 9-Fluorenylmethyl *N*-succinimidyl carbonate (Fmoc-OSu) were combined and dissolved using a 1 to 1 mixture of Milli-Q H_2O and acetone (30 mL total volume). This reaction was performed on a 10 millimolar (mmol) scale with respect to the amino acid (~1 gram). For $^{13}\text{C}-\text{C}_\alpha$ alanine, this corresponds to 0.9009 grams of amino acid, 0.8401 grams of NaHCO_3 , and 3.3733 grams of Fmoc-OSu. After stirring for 24 hours at room temperature, the reaction was quenched with 2 M KHSO_4 until the pH was ~2 (~3 mL of 2 M KHSO_4). Under acidic conditions, the Fmoc-protected ^{13}C alanine precipitated out of the solution. The white and fluffy precipitate was immediately transferred to a filter flask and washed with cold Milli-Q water (~50 mL). This washing procedure helped remove excess salts present from the NaHCO_3 and KHSO_4 reagents. The precipitate was rinsed with a small amount of acetone to help dry and transferred to a labeled and weighed (uncapped) 50-mL conical centrifuge tube. The product was frozen with liquid N_2 and lyophilized to remove residual solvent. This washing procedure was repeated at least one more time to help remove excess salts and lyophilized again to dry the product before characterization.

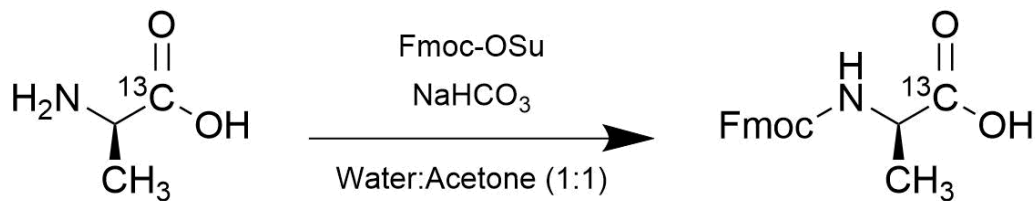


Figure 2.1 Fmoc protection of ^{13}C - C_α alanine. The amino acid is dissolved in 50/50 water/acetone and Fmoc-OSu and NaHCO_3 are added in equimolar amounts. The Fmoc-protected amino acid is precipitated out with KHSO_4 after 24 h and washed several times with deionized water to remove excess salts.

After the product was washed, the successful addition of the Fmoc group onto the amino acid was confirmed by electrospray-ionization mass spectrometry in positive ion mode. ESI-MS is an excellent characterization tool for readily-ionizable molecules, like isotope-labeled amino acids and peptides. ESI-MS is a soft ionization method, meaning the analytes do not fragment during the ionization process. The lack of fragmentation makes data analysis of biomolecules much easier to interpret, compared to traditional hard ionization techniques. In ESI, a liquid sample flows through a capillary with an applied high voltage, forming tiny charged droplets. The charged droplets are desolvated with a heating gas, decreasing the size and increasing the charge density. Upon the Rayleigh limit, where the charge repulsions are maximized, the droplets burst apart into gas phase ions. The gas phase ions are separated by a mass analyzer and further detected.

An appropriate sample concentration for this technique is $\sim 10 \mu\text{g}$ analyte per mL of solution, which is prepared by serial dilutions. To prepare the sample stock solution, $\sim 1 \text{ mg}$ of Fmoc ^{13}C - C_α amino acid was dissolved in 1 mL of a 70% acetonitrile and 30% water mixture. It is important to note here that only high purity solvents should be used with MS instrumentation; impurities present in lower solvent grades can negatively impact the experimental accuracy and reproducibility and lead to instrument damage. Additionally, the sensitivity of this technique is

enhanced when a volatile solvent mixture is employed instead of 100% water (e.g., 70% acetonitrile with 30% water) due to the decreased surface tension of the solvent mixture.

The ~1 mg/mL amino acid stock solution was vortexed until fully dissolved. If the sample does not dissolve, further dilute the stock by adding more solvent and note the final concentration. Additionally, the stock solution can be centrifuged for ~10 minutes and the supernatant can be used to prepare the dilution. A 10 µg/mL sample solution was prepared by mixing 10 µL of stock (1 mg/mL), 989 µL of solvent (70% acetonitrile in water), and 1 µL of concentrated formic acid, which helps with protonation/ionization. The diluted sample was characterized by ESI-MS. A mass spectrum of a representative Fmoc-protected ^{13}C - C_α alanine sample is shown in Figure 2.2.

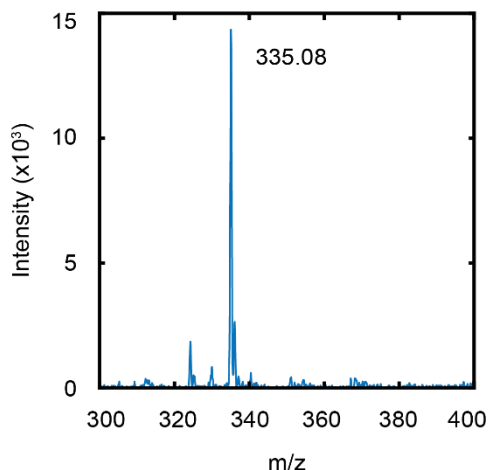


Figure 2.2 Mass spectrum of Fmoc ^{13}C - C_α alanine. The signal at 335.08 m/z is assigned to the $[\text{M}+\text{Na}]^+$ adduct, confirming the successful Fmoc protection of the amine. The molecular weight of Fmoc ^{13}C - C_α alanine is 312 g/mol.

2.2.1.2 ^{18}O -exchange with an Fmoc-protected ^{13}C - C_α amino acid

To prepare the $^{13}\text{C}^{18}\text{O}$ label, the oxygens (^{16}O) in the Fmoc-protected ^{13}C - C_α amino acid are exchanged with heavier isotopes (^{18}O) through an acid-catalyze exchange.⁸ Unlike with the

Fmoc-protection reaction, this reaction is sensitive to water, even from residual water vapor present in the air. Therefore, Schlenk techniques must be used for this reaction. A Schlenk line and appropriate glassware with constant N_2 (g) flow must be used along with dry reagents. Usually, small quantities of reagents are purchased and used immediately to ensure water is not introduced. Additionally, the catalyst (4 M HCl) in dioxane is particularly air and water-sensitive, so it is best to purchase small volumes of this reagent and use it quickly. Prior to adding the reagents, the glassware is flamed dried (typically three times) under vacuum to remove residual water vapor. The ^{18}O -exchange reaction I've used, which was also modified from previous literature, is summarized in Figure 2.3.⁸

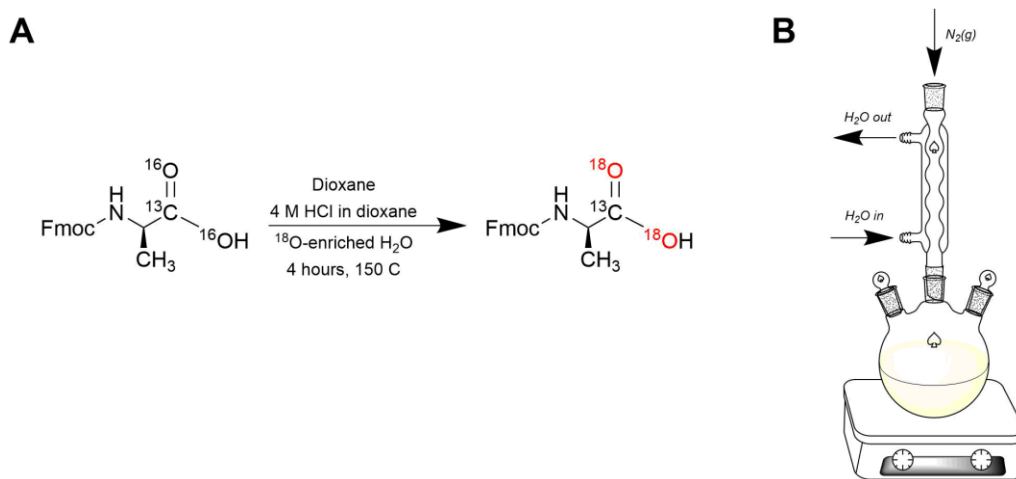


Figure 2.3 Reaction scheme and experimental setup for ^{18}O -exchange of Fmoc ^{13}C - C_{α} alanine. (A) Both ^{16}O oxygens present in the amino acid are exchanged with the heavier isotope from ^{18}O -enriched H_2O (98%) under acidic conditions at high temperature ($150\text{ }^{\circ}C$). (B) The apparatus for the ^{18}O -exchange reaction. A Schlenk line with appropriate glassware is used to minimize the solution's interaction with residual water.

The ^{18}O -exchange reaction is usually carried out on a 1-gram scale with respect to the amino acid. After the glassware was flamed dried three times, the amino acid was quickly added

to the 50-mL three-neck round bottom flask. Adding the amino acid this way does introduce minimal water vapor to the flask, but flame drying the reactant is not ideal, as it could decompose the starting material. Additionally, residual water present in the flask should evaporate during the reflux. After resealing the septum, the $N_2(g)$ port was opened to the apparatus. A mixture of dioxane (8 mL) and 4 M HCl in dioxane (4 mL) was used to dissolve the amino acid. The reagents were added under $N_2(g)$ atmosphere. The mixture was stirred and heated to $\sim 150^\circ C$. The reaction was heated for ~ 30 minutes before adding 1 mL of ^{18}O -enriched water ($\sim 98\%$). After refluxing 4 hours at $150^\circ C$, the round bottom flask was removed from the heat and cooled to room temperature (~ 20 minutes). The flask containing the light-yellow solution was removed from the condenser, frozen with $N_2(l)$, and lyophilized overnight to remove the solvent. This process was repeated, starting with the addition of dioxane and 4 M HCl in dioxane.

After the third exchange, the solution was transferred to a labeled and weighed 50-mL conical tube, frozen with $N_2(l)$, and lyophilized overnight. The dry product should appear slightly yellow or orange, due to HCl from the reaction. It is possible that an organic salt is also formed as a side product during this reaction. If the sample is darker in color (burnt orange or brown), there is likely more of this undesired side product that needs to be removed. The amino acid can be further purified by centrifugation with cold, dry diethyl ether. For this step, it is critical to use a new bottle of diethyl ether (with a sure seal if possible) to minimize the amount of water introduced to the sample, which can reverse the ^{18}O -exchange. To purify the exchanged amino acid, ~ 10 mL of cold, dry diethyl ether was added to the product and centrifuged at 5,000 rotations per minute (rpm) for 5 minutes. A miniscule amount of brown precipitate crashed out of solution, likely the impurity. The light yellow/brown supernatant was transferred to a new 50-mL conical tube and dried with compressed air. A light brown/yellow film remained in the conical tube, which was

resuspended in ~5 mL of cold, dry diethyl ether. The washes were repeated at least twice more, producing an off-white/light yellow precipitate each time.

ESI-MS was used to determine the labeling efficiency of each precipitate. The sample was prepared similarly to previously described with the Fmoc-protected amino acid, but using 100% acetonitrile as the solvent system, as introducing water reverts the ^{18}O -exchange process. Typically, three ^{18}O -exchanges result in ~90% or higher labeling efficiency, which is the lowest percentage desired for 2D IR studies. During the reaction, the two carboxylate oxygens (^{16}O) are exchanged with the heavier ^{18}O isotope. There is a mixture of three isotopic species present in solution: unlabeled ($^{13}\text{C}^{16}\text{O}^{16}\text{O}$), single labeled ($^{13}\text{C}^{16}\text{O}^{18}\text{O}$), and double labeled ($^{13}\text{C}^{18}\text{O}^{18}\text{O}$) amino acid. The two carboxylate oxygens are chemically equivalent due to resonance; this means that each oxygen is equally likely to form the amide bond during peptide synthesis. Therefore, a high yield of the double labeled amino acid ($^{13}\text{C}^{18}\text{O}^{18}\text{O}$) is necessary to ensure the desired residue is correctly labeled. Equation 2.1 is used to approximate the ^{18}O -labeling efficiency using the peak intensity ratios in the mass spectrum. An example of ^{18}O -enriched Fmoc ^{13}C - C_α alanine mass spectrum is shown in Figure 2.4.

$$\text{Labeling efficiency} = \frac{\text{Intensity} (^{13}\text{C}^{18}\text{O}^{18}\text{O} + \frac{1}{2} ^{13}\text{C}^{16}\text{O}^{18}\text{O})}{\text{Intensity} (^{13}\text{C}^{16}\text{O}^{16}\text{O} + ^{13}\text{C}^{16}\text{O}^{18}\text{O} + ^{13}\text{C}^{18}\text{O}^{18}\text{O})} \quad (2.1)$$

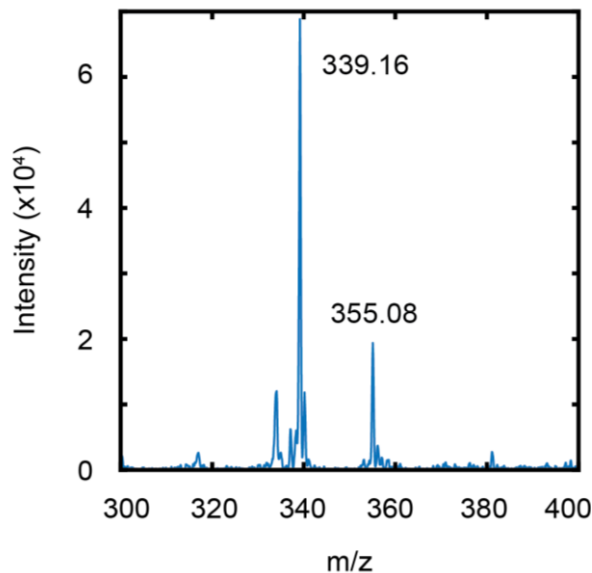


Figure 2.4 Mass spectrum of ¹⁸O-enriched Fmoc ¹³C-C_α alanine. The peak intensities of the Na⁺ species (339 m/z for double labeled, 337 m/z for the single labeled, and 335 m/z for unlabeled alanine) were used to calculate the ¹⁸O-labeling efficiency (93% for this sample). The smaller peak at 355.08 m/z is from the [M+K]⁺ adduct.

2.2.2 Fmoc solid-phase peptide synthesis

Prior to automated solid-phase peptide synthesis (SPPS), peptides were often synthesized by solution-phase methods or through bacterial expression. While these traditional methods are still valuable today, SPPS is often the method of choice for several reasons. SPPS is more efficient than traditional methods, both from time and cost perspectives.¹³ When coupled with automated synthesizers, the amount of reagent and solvent required is significantly reduced. For my research, I have exclusively used an automated, microwave-assisted peptide synthesizer from Liberty Blue™ (CEM, Matthews, NC, USA). Standard reagents and protocols for Fmoc synthesis (deprotection, activation, etc.) were directly obtained from CEM and were used without modification. SPPS theory and its experimental implementation are described in detail below.

An overview of the cyclic process of Fmoc SPPS is illustrated in Figure 2.5. This method involves a series of deprotection and coupling steps to sequentially build the peptide chain on a stationary resin.¹³ The resin is usually a polymer, like polyethylene glycol (PEG), with an attached acid-labile linker (Figure 2.5). Unlike natural protein expression, SPPS builds peptides from the C-terminus to the N-terminus. Therefore, the desired C-terminal chemistry (amidated or acidified) is dictated by the resin linker. For my work, I have used the Rink Amide ProTide resin (CEM, Matthews, NC, USA), which yields an amidated C-terminus upon cleavage with trifluoroacetic acid (TFA). The linker is protected with an Fmoc group, which must be removed before attaching the first amino acid. The initial deprotection step of the linker affords a free amine. The linker's free amine is then coupled with the carboxylic acid of C-terminal amino acid to form the first peptide bond. However, the carboxylic acid and amine do not readily undergo peptide bond formation. The carboxylic acid must first be "activated" into a more reactive species. This is achieved with two coupling reagents: an activator (diisopropylcarbodiimide, DIC) and an activator base (Oxyma). DIC converts the carboxylic acid to form an O-acylurea intermediate. Oxyma is then added, which attacks the carbonyl group of the DIC-activated amino acid, resulting in an Oxyma-activated amino acid ester and *N,N'*-diisopropylurea byproduct, which is washed away. The free amine on the linker attacks the carbonyl of the Oxyma-activated ester to form the desired peptide bond and regenerates Oxyma. The excess reagents are washed away immediately, leaving behind the first amino acid on the resin. The deprotection and coupling steps are repeated until the desired peptide sequence is obtained. A final deprotection step is required to remove the Fmoc protecting group on the N-terminal amino acid.

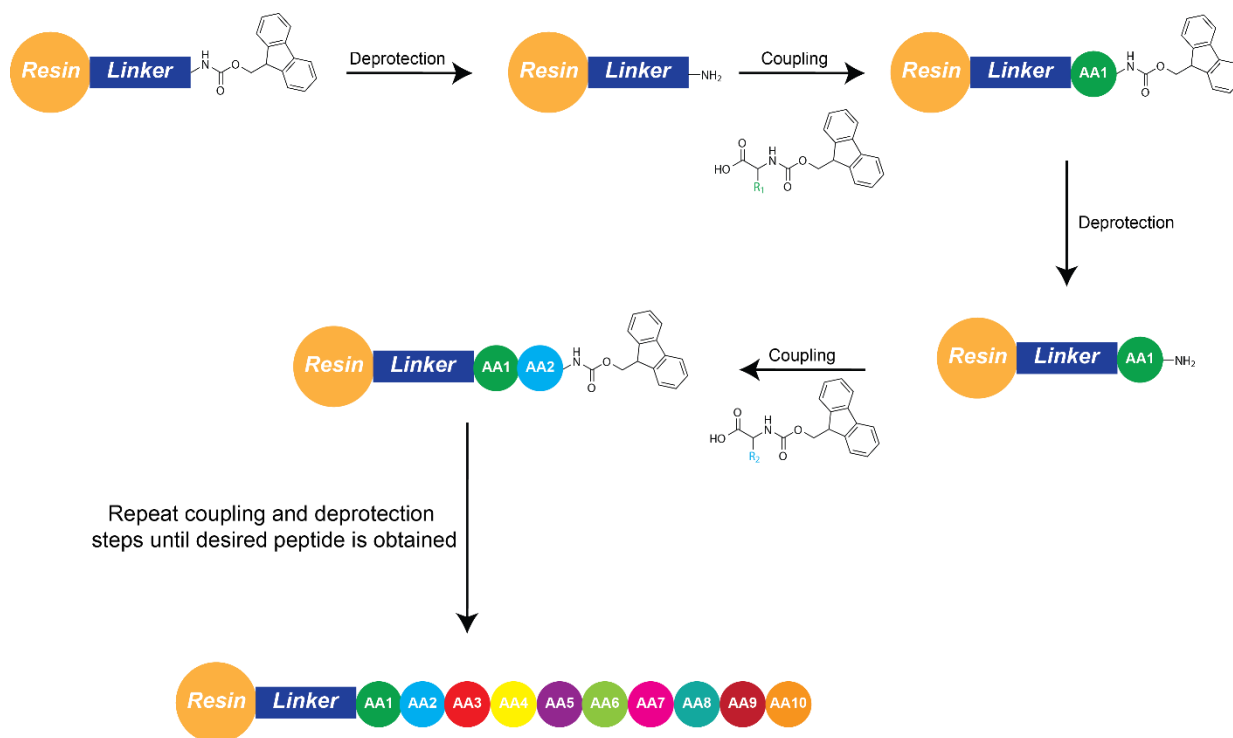


Figure 2.5 Schematic of Fmoc solid-phase peptide synthesis. First, the Fmoc group is removed from the linker (dark blue) to afford a free amine. Next, the first amino acid (AA1, green) along with coupling reagents (an activator and activator base, not pictured) are added and the C-terminal amide bond is formed through a condensation reaction (top right image). This cycle is repeated until the desired peptide is built on the resin. A final deprotection step removes the N-terminal Fmoc protecting group.

Although SPPS is a highly efficient method, the yield does considerably drop as more amino acids are added to the peptide chain. This disadvantage can be overcome with microwave-assisted peptide synthesis. Microwave reactors improve the efficiency of peptide synthesis due to the highly precise and homogeneous nature of heating.¹⁴ The theoretical peptide yield for microwave-assisted SPPS is approximated as 0.99^n multiplied by 100, where n is the number of amino acids. For short peptides (~10 residues), the yield is quite high (~90%). However, as the length is increased to ~50 residues, the yield significantly decreases (~60%). It is also important to note that the peptide yield will inevitably drop during successive cleavage from the resin and purification steps. Larger peptide sequences are also likely to encounter amino acid deletions

within the sequence. To avoid deletions, multiple coupling steps can be implemented to ensure the maximum amount of free amino groups are chemically linked to the next amino acid. I have found that double coupling methods are essential when synthesizing $^{13}\text{C}^{18}\text{O}$ -labeled peptides. During my first isotope-labeled peptide synthesis, I used standard single coupling protocols and observed an amino acid deletion in the labeled position upon characterization. This could have resulted from the ^{18}O -exchange impurity, where the isotope-labeled amino acid mass would have been less than anticipated while preparing the amino acid solution. Precipitation with dry ether removes some of the impurity, but without enhanced purification methods like HPLC, it is likely still present. Double coupling this position during synthesis ensures a sufficient amount of the isotope is fully incorporated into the peptide sequence.

For the unlabeled model α -helical peptide synthesis (MAHP, sequence: DPAEAKAAAGR-NH₂), the standard Rink Amide ProTide resin was employed. This resin contains a polyethylene glycol polystyrene (PEG PS) core and is suitable for C-terminal amidated peptides with fewer than 30 residues. The resin is first swelled with 15 mL of wash solvent (dimethylformamide, DMF) for 5 minutes; the high swelling option ensures the following reagents will diffuse quickly and homogeneously throughout the resin core. Next, the Fmoc group on the linker is removed with a deprotection solution of 10% piperazine (weight/volume) in 90% *N*-Methylpyrrolidone (NMP) and 10% ethanol (EtOH) (volume/volume) under standard deprotection methods. After the Fmoc group is removed, the first amino acid (arginine) is coupled onto the linker. Arginine contains a sterically-hindered guanidine sidechain with a 2,2,4,6,7-pentamethyldihydrobenzofuran-5-sulfonyl (Pbf) protecting group, making it one of the bulkiest amino acids. Arginine is the only amino acid in MAHP's sequence that requires double coupling to ensure sufficient addition onto the linker. The standard single coupling procedure involves

microwaving the amino acid (0.2 M in DMF), activator (0.5 M DIC in DMF), and activator base (1 M Oxyma in DMF) at 75°C for 15 seconds and 90°C for ~2 minutes and then removing the reagents with wash solvent (DMF). Again, this procedure is repeated once more with arginine to guarantee coupling onto the linker. The deprotection and coupling reactions are repeated with the remaining amino acids with the standard single coupling method. A final deprotection step removes the Fmoc group from the N-terminal amino acid and is followed by several DMF washes.

After the peptide synthesis is complete, the resin is carefully transferred from the reaction vessel with dichloromethane (DCM) into a labeled 50-mL conical tube. The DCM is gently evaporated in the fume hood, resulting in a dry, pale-yellow resin. The tube containing the dried resin is sealed with Parafilm to minimize contact with water and stored in the freezer at -20°C. I've found that MAHP on resin is stable at -20°C for at least a year. I typically synthesize MAHP (and other peptides) on a 0.10 mmol scale, which yields enough peptide for several 2D IR experiments. The reagent concentrations depend upon the amount of peptide synthesized, so it is important to reference the Liberty Blue guidelines when scaling the synthesis up or down.

2.2.3 Peptide cleavage from resin and precipitation with ether

After synthesis, the peptide is cleaved from the resin and the sidechain protecting groups are removed using an acidic cleavage cocktail. The cleavage cocktail composition is highly dependent upon the types of residues present. Many linkers (Rink, Wang, etc.) are acid-labile and readily cleaved with a mixture of concentrated TFA with a much smaller percentage of scavenger species, which are dependent upon the sidechains present. For my peptide samples, I have used standard cleavage protocols provided by ThermoFisher. In particular, MAHP does not contain any highly-reactive sidechains (e.g., cysteine, methionine, histidine, etc.). Therefore, a cleavage

cocktail of 95% TFA, 2.5% H₂O, and 2.5% triisopropylsilane (TIPS) is sufficient. In this reaction, TFA severs the peptide from the resin along with the sidechain protecting groups. H₂O and TIPS bind to the free sidechain protecting groups in solution, preventing them from reattaching to the peptide. For a 0.10 mmol synthesis, usually a third to half of the resin batch is cleaved. I've found that it's unfortunately not useful to weigh the resin for the cleavage procedure; the resin is highly sticky and does not produce an accurate mass reading. However, it is critical to be as consistent as possible when measuring the dry resin and adding the cleavage cocktail solution. The resin is carefully transferred to a 6-dram glass vial with a small stir bar on a stir plate in the fume hood. Approximately 5–6 mL of cleavage cocktail is slowly added to the dry resin, which causes it to react vigorously (smoke and heat are given off). The reaction mixture was stirred for ~2.5–3 hours in the hood at room temperature. It is important that the resin does not interact with the cleavage cocktail for >4 hours due to undesired side reactions.

After the cleavage reaction is complete, the resin is filtered from the solution and discarded. The solution, which contains the crude peptide and scavenger-bound sidechain protecting groups, is filtered directly into a labeled and weighed 50-mL centrifuge tube. The solvent is dried and a thin, yellow film/gel remains in the tube. The peptide is precipitated out with cold diethyl ether. The cold mixture is centrifuged at 5,000 rpm for 5–10 minutes. After centrifugation, the white fluffy peptide should settle at the bottom of the tube. The ether supernatant, which contains the soluble scavenger-bound sidechain protecting groups, is gently removed by a Pasteur pipette and discarded. The ether washes are repeated at least twice more to remove the scavenger groups from the crude peptide. Once most of the supernatant is removed, the remaining ether can be gently evaporated in the hood to minimize loss of the dry peptide, which is very sticky and volatile at this stage. Once the cleaved peptide is completely dry, the tube is sealed with Parafilm and stored

at -20°C until it is ready for HPLC purification. In general, peptide cleavage from the resin should be timed as closely to HPLC, if possible, to preserve the sidechain group chemistry.

2.2.4 High-performance liquid chromatography peptide purification

High performance liquid chromatography (HPLC) is an indispensable tool for peptide purification. In HPLC, analytes are loaded onto a stationary phase, usually a fused silica column, and eluted from the column with a mobile phase (i.e., solvent system). The analytes in a mixture have different affinities for the stationary phase, depending upon the specific chemistry. Reversed-phase HPLC (RP-HPLC), which uses a nonpolar octadecylsilane (C18) stationary phase, is best suited for peptide separation. Hydrophilic peptides do not interact strongly with the nonpolar column and elute first. Hydrophobic peptides interact more favorably with the stationary phase and elute at later times. RP-HPLC can be performed with a single solvent as the mobile phase (i.e., isocratic elution) or by changing the solvent system over time (i.e., gradient elution). Gradient elution improves peptide separation and is much faster compared to isocratic methods. An ultraviolet-visible (UV-Vis) detector is often used to monitor peptide elution from the column. The detector monitors 215 nm (the wavelength where the peptide backbone absorbs UV light) and 280 nm (the wavelength where aromatic residues, like tryptophan, absorb UV radiation). A fraction collection system is used to collect each species based on the characteristic UV-Vis absorption.

To prepare MAHP for HPLC, the crude peptide was dissolved in water (HPLC grade) to make a ~2 mg/mL stock. The stock was vortexed and immediately filtered through a 0.20- μ m filter. For purification, typically ~2 mL of peptide solution was loaded onto the preparative column (~4 mg of crude peptide) during each injection. Since some hydrophobic peptides (e.g., amyloids) tend to aggregate on the column, a quick 30-minute cleaning gradient was performed at the

beginning and end of each day when using the XBridge BEH C18 preparative column. To clean the column, ~1 mL of dimethylsulfoxide (DMSO) was loaded onto the column and a 10% change per minute gradient of 100% Solvent A (water with 0.045% HCl) to 100% Solvent B (90% acetonitrile in water with 0.045% HCl) was performed. After 10 minutes, the column was flushed with 100% Solvent B for 10 minutes and then equilibrated with 100% Solvent A for 10 minutes before the peptide injection. To purify MAHP, a 2% change per minute gradient was used and the peptide elution was monitored at 215 nm. The solvent gradient started with 0% Solvent A (100% water with 0.045% HCl) and ended with 40% Solvent B (90% acetonitrile in water with 0.045% HCl) over 20 minutes, where the peptide's retention time was consistently ~11 minutes (~22% Solvent B composition). At 20 minutes, the gradient increased from 40% to 100% Solvent B over 1 minute. 100% Solvent B was flushed through the column for 10 minutes to elute the remaining hydrophobic analytes in the sample. The column was then equilibrated with Solvent A for 10 minutes and the peptide injections were repeated for the remaining crude peptide solution. An example of the binary gradient for MAHP and resulting chromatogram is shown in Figure 2.6. All pure MAHP fractions were collected, combined into a 50-mL centrifuge tube, and lyophilized for several days (depending on the sample volume). A single round of HPLC purification is sufficient for MAHP. Typically, MAHP can be fully purified in ~10–20 injections (~1–2 days) on the preparative column, compared to several weeks on the analytical column. However, the matched analytical column (XBridge BEH C18 analytical column) can be useful for initial gradient optimization if the peptide sample is limited or contains an expensive label.

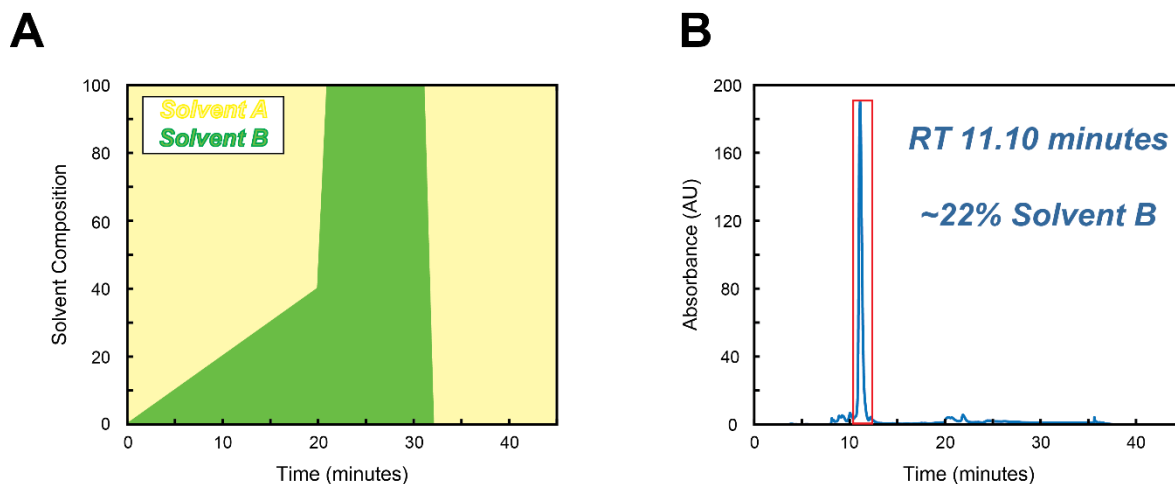


Figure 2.6 Optimized HPLC gradient and chromatogram for MAHP. (A) A binary gradient of 0% to 40% Solvent B (green) starting with Solvent A (yellow) over 20 minutes is sufficient to elute MAHP. (B) The corresponding chromatogram of MAHP monitored at 215 nm. The pure peptide elutes ~11 minutes (~22% Solvent B composition). The pure fraction (denoted in the red box) is collected and lyophilized.

It is important to note that different counterions can be used in HPLC solvents, depending upon the chemical nature of the peptide. We tend to use a smaller percentage of HCl instead of TFA, which is a standard acidic counterion. TFA absorbs strongly at $\sim 1680\text{ cm}^{-1}$, which can overlap with the weak parallel β -sheet mode in infrared spectra. When switching between counterions, it is important to consult the instrument and column manuals to ensure the counterion is compatible with the system. For HCl, 0.045% by volume is within the acceptable concentration and pH range of the XBridge columns and instrument.

2.2.5 Electrospray-ionization mass spectrometry peptide characterization

Once the peptide is lyophilized into a white, fluffy powder, it is ready for characterization with ESI-MS. The MAHP solution was prepared as previously described in Section 2.2.1, instead using a solvent system of 70% methanol and 30% water (high purity grades). A generic mass spectrum for pure, unlabeled MAHP is shown in Figure 2.7. The $[M+2H]^{2+}$ species is consistently

the most intense signal observed for MAHP samples under these conditions. After the correct peptide mass is confirmed, the diluted sample can be discarded. If there is limited sample, the concentrated stock should be combined with the dry stock and lyophilized again.

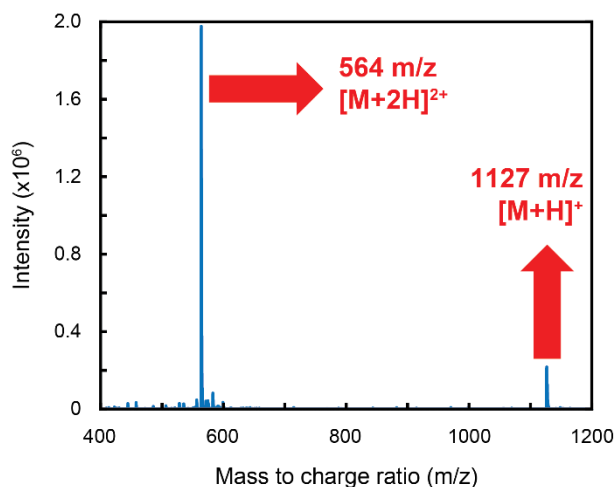


Figure 2.7 Mass spectrum of pure MAHP. Signals observed in mass spectra correspond to protonated species of MAHP (1126 g/mol). The most intense signal at 564 m/z corresponds to the doubly protonated peptide $[M+2H]^{2+}$. The weaker signal at 1127 m/z is from the singly protonated $[M+H]^+$ species.

2.3 Preparation of peptide samples for CD and 2D IR measurements

All peptides were prepared in deuterated solvents to prevent interferences from water bending modes in the amide I' region in 2D IR measurements. MAHP samples were prepared under several different conditions for 2D IR analysis. MAHP is a model peptide that has a pH-dependent secondary structure due to the titration of the aspartic and glutamic acid sidechains (pKa ~4).¹⁵ MAHP also exhibits an increase in helical content with the addition of the cosolvent 2,2,2-trifluoroethanol (TFE).¹⁵ To prepare the peptide for 2D IR experiments, a concentrated MAHP solution (>10 mM) was first prepared in D₂O. The stock concentration was quantified using the Nanodrop instrument. MAHP does not contain any aromatic residues (tryptophan, tyrosine, or

phenylalanine) and cannot be quantified at 280 nm. Instead, the peptide backbone wavelength (~205 nm) is used, although it is much weaker. The estimated molar absorptivity for MAHP is 28.53 L/g*cm, which was calculated based upon the number of amino acid residues and contributing sidechain absorptions at 205 nm.¹⁶ Following MAHP quantification, sample dilutions (5 mM) were prepared at different pH values and with varying concentrations of TFE (up to 40% by volume) in microfuge tubes. Figure 2.8 depicts a generalized sample composition for a typical MAHP 2D IR experiment. The solution pH was adjusted using sodium deuterioxide (20% by weight in D₂O) and deuterium chloride (30% by weight in D₂O) and the exact value was recorded with a micro-pH probe. If applicable, TFE was added (40% v/v) to the 5 mM MAHP samples and the pH was checked again to ensure the acid did not significantly drop the pH value (>1). The remaining solvent volume was accounted for with neat D₂O. After the sample mixtures were prepared, the tubes were sealed with Parafilm and incubated at room temperature for at least 1 hour before collecting spectra. After incubation, a small volume of the sample (~5–20 μL) was sandwiched between two CaF₂ windows separated by a 50 μm Teflon spacer.

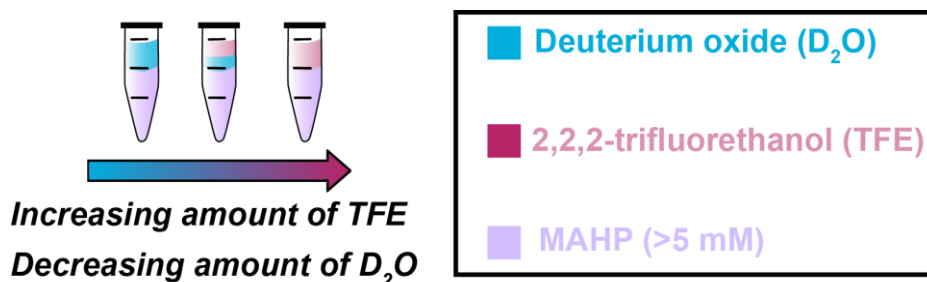


Figure 2.8 Sample composition for MAHP 2D IR and CD experiments. 100 μL of sample is prepared containing equivalent amounts of MAHP stock with varying amounts of D₂O and TFE. Concentrated MAHP stock is diluted to a final concentration of 5 mM with the solvent system. The solution pH is adjusted before TFE is added (up to 40% by volume).

2.4 Experimental setup for 2D IR spectroscopy

2D IR is a third-order, nonlinear spectroscopic technique that can provide additional information about molecular vibrations compared to linear spectroscopies.^{17–21} By spreading an IR spectrum over two frequency axes, the relationship between multiple vibrational modes can be investigated. The pulse sequence and example of the 2D IR process is shown in Figure 2.9.¹⁷ The 2D IR pulse sequence consists of a pair of pump pulses and one probe pulse (Figure 2.9A). The first pump pulse, ω_1 , establishes a coherence between the ground state and the first excited vibrational state and the second pump pulse, ω_2 , creates a population with this state (Figure 2.9B, yellow arrow). The waiting time between the two pump pulses (t_1) is known as the coherence time and can be Fourier transformed to yield the “pump” frequency axis. After a known delay (t_2), the probe pulse, ω_3 , interacts with the system. The probe pulse can: (1) create another coherence with the second excited vibrational state, known as excited state absorption (ESA, Figure 2.9B, red line); (2) stimulate emission to the ground state (Figure 2.9B, downwards blue line) or (3) stimulate ground state bleach (Figure 2.9B, upwards blue line). The coherence time between the probe pulse and the emitted signal is Fourier transformed to yield the “probe” frequency axis. The pump and probe frequency axes are plotted against each other to create the 2D IR spectrum (Figure 2.9C). By correlating vibrational modes over two frequency axes, more detailed information about the molecular system of interest can be revealed.

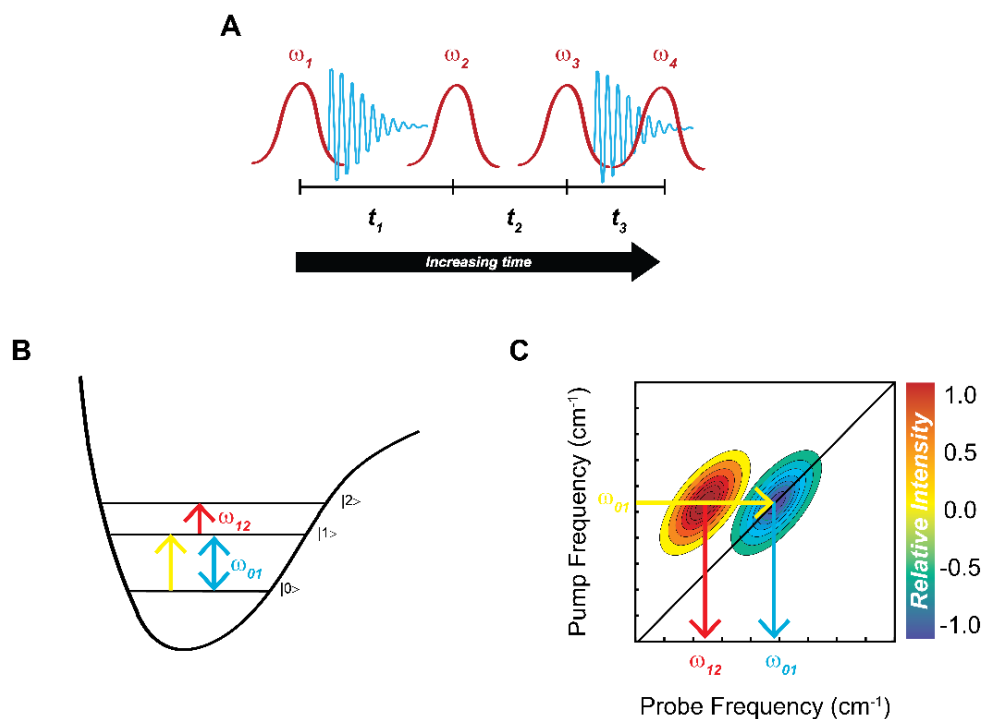


Figure 2.9 Overview of 2D IR process. (A) 2D IR pulse sequence. Two pump pulses and a probe pulse are required to generate the 2D IR signal (second blue coherence). (B) Energy level diagram of 2D IR process. (C) Example 2D IR spectrum. The spectrum is plotted as a contour function, where the negative intensities (from GSB and SE processes, ω_{01}) are blue and the positive intensities (excited state absorption, ω_{12}) are red.

Experimental 2D IR spectroscopy relies on femtosecond light pulses, which can only be generated with commercial ultrafast laser systems. There are different methods for implementing 2D IR spectroscopy, but I will focus on the pulse shaper method (i.e., pump-probe geometry).^{17,22} Generally, pulse shaping has many advantages over other 2D IR methods, although other methods still have merit and remain in use today.²³ Implementing a mid-IR pulse shaper allows for complete control over the pulse phases and the data acquisition time is much faster due to the computer-generated time delays.^{17,22} Additionally, using a pulse shaper can simplify alignment because the pump pulses are generated on the same beam line.²² An example of the 2D IR laser setup I've used is shown in Figure 2.10.

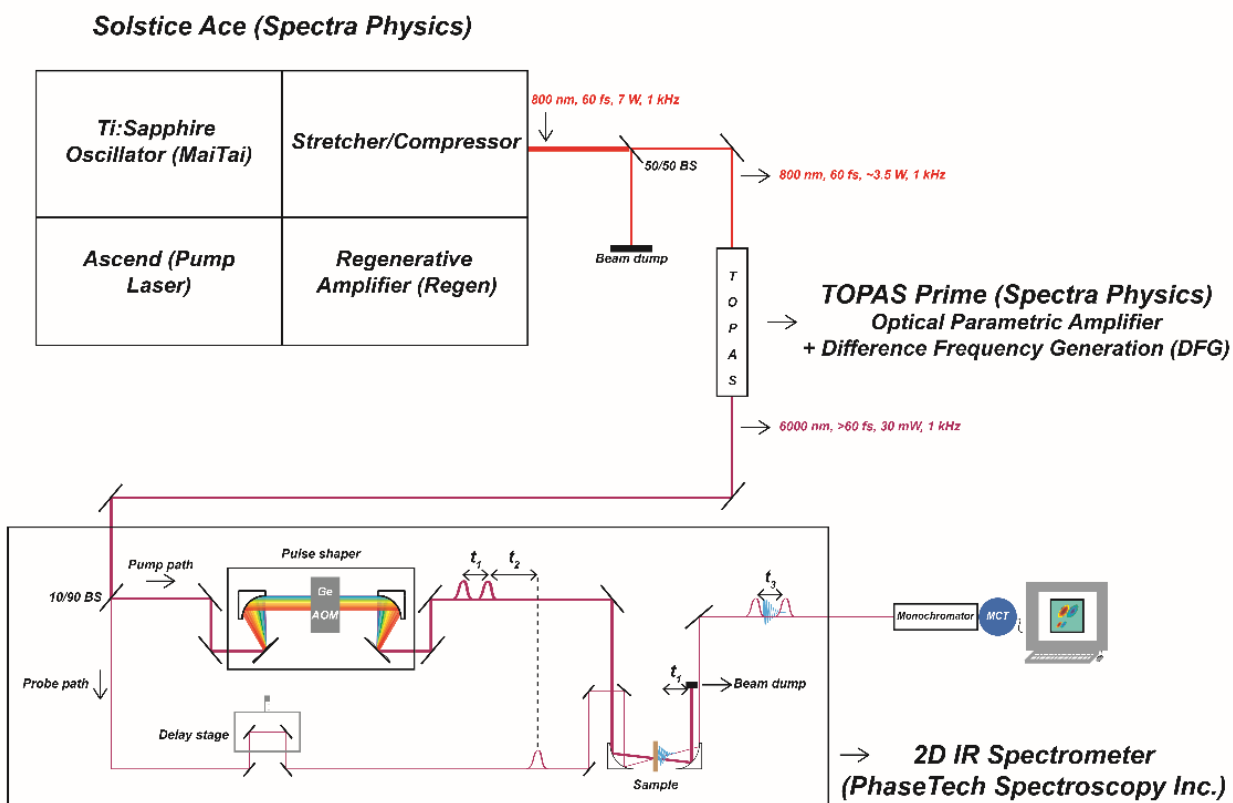


Figure 2.10 Schematic of experimental 2D IR setup. The experimental setup consists of three main parts: the ultrafast laser system (Solstice Ace, Spectra Physics, top left), the OPA and DFG (TOPAS, Spectra Physics, top right), and the 2D IR spectrometer with pulse shaper (2DQuick IR, PhaseTech Spectroscopy Inc., bottom left).

Mid-IR femtosecond pulses cannot currently be generated from a commercial laser system. Instead, visible ultrafast pulses are first generated by a commercial laser system and converted to infrared pulses using an optical parametric amplifier (OPA) and difference frequency generation (DFG). For all of my research, I've used a Solstice Ace laser system (Spectra Physics, CA, USA). This system initially generates 800 nm femtosecond pulses by pumping a Ti:Sapphire oscillator (MaiTai, Spectra Physics, CA, USA) with a 532 nm continuous wave pump laser. These pulses were intensified using a regenerative amplifier through a process called chirp pulse amplification pumped with a high-power Nd:YVO₄ laser (Ascend, Spectra Physics, CA, USA). The Solstice Ace

system outputs 800-nm pulses (7 mJ, 60 fs, 1 kHz). In our experimental setup, the output pulses from the Solstice were attenuated by a 50/50 beam splitter and half of the beam was dumped. The other beamline was directed into an OPA (TOPAS, Spectra Physics, CA, USA). The 800-nm pulses were overlapped onto a β -barium borate crystal (BBO) to generate signal and idler pulses in the near infrared spectral region. The signal and idler pulses were overlapped onto a AgGaS_2 crystal, which generated mid-IR light through difference frequency generation (DFG). The mid-IR output is controlled by the signal and idler frequencies through the following equations:

$$\omega_{pump} = \omega_{signal} + \omega_{idler} \quad (2.2)$$

$$\omega_{mid\ IR} = \omega_{signal} - \omega_{idler} \quad (2.3)$$

In these equations, ω_{pump} is the input light ($\sim 12,500\text{ cm}^{-1}$ for 800 nm), $\omega_{mid\ IR}$ is the output frequency ($\sim 1,667\text{ cm}^{-1}$ for $6\ \mu\text{m}$ light where proteins absorb), and ω_{signal} and ω_{idler} are variables. This system of equations allows us to solve for the signal and idler frequencies needed for the desired output frequency ($\omega_{mid\ IR}$). Adding the two equations results yields the signal frequency, which is greater than the idler frequency by convention. Likewise, subtracting the equations provides the idler frequency term. To satisfy $\omega_{mid\ IR} = 1,667\text{ cm}^{-1}$, the signal and idler frequencies are set at $\sim 7,083.5\text{ cm}^{-1}$ ($\sim 1,412\text{ nm}$) and $\sim 5,416.5\text{ cm}^{-1}$ ($\sim 1,852\text{ nm}$), respectively.

After the DFG process, the mid-IR beam was directed into a commercial 2DQuick IR spectrometer (PhaseTech Spectroscopy Inc., WI, USA). More details regarding the spectrometer design are provided elsewhere.^{17,22} First, the mid-IR beam was split into an intense pump ($\sim 90\%$) and a weaker probe line ($\sim 10\%$). The resultant pump beam was “shaped” using a germanium acousto-optic modulator (Ge AOM). Sound waves that travel across the Ge crystal alter the lattice spacing, which transformed the output pump frequency. The modulated beam was recombined

with a diffraction grating, producing two individual pump pulses. The pump and probe pulses were spatially and temporally overlapped at the sample, which generated the nonlinear signal along the probe line. The probe line, which contains the signal, was dispersed by a monochromator onto a mercury cadmium telluride (MCT) detector array (Princeton Instruments, NJ, USA). 2D IR spectra were processed by the QuickControl software (PhaseTech Spectroscopy Inc., WI, USA). Data analysis was performed using a custom MATLAB script and additional post-processing was completed with Adobe Illustrator.

The MCT array should be calibrated daily with a standard to minimize variations in data collected over the span of several months or years. During my first few years in the group, we used water lines from ambient water vapor to calibrate the detector because it has many vibrational modes spanning the protein region ($\sim 1550\text{--}1700\text{ cm}^{-1}$). However, this method did not work well with our spectrometer setup (i.e., the water modes were not well-resolved) and was sensitive to humidity changes, which fluctuated daily. Instead, small molecule calibrant molecules tend to work best because they are consistent and largely insensitive to humidity fluctuations in lab. 4-nitrobenzaldehyde (4NBA, $\sim 300\text{--}500\text{ mM}$ in toluene) is a small organic molecule that absorbs mid-IR light at 1535 cm^{-1} , 1605 cm^{-1} , and 1711 cm^{-1} in toluene, which was measured on our commercial Nicolet iS20 FTIR spectrometer (ThermoFisher, MA, USA). These three vibrational modes are useful because they span the isotope and amide I' spectral regions. To calibrate the detector, the first 4NBA probe spectrum (50 scans averaged) was collected as described and the pixels were matched to the absorption minima frequencies. These calibrated pixels were used during spectral processing for the remaining data set collected on the same day.

2.5 References

- (1) Rygula, A. et al. Raman Spectroscopy of Proteins: A Review. *J. Raman Spectrosc.*, **2013**, *44*, 1061–1076.
- (2) Deb, S. K. et al. Detection and Relative Quantification of Proteins by Surface Enhanced Raman Using Isotopic Labels. *J. Am. Chem. Soc.*, **2008**, *130*, 9624–9625.
- (3) Peuker, S. et al. Efficient Isotope Editing of Proteins for Site-Directed Vibrational Spectroscopy. *J. Am. Chem. Soc.*, **2016**, *138*, 2312–2318.
- (4) Ruf, J. and Buhrke, D. Needles in a Haystack: H-Bonding in an Optogenetic Protein Observed with Isotope Labeling and 2D-IR Spectroscopy. *Phys. Chem. Chem. Phys.*, **2021**, *23*, 10267–10273.
- (5) Ghosh, A. et al. Tidal Surge in the M2 Proton Channel, Sensed by 2D IR Spectroscopy. *Proc. Natl. Acad. Sci.*, **2011**, *108* (15), 6115–6120.
- (6) Buchanan, L. E. et al. Mechanism of IAPP Amyloid Fibril Formation Involves an Intermediate with a Transient β -Sheet. *Proc. Natl. Acad. Sci.*, **2013**, *110* (48), 19285–19290.
- (7) Yang, H. et al. Obtaining Information about Protein Secondary Structures in Aqueous Solution Using Fourier Transform IR Spectroscopy. *Nat. Prot.*, **2015**, *10* (3), 382–396.
- (8) Marecek, J. et al. A Simple and Economical Method for the Production of ^{13}C , ^{18}O -Labeled Fmoc-Amino Acids with High Levels of Enrichment: Applications to Isotope-Edited IR Studies of Proteins. *Org. Lett.*, **2007**, *9* (24), 4935–4938.
- (9) Barth, A. The Infrared Absorption of Amino Acid Side Chains. *Prog. Biophys. Mol. Biol.*, **2000**, *74* (3–5), 141–173.
- (10) Abaskharon, R. M. et al. Isotope-Labeled Aspartate Sidechain as a Non-Perturbing Infrared Probe: Application to Investigate the Dynamics of a Carboxylate Buried Inside a Protein. *Chem. Phys. Lett.*, **2017**, *683*, 193–198.
- (11) Cao, C. and Yin, J. C. Selective ^{15}N -Labeling of the Side-Chain Amide Groups of Asparagine and Glutamine for Applications in Paramagnetic NMR Spectroscopy. *J. Biomol. NMR*, **2014**, *59*, 251–261.
- (12) Cruz, L. J. et al. “One-Pot” Preparation of N-Carbamate Protected Amino Acids via the Azide. *Org. Process Res. Dev.*, **2004**, *8* (6), 920–924.
- (13) Behrendt, R. et al. Advances in Fmoc Solid-Phase Peptide Synthesis. *J. Pept. Sci.*, **2016**, *22* (1), 4–27.
- (14) Pedersen, S. L. et al. Microwave Heating in Solid-Phase Peptide Synthesis. *Chem. Soc. Rev.*, **2012**, *41*, 1826–1844.
- (15) Forood, B. et al. Stabilization of α -Helical Structures in Short Peptides via End Capping. *Proc. Natl. Acad. Sci.*, **1993**, *90*, 838–842.
- (16) Anthis, N. J. and Clore, G. M. Sequence-Specific Determination of Protein and Peptide Concentrations by Absorbance at 205 nm. *Protein Sci.*, **2013**, *22*, 851–858.

- (17) Middleton, C. T. et al. Residue-Specific Structural Kinetics of Proteins through the Union of Isotope Labeling, Mid-IR Pulse Shaping, and Coherent 2D IR Spectroscopy. *Methods*, **2010**, 52 (1), 12–22.
- (18) Ganim, Z. et al. Amide I Two-Dimensional Infrared Spectroscopy of Proteins. *Acc. Chem. Res.*, 2008, 41 (3), 432–441.
- (19) Baiz, C. R. et al. An Introduction to Protein 2D IR Spectroscopy. *Ultrafast Infrared Vib. Spectrosc.*, **2013**, 22, 361–403.
- (20) Larsen, O. F. A. et al. Probing the Structure of a Rotaxane with Two-Dimensional Infrared Spectroscopy. *Proc. Natl. Acad. Sci. U. S. A.*, **2005**, 102 (38), 13378–13382.
- (21) Ghosh, A. et al. Watching Proteins Wiggle: Mapping Structures with Two-Dimensional Infrared Spectroscopy. *Chem. Rev.*, **2017**, 117 (16), 10726–10759.
- (22) Skoff, D. R. et al. Simplified and Economical 2D IR Spectrometer Design Using a Dual Acousto-Optic Modulator. *Chem. Phys.*, **2013**, 422, 8–15.
- (23) Rock, W. et al. 2D IR Spectroscopy using Four-Wave Mixing, Pulse Shaping, and IR Upconversion: A Quantitative Comparison. *J. Phys. Chem. A.*, **2013**, 117 (29), 6073–6083.

Chapter 3. Structural differences in a short α -helix revealed by two-dimensional infrared spectroscopy and isotope labeling

3.1 Abstract

α -helical secondary structures impart specific mechanical and physiochemical properties to peptides and proteins, enabling them to perform a vast range of molecular tasks ranging from membrane insertion to molecular allostery. However, loss of helical content in specific regions can inhibit the polypeptide's native function or induce new, potentially toxic, biological activities. Thus, identifying specific residues that exhibit loss or gain of helicity within α -helical peptides and proteins is critical for understanding the molecular basis for peptide and protein function. Here, we examine the ability of two-dimensional infrared (2D IR) spectroscopy coupled with isotope labeling to detect subtle changes in peptide α -helicity. 2D IR spectra were collected of a set of peptide isotopomers (DPAEAAKAAAGR-NH₂), under optimized solvent conditions, which allowed the α -helicity of the peptide to be tuned systematically. These results demonstrate that a ¹³C¹⁸O probe pair at the i and $i+3$ residues can report on subtle helicity changes along the length of a 12-residue model α -helix. These probes revealed strong hydrogen-bonding and vibrational coupling spanning the N-terminal and central residues (3–8) with a more disordered conformation at the C-terminus (8–11) in the predominantly helical state. Additionally, a quantitative signal strength analysis in the low-frequency region (1540–1600 cm⁻¹) was implemented to establish contributions from the underlying sidechain mode (likely Asp1), which verified the isotopic signals were arising from local helix interactions. These results demonstrate that 2D IR in tandem with $i, i+3$ isotope labeling schemes can capture residue-specific molecular interactions in an α -

helix in real time, which can be further applied for structural characterization of short helical peptide drug candidates and nanomaterials.

3.2 Introduction

Secondary structures impart unique mechanical and physiochemical properties to proteins, allowing them to act as efficient molecular machines.¹⁻³ In particular, α -helices are the most common secondary structural motif that polypeptides adopt.⁴ This secondary structure is critical for a wide array of molecular functions, including membrane insertion,⁵⁻⁷ protein-protein and protein-DNA interactions,⁸⁻¹⁰ and intra/intermolecular allostery.¹¹⁻¹³ These diverse biological activities have raised interest in α -helical peptides as drug candidates and novel peptide nanomaterials.^{1,2,14,15} However, denaturation or transformation of α -helices into other secondary structures may lead to loss of native function or gain of toxic function.¹⁶⁻¹⁸ For example, industrial nanoparticles, which are commonly implemented in cosmetics, textiles, and medicine, can risk unintentional exposure to proteins in our bodies through inhalation or ingestion.¹⁹⁻²² Nanoparticles are known to induce structural rearrangements in polypeptides, which predominantly affect α -helical structures.²³⁻²⁶ Thus, the crucial relationship between highly-abundant α -helical motifs in peptides and proteins and their biological function makes revealing these structural changes of great importance.

Two-dimensional infrared (2D IR) spectroscopy has been demonstrated to provide exquisite insight into polypeptide secondary structures.²⁷⁻³² To date, most 2D IR studies of peptides and proteins have examined the amide I' transition (which comprises primarily backbone carbonyl stretching) because it is sensitive to secondary structure.³³⁻³⁵ When coupled with isotope labeling methods, 2D IR is capable of single-residue structural resolution.³⁶⁻⁴³ Although the vast majority

of these studies have focused on β -sheet peptides, several reports have employed 2D IR and isotope labeling to characterize helical peptides.^{44–47} It is important to note that both hydrogen bonding interactions and vibrational coupling affect the observed frequency of the amide I' vibrational transition.^{33,41,48–51} Hydrogen bonding weakens the carbonyl double bond, lowering its vibrational frequency relative to carbonyls that are not hydrogen bonded.^{48,52} On the other hand, vibrational coupling occurs via either mechanical (through-bond) or electrostatic (through-space) interactions.⁵² Polypeptides experience both kinds of vibrational coupling, with the strongest mechanical interactions occurring between adjacent residues.^{43,45,51} When polypeptides exhibit a higher degree of order, patterns of vibrational couplings between individual transition dipoles lead to delocalization of vibrational modes over the extended structure, giving rise to distinctive spectral signatures (frequencies, intensities, lineshapes) in an IR spectrum.^{33,34}

There is some debate on which type of underlying molecular interactions dominate the spectral features observed in 2D IR spectra of isotope-labeled in α -helices. Fang and coworkers employed double $^{13}\text{C}^{18}\text{O}$ probes spaced one, two, or three residues apart in a stable α -helix to determine how the relative positions of the isotope labels influenced vibrational signatures.⁴⁵ Experimental spectra demonstrated varying shifts of the $^{13}\text{C}^{18}\text{O}$ -labeled amide I' modes depending on the relative label positions. When supplemented with extensive calculations, these results yielded the inter-residue coupling constants (β) in α -helix, with the strongest vibrational coupling occurred between adjacent residues ($\beta_{12} = 8.5 \pm 1.8 \text{ cm}^{-1}$, $\beta_{12} > 0$) followed by the i and $i+3$ positions ($\beta_{14} = 6.6 \pm 0.8 \text{ cm}^{-1}$, $\beta_{14} < 0$). They attributed coupling arising from adjacent residues primarily to through-bond vibrational coupling, whereas electrostatic coupling between the i and $i+3^{\text{rd}}$ residues, which corresponds to the α -helical repeat length of 3.6 residues, should be unique to this particular secondary structure.

A subsequent study by Backus and colleagues utilized 2D IR with $^{13}\text{C}^{18}\text{O}$ isotope labeling to probe local molecular interactions within a photoswitchable α -helix.⁴⁷ This study revealed that even single $^{13}\text{C}^{18}\text{O}$ isotope labels experienced significant frequency shifts as the peptide switched between α -helical and denatured states. As vibrational coupling between unlabeled $^{12}\text{C}^{16}\text{O}$ and single $^{13}\text{C}^{18}\text{O}$ amide I' modes has a negligible effect on their respective frequencies due to the large energy difference, they attributed frequency shifts to intramolecular hydrogen bonding between the i and $i+4^{\text{th}}$ residues. An entirely novel labeling scheme reported by Maekawa and colleagues, which utilized ^{15}N and $^{13}\text{C}^{18}\text{O}$ labeled residues, led to the formation of crosspeaks between the amide I' and II' modes in 2D IR spectra of a model 3_{10} -helix.⁵³ While this study was performed on a 3_{10} -helix rather than an α -helix, and thus the repeat length along the helical axis differs, the conclusions should prove general to all helical peptides.

Despite many recent advances in this field, there are currently limitations to probing the structure and dynamics of α -helical motifs with 2D IR and isotopic labeling methods. One major drawback is sidechain interference in the isotopic region.⁵⁴ For example, aspartate ($\epsilon \sim 820 \text{ M}^{-1} \text{ cm}^{-1}$), glutamate ($\epsilon \sim 830 \text{ M}^{-1} \text{ cm}^{-1}$), and arginine ($\epsilon \sim 500 \text{ M}^{-1} \text{ cm}^{-1}$) sidechains contain IR-active functional groups that absorb between $\sim 1550\text{--}1610 \text{ cm}^{-1}$ in deuterated solvent.⁵⁴ While the extent of sidechain IR absorption in polypeptides is dependent upon many factors, including solvent exposure, protonation state, and chain length, these molecular vibrations coincide with the $^{13}\text{C}^{18}\text{O}$ -edited amide I' transition.^{54,55} Some 2D IR studies have circumvented this complication by mutating native residues to those that do not contain sidechains with overlapping vibrational signatures, which was successfully demonstrated with a 2D IR study of the influenza A M2 proton channel.⁵⁶ However, the need to employ mutants limits our understanding of the structure and dynamics of the native peptide or protein. Another drawback of probing α -helical structures with

isotopes is the effects of vibrational coupling in α -helices is inherently weaker compared to the more commonly studied extended β -sheet structures.^{27,41,43,45,51,57} The local amide backbones in β -sheets experience both intra- and intermolecular couplings. In β -sheet structures, nearest neighbor (intra-strand) couplings are relatively small and positive in sign, while coupling between strands (inter-strand) are much larger and negative in sign, which dominate the amide I' spectral shift.^{27,41,51} Conversely, α -helices exhibit large, positive couplings between adjacent residues, which opposes the large, negative couplings between turns.^{43,45,57} Additionally, extended β -sheet structures contain a greater number of oscillators, leading to a greater delocalization of the vibrational modes and thus larger changes in spectral features. Overall, competition between intra-helical coupling makes α -helical structures less straightforward to analyze with individual isotope labels compared to β -sheets.

In this study, we aim to resolve the remaining challenges with studying α -helical structures with 2D IR and isotope labeling to make it a more inclusive tool for characterizing peptide and protein structures. While previous studies have primarily focused on stable and binary helices, this study aims to determine how sensitive isotope-labeled modes are to subtle changes in α -helicity, such as when an α -helix begins to unravel slightly. Additionally, we closely examine the underlying mechanisms, such as hydrogen bonding and transition dipole coupling, that are responsible for the characteristic signatures of α -helical isotopologues. As discussed above, another critical challenge to measuring isotopic signals within this particular secondary structure is the competition between overlapping sidechain modes. To address all of these questions, we applied 2D IR spectroscopy to study systematic changes in a model peptide with a solvent-dependent secondary structure, which provided a way to precisely control the peptide's helicity.⁵⁸

Both single and paired $^{13}\text{C}^{18}\text{O}$ probes were used to monitor the structural change from disordered to α -helical in the model system. The findings presented here suggest that both vibrational coupling and hydrogen bonding contribute to the spectral features, with hydrogen bonding being the major determinant of the redshift in mode frequency while vibrational coupling leads to greatly enhanced mode intensity as the organized structure forms. This increase in intensity also provides an avenue to differentiate coupled isotopes from overlapping sidechain modes. We also probed two ^{13}C labeling schemes (Figure 3.1), but as we will see, these isotopes were not well-resolved.

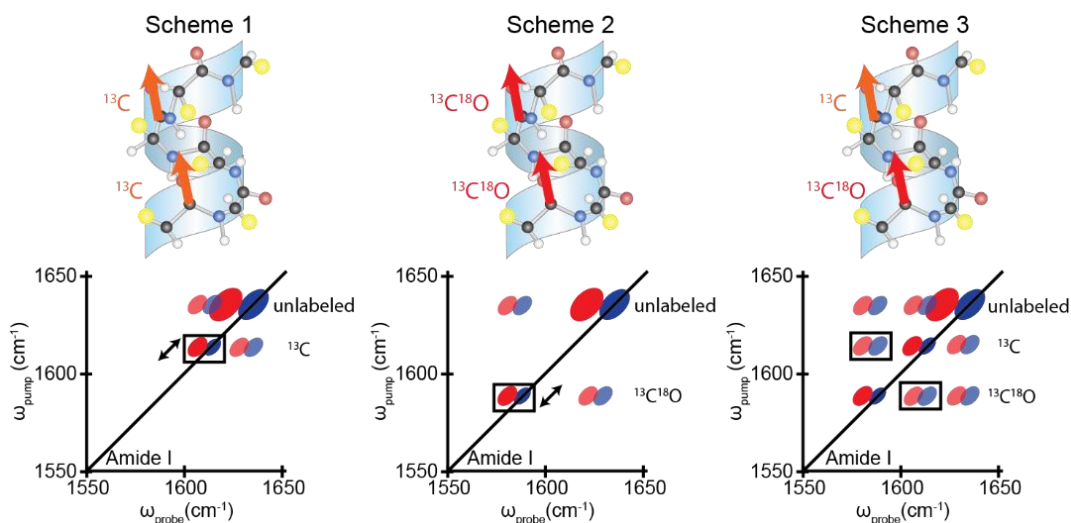


Figure 3.1 Cartoon depiction of isotope labeling schemes for α -helices (top) and predicted 2D IR spectra (bottom). Orange and red arrows denote ^{13}C and $^{13}\text{C}^{18}\text{O}$ isotopes, respectively. For each scheme, isotope-labeled spectral features (boxed) will be used to probe the sensitivity of each scheme, if applicable.

3.3 Materials and Methods

Materials. The 12-residue model α -helical peptide (MAHP, DPAEAAKAAAGR-NH₂) was obtained through solid-phase peptide synthesis using standard 9-fluorenylmethoxycarbonyl (Fmoc) chemistry with piperazine deprotection and diisopropylcarbodiimide/Oxyma activation on

a Liberty Blue microwave-assisted peptide synthesizer (CEM, NC, USA). Rink Amide ProTide resin (CEM, NC, USA) with high linker loading (0.70 milliequivalents per gram) was used as the solid support to yield an amidated C-terminus. Peptide cleavage from the resin and sidechain-protecting group removal was achieved with a cleavage cocktail of 95% trifluoroacetic acid, 2.5% triisopropyl silane, and 2.5% deionized water after 3 hours. The resin was filtered from the peptide solution and the excess solvent was removed from the solution. The peptide was precipitated in cold diethyl ether by centrifugation (5,000 rpm for 5 minutes) three times and the supernatant was discarded. The crude peptide was dissolved in high-purity water (~2 mg/mL) and filtered (0.20 μ m diameter). The peptide was purified by reversed-phase high performance liquid chromatography (Ultimate 3000, ThermoFisher Scientific, MA, USA) using an XBridge BEH preparative column (Waters Corporation, MA, USA). A binary gradient of pure water (Solvent A) to 90% acetonitrile in water (Solvent B) with 0.045% HCl (v/v) was implemented for purification. The gradient was varied from 0–40% Solvent B over 20 minutes, and the peptide eluted from the column at ~11 minutes (~22% Solvent B composition), which was monitored by ultraviolet absorption at 214 nm. The eluted fractions were lyophilized (Labconco, MO, USA) and stored at -20 °C. A ~1 mg/mL stock solution of pure peptide was prepared in a 70/30 acetonitrile/water mixture, using high-purity grade solvents. A ~10 μ g/mL peptide dilution was prepared in the same solvent system and 0.1% formic acid (v/v) was added to facilitate protonation during mass spectrometry analysis. The diluted sample was characterized by electrospray-ionization mass spectrometry (Orbitrap XL Penn, ThermoFisher Scientific, MA, USA). Peptide isotopologues were synthesized and purified in the same manner, substituting isotope-enriched (^{13}C and $^{13}\text{C}^{18}\text{O}$) Fmoc-protected amino acids at appropriate positions (Ala3, Ala5, Ala6, Ala8, and Gly11) during peptide synthesis.

L-alanine-1-¹³C and L-glycine-1-¹³C (99% enrichment, Millipore Sigma, MO, USA) were individually Fmoc protected using a mixture of 1:1:1 mole ratio amino acid (10 mmol), sodium bicarbonate, and Fmoc-succinimide dissolved using a 1:1 mixture of water and acetone (30 mL total). The reaction mixture stirred at room temperature (25 °C) for 24 hours and was quenched with 2 M potassium sulfate (~3 mL) until the solution reached a pH of 2, which precipitated the Fmoc-protected amino acid. The product was washed sparingly with ice-cold deionized water by vacuum filtration to remove residual salts present. The Fmoc-protected amino acid was lyophilized overnight to remove residual water. The Fmoc-protected amino acid was characterized with electrospray-ionization mass spectrometry as previously described (Orbitrap XL Penn, ThermoFisher Scientific, MA, USA).

Fmoc-alanine-1-¹³C¹⁸O¹⁸O and Fmoc-glycine-1-¹³C¹⁸O¹⁸O were individually prepared by an acid-catalyzed ¹⁸O-exchange using Schlenk techniques under nitrogen atmosphere. Briefly, 1 gram of Fmoc-1-¹³C amino acid was dissolved in a mixture of dioxane (8 mL) and 4 N HCl in dioxane (4 mL) in a 50-mL round bottom flask. The reaction mixture was heated to reflux (~20 minutes, 150 °C) and 1-mL of ¹⁸O-enriched water (98%, Cambridge Isotope Laboratories, MA, USA) was injected. After ¹⁸O-enriched water addition, the reaction refluxed for ~4 hours at 150 °C. The solvent was removed either by vacuum on the Schlenk line (~2–4 hours) or by lyophilization overnight. The ¹⁸O-exchange reaction was repeated twice more with the amino acid to achieve >90% ¹⁸O-labeling efficiency, which was determined by electrospray ionization mass spectrometry. Before characterization, the amino acid was precipitated and washed with dry diethyl ether by centrifugation (5,000 rpm, 5 minutes, 3x total) to remove undesired organic salts formed during the ¹⁸O-exchange reaction. Precipitates resulting from these washes were combined using dry dioxane and lyophilized overnight. For sample characterization with mass spectrometry,

100% acetonitrile was used as the sample's solvent system to avoid significant back-exchange with ^{16}O -water. A $\sim 10\ \mu\text{g/mL}$ dilution of the ^{18}O -enriched amino acid was prepared from a $\sim 1\ \text{mg/mL}$ in 100% acetonitrile and characterized with mass spectrometry as previously described. The Na^+ adduct isotopic ratios ($^{13}\text{C}^{18}\text{O}^{18}\text{O}$, $^{13}\text{C}^{18}\text{O}^{16}\text{O}$, and $^{13}\text{C}^{16}\text{O}^{16}\text{O}$) in the labeled amino acid's mass spectrum were used to determine the overall labeling efficiency.

All purified peptide samples were dissolved in deuterated solvents to ensure strong water bending modes did not overlap with the amide I' mode in 2D IR measurements. Concentrated stock solutions ($\sim 10\ \text{mM}$) were prepared in D_2O and quantified by ultraviolet-visible absorption measurements at 205 nm on a Nanodrop One-C spectrometer (ThermoFisher Scientific, MA, USA). 5 mM peptide solutions were prepared from the stock and diluted with D_2O and a cosolvent, 2,2,2-trifluoroethanol (TFE), if applicable. The diluted peptide solution pH was monitored with a micro-pH probe and adjusted with small (sub- μL) aliquots of sodium deuterioxide and deuterium chloride stocks as necessary. For the high helicity solvent condition (high pH with 40% TFE v/v), the solution pH was adjusted prior to adding the cosolvent and measured again afterwards to ensure the acid did not cause a significant (<1 unit) decrease in pH.

The peptide mixtures were vortexed, sealed with Parafilm, and incubated at room temperature for at least an hour prior to 2D IR measurements. After an hour, $\sim 10\ \mu\text{L}$ (or less) of peptide solution was placed between two CaF_2 windows (Crystran, UK) separated by a 50- μm Teflon spacer under N_2 atmosphere for 2D IR measurements. For CD experiments, $\sim 40\ \mu\text{L}$ of peptide solution was sandwiched between two quartz windows (0.1 mm pathlength, Starna Cells, CA, USA). The decreased cell pathlength was implemented in CD experiments to directly compare the same sample conditions with 2D IR measurements. The quartz cuvette was inserted into an

adapter (Starna Cells, CA, USA) to accommodate for the difference in the CD instrument's standard pathlength holder (10 mm).

The following small organic molecules and amino acids were used as model compounds for TFE solvatochromatic studies in 2D IR studies: *N*-methylacetamide (NMA), *N*-methyl-2-pyrrolidone (NMP), L-aspartic acid (Asp), L-arginine (Arg). Concentrated stocks of each compound were prepared in neat D₂O. Separate dilutions of each compound were made with (1) neat D₂O and (2) TFE (40% v/v) and D₂O to maintain the analyte concentration. The final concentration for the diluted model compounds in D₂O were 68 mM (NMA), 60 mM (NMP), 50 mM (Asp), and 29 mM (Arg). These samples were vortexed, sealed with Parafilm, and incubated at room temperature for at least an hour prior to 2D IR measurements. After incubation, the sample solution (~10 μL) was placed between two CaF₂ windows separated by a 50 μm Teflon spacer under N₂ atmosphere for 2D IR experiments.

Methods. 2D IR data collection and processing methods are described in detail elsewhere.⁵⁹ Briefly, ultrafast 800-nm pulses were generated by a Ti:Sapphire oscillator and amplified with a neodymium-doped yttrium vanadate (Nd:YVO₄)-pumped regenerative amplifier housed in a single compact laser system (Solstice Ace, Spectra-Physics, CA, USA). The Solstice output pulses (800 nm, 7 mJ, 1 kHz, 60 fs) were directed into a 50/50 beam splitter, where half the beam was sent into an optical parametric amplifier coupled with difference frequency generation (TOPAS-Prime, Spectra-Physics, CA, USA) to produce ultrafast mid-IR pulses. The mid-IR pulses (6 μm, 30 μJ, 1 kHz, 70 fs) were directed into a commercial 2D IR spectrometer (2DQuick IR, PhaseTech Spectroscopy, WI, USA) purged with dry, compressed air. The mid-IR beam was split into pump (~90%) and probe (~10%) paths, where the pump beam was directed into a germanium acousto-optic modulator (Ge AOM) pulse shaper, where time delays between the first

two pulses (t_1) were computer-generated. After the pump pulse was shaped, both beam paths were focused onto the sample to generate the nonlinear response along the probe line. The time delay between the second and third pulses (t_2) was kept constant (i.e., zero delay) for all measurements. Additionally, all mid-IR pulses had uniform polarizations (i.e., parallel polarization). After the beams were overlapped on the sample, the nonlinear signal was generated in the same direction along the probe beam. The probe line (containing the nonlinear signal) was directed into a monochromator (Princeton Instruments, NJ, USA) and measured with a 128-pixel mercury cadmium telluride (MCT) array (PhaseTech Spectroscopy, WI, USA). Raw data was initially processed through the QuickControl software (PhaseTech Spectroscopy, WI, USA) and further processed using MATLAB with a custom script. Adobe Illustrator software was used to generate the final 2D IR spectra.

Electronic circular dichroism (CD) measurements were made on a J-810 spectropolarimeter (Jasco, MD, USA) purged with $N_2(g)$ to prevent optic damage. All measurements were made at 24 °C. Spectra were collected from 190–260 nm in 1-nm increments at a scan rate of 100 nm per minute. Standard sensitivity (100 mdeg) was used for all CD measurements. Three spectra per sample were collected, averaged and smoothed in Microsoft Excel. The final spectra were plotted in MATLAB and further processed with Adobe Illustrator.

3.4 Results and Discussion

3.4.1 Peptide α -helicity is controlled through solvent conditions

Published 2D IR studies of α -helices focused on either stable helical structures or those that could be switched between completely helical and completely disordered states.^{44,45,47} In this study, we aim to identify and localize structural changes as a peptide gains or loses α -helicity. As

such, MAHP was identified as an ideal model system based on literature indicating that its helicity could be modulated gradually via pH.⁵⁸ In acidic conditions, MAHP adopts a disordered configuration. As the pH of the solution is increased, the peptide's ionizable sidechains become deprotonated and favorable intramolecular interactions (e.g., salt bridge formation between the E and K residues and deprotonation of the N-terminal D residue) promote and stabilize the peptide's linear α -helical structure. Such solvent-dependent behavior allows us to precisely control the peptide's conformation and examine isotopic spectral features at each point.

The initial study reported a qualitative increase in α -helicity with pH using CD, but did not quantify the amount of α -helical content as a function of pH.⁵⁸ To do so, and thus confirm that the structure of MAHP changed sufficiently to serve as a model system for this study, CD spectra were obtained across a pH range of 3–10. The CD signature of α -helices is distinct—there is a maximum at 190 nm and two minima at 208 nm and 222 nm.⁶⁰ The 222 nm band, which arises from an $n \rightarrow \pi^*$ electronic transition, is commonly used to quantify helical content in peptides and proteins.^{58,60} To extract quantitative information about α -helical content within a peptide, the experimental mean residue ellipticity (MRE) value must be compared to the theoretical MRE for the same peptide.⁶⁰ In a CD experiment, MRE is a normalized value of the measured molar ellipticity, which varies significantly depending upon the peptide/protein system and experimental conditions (i. e., number of residues, concentration, pathlength, etc.).⁶⁰ The following equation was used to compute the normalized MRE ($[\theta]$) value:

$$[\theta] \left(\frac{\text{deg} * \text{cm}^2}{\text{dmol}} \right) = \frac{\theta}{l * C * N} \quad (3.1)$$

where θ is the measured ellipticity (millidegrees), l is the pathlength (mm), C is the concentration (mol/L), and N is the number of residues.⁶⁰ The experimental MRE values for each solvent condition was compared to the theoretical MRE value of MAHP in a perfectly helical state. The following equation was used to calculate the theoretical maximum MRE ($[\theta]_H$) value for a perfectly helical peptide with N residues:

$$[\theta]_H = -40,000 * \left(1 - \frac{x}{N}\right) + 100 * T \quad (3.2)$$

where x is a chain-length dependent constant used to correct for non-hydrogen bonded carbonyls and T is the temperature ($^{\circ}\text{C}$).⁶¹ The constant x has been previously estimated to range from $\sim 0-3$, where x is inversely dependent upon chain length.⁶¹ MAHP is a relatively short peptide with 12 residues, thus x was estimated as 2.5 based on the CD unfolding curves from the study by Scholtz and coworkers.⁶¹ Taken together, this yielded a $[\theta]_H$ value of $\sim -29,667 \frac{\text{deg}\cdot\text{cm}^2}{\text{dmol}}$ at 24 $^{\circ}\text{C}$. Furthermore, we can calculate the percent peptide helicity as a function of solvent condition:

$$\% \text{ helicity} = \frac{[\theta]}{[\theta]_H} * 100 \quad (3.3)$$

CD measurements at 222 nm revealed a pH-dependent increase in helicity for MAHP (Figure 3.2, solid lines). MAHP exhibited $\sim 8\%$ helicity at pH 3, indicating that the peptide is primarily disordered under this condition. Isotopes placed in the center of the helix would be expected to exhibit weak coupling at this solvent condition. At high pH (~ 10), the peptide's helicity was increased to $\sim 25\%$, but for the 12-residue MAHP this corresponds to only 3 residues adopting an α -helical configuration which corresponds to just less than a full turn. As such, we could not be confident that paired isotope labels would reliably report coupling. To further enhance the peptide's helicity, the helix-stabilizing cosolvent 2,2,2-trifluoroethanol (TFE) was introduced to

MAHP under the same pH conditions.^{62–65} CD spectra revealed that TFE (40% v/v) induced a greater effect on peptide helicity compared to pH alone (Figure 3.2, dashed lines). At high pH (~10) with 40% TFE (v/v), the peptide exhibited ~60% helical character, which corresponds to ~2 helical turns in MAHP. Under this condition, the isotope labels placed in the center of MAHP are expected to participate in a well-organized α -helix and thus experience strong vibrational coupling due to their proximity. Increased vibrational coupling between the isotope pairs should yield prominent spectral changes (i.e., frequency shifts, intensity changes, and crosspeaks) indicative of helix formation. Additionally, helix formation is stabilized by intramolecular hydrogen bonding, which should induce a larger, negative frequency shift (up to $\sim 20\text{ cm}^{-1}$).⁴⁸ In contrast, one or both of the peptide termini likely remain frayed under these conditions. Isotopic pairs placed three residues apart in a frayed region would exhibit weak coupling spectral features (i.e., constant frequencies, low intensities, and no observable off-diagonal features). Thus, we anticipate isotopic pairs placed at the helix center versus termini should yield distinct signatures in 2D IR spectra.

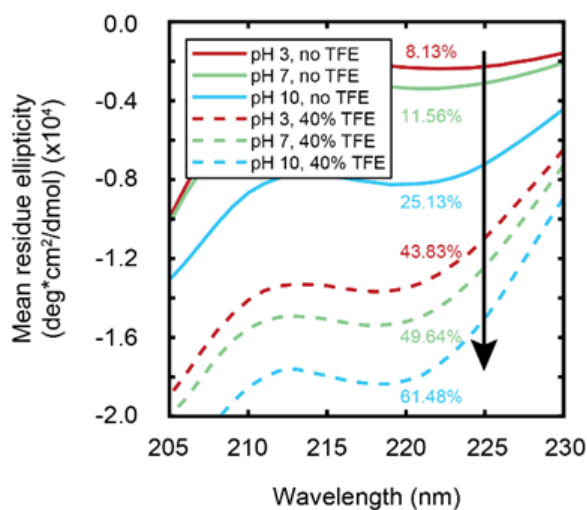


Figure 3.2 Solvent conditions modulate peptide α -helicity. CD spectra revealed an increase in pH from 3–10 resulted in an increase in α -helicity (solid lines, 8.13%–25.13%). The addition of 40% TFE (v/v) further enhanced the peptide’s helicity with increasing pH (dashed lines, 43.83%–61.48%).

3.4.2 TFE enhances peptide α -helicity and blueshifts frequencies in 2D IR

While TFE increases α -helicity in MAHP, likely by creating a more hydrophobic environment that promotes the formation of intramolecular hydrogen-bonding, this environmental change can also result in solvatochromic shifts in IR frequencies.^{62,66–68} Therefore, before examining 2D IR spectral features that arise as MAHP transitions from a disordered to α -helical structure, we must first find a way to decouple frequency shifts that arise from changes in structure versus those that arise from changes in solvent environment. To this end, we measured solvatochromic shifts in small model compounds. *N*-Methylacetamide (NMA) and *N*-Methyl-2-Pyrrolidone (NMP) are both contain a single amide bond and have been used previously as peptide analogues for IR studies.^{48,69,70} Additionally, IR solvatochromic shifts of two amino acids, Arg and Asp, were studied. While the amino acids do not contain a true amide bond, the carboxylate and guanidino sidechain groups have vibrational modes within the amide I' spectral region.⁵⁴ The chemical structures of each model compound are depicted below in Figure 3.3.

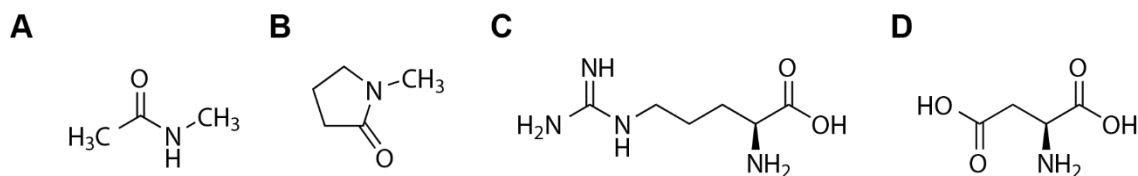


Figure 3.3 Chemical structures of model compounds used for solvatochromism study. Small organic molecules (A) NMA and (B) NMP were used to model the amide vibration. Amino acids (C) L-arginine and (D) L-aspartic acid were used as model compounds.

2D IR spectra were collected of the model compounds in (1) neat D₂O and (2) in a mixture of 40% TFE in D₂O. In the presence of TFE, all model compounds exhibited 5–6 cm⁻¹ blueshift compared to the same compound dissolved in neat D₂O (Figure A1.6 and Table A1.1). The

blueshift confirms that the carbonyl bonds are strengthened in TFE, consistent with a reduction in the available hydrogen-bond partners in solution. While the $\sim 6\text{ cm}^{-1}$ blueshift is considerable, vibrational coupling is expected to redshift the amide I' frequencies. Therefore, while solvent-induced frequency shifts may dampen structural-induced frequency shifts in the model peptide, they should not create “false positives” or prevent data analysis.

Based on CD experiments (Figure 3.2), three solvent conditions were selected to characterize the model peptide's spectral signatures with 2D IR. The first condition is at pH 3 without TFE, which corresponds to a disordered structure. The second condition is at pH 10 without TFE, which corresponds to an intermediate/partially helical secondary structure. The last condition is at pH 10 with the addition of the cosolvent, which corresponds to a mostly helical structure. Representative 2D IR spectra of unlabeled MAHP at each solvent conditions are shown in Figure 3.4. As the peptide's helicity increases, the amide I' frequency redshifts and the antidiagonal linewidth qualitatively narrows, a characteristic signature of higher-ordered secondary structures.⁴⁰ It is important to note that the amide I' frequency of MAHP continues to redshift as helicity increases, even once TFE is added. While the amide I' mode shift is likely dampened by the solvatochromic effect of the cosolvent, the increase in vibrational coupling as the α -helix forms is strong enough to dominate the overall spectral shift.

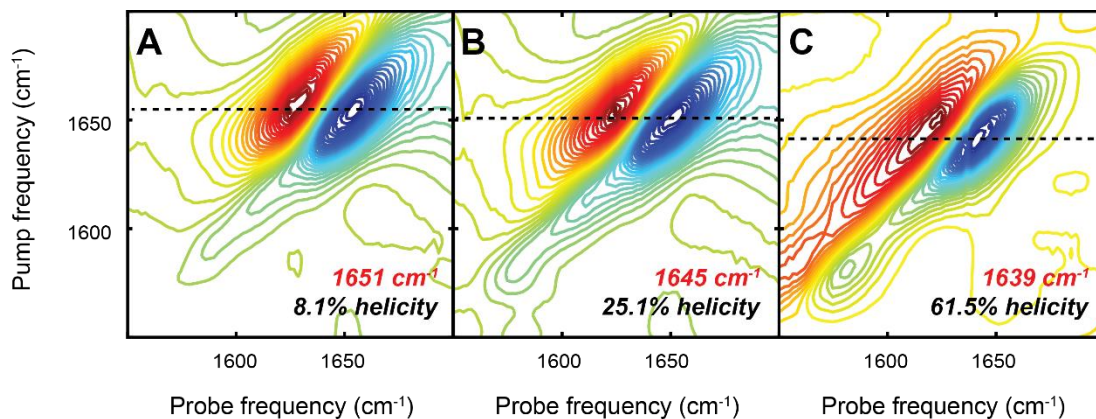


Figure 3.4 2D IR spectra of unlabeled MAHP under optimized solvent conditions. MAHP adopting a (A) disordered structure (low pH without TFE), (B) partially-helical structure (high pH without TFE), and (C) predominantly helical secondary structure (high pH with 40% TFE v/v). Amide I' frequencies (red) and percent helicities quantified by CD experiments (black) are noted at the bottom-right of each spectrum. Aspartate sidechain presents as a shoulder near $\sim 1580\text{--}1590\text{ cm}^{-1}$ at (A and B) low and intermediate conditions and an isolated transition at (C) the highest helicity.

3.4.3 Dual $^{13}\text{C}^{18}\text{O}$ probes detect α -helix formation spanning central residues

After establishing solvent conditions that corresponded to distinct helical states in the model peptide, three isotope-labeling variations were investigated by 2D IR: (1) double ^{13}C , (2) double $^{13}\text{C}^{18}\text{O}$, and (3) mixed $^{13}\text{C}/^{13}\text{C}^{18}\text{O}$. Isotopic probes were incorporated at the i and $i+3$ positions in the model peptide's sequence, where the carbonyls should be oriented parallel to each other when the α -helix is folded. For initial experiments, the central residues were labeled at residues A5 and A8, as these residues span the center of the MAHP sequence where α -helical turns are hypothesized to be most stable. 2D IR spectra of each labeling scheme incorporated into MAHP were examined under the three distinct solvent conditions previously discussed. Representative 2D IR spectra of the double ^{13}C labeling scheme (i.e., Scheme 1, MAHP LS1, ^{13}C -labeled at A5 and A8) are shown in Figure 3.5. In the disordered configuration (Figure 3.5A), there is a clear isotope peak at $\sim 1606\text{ cm}^{-1}$ redshifted $\sim 44\text{ cm}^{-1}$ from the bulk amide I' mode. The ^{13}C transition is quite broad along the diagonal (Figure 3.5A), indicative of variations in the isotopes'

environment, which is expected in a random coil conformation. In the intermediate condition, there are two transitions: one at 1606 cm^{-1} with more intensity, and another $\sim 1580\text{ cm}^{-1}$, likely due to the aspartate sidechain mode (Figure 3.5B). While the more intense $\sim 1606\text{ cm}^{-1}$ mode could indicate an increase in coupling between the ^{13}C pair, it is difficult to discern due to the broadened transition. As the helicity is increased (Figure 3.5C), the isotope peak appears to redshift to $\sim 1593\text{ cm}^{-1}$. This significant redshift in the isotopic frequency is likely due to local intramolecular hydrogen bonding, which stabilizes helical structures. From these 2D IR experiments, it was clear that the dual ^{13}C labels were not ideal for tracking changes in peptide helicity from this system due to insufficient separation from the bulk amide I' transition and extensive broadening in the low-frequency region.

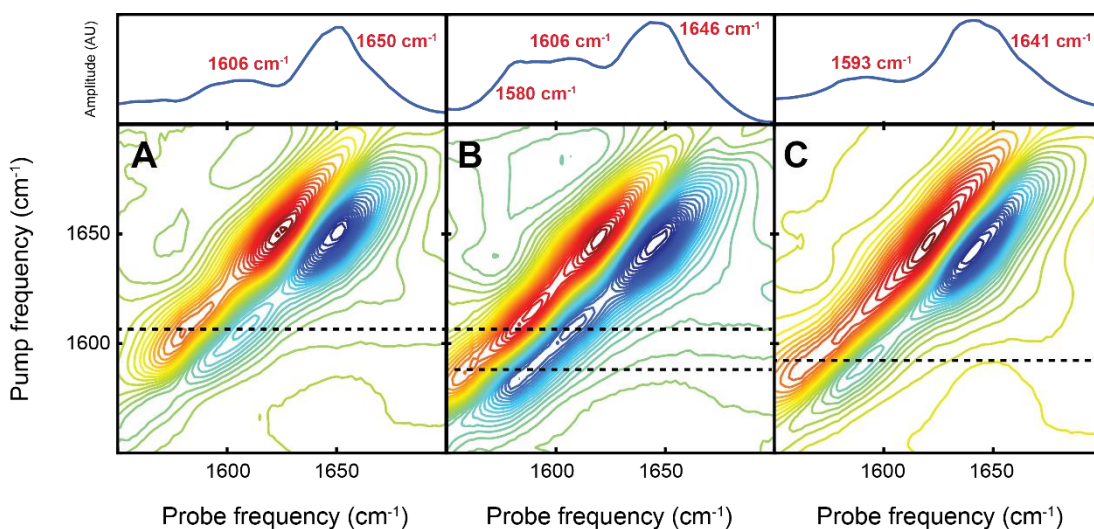


Figure 3.5 2D IR spectra of MAHP LS1 as a function of peptide α -helicity. Double ^{13}C -edited A5 and A8 MAHP experiencing a (A) disordered, (B) intermediate, and (C) helical structure. The isotope labels appear as a distinct transition in the disordered peptide configuration (A, dashed line), but the isotope transition broadens as the peptide folds into a helix (B and C, dashed lines). In (B), the low-frequency shoulder arises from the aspartate residue.

Next, 2D IR spectra of the double $^{13}\text{C}^{18}\text{O}$ -edited MAHP (i.e., Scheme 2, MAHP LS2, $^{13}\text{C}^{18}\text{O}$ -labeled at A5 and A8) were collected (Figure 3.6). The heavier $^{13}\text{C}^{18}\text{O}$ isotope shifts the local amide I' backbones further from the bulk amide I' transition compared to ^{13}C ($\sim 62\text{ cm}^{-1}$, Figure 3.6A). The larger frequency separation generally provides better spectral resolution to examine changes in the labeled mode, although it is important to note aspartate is located in this region. The $^{13}\text{C}^{18}\text{O}$ pair appears as an isolated transition at $\sim 1589\text{ cm}^{-1}$ in the random coil structure (Figure 3.6A), which redshifts to $\sim 1581\text{ cm}^{-1}$ and gains intensity as the helix begins to fold (Figure 3.6B). These spectral signatures (i.e., redshifted frequency and higher intensity) reflect increased ordering, which arises from hydrogen bond formation and vibrational coupling, although these interactions cannot be decoupled. At the highest helical condition, the isotope pair is centered near $\sim 1584\text{ cm}^{-1}$, but is more intense compared to the intermediate structure (Figure 3.6C). This slight blueshift was due to TFE (see Section 3.4.2). The intensity gain suggests stronger vibrational coupling of the isotopes, indicative of increased α -helicity. From this study, it is clear that $^{13}\text{C}^{18}\text{O}$ probes features are more resolved compared to ^{13}C labels in this peptide system. These features are suggestive of helix formation through hydrogen bonding interactions and vibrational coupling, although the two events cannot be isolated from this set of experiments. In the following section, we will discuss how single labeling was utilized to assign the origin of these features.

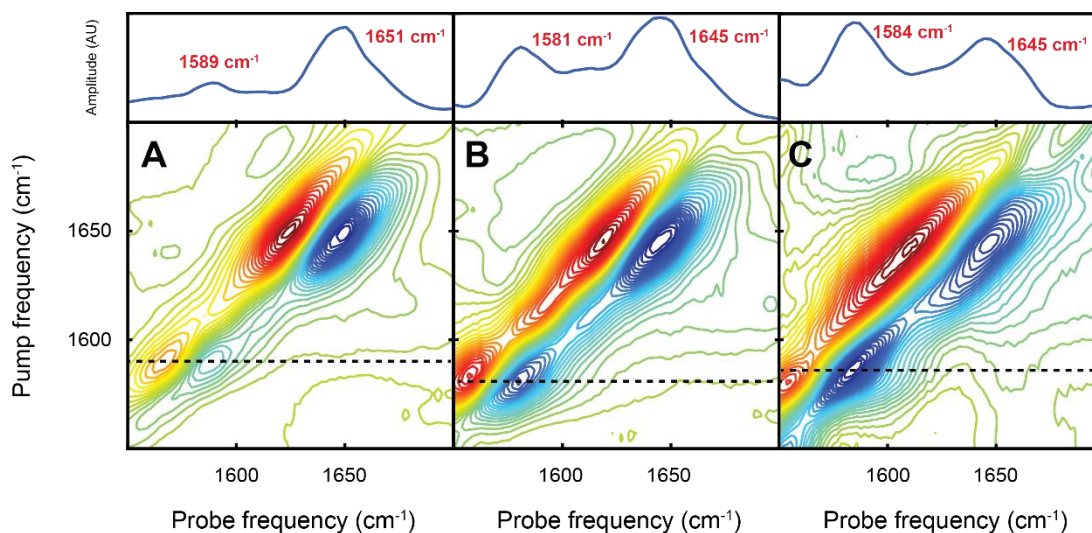


Figure 3.6 Representative 2D IR spectra of MAHP LS2 at varying degrees of α -helicity. The $^{13}\text{C}^{18}\text{O}$ mode is highlighted with horizontal dashed lines in each spectrum. (A) The isotopes appear at $\sim 1589\text{ cm}^{-1}$ in the random coil configuration. (B) As the helix begins to form, the isotope mode intensifies and redshifts to $\sim 1581\text{ cm}^{-1}$. (C) The isotope mode remains near $\sim 1584\text{ cm}^{-1}$ and intensifies in the helical conformation.

Finally, the mixed labeling scheme incorporated into MAHP (i.e., Scheme 3, MAHP LS3, ^{13}C at A5 and $^{13}\text{C}^{18}\text{O}$ at A8) was examined by 2D IR to determine whether or not crosspeaks could be resolved between two different isotopic modes. The representative 2D IR data for MAHP LS3 is illustrated in Figure 3.7. Two distinct features were observed at $\sim 1589\text{ cm}^{-1}$ and $\sim 1612\text{ cm}^{-1}$ in the low helicity condition, which matches with the frequencies observed in the double-labeled $^{13}\text{C}^{18}\text{O}$ - and ^{13}C -labeled peptides, respectively (Figures 3.6A and 3.5A), in the disordered peptide configuration. At the intermediate condition, both labeled modes double in intensity and redshift $\sim 10\text{ cm}^{-1}$ (Figure 3.7B). Again, the increased intensities reflect stronger local transition dipole coupling, revealing a higher degree of structural ordering (i.e., local disordered to helix transition). This magnitude in redshift ($\sim 10\text{ cm}^{-1}$) is characteristic of hydrogen bonding, which is another defining feature of helix stabilization. However, this spectral region is not well-resolved enough to detect crosspeaks between the isotope labels, if present. Interestingly, only one strong transition

is observed around $\sim 1580\text{ cm}^{-1}$ when the peptide's helicity was maximized (Figure 3.7C). This distinct mode has a higher-frequency shoulder along the diagonal trace (Figure 3.7C, top panel), which could suggest that the ^{13}C -labeled A8 residue is experiencing hydrogen bonding and vibrational coupling, but cannot be spectrally resolved. For this system, this observation significantly complicates our characterization of the α -helix due to the additional sidechain interferences. From these initial 2D IR measurements, it can be concluded that ^{13}C was overall lacking at identifying local changes in peptide α -helicity.

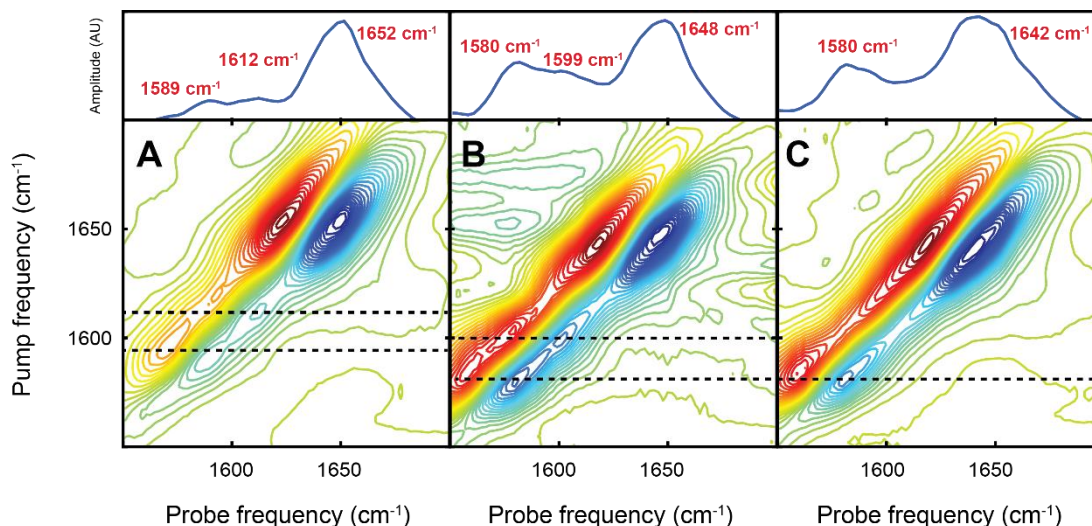


Figure 3.7 2D IR spectra of MAHP LS3 as a function of peptide α -helicity. The ^{13}C and $^{13}\text{C}^{18}\text{O}$ features are denoted with horizontal dashed lines. (A) Both isotopes appear as isolated transitions when the peptide is disordered. (B) As the helix forms, both isotopes redshift $\sim 10\text{ cm}^{-1}$. (C) At the high helicity condition, a single transition is observed at $\sim 1581\text{ cm}^{-1}$ with an unresolved shoulder on the high-frequency side.

3.4.4 Double $^{13}\text{C}^{18}\text{O}$ labeling suggests terminal conformational differences

Overall, labeling scheme 2 (i.e., double $^{13}\text{C}^{18}\text{O}$ editing at i and $i+3$ positions) was the most straightforward scheme for examining changes in isotopic signatures, which suggested local

differences between disordered and α -helical secondary structures (Figure 3.6). To further probe the helix formation, the N-terminus (A3 and A6) and C-terminus (A8 and G11) were also edited with a pair of $^{13}\text{C}^{18}\text{O}$ isotopes. The isotopic signatures were monitored with 2D IR under the same solvent conditions to examine the helical termini conformations as a function of peptide helicity. The spectra for the double $^{13}\text{C}^{18}\text{O}$ labeling of N-terminal and C-terminal ends are shown in Figures 3.8 and 3.9, respectively. The labeled N-terminus followed the same trend as the central labeling scheme (Figure 3.6), where the isotopic mode redshifted $\sim 12\text{ cm}^{-1}$ and exhibited an intensity enhancement approximating the amide I' mode (Figure 3.8). However, the $^{13}\text{C}^{18}\text{O}$ -edited C-terminus displays a similar trend but to a lesser extent—the isotope transition shifted $\sim 9\text{ cm}^{-1}$ and the intensity was comparatively weaker (Figure 3.9). Again, the slight blueshifted amide I' frequencies here are attributed to the cosolvent. The frequency shift in the A8 and G11 signatures infers more hydrogen bonding interactions occur in the helical state compared to the unfolded conformation, but there seems to be a greater degree of disorder in this region. While the intensity of the isotopic probes increases, the magnitude is approximately half compared to when the probes are inserted at the N-terminus. Overall, these findings suggest the C-terminal $^{13}\text{C}^{18}\text{O}$ probes (A8 and G11) do not participate in the helix to the extent of the other positions (A3, A5, and A6). This result is logical when considering the G11 residue exhibits a high degree of conformational flexibility due to its small hydrogen sidechain, which is known to destabilize helical structures.^{58,71} In summary, $^{13}\text{C}^{18}\text{O}$ probe pairs inserted at the helical termini revealed that when the α -helix is folded, the C-terminus (A8 and G11) adopts a less restricted structure compared to the other labeled positions examined (A3, A5, and A6).

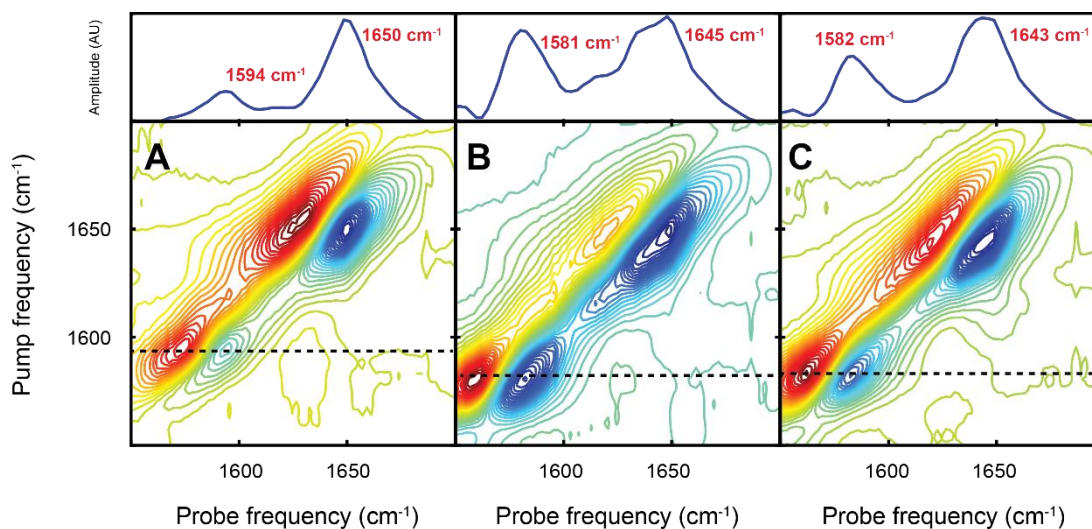


Figure 3.8 N-terminal MAHP LS2 (A3 and A6) spectra as a function of α -helicity. The $^{13}\text{C}^{18}\text{O}$ labels are denoted by dashed lines. (A) Isotope pair appears as an isolated transition at $\sim 1594\text{ cm}^{-1}$ in the low helicity condition. (B) The isotope mode gains intensity and shifts to $\sim 1581\text{ cm}^{-1}$ upon helicity increase. (C) $^{13}\text{C}^{18}\text{O}$ mode remains at $\sim 1582\text{ cm}^{-1}$ at the highest helical condition.

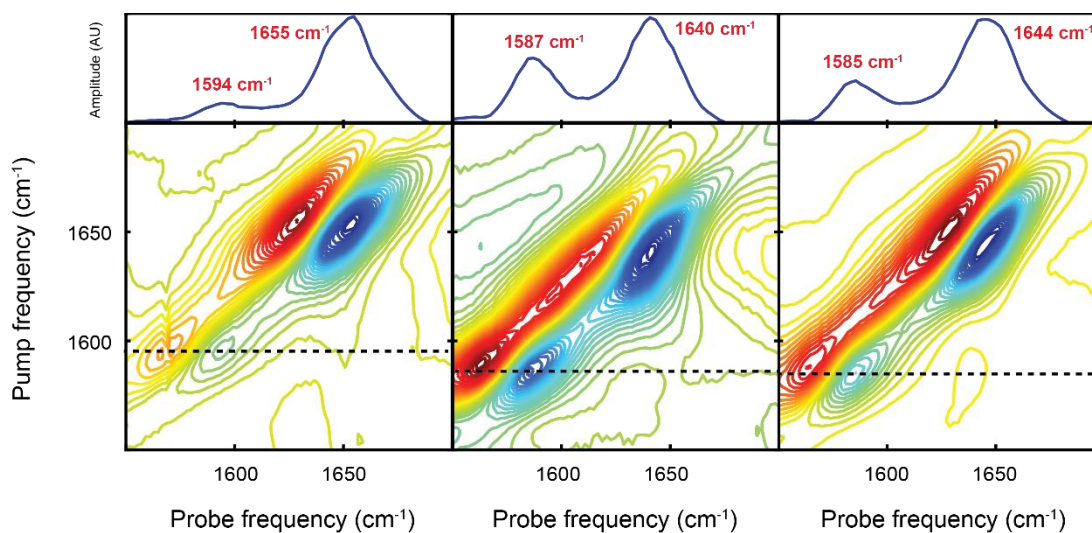


Figure 3.9 C-terminal MAHP LS2 (A8 and G11) spectra as a function of α -helicity. Isotope-edited features are represented by horizontal dashed lines. (A) The labeled mode is present at $\sim 1594\text{ cm}^{-1}$ in the disordered structure. (B and C) As the helicity increases, the isotope mode gains intensity and redshifts, but to a lesser extent compared to the other labeled positions.

3.4.5 Semi-quantitative intensity ratio comparison of sidechain and isotopes

While we have demonstrated that $^{13}\text{C}^{18}\text{O}$ labels three residues apart report molecular changes in an α -helix upon folding, we still need to address the underlying sidechain feature present in all of the MAHP samples. This feature is likely due to the ionizable aspartate residue, which simultaneously appears in the region of interest between $\sim 1580\text{--}1590\text{ cm}^{-1}$.⁵⁴ Here, we reveal the sidechain absorption is much weaker compared to the double $^{13}\text{C}^{18}\text{O}$ -labeled samples due to vibrational coupling effects. When two isotopes are oriented in the helical turn, their transition dipole strengths delocalize. This delocalization of charge induces a larger transition dipole and redistributes the oscillator strength. Since we are examining different positions along the same α -helix, which inherently experiences some structural and solvent variations, ratios were hypothesized to be sufficient at capturing qualitative coupling differences. A more rigorous approach would quantify the transition dipole coupling strengths, which has been previously applied to the amide I' signal in 2D IR studies.^{27,57} However, TDS calculations are not as sensitive to weaker signals, such as those arising from sidechains and isotopes. Here, we quantified the ratios between the low-frequency (sidechain and isotope signal contributions) and amide I' signals for the unlabeled, single $^{13}\text{C}^{18}\text{O}$ -labeled, and double $^{13}\text{C}^{18}\text{O}$ -labeled peptides. Examining the single $^{13}\text{C}^{18}\text{O}$ -edited (A5) peptide provided a way to compare how removing coupling between identical residues influenced the overall signal strength.

Representative 2D IR spectra in the low-frequency spectral region ($1540\text{--}1600\text{ cm}^{-1}$) and quantitative intensity ratios are summarized in Figure 3.10, Figure 3.11, and Table 3.1, respectively. Additional 2D IR spectra along with a full description of the ratio calculations are provided in Appendix 1. The sidechain signal strength in the unlabeled peptide spectrum is $\sim 16\text{--}18\%$ of main amide I' mode at the high pH condition(s). The low-frequency transition for the

single $^{13}\text{C}^{18}\text{O}$ -labeled (A5) peptide is approximately twice as intense as the sidechain alone under the same condition(s). It is critical to note that a single isotope does not experience the same vibrational coupling enhancement compared to the dual probes, where the transition dipole strength is delocalized over two residues. The low-frequency ratio calculated for A5 MAHP, which arises from a single label and the sidechain contributions, is consistent with a previous 2D IR study employing single labels in an α -helix with aspartate residues.⁷² For the N-terminal (A3A6) and centrally (A5A8) labeled peptides, the ratio is greatly enhanced (~ 5 – 6 x more intense) compared to the unlabeled peptide at the same condition. This verifies that, for these samples, coupling between the isotope pair is the primary contributor to signal strength and are suppressing the sidechain's signal. For the C-terminal labeling scheme (A8G11), the overall signal strength is weaker and comparable to the single $^{13}\text{C}^{18}\text{O}$ mode intensity, especially at the highest helical condition. Additionally, there is more variations in the intensity ratios for the A8G11 spectra, which reflects more structural and/or solvent fluctuations. In conclusion, two coupled isotopes contribute substantially more to the overall signal strength compared to the underlying sidechain or a single $^{13}\text{C}^{18}\text{O}$ probe. This ratio comparison supports isotopic coupling in a folded α -helix induces a larger intensity gain in this region in 2D IR measurements, allowing the local interactions to be measured in the presence of the sidechain mode.

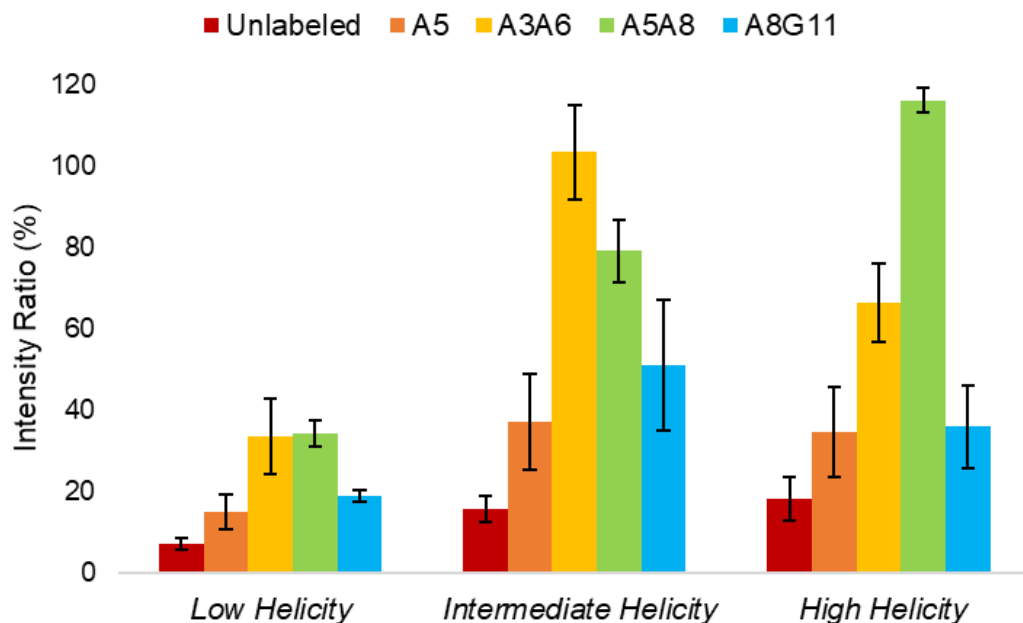


Figure 3.10. Summary of intensity ratios (low-frequency to amide I' mode) for unlabeled, single, and double $^{13}\text{C}^{18}\text{O}$ -labeled MAHP as a function of α -helicity. The unlabeled (red) intensity increased at higher α -helicity due to sidechain ionization. A single $^{13}\text{C}^{18}\text{O}$ isotope at A5 (orange) displayed the same trend as the unlabeled sample. The double $^{13}\text{C}^{18}\text{O}$ -edited samples (A3A6, yellow; A5A8, green; A8G11, blue) exhibited enhanced intensities in the intermediate and high conditions due to increased vibrational coupling between probes. The average intensity values and respective standard deviations are listed in Table 3.1.

Table 3.1 Low-frequency to amide I' mode intensity comparison for ¹³C¹⁸O samples	
<i>¹³C¹⁸O-labeled positions</i>	<i>Average Low-Frequency to Amide I' Mode Intensity Ratio (%)</i>
Unlabeled (low helicity)	7.0 ± 1.4
Unlabeled (intermediate helicity)	15.8 ± 3.2
Unlabeled (high helicity)	18.2 ± 5.2
A5 (low helicity)	15.1 ± 4.3
A5 (intermediate helicity)	37.0 ± 11.8
A5 (high helicity)	34.7 ± 11.1
A3A6 (low helicity)	33.6 ± 9.4
A3A6 (intermediate helicity)	103.4 ± 11.7
A3A6 (high helicity)	66.4 ± 9.5
A5A8 (low helicity)	34.3 ± 3.1
A5A8 (intermediate helicity)	79.1 ± 7.7
A5A8 (high helicity)	116.2 ± 2.9
A8G11 (low helicity)	18.9 ± 1.5
A8G11 (intermediate helicity)	51.2 ± 16.1
A8G11 (high helicity)	35.9 ± 10.1

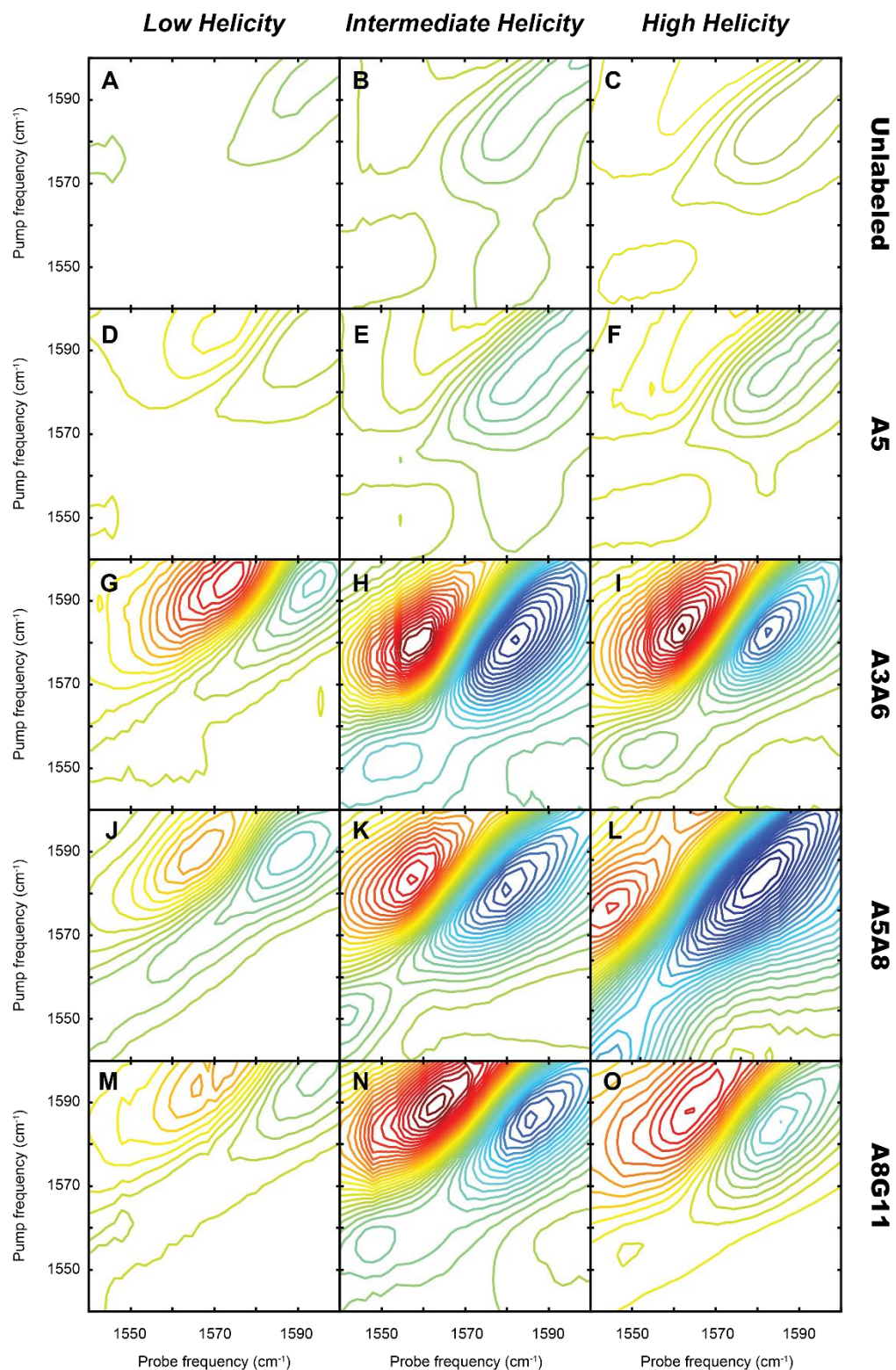


Figure 3.11 Representative 2D IR spectra of unlabeled, single, and double $^{13}\text{C}^{18}\text{O}$ -labeled MAHP in the low-frequency spectral window. (A–C) Unlabeled, (D–F) A5-labeled, (G–I) A3A6-labeled, (J–L) A5G8-labeled, and (M–O) A8G11-labeled MAHP at low, intermediate, and high helicity conditions (left to right). See Appendix 1 for more details on this calculation.

3.5 Conclusions

In summary, we have demonstrated how 2D IR supplemented with isotope labeling methods can measure sensitive molecular interactions in a model α -helix. By incorporating dual $^{13}\text{C}^{18}\text{O}$ probes three residues apart in the α -helix, we were able to monitor local intensity changes arising from local transition dipole coupling, allowing us to isolate where these particular structures formed. The isotopic transition revealed that the N-terminal and central region (A3, A5, and A6) underwent hydrogen bonding and vibrational coupling as a function of α -helicity, while the C-terminus remained less ordered (A8 and G11). Additionally, single labeling with $^{13}\text{C}^{18}\text{O}$ at the central A5 position allowed us to decouple the effects of hydrogen bonding and vibrational coupling, revealing that hydrogen bonding was the primary contributor to the $\sim 10\text{ cm}^{-1}$ redshift. Lastly, we addressed the interference of sidechain vibrations in the spectral region of interest by showing that two coupled $^{13}\text{C}^{18}\text{O}$ probes induce a large enough intensity difference to effectively suppress the sidechain mode.

Taken together, these results suggest that as the peptide folds it adopts ~ 2 helical turns spanning the N-terminal (A3 and A6) and central (A5 and A8) residues, but remains more flexible between positions A8 and G11. These findings are also in good agreement with CD measurements ($\sim 60\%$, Figure 3.2). This structure is also supported by the design of the model peptide, where the N-terminus is stabilized by a hydrogen bond with the D1 sidechain and a salt bridge between residues E4 and K7.⁵⁸ Additionally, residues P2 and G11 are known to demarcate MAHP's helical ends due to the helix-breaking propensity.⁵⁸ G11's inherent conformational flexibility supports the weaker coupling features (i.e., lesser frequency shifts and intensity gains) observed in 2D IR spectra (Figure 3.11).

While $^{13}\text{C}^{18}\text{O}$ probes were sensitive to the degree of peptide α -helicity in 2D IR measurements, ^{13}C labels were largely ineffective at capturing the same molecular events. In particular, the mixed labeling scheme (Scheme 3, $^{13}\text{C}^{18}\text{O}/^{13}\text{C}$) lacked crosspeaks, which would have been an additional spectral marker of vibrational coupling across the helical turn. In theory, a mixed amide I/II labeling scheme with $^{13}\text{C}^{18}\text{O}$ and ^{15}N placed four residues apart could be used to monitor α -helix formation through crosspeaks, which has been previously applied to a 3_{10} -helix but in a different solvent system (CDCl_3 vs. D_2O).⁵³ Future work would need to address how to mitigate D_2O interferences from an $i, i+4$ mixed amide I'/II' labeling in an α -helix to be compatible with peptide and protein IR structural studies.

Additionally, future work could focus on collecting rephasing and nonrephasing spectra of isotope-edited α -helices, which may be more sensitive to crosspeaks compared to absorptive 2D spectra.⁵³ The data presented here was collected using a mid-IR pulse shaper, where the two pump pulses are collinear and have the same polarization. All data provided in this study was collected utilizing a parallel polarization, where all pulses and the emitted signal are polarized in the same direction (i.e., ZZZZ). Implementing a perpendicular polarization scheme, where the pump and probe pulses' have polarizations which are 90° offset (i.e., ZZXX), can help enhance crosspeaks in this experimental setup. However, the perpendicular polarization scheme was not informative in this isotope study (Appendix 1, Figures A1.11 and A1.12). 2D IR pump-probe measurements generally do not allow for fine polarization adjustments to the two individual pump pulses. Future work could examine these labeling schemes implementing a four-wave mixing 2D IR geometry or utilize more specific polarization schemes, which may help resolve crosspeaks obscured by the strong diagonal peaks.⁷³

Potential sidechain interferences in the MAHP sequence include Asp, Glu, and Arg. The

strongest sidechain feature, likely the underlying carboxylate from Asp, coincides with the isotope mode ($\sim 1580\text{--}1590\text{ cm}^{-1}$).⁵⁴ While the sidechain is more intense at high pH (i.e., intermediate and high helicity conditions), the signals from two coupled isotopes exceed the sidechain absorption by at least 50% (Figures 3.10 and 3.11). While spectral subtraction methods can be implemented, a wide range of experimental factors (e.g., calibration, laser power fluctuations, peptide concentration, scatter, etc.) that affect 2D IR signals can complicate the subtraction process and introduce artifacts.⁷² Here, a semi-quantitative comparison was drawn between the unlabeled, single, and double $^{13}\text{C}^{18}\text{O}$ -labeled peptides in the low frequency region ($1540\text{--}1600\text{ cm}^{-1}$). This intensity-ratio evaluation indicated the strong spectral features originated from coupling between the isotopes, rather than the underlying sidechain absorption (Table 3.1). As previously mentioned, transition dipole strength measurements could be applied to quantify coupling, but these measurements are difficult with weaker signals, such as those arising from one or two isotopes.⁵⁷ These issues could be overcome by altering sample conditions (increasing concentration or pathlength) or by introducing additional isotope labels (e.g., uniformly labeling domains)³⁸ to improve signal strength.

Future work could harness sidechains as label-free vibrational probes in peptides and proteins. For example, the aspartate residue in MAHP provides a well-resolved IR signal, which could probe local molecular changes as the helix folds. Aspartate mutation in the MAHP sequence has been shown to significantly decrease its helical content, revealing its crucial role in helix stabilization through end capping.^{58,71,74} The mechanism N-terminal stabilization through end capping could be further clarified through 2D IR lineshape analysis and waiting time studies of the sidechain carboxylate group in this model peptide.^{69,75–77} Additionally, the vibrational lifetime of the aspartate sidechain likely differs in the protonated and unprotonated forms. Lifetimes have

been previously used to suppress different protein signals in 2D IR experiments, which could have the potential to resolve isotopic signals underneath native sidechain modes.⁷⁸ This approach could also be extended to the C-terminal Arg residue at higher pH (>10) to explore ionization effects on its local environment.

3.6 References

- (1) Tsai, C. Y. et al. Helical Structure Motifs Made Searchable for Functional Peptide Design. *Nat. Commun.*, **2022**, 13 (1), 1–14.
- (2) Li, T. et al. Peptide-Based Nanomaterials: Self-Assembly, Properties and Applications. *Bioact. Mater.*, **2022**, 11, 268–282.
- (3) Newberry, R. W. and Raines, R. T. Secondary Forces in Protein Folding. *ACS Chem. Biol.*, **2019**, 14 (8), 1677–1686.
- (4) Kuriyan, J.; Konforti, B.; Wemmer, D. *The Molecules of Life*, First.; Scholl, S., Ed.; Garland Science: New York and London, **2013**.
- (5) Respondek, M. et al. Mapping the Orientation of Helices in Micelle-Bound Peptides by Paramagnetic Relaxation Waves. *J. Am. Chem. Soc.*, **2007**, 129 (16), 5228–5234.
- (6) Tossi, A. et al. Amphipathic, α -Helical Antimicrobial Peptides. *Pept. Sci.*, **2000**, 55, 4–30.
- (7) Sato, H. and Feix, J. B. Peptide-Membrane Interactions and Mechanisms of Membrane Destruction by Amphipathic α -Helical Antimicrobial Peptides. *Biochim. Biophys. Acta - Biomembr.*, **2006**, 1758 (9), 1245–1256.
- (8) Jochim, A. L. and Arora, P. S. Assessment of Helical Interfaces in Protein-Protein Interactions. *Mol. Biosyst.*, **2017**, 5 (9), 924–926.
- (9) Lee, E. Y. et al. Helical Antimicrobial Peptides Assemble into Protofibril Scaffolds That Present Ordered DsDNA to TLR9. *Nat. Commun.*, **2019**, 10 (1012), 1–10.
- (10) Dovega, R. et al. Structural and Biochemical Characterization of Human PR70 in Isolation and in Complex with the Scaffolding Subunit of Protein Phosphatase 2A. *PLoS One*, **2014**, 9 (7), 1–12.
- (11) Johnson, L. N. and Barford, D. Glycogen Phosphorylase. The Structural Basis of the Allosteric Response and Comparison with Other Allosteric Proteins. *J. Biol. Chem.*, **1990**, 265 (5), 2409–2412.
- (12) Xu, M. et al. Allosterically Activated Protein Self-Assembly for the Construction of Helical Microfilaments with Tunable Helicity. *Angew. Chemie - Int. Ed.*, **2018**, 57 (18), 5029–5032.
- (13) Yang, L. W. et al. Ligand-Induced Protein Responses and Mechanical Signal Propagation Described by Linear Response Theories. *Biophys. J.*, **2014**, 107 (6), 1415–1425.
- (14) Friedrich, C. et al. Salt-Resistant Alpha-Helical Cationic Antimicrobial Peptides. *Antimic.*, **1999**, 43 (7), 1542–1548.
- (15) Oliveira-bravo, M. et al. LL-37 Boosts Immunosuppressive Function of Placenta-Derived Mesenchymal Stromal Cells. *Stem Cell Res. Ther.*, **2016**, 7 (189), 1–11.

- (16) Vlasova, I. M. et al. Study of the Denaturation of Human Serum Albumin. *J. Appl. Spectrosc.*, **2009**, 76 (4), 536–541.
- (17) Soto, C. et al. The α -Helical to β -Strand Transition in the Amino-Terminal Fragment of the Amyloid Beta Peptide Modulates Amyloid Formation. *J. Biol. Chem.*, **1995**, 270 (7), 3063–3067.
- (18) Brange, J. et al. Toward Understanding Insulin Fibrillation. *J. Pharm. Sci.*, **1997**, 86 (5), 517–525.
- (19) Newman, M. D. et al. The Safety of Nanosized Particles in Titanium Dioxide and Zinc Oxide-Based Sunscreens. *J. Am. Dermatology*, **2009**, 61 (4), 685–692.
- (20) N, G.; K, V. Application of Nano Silver Particles on Textile Materials for Improvement of Antibacterial Finishes. *Glob. J. Nanomed.*, **2017**, 2 (3), 42–45.
- (21) Nune, S. K. et al. Nanoparticles in Medical Imaging. *Expert Opin. Drug Deliv.*, **2009**, 6 (11), 1175–1194.
- (22) De Jong, W. H. et al. Drug Delivery and Nanoparticles: Applications and Hazards. *Int. J. Nanomed.*, **2008**, 3 (2), 133–149.
- (23) Kondo, A. and Mihara, J. Comparison of Adsorption and Conformation of Hemoglobin and Myoglobin on Various Inorganic Ultrafine Particles. *J. Colloid Interface Sci.*, **1996**, 221 (23), 214–221.
- (24) Brandes, N. et al. Adsorption-Induced Conformational Changes of Proteins onto Ceramic Particles: Differential Scanning Calorimetry and FTIR Analysis. *J. Colloid Interface Sci.*, **2006**, 299, 56–69.
- (25) Mollmann, S. H. et al. Interfacial Adsorption of Insulin Conformational Changes and Reversibility of Adsorption. *Eur. J. Pharm. Sci.*, **2005**, 27, 194–204.
- (26) Mandal, H. S. and Kraatz, H. Effect of the Surface Curvature on the Secondary Structure of Peptides Adsorbed on Nanoparticles. *J. Amer. Chem. Soc.*, **2007**, 129, 6356–6357.
- (27) Lomont, J. P. et al. Not All β -Sheets Are the Same: Amyloid Infrared Spectra, Transition Dipole Strengths, and Couplings Investigated by 2D IR Spectroscopy. *J. Phys. Chem. B*, **2017**, 121, 8935–8945.
- (28) Alperstein, A. M. et al. Amyloid Found in Human Cataracts with Two-Dimensional Infrared Spectroscopy. *Proc. Natl. Acad. Sci.*, **2019**, 116 (14), 6602–6607.
- (29) Thielges, M. C. Transparent Window 2D IR Spectroscopy of Proteins. *J. Chem. Phys.*, **2021**, 155 (4), 1–14.
- (30) Kim, Y. S. and Hochstrasser, R. M. Applications of 2D IR Spectroscopy to Peptides, Proteins, and Hydrogen-Bond Dynamics. *J. Phys. Chem. B*, **2009**, 113 (24), 8231–8251.
- (31) Mukherjee, P. et al. Picosecond Dynamics of a Membrane Protein Revealed by 2D IR. *Proc. Natl. Acad. Sci.*, **2006**, 103 (10), 3528–3533.
- (32) Ghosh, A. and Hochstrasser, R. M. A Peptide's Perspective of Water Dynamics. *Chem. Phys.*, **2011**, 390 (1), 1–13.
- (33) Baiz, C. R. et al. An Introduction to Protein 2D IR Spectroscopy. *Ultrafast Infrared Vib. Spectrosc.*, **2013**, 22, 361–403.
- (34) Ghosh, A. et al. Watching Proteins Wiggle: Mapping Structures with Two-Dimensional Infrared Spectroscopy. *Chem. Rev.*, **2017**, 117 (16), 10726–10759.

- (35) Demirdöven, N. et al. Two-Dimensional Infrared Spectroscopy of Antiparallel β -Sheet Secondary Structure. *J. Am. Chem. Soc.*, **2004**, 126 (25), 7981–7990.
- (36) Shim, S. et al. Two-Dimensional IR Spectroscopy and Isotope Labeling Defines the Pathway of Amyloid Formation with Residue-Specific Resolution. *Proc. Natl. Acad. Sci.*, **2009**, 106 (16), 6614–6619.
- (37) Flanagan, J. C. and Baiz, C. R. Site-Specific Peptide Probes Detect Buried Water in a Lipid Membrane. *Biophys. J.*, **2019**, 116 (9), 1692–1700.
- (38) Moran, S. D. et al. Two-Dimensional IR Spectroscopy and Segmental ^{13}C Labeling Reveals the Domain Structure of Human γD -Crystallin Amyloid Fibrils. *Proc. Natl. Acad. Sci.*, **2012**, 109 (9), 3329–3334.
- (39) Buchanan, L. E. et al. Structural Motif of Polyglutamine Amyloid Fibrils Discerned with Mixed-Isotope Infrared Spectroscopy. *Proc. Natl. Acad. Sci.*, **2014**, 111 (16), 5796–5801.
- (40) Woys, A. M. et al. 2D IR Line Shapes Probe Ovispirin Peptide Conformation and Depth in Lipid Bilayers. *J. Am. Chem. Soc.*, **2010**, 132 (8), 2832–2838.
- (41) Woys, A. M. et al. Parallel β -Sheet Vibrational Couplings Revealed by 2D IR Spectroscopy of an Isotopically Labeled Macrocyclic: Quantitative Benchmark for the Interpretation of Amyloid and Protein Infrared Spectra. *J. Am. Chem. Soc.*, **2012**, 134 (46), 19118–19128.
- (42) Kim, Y. S. et al. Two-Dimensional Infrared Spectra of Isotopically Diluted Amyloid Fibrils from A β 40. *Proc. Natl. Acad. Sci.*, **2008**, 105 (22), 7720–7725.
- (43) Maj, M. et al. Site-Specific Detection of Protein Secondary Structure Using 2D IR Dihedral Indexing: A Proposed Assembly Mechanism of Oligomeric HIAPP. *Chem. Sci.*, **2018**, 9 (2), 463–474.
- (44) Huang, R. et al. Nature of Vibrational Coupling in Helical Peptides: An Isotopic Labeling Study. *J. Am. Chem. Soc.*, **2004**, 126 (8), 2346–2354.
- (45) Fang, C. et al. Two-Dimensional Infrared Spectroscopy of Isotopomers of an Alanine Rich α -Helix. *J. Phys. Chem. B*, **2004**, 108 (29), 10415–10427.
- (46) Kim, Y. S. et al. Two-Dimensional Infrared Spectroscopy of the Alanine Dipeptide in Aqueous Solution. *J. Phys. Chem. B*, **2005**, 109 (15), 7511–7521.
- (47) Backus, E. H. G. et al. 2D-IR Study of a Photoswitchable Isotope-Labeled α -Helix. *J. Phys. Chem. B*, **2010**, 114 (10), 3735–3740.
- (48) Torii, H. et al. Effects of Intermolecular Hydrogen-Bonding Interactions on the Amide I Mode of N-Methylacetamide: Matrix-Isolation Infrared Studies and Ab Initio Molecular Orbital Calculations. *J. Phys. Chem. B*, **1998**, 102 (1), 309–314.
- (49) Decatur, S. M. Elucidation of Residue-Level Structure and Dynamics of Polypeptides via Isotope-Edited Infrared Spectroscopy. *Acc. Chem. Res.*, **2006**, 39 (3), 169–175.
- (50) Donaldson, P. Photon Echoes and Two Dimensional Spectra of the Amide I Band of Proteins Measured by Femtosecond IR – Raman Spectroscopy. *Chem. Sci.*, **2020**, 11 (33), 8862–8874.
- (51) Kubelka, J. et al. Contribution of Transition Dipole Coupling to Amide Coupling in IR Spectra of Peptide Secondary Structures. *Vib. Spectrosc.*, **2006**, 42 (1), 63–73.

- (52) Ganim, Z. et al. Amide I Two-Dimensional Infrared Spectroscopy of Proteins. *Acc. Chem. Res.*, **2008**, 41 (3), 432–441.
- (53) Maekawa, H. et al. Couplings between Peptide Linkages across a 3_{10} -Helical Hydrogen Bond Revealed by Two-Dimensional Infrared Spectroscopy. *J. Am. Chem. Soc.*, **2009**, 131 (6), 2042–2043.
- (54) Barth, A. The Infrared Absorption of Amino Acid Side Chains. *Prog. Biophys. Mol. Biol.*, **2000**, 74 (3–5), 141–173.
- (55) Ghosh, A. et al. 2D IR Spectroscopy of Histidine: Probing Side-Chain Structure and Dynamics via Backbone Amide Vibrations. *J. Phys. Chem. B*, **2014**, 118 (28), 7799–7805.
- (56) Ghosh, A. et al. Tidal Surge in the M2 Proton Channel, Sensed by 2D IR Spectroscopy. *Proc. Natl. Acad. Sci.*, **2011**, 108 (15), 6115–6120.
- (57) Grechko, M. and Zanni, M. T. Quantification of Transition Dipole Strengths Using 1D and 2D Spectroscopy for the Identification of Molecular Structures via Exciton Delocalization: Application to α -Helices. *J. Chem. Phys.*, **2012**, 137, 1–9.
- (58) Forood, B. et al. Stabilization of α -Helical Structures in Short Peptides via End Capping. *Proc. Natl. Acad. Sci.*, **1993**, 90, 838–842.
- (59) Middleton, C. T. et al. Residue-Specific Structural Kinetics of Proteins through the Union of Isotope Labeling, Mid-IR Pulse Shaping, and Coherent 2D IR Spectroscopy. *Methods*, **2010**, 52 (1), 12–22.
- (60) Greenfield, N. J. Using Circular Dichroism Spectra to Estimate Protein Secondary Structure. *Nat. Protocols*, **2007**, 1 (6), 2876–2890.
- (61) Scholtz, J. M. et al. Parameters of Helix-Coil Transition Theory for Alanine-Based Peptides of Varying Chain Lengths in Water*. *Biopolymers*, **1991**, 31, 1463–1470.
- (62) Buck, M. Trifluoroethanol and Colleagues: Cosolvents Come of Age. Recent Studies with Peptides and Proteins. *Q. Rev. Biophys.*, **1998**, 31 (3), 297–355.
- (63) Myers, J. K. et al. Trifluoroethanol Effects on Helix Propensity and Electrostatic Interactions in the Helical Peptide from Ribonuclease T1. *Protein Sci.*, **1998**, 7 (2), 383–388.
- (64) Albert, J. S. and Hamilton, A. D. Stabilization of Helical Domains in Short Peptides Using Hydrophobic Interactions. *Biochemistry*, **1995**, 34 (3), 984–990.
- (65) Roccatano, D. et al. Mechanism by Which 2,2,2-Trifluoroethanol/Water Mixtures Stabilize Secondary-Structure Formation in Peptides: A Molecular Dynamics Study. *Proc. Natl. Acad. Sci.*, **2002**, 99 (19), 12179–12184.
- (66) Błasiak, B. et al. Vibrational Solvatochromism: Towards Systematic Approach to Modeling Solvation Phenomena. *J. Chem. Phys.*, **2013**, 139 (4), 1–13.
- (67) Błasiak, B. et al. Vibrational Probes: From Small Molecule Solvatochromism Theory and Experiments to Applications in Complex Systems. *Acc. Chem. Res.*, **2017**, 50 (4), 968–976.
- (68) Błasiak, B. et al. Vibrational Solvatochromism of Nitrile Infrared Probes: Beyond the Vibrational Stark Dipole Approach. *Phys. Chem. Chem. Phys.*, **2016**, 18 (27), 18094–18111.

- (69) Woutersen, S. et al. Hydrogen-Bond Lifetime Measured by Time-Resolved 2D-IR Spectroscopy: *N*-Methylacetamide in Methanol. *Chem. Phys.*, **2001**, 266 (2–3), 137–147.
- (70) Peng, C. S. et al. Direct Observation of Ground-State Lactam-Lactim Tautomerization Using Temperature-Jump Transient 2D IR Spectroscopy. *Proc. Natl. Acad. Sci.*, **2013**, 110 (23), 9243–9248.
- (71) Aurora, R. and Rose, G. D. Helix Capping. *Protein Sci.*, **1998**, 7 (1), 21–38.
- (72) Kratochvil, H. T. et al. Probing the Effects of Gating on the Ion Occupancy of the K⁺ Channel Selectivity Filter Using Two-Dimensional Infrared Spectroscopy. *J. Am. Chem. Soc.*, **2017**, 139 (26), 8837–8845.
- (73) Farrell, K. M. et al. A Polarization Scheme That Resolves Cross-Peaks with Transient Absorption and Eliminates Diagonal Peaks in 2D Spectroscopy. *Proc. Natl. Acad. Sci.*, **2022**, 119 (6).
- (74) Wu, H. et al. Design of a Short Thermally Stable α -Helix Embedded in a Macrocycle. *ChemBioChem*, **2018**, 19 (9), 902–906.
- (75) Giubertoni, G. et al. Effect of Intramolecular Hydrogen-Bond Formation on the Molecular Conformation of Amino Acids. *Commun. Chem.*, **2020**, 3 (1), 1–6.
- (76) Hagarman, A. et al. Amino Acids with Hydrogen-Bonding Side Chains Have an Intrinsic Tendency to Sample Various Turn Conformations in Aqueous Solution. *Chem. - A Eur. J.*, **2011**, 17 (24), 6789–6797.
- (77) Shin, J. Y. et al. Imidazole and 1-Methylimidazole Hydrogen Bonding and Nonhydrogen Bonding Liquid Dynamics: Ultrafast IR Experiments. *J. Phys. Chem. B*, **2019**, 123 (9), 2094–2105.
- (78) Middleton, C. T. et al. Utilizing Lifetimes to Suppress Random Coil Features in 2D IR Spectra of Peptides. *J. Phys. Chem. Lett.*, **2011**, 2 (18), 2357–2361.

Chapter 4. Establishing conditions for structural analysis of nanoparticle-bound peptides and proteins with two-dimensional infrared spectroscopy

4.1 Abstract

In this chapter, sample conditions necessary for future 2D IR studies of polypeptides in the presence of nanoparticles were established. For initial studies, a model α -helical peptide (EK-helix) and protein (lysozyme) were studied in the presence of gold colloids. Three distinct nanoparticle sizes were tested: 20 nm, 60 nm, and 74 nm gold colloids stabilized in citrate solution. The 20 nm and 60 nm gold colloids stabilized by 0.1 mg/mL sodium citrate were purchased from Alfa Aesar and used as supplied. The 74 nm gold colloids in citrate solution were synthesized by a collaborator in the Macdonald lab at Vanderbilt University and used as provided. The citrate stabilizer (0.1 mg/mL) did not impact peptide/protein structure or absorb IR light at sub milligram per milliliter concentrations. Centrifugation and sonication, which were techniques required for nanoparticle solvent exchange and isolations, did not alter the secondary structure of the model peptide/protein. Peptide/protein addition to the commercial nanoparticles resulted in no nanoparticle isolation after centrifugation, which was unexpected. The commercial nanoparticles were only separated from solution at low protein concentrations (nM), which were not feasible for 2D IR characterization. The synthesized gold colloids were mixed independently with the model peptide and protein systems, which each displayed a different affinity. Lysozyme did not associate strongly with the gold colloids, as indicated by a slight redshift (~2 nm) in the LSPR band and the substantial removal of protein upon centrifugation. EK-helix interacted with the synthesized gold colloids, as reflected by a noticeable color change of the mixture and a larger redshift (~9 nm) in the LSPR peak. EK-helix stabilized the gold nanoparticles in solution, which could not be removed

by centrifugation. 2D IR spectra were collected of model peptide and protein with gold colloids added, but indicated no major structural changes were induced by the nanoparticles. Further characterization methods will be required to identify the different nanoparticle stabilization mechanisms induced by peptides and proteins. Other purification techniques could also be implemented to isolate the nanoparticles from free peptide/protein in solution, if desired. Importantly, the gold colloids did not exhibit major IR light scattering, which allows peptide/protein spectra to be collected without implementing spectral deconvolution methods.

4.2 Introduction

It is important to understand the impacts of nanomaterial exposure on all aspects of our world, especially biological systems.¹⁻³ Nanomaterials range in size from ~1–1000 nm, are comprised of various materials (e.g., metals, polymers, etc.), and adopt many shapes (e.g., spheres, cubes, stars, etc.).⁴⁻¹¹ The combination of nanoparticle size, composition, and shape modulates specific interactions with biological molecules and cells.¹²⁻¹⁷ The molecular associations between biological molecules and nanoparticles can be utilized for different biomedical applications, such as imaging, drug delivery, and sensing.¹⁸⁻²⁴ However, despite their increasing use in medicine and other industries, much remains unclear about interactions between nanoparticles and biological entities on the molecular level.

Nanoparticles can be tailored to induce selective interactions with various biological targets.²⁵⁻²⁷ Some nanomaterials can elicit strong associations with biomacromolecules, like DNA- and protein-magnetic nanoparticles.²⁸⁻³⁴ Other nanomaterials can be decorated with polymers, like short peptides or polyethylene glycol (PEG), to evade biological molecules.^{4,35-37} When biological molecules associate with nanoparticles, they tend to rapidly coat the surface and create a

biomolecular corona. The biomolecular corona gives the nanoparticle a new identity and dictates future interactions with other species.³⁸⁻⁴⁰ Proteins comprise a large percentage of biological media, such as blood serum.^{41,42} Nanoparticle introduction into biological media, like blood serum, can elicit favorable protein interactions, resulting in protein corona formation. Therefore, understanding the molecular compositions and resultant biological activities of protein coronas is critical not only for their medical use, but also application within other industries where they likely come in contact with biological species.

A protein's structure is vital for proper function. This holds true with protein coronas as well, where the protein's global configuration will guide the complex's interactions with different species.⁴³⁻⁴⁵ When proteins come in contact with nanoparticles, they can sometimes undergo structural changes to facilitate energetically favorable interactions.^{46,47} Even slight modifications in protein structure can result in drastically different biological activities of protein coronas, like autoimmune responses.⁴⁸ Therefore, elucidating structural changes in protein coronas, whether intentional or unexpected, is vital for a more complete understanding of their biocompatibility.

Many protein corona studies employ molecular spectroscopy to identify structural alterations before and after nanoparticle exposure.⁴⁹⁻⁵¹ Common techniques to probe protein structure in the presence of nanoparticles include fluorescence, circular dichroism, and vibrational spectroscopies (e.g., Fourier transform IR and Raman), which provide information on global structural and conformational changes.⁵¹⁻⁵⁴ However, proteins can also exhibit minor structural rearrangements, which could be lost without high-resolution techniques or additional labeling procedures. Therefore, spectroscopic techniques that can also capture site-specific structural changes are extremely advantageous for protein corona studies.

Two-dimensional infrared (2D IR) spectroscopy coupled with isotope labeling is capable of tracking site-specific structural changes within peptides and proteins.⁵⁵⁻⁵⁸ Isotopes, like ¹³C or ¹³C¹⁸O, can be incorporated at specific locations within the polypeptide sequence through solid-phase peptide synthesis or protein expression in isotope-enriched media.^{59,60} Integrating isotopes within the peptide backbone redshifts the residue's molecular vibration, spectrally isolating it from the bulk protein amide I' transition. Vibrational coupling of the labeled mode can be examined through spectral features (e.g., frequency shifts, intensity changes, lineshapes, crosspeaks, etc.), thus achieving residue-specificity. In addition, 2D IR spectroscopy has been utilized to examine molecular interactions at nanoparticle surfaces.^{61,62} Some nanoparticles (e.g., gold and silver colloids) do not strongly absorb or scatter light in the amide I' region.^{63,64} This allows protein structure and dynamics to be tracked without spectral interferences from nanomaterials, which has been demonstrated with glutathione in the presence of silver nanoparticles.^{65,66}

The overarching goal of this project was to examine detailed structural changes in peptides and proteins upon nanoparticle exposure with 2D IR spectroscopy and isotope labeling. In particular, α -helical proteins have been shown to commonly denature upon nanoparticle contact.^{63,67-70} Common serum proteins, like albumin and fibrinogen, contain a large percentage of α -helical structure, providing motivation to study changes in protein helicity when exposed to nanoparticles.^{71,72} Therefore, I chose to examine model α -helical peptides and proteins for my initial nanoparticles studies due to their high natural abundance and diverse roles in various biological activities. For preliminary experiments, I selected a robust model α -helix (EK-helix, Ac-AEAAAKEAAAKEAAKA-NH₂) that is stable over a wide pH range to avoid structural differences arising from sample conditions.⁷³ I also chose to examine a model protein (hen-egg white lysozyme, HEWL) containing a high abundance of helical character, which has been well-

characterized and implemented in several protein corona studies.^{70,74–78} While there have been several protein corona studies with HEWL, I could not gain access to the exact nanoparticles used in this specific FTIR study due to proprietary rights from the company.⁷⁰ We initially explored similar nanoparticles used in these studies (e.g., silica and alumina), but these species experienced significant solubility issues and thus were not carried forward. I eventually settled on gold colloids for the preliminary nanoparticle systems, which are easily quantifiable, suspend well in aqueous media, and are abundant throughout protein corona literature.^{4,14,63,64,78} I have used both commercially-purchased and synthesized citrate-capped gold colloids, which were synthesized by a collaborator in the Macdonald lab at Vanderbilt. In this Chapter, I will discuss my preliminary work on sample preparation and characterization of model peptide and protein corona samples.

4.3 Materials and Methods

EK-helix (Ac-AEAAAKEAAAKEAAKA-NH₂) was synthesized on an automated microwave-assisted Liberty Blue peptide synthesizer using standard Fmoc chemistry as described in detail in Chapter 2. The N-terminus was acetylated immediately following Fmoc deprotection. N-terminal acetylation was carried out using a solution of 10% acetic anhydride (v/v) in dimethylformamide (DMF) using the standard amino acid coupling method. The peptide was cleaved from the resin (Rink Amide ProTide) and the sidechain protecting groups were removed using a cleavage cocktail of 95% trifluoroacetic acid (TFA), 2.5% triisopropylsilane (TIPS), and 2.5% H₂O. The cleavage cocktail was filtered from the resin and dried with compressed air. After the solution was dried into a film, the peptide was precipitated with cold diethyl ether and washed 3x by centrifugation (5,000 rpms for 5 minutes). The crude peptide was dissolved in HPLC-grade H₂O, vortexed, and filtered through a 0.20- μ m filter to prepare a ~2 mg/mL solution for RP-HPLC purification. The same gradient used for MAHP (See Chapter 2, Section 2.2.4) was sufficient to

elute EK-helix at ~28% Solvent B (90% acetonitrile in H₂O with 0.045% HCl) composition. The peptide fractions were collected and lyophilized. EK-helix (1612.81 g/mol) was characterized by electrospray ionization mass spectrometry using the same preparation methods as the MAHP peptide (See Chapter 2, Section 2.2.5). The mass spectrum of purified EK-helix is shown in Figure 4.1. Purified HEWL (~14,300 g/mol) was purchased from Millipore Sigma and used without any further modifications.

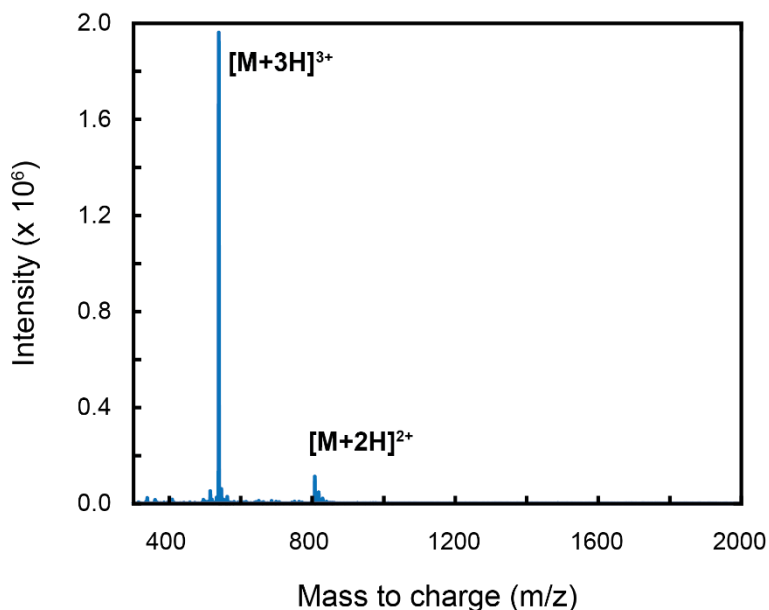


Figure 4.1 Mass spectrum of EK-helix. Signals observed in the mass spectrum are characteristic of the EK-helix peptide (1612.81 g/mol). The most intense peak at 538.6 m/z represents $[M+3H]^{3+}$. The weaker signal at 807.4 m/z corresponds to $[M+2H]^{2+}$. No peak is observed for the $[M+H]^+$ species.

Concentrated stocks of purified peptide (~10 mM) and protein (~20 mg/mL) were prepared in D₂O or H₂O with 0.1 mg/mL sodium citrate, depending on the experiment. The stock solution pH was recorded using a standardized micro pH probe (ThermoFisher, MA, USA). The peptide and protein stocks were quantified by UV-Visible spectroscopy on a Nanodrop One C spectrometer (ThermoFisher, MA, USA) using the pedestal option (1-cm pathlength). EK-helix

does not contain tryptophan and was therefore quantified at 205 nm using the calculated molar absorptivity value ($\epsilon_{\text{EK-helix}} = 27.58 \text{ L g}^{-1} \text{ cm}^{-1}$).⁷⁹ HEWL was quantified at 280 nm using the lysozyme setting installed on the Nanodrop software ($\epsilon_{\text{HEWL}} \sim 39,000 \text{ M}^{-1}\text{cm}^{-1}$). 1 mM EK-helix and ~10 mg/mL (~0.70 mM) HEWL dilutions were prepared at low pH for initial 2D IR and CD experiments. The solutions were incubated at room temperature for at least 1 hour prior to collecting spectra.

Gold colloids (10, 20, and 60 nm diameters) with 0.1 mg/mL added sodium citrate were commercially purchased (Alfa Aesar, MA, USA). All nanoparticle suspensions were stored at 4 °C and covered with aluminum foil to prevent exposure to light. Supplementary information about these nanoparticles, which was provided by the company, is listed below in Table 4.1. Additionally, 74 nm gold colloids capped with sodium citrate were synthesized and characterized by a collaborator in the Macdonald lab according to a published protocol.⁸⁰ For typical nanoparticle experiments, a 1-mL aliquot of nanoparticle stock was transferred to a 2-mL microfuge tube and centrifuged (17,000g, 20 minutes) to separate the nanoparticles from the solution, which formed a purple/red pellet at the bottom of the tube. The solvent was exchanged at least twice with deuterated solvent to avoid overlapping water absorptions in IR experiments. To minimize nanoparticle loss, a maximum of ~900 μL of supernatant was carefully removed from the 1-mL aliquot and was replaced with the same amount of deuterated solvent. The nanoparticle concentrations were quantified with UV-Visible spectroscopy according to their localized surface plasmon resonance (LSPR) band on the Nanodrop One C (ThermoFisher, MA, USA) using the cuvette feature. A 1-cm pathlength quartz cuvette (Starna Cells, 1 mL total solution volume) was used to quantify all nanoparticle-containing solutions to avoid contaminating the pedestal. A

minimum of ~600 μL of blank (D_2O with 0.1 mg/mL sodium citrate) and nanoparticle solution was required in the 1-mL cuvette for the quantification.

Table 4.1 Supplementary information for gold nanoparticles supplied in 0.1 mg/mL sodium citrate from Alfa Aesar							
<i>Diameter (nm)</i>	<i>SPR (nm)</i>	<i>Particles per mL</i>	<i>Molar extinction ($M^{-1}\text{cm}^{-1}$)</i>	<i>Particle volume (nm^3)</i>	<i>Surface area (nm^2)</i>	<i>Molar mass (g/mol)</i>	<i>Molar concentration (M)</i>
10	515-520	5.98E+12	1.01E+08	5.24E+02	3.14E+02	6.11E+06	9.93E-09
20	524	6.54E+11	9.21E+08	4.19E+03	1.26E+03	4.89E+07	1.09E-09
60	540	1.96E+10	3.07E+10	1.13E+05	1.13E+04	1.32E+09	3.25E-11

Peptide/protein and nanoparticle mixtures were prepared in deuterated solvents to avoid overlapping water bending modes in the amide I' region. After the nanoparticle solution was exchanged twice with deuterated solvent and quantified, the solvent was again removed by centrifugation (17,000g, 20 minutes). 900 μL of supernatant was gently removed and replaced with the appropriate volume of peptide/protein stock and solvent. The final concentration of nanoparticles in solution was quantified as previously described. The final peptide and protein concentrations were ~1 mM (slightly less for HEWL, ~0.70 mM). Sodium citrate was present at a low concentration (0.1 mg/mL) to stabilize the colloidal charge in solution. The nanoparticle-containing samples were vortexed, sealed with Parafilm, and incubated at room temperature for at least ~1 hour in the dark to avoid light exposure. For some experiments, the loosely-bound peptide/protein was removed by centrifugation to keep the “hard” corona. The supernatant

containing the free peptide/protein was removed and neat solvent was added. The “hard” corona was resuspended by briefly (~few seconds) sonicating and vortexing the mixture. The supernatant containing the free peptide/protein was saved and quantified, which could be used to roughly estimate the amount of peptide/protein associating with the nanoparticle. The “hard” protein corona mixture was also quantified at the peptide/protein and LSPR wavelengths on a Nanodrop One C spectrometer (ThermoFisher Scientific, MA, USA) using the cuvette option.

After incubation, 2D IR samples were prepared by adding ~10 μL of sample solution between two CaF_2 windows with a 50- μm Teflon spacer under N_2 (g) flow. For CD experiments, 40 μL of EK-helix (Starna Cells, 0.1 mm pathlength) and 20 μL of HEWL (Starna Cells, 0.01 mm pathlength) were sandwiched between two quartz windows. The decreased pathlength was utilized in CD experiments so the same sample conditions could be directly compared with 2D IR experiments. The quartz cuvette was gently placed into an adapter (Starna Cells) to accommodate for the difference in the CD sample holder’s pathlength (i.e., 10 mm).

2D IR measurements were collected and processed as described in detail in Chapter 2 (Section 2.4). CD spectra were collected on a J-810 CD spectropolarimeter (Jasco, MD, USA) purged with N_2 (g) in the Biophysical Core at Vanderbilt University. CD spectra were collected from 190–260 nm in 1-nm increments with standard sensitivity (100 mdeg). Three spectra were collected for each sample and blank, which were averaged and smoothed in Microsoft Excel. The final spectra were analyzed with a custom MATLAB script and processed in Adobe Illustrator.

4.4 Results and Discussion

4.4.1 Citrate does not impact model peptide/protein signal or structure

Nanoparticles are typically capped with ligands (i.e., small organic molecules) to precisely control growth and impart colloidal stability.^{81–83} Additionally, ligands can impart unique characteristics to the nanoparticle, providing more tunability to the system.^{84–86} A common capping agent for gold and silver colloids is citrate.^{87,88} The molecular structure of citrate is shown below in Figure 4.2A. Citrate contains three carboxylate groups, which could interfere with the amide I' region. 2D IR spectra of sodium citrate in D₂O was measured to determine if citrate-capped nanoparticles would be practical for IR studies. 2D IR spectrum of citrate (0.1 mg/mL in D₂O) did not exhibit any absorption in the spectral region of interest (Figure 4.2B). Additionally, no IR absorption was detected upon a 10-fold increase in citrate concentration (Figure 4.2C). Thus, at concentrations below ~1 mg/mL, citrate should not interfere with the amide I' signal.

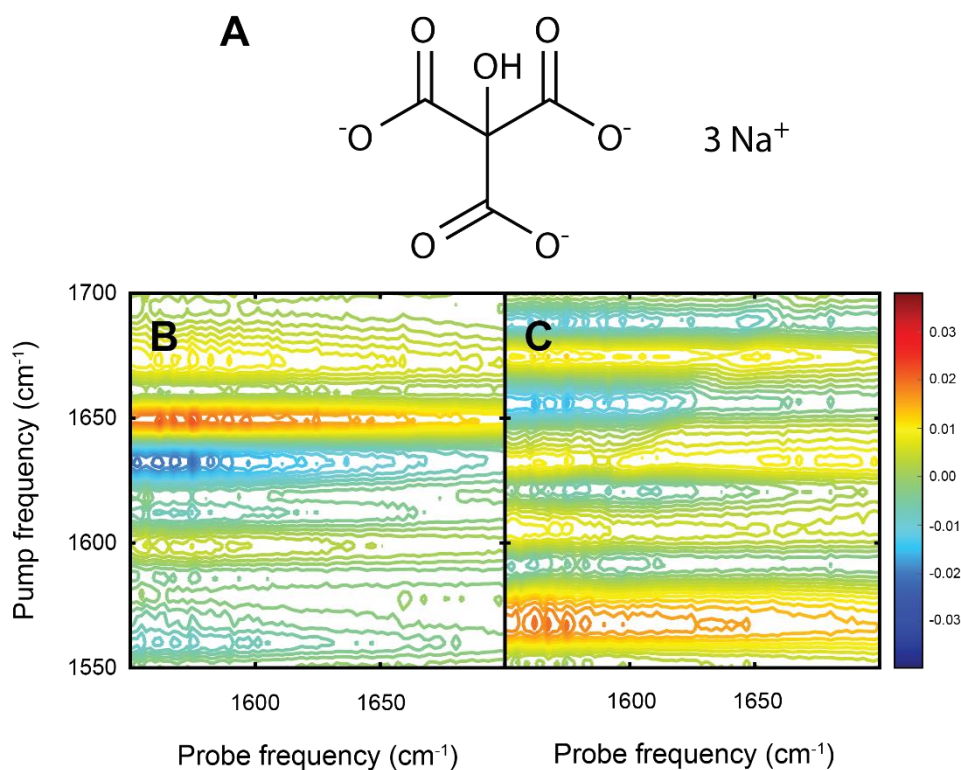


Figure 4.2 Citrate does not absorb in amide I' region at relevant concentrations. (A) Molecular structure of citrate anion stabilized with three sodium cations. 2D IR spectra of (B) 0.1 mg/mL and (C) 1 mg/mL sodium citrate in D₂O with relative intensity bar (right). No interference from the citrate ion is detected at either concentration.

After confirming there was no spectral interference from sodium citrate at the concentrations present in the colloidal suspensions, citrate's effect on the model peptide's secondary structure was examined. Even at low concentrations, citrate in solution could alter peptide/protein structure. To investigate the impact of low (0.1 mg/mL) citrate concentrations on peptide structure, 2D IR and CD spectra of EK-helix was collected determine if there were any major structural interferences. No discernable differences in amide I' frequency were observed in the 2D IR spectra for EK-helix upon adding sodium citrate (Figure 4.3).

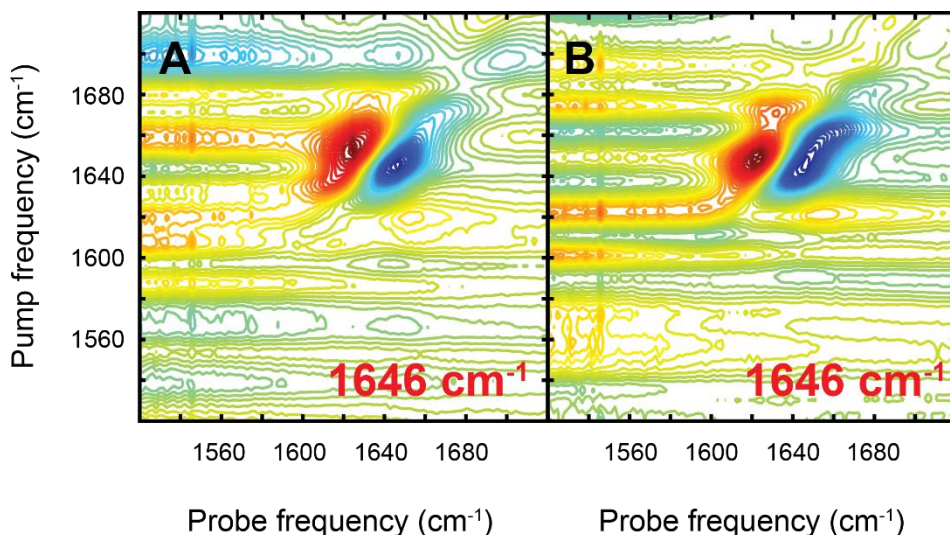


Figure 4.3 Amide I' frequency of EK-helix is unaffected by citrate. 2D IR spectra of 1 mM EK-helix in D₂O (A) neat and (B) with 0.1 mg/mL sodium citrate added. The amide I' mode remains centered at 1646 cm⁻¹ in both sample conditions.

CD measurements of the model peptide without and with added citrate were also collected to verify α -helical content at 222 nm, as described in detail with MAHP in Chapter 3. Standard ellipticity values measured for EK-helix were converted to mean residue ellipticity using the following equation:

$$[\theta] \left(\frac{\text{deg} * \text{cm}^2}{\text{dmol}} \right) = \frac{\theta}{l * C * N} \quad (4.1)$$

where θ is the measured ellipticity (millidegrees), l is the pathlength (mm), C is the molar concentration (M), and N is the number of residues.⁸⁹ The theoretical maximum MRE value at 222 nm for EK-helix was determined from the following equation:

$$[\theta]_H = -40,000 * \left(1 - \frac{x}{N} \right) + 100 * T \quad (4.2)$$

where x is a constant used to correct for non-hydrogen bonded carbonyls, N denotes the number of residues, and T is the temperature ($^{\circ}\text{C}$).⁹⁰ The constant x has been previously estimated to range from $\sim 0-3$, where x is inversely proportional to chain length. EK-helix is a relatively short peptide with 17 residues, thus x was estimated as 2.5 based on the previous CD unfolding experiments by Scholtz and coworkers.⁹⁰ This yielded a $[\theta]_H$ value of $\sim -31,717 \frac{\text{deg} * \text{cm}^2}{\text{dmol}}$ at 24 $^{\circ}\text{C}$ for EK-helix using equation 4.2. Thus, we can estimate the percentage of peptide α -helicity as a function of added citrate:

$$\% \text{ helicity} = \frac{[\theta]}{[\theta]_H} * 100 \quad (4.3)$$

CD measurements at 222 nm further supported that there were no major structural changes in the model peptide's helicity (Figure 4.4). From these initial studies, it was determined that at low concentrations (sub-milligram), sodium citrate does not absorb IR light in the protein wavelength region or impact the model peptide's secondary structure.

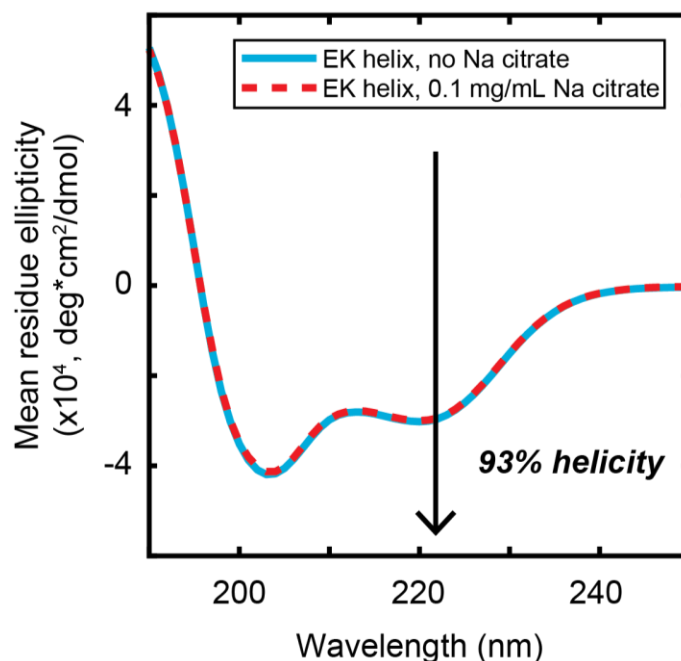


Figure 4.4 Peptide α -helicity remains constant in the presence of citrate. CD spectra of 1 mM EK-helix (blue line) without citrate and (red dashed line) with 0.1 mg/mL citrate added. The percent helicity was \sim 93% for sample conditions, indicating citrate does not alter the peptide's secondary structure.

4.4.2 Centrifugation/sonication do not alter model peptide/protein structure

Protein coronas can be comprised of multiple layers of different species. The region where the protein directly associates with the nanoparticle is known as the “hard” corona. The “hard” corona can induce multifaceted networks of more loosely-coordinated proteins, which do not directly interact with the nanoparticle but are still an integral part of the complex. The protein layer that associates indirectly with the nanoparticle is known as the “soft” corona. To examine the “hard” corona, the loosely-bound proteins must be separated and removed. The most common method of isolating nanoparticle-bound proteins is through centrifugation.^{91–94} Therefore, it was important to establish the conditions used to prepare the nanoparticles did not impact peptide/protein structure prior to characterization. 2D IR and CD spectra of EK-helix and HEWL were collected before and after three rounds of centrifugation, which matched the conditions used

for nanoparticle isolations. Centrifugation is a common method for protein isolations, so I did not anticipate structural differences would arise from this technique. As projected, no major changes in the amide I' frequency were observed for either the peptide or protein (Figure 4.5). Again, CD measurements were used to confirm the approximate percent helicities estimated at 222 nm signal. For lysozyme, the theoretical MRE was estimated to be $\sim -37,290 \frac{\text{deg}\cdot\text{cm}^2}{\text{dmol}}$ using the values $x = 1$, $N = 129$, and $T = 24 \text{ }^\circ\text{C}$. CD measurements verified no loss in peptide or protein helicity (Figure 4.5).

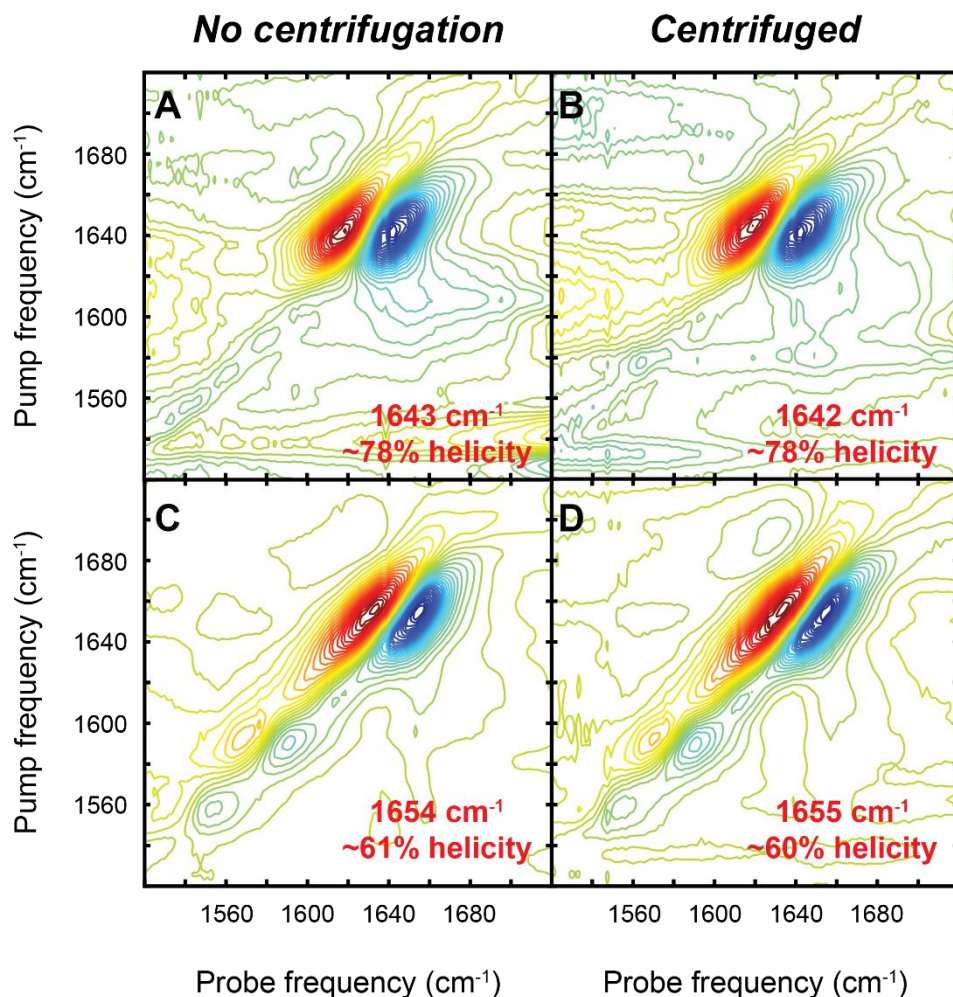


Figure 4.5 Centrifugation retains model peptide and protein secondary structure. 2D IR spectra of EK-helix (top panel) and HEWL (bottom panel) (A, C) before and (B, D) after centrifugation. No significant changes in the amide I' mode or percent helicities (calculated by CD) were observed.

Additionally, the effect of sonication on protein structure was established. Brief sonication was required to resuspend the synthesized gold nanoparticles after centrifugation, which is discussed in further detail in the next section. Sonication is much harsher than centrifugation and has been shown to induce protein structural changes or aggregation.⁹⁵⁻⁹⁷ 2D IR spectra of lysozyme (~10 mg/mL in D₂O) was collected before and after ~60 minutes of sonication. No major differences were reflected by the amide I' mode (Figure 4.6). Therefore, a few seconds of

sonication required for nanoparticle resuspension are not expected to disrupt HEWL's secondary structure.

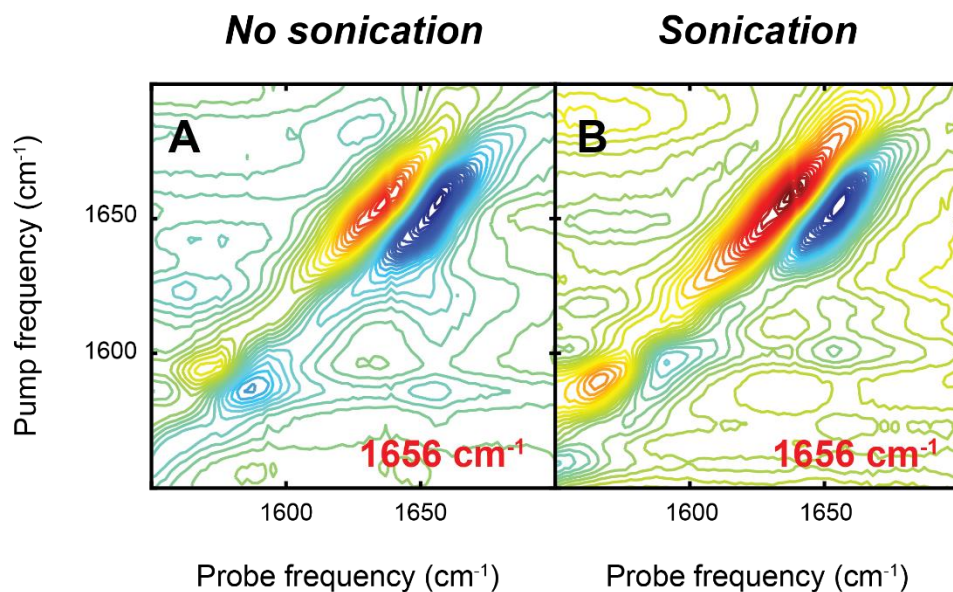


Figure 4.6 Sonication does not disrupt HEWL structure. No variations in the amide I' frequency were observed in 2D IR spectra (A) before and (B) after an hour of sonication.

4.4.3 Commercial AuNPs remain suspended upon peptide/protein addition

After confirming the citrate additive and sample preparation methods did not impact protein secondary structure, the model peptide and protein were mixed with 20 nm citrate-capped gold nanoparticles (Alfa Aesar, MA, USA). The analyte concentrations for these initial isolations are listed in Table 4.2. After the nanoparticle solution was exchanged with the deuterated equivalent solvent, the peptide stocks were added to the nanoparticle pellet. The solution was resuspended, incubated in the dark for ~1 hour, and centrifuged. However, after centrifugation (17,000g for 20 minutes), the nanoparticles no longer crashed out of solution.

<i>Model peptide/protein used</i>	<i>Total [peptide/protein] in solution</i>	<i>NP diameter</i>	<i>Total [NP] in solution</i>	<i>Crashed Out?</i>
EK-helix	1 mM	20 nm	100 pM	No
Lysozyme	5 mg/mL	20 nm	100 pM	No

These experiments were repeated at least 3 times along with solvent-matching blanks. As expected, the nanoparticles were easily separated from the peptide/protein-free solutions upon centrifugation, while the nanoparticles remained suspended in peptide/protein-containing mixtures. From these centrifugation experiments, it was clear that peptide/protein addition prevented the nanoparticles from pelleting out of solution. Without nanoparticle isolation, only the entire protein corona could be examined. I troubleshooted the nanoparticle isolations by adjusting several experimental variables, which are summarized in Table 4.3. The simplest variable to test first was centrifugation conditions (speed, time, and temperature). The fastest speed on our lab benchtop microcentrifuge (accuSpin Micro 17, Fisher Scientific, PA, USA) is 17,000 g (i.e., 13,000 rpm). Therefore, extending the centrifugation time to an hour was first tested with the 20 nm gold nanoparticle-peptide/protein mixtures, but it did not result in nanoparticle isolation.

Next, I switched to a refrigerated benchtop microcentrifuge (Eppendorf Centrifuge 5417R) and an ultracentrifuge (Beckman Optima TL Ultracentrifuge) in the Department of Cell and Developmental Biology (CDB) shared instrument core at Vanderbilt. Different combinations of speed, temperature, and time were tested on HEWL/gold nanoparticle mixtures (Table 4.3). The nanoparticles remained suspended in the protein solutions even at extremely high rotational forces (~100,000g) for extended times (~1 hour) and chilled (4 °C).

Additional factors, such as the nanoparticle diameter, nanoparticle concentration, protein concentration, and incubation time were also examined. The only conditions where the nanoparticles were successfully separated from the mixture were at extremely low protein concentrations (~10 pM). It appeared that when the protein (HEWL) concentration was equal to or less than the nanoparticle concentration, the nanoparticles would crash out. While the nanoparticle concentration was limited by the stock concentration (Table 4.1), the protein concentration could be adjusted to closely match the nanoparticle concentrations through serial dilutions. To test this hypothesis, the protein concentration was systematically altered by a factor of 10 while keeping the nanoparticle concentration constant. This observation held true until the [HEWL] >> [NP] by a factor of 1000. Therefore, when the molar ratio of the protein to nanoparticle exceeded ~1000, the proteins irreversibly stabilized the nanoparticles in solution through a concentration-dependent mechanism. Due to the extremely low protein concentration required for isolations, the commercial citrate-capped gold nanoparticles were not feasible for IR studies under the conditions tested.

Table 4.3 Sample conditions used for troubleshooting nanoparticle isolations

<i>Model peptide / protein</i>	<i>[Peptide / Protein]</i>	<i>NP diameter</i>	<i>[NP]</i>	<i>Incubation time (minutes)</i>	<i>Centrifugal force</i>	<i>Cent. time (minutes)</i>	<i>Cent. temp.</i>	<i>Crashed out?</i>
EK-helix	1 mM	20 nm	100 pM	60	17,000g	15	25 °C	No
EK-helix	1 mM	20 nm	100 pM	60	17,000g	60	25 °C	No
HEWL	5 mg/mL	20 nm	100 pM	60	17,000g	20	25 °C	No
HEWL	5 mg/mL	20 nm	100 pM	60	17,000g	60	25 °C	No
HEWL	100 µg/mL	20 nm	100 pM	60	17,000g	20	25 °C	No
HEWL	100 µg/mL	20 nm	100 pM	60	17,000g	60	25 °C	No
HEWL	10 µg/mL	20 nm	100 pM	60	17,000g	20	25 °C	No
HEWL	10 µg/mL	20 nm	100 pM	60	17,000g	60	25 °C	No
HEWL	1 mg/mL	20 nm	100 pM	60	24,000g	30	25 °C	No
HEWL	1 mg/mL	20 nm	100 pM	60	25,000g	30	15 °C	No
HEWL	1 mg/mL	20 nm	100 pM	60	50,000g	10	4 °C	No
HEWL	1 mg/mL	20 nm	100 pM	60	100,000g	60	4 °C	No
HEWL	1 mg/mL	60 nm	10 pM	5	17,000g	60	25 °C	No
HEWL	10 pM	20 nm	100 pM	5	17,000g	72	25 °C	Yes
HEWL	10 pM	60 nm	10 pM	5	17,000g	72	25 °C	Yes
HEWL	10 pM	20 nm	100 pM	5	17,000g	20	25 °C	Yes
HEWL	100 pM	20 nm	100 pM	5	17,000g	20	25 °C	Yes
HEWL	1 nM	20 nm	100 pM	5	17,000g	20	25 °C	Yes
HEWL	100 pM	20 nm	1 nM	5	17,000g	20	25 °C	Yes
HEWL	1 nM	20 nm	1 nM	5	17,000g	20	25 °C	Yes
HEWL	10 nM	20 nm	1 nM	5	17,000g	20	25 °C	Yes
HEWL	100 nM	20 nm	1 nM	5	17,000g	20	25 °C	Yes, but visibly less

4.4.4 Synthesized AuNPs exhibit opposite affinities for peptide/protein

Next, I switched to the synthesized gold nanoparticles to see if they exhibited the same behavior as the commercial nanoparticles. A 1-mL aliquot of the 74 nm gold nanoparticles in citrate solution were exchanged with deuterated solvent as previously described. A brief (~5 second) sonication was required to fully resuspend the nanoparticles, which should not impact HEWL structure (Figure 4.6). After the last exchange, deuterated solvent was added to the nanoparticles and the mixture was quickly sonicated and vortexed to resuspend. The HEWL stock solution was added to the nanoparticle mixture last to avoid additional sonication. The mixture was vortexed and incubated for ~1 hour in the dark. After incubation, the mixture was then centrifuged at 17,000g for 20 minutes, which was sufficient to pellet the nanoparticles. Additional information about the synthesized gold colloids and HEWL/nanoparticle concentrations for this experiment are listed in Table 4.4.

NP diameter (nm)	[NP] in stock (pM)	Literature LSPR (nm)	Particles per mL	[HEWL] (mM)	Crashed out?
74	17.3	544	1.04E+10	0.070	Yes

Unlike with the commercial nanoparticles, the synthesized gold colloids were successfully isolated in the presence of the model protein. 2D IR spectra were collected of HEWL in the presence of the 74 nm gold colloids after ~3 hours of incubation in the dark, first without any washes and then with 1–2 washes to remove excess protein. The LSPR band was recorded before and after the addition of HEWL, which can be used identify interactions between the protein and

nanoparticle.^{23,66,98} No major changes in the location or intensity of the LSPR band was observed upon adding HEWL (Table 4.5). Additionally, the amide I' mode did not change when HEWL was incubated with the 74 nm gold nanoparticles for ~3 hours (Figure 4.7). The protein-nanoparticle mixture was centrifuged to remove excess weakly-associated HEWL. The supernatant was removed and the protein coronas were resuspended in deuterated solvent through brief sonication and vortexing. 2D IR spectra were collected immediately after each wash. The amide I frequency did not change after one wash, but the signal strength decreased ~10-fold (Figure 4.7B). After two washes, no observable HEWL signal was detected (Figure 4.7C). Together, these initial results suggest that the gold nanoparticles do not associate strongly or impact HEWL secondary structure.

Table 4.5 Representative LSPR data for gold nanoparticles with model protein		
<i>Sample</i>	<i>LSPR (nm)</i>	<i>Intensity</i>
Gold nanoparticles	550 nm	9.71
Gold nanoparticles + HEWL	552 nm	8.82

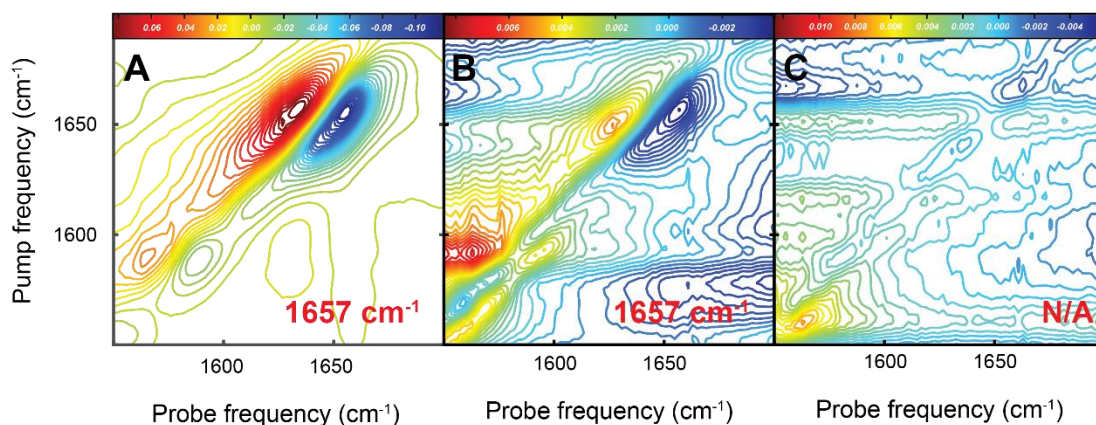


Figure 4.7 2D IR spectra of HEWL with synthesized gold nanoparticles. HEWL with gold colloids after ~3 hours of incubation with (A) no washes, (B) one wash, and (C) two washes. Intensity bars for each spectrum are at the top of each panel. The amide I' signal strength substantially decreases after one wash (A and B). No protein signal is observed after two washes (C).

Additionally, EK-helix was mixed with the synthesized gold nanoparticles. A noticeable color change from pink to light purple occurred immediately upon adding the peptide, which was not observed in the HEWL experiment. Interestingly, centrifuging EK-helix and gold colloids mixtures did not separate the synthesized gold nanoparticles as expected. In the presence of the model peptide, the LSPR peak redshifted ~9 nm and the intensity decreased significantly, indicating the peptide was associating with the nanoparticles (Table 4.6). 2D IR spectra were collected of EK-helix before and after the nanoparticles (Figure 4.8). EK-helix's amide I' frequency remained constant in the presence of the gold nanoparticles, suggesting no structural change.

Table 4.6 Representative LSPR data for gold nanoparticles with model peptide		
Sample	LSPR (nm)	Intensity
Gold nanoparticles	550 nm	14.15
Gold nanoparticles + EK-helix	559 nm	3.56

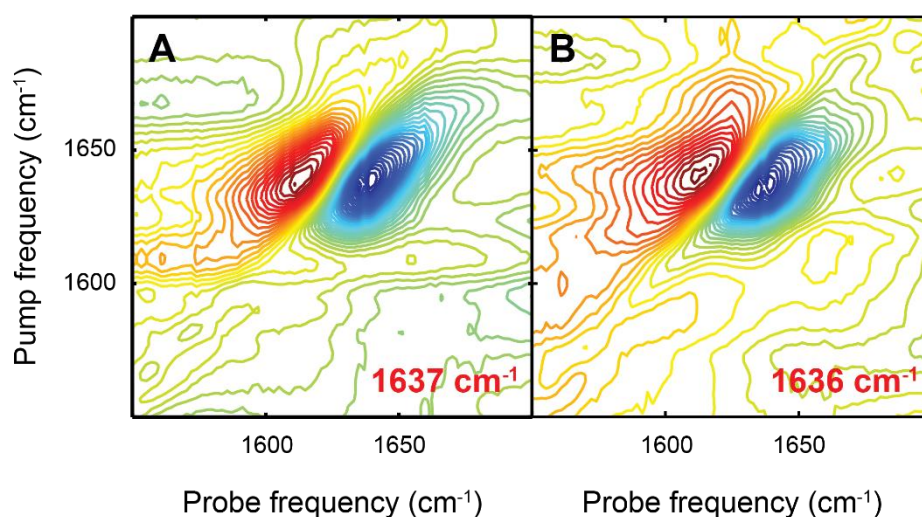


Figure 4.8 2D IR spectra of EK-helix with synthesized gold nanoparticles. 1 mM EK-helix (A) in D₂O and (B) mixed with gold colloids (17 pM, 74 nm). The amide I' mode remained constant after exposure to the gold nanoparticles, indicating no structural change.

4.5 Conclusions

In this chapter, 2D IR spectroscopy was used to examine model peptide and protein signals in the presence of gold colloids. Model peptides and proteins with a high degree of helicity were chosen for initial studies because α -helices are common secondary structures in proteins altered upon nanoparticle exposure.^{63,67–70} For the model peptide, a short model α -helix (EK-helix) with a robust secondary structure was used. Additionally, hen egg white lysozyme (HEWL) was

selected as the model protein for initial experiments due to its high helical content. Both commercially purchased and synthesized gold colloids capped with citrate were implemented in these experiments. The gold colloids were stored in an aqueous suspension in sodium citrate (0.1 mg/mL). Therefore, it was first imperative to establish if this additive disrupted the peptide/protein secondary structure. Additionally, citrate has functional groups that absorb in the protein spectral region, which could obscure the underlying amide signals. Citrate did not alter the peptide/protein secondary structure (Figures 4.3 and 4.4) or display any IR absorption (Figure 4.2) at this concentration. It was also important to establish that preparation methods required for nanoparticle samples did not change peptide or protein structure. The nanoparticle solvent was exchanged for a deuterated solvent (D_2O with 0.1 mg/mL sodium citrate) to avoid overlapping absorptions from water in the amide I' region. The solvent exchange required centrifugation and brief sonication; therefore, the impact of these two procedures on peptide/protein secondary structure were also examined. As expected, centrifugation did not impact peptide or protein secondary structure (Figure 4.5). Sonication also did not affect the model protein's structure, which was reflected by no changes in the amide I' mode (Figure 4.6).

After confirming the sample preparation methods did not alter peptide or protein secondary structure, the model peptide and protein were mixed with the gold colloids. The commercial nanoparticles remained irreversibly suspended in the presence of HEWL under most conditions tested (Table 4.3), which was unexpected. Most protein corona publications use centrifugation to isolate nanoparticles from protein solutions, but do not elaborate on details or challenges with these isolations.⁹²⁻⁹⁴ Nanoparticles are very sensitive to solution conditions (pH, charge, additives, etc.), and it is no surprise that adding highly-ionic species like proteins could influence their solution stability.^{54,74,87,88,94} The initial studies with the commercial gold colloids suggested that at high

concentrations (i.e., when HEWL concentration exceeded the nanoparticle concentration by ~1000x), the protein seemingly stabilized the gold colloids (both 20 nm and 60 nm) in solution and could not be removed by standard centrifugation methods (Table 4.3). However, the synthesized gold colloids (74 nm) were readily precipitated from HEWL-containing solutions (Table 4.4). Since the experiments were carried out under the same conditions (i.e., protein concentration, solvent system, pH, temperature, incubation times, etc.), this effect is likely due to the inherent differences in the synthesized and commercially-supplied nanoparticle stocks. The nanoparticle concentrations could affect this behavior, although the 60-nm and 74-nm colloids were used at similar concentrations (i.e., ~10 and 17 pM, respectively). A more likely explanation for this behavior is the presence of another highly-ionic species, which could have interacted strongly with the protein. Degradation of the purchased nanoparticles was unlikely, as there was no precipitate in the stock solution or in the deuterated samples. In summary, commercial nanoparticles should be used with caution, as they could contain unknown additives or not be the exact composition advertised by the company. Moving forward, synthesizing nanoparticles in lab would be the preferred option because the precise composition is known and can be readily modified.

In summary, 2D IR spectroscopy is capable of examining structural changes within proteins and peptides induced by nanoparticles in solution. I have examined a model helical peptide and protein in the presence of citrate-stabilized gold colloids (74 nm), which displayed opposite affinities for the particles. When EK-helix was mixed with the synthesized gold colloids, there was an apparent color change (from pink to light purple) and the nanoparticles could not be isolated by centrifugation. However, when HEWL was added to the gold nanoparticle solution, there was no color change and the nanoparticles were readily isolated from the mixture. There was

no significant LSPR shift upon incubation with HEWL (~2 nm redshift, Table 4.5), but there was a ~9 nm redshift with EK-helix (Table 4.6). 2D IR spectra of the model peptide/protein incubated with gold colloids did not display any structural changes (Figures 4.7 and 4.8). Additionally, HEWL likely did not associate strongly with the nanoparticles, as it was washed away after two rounds of centrifugation (Figure 4.7). Further characterization of the nanoparticle-peptide/protein complexes will be required to further optimize and determine the types and strengths of interactions present in these complex samples. For example, CD spectroscopy can confirm there is no peptide/protein denaturation upon nanoparticle exposure, which is not as straightforward to monitor through the amide I' feature alone. If partial unfolding is observed with a specific peptide/protein, the isotope labeling can be implemented to examine regions that undergo structural changes with 2D IR. Dynamic light scattering (DLS) can be used to determine the sizes of the protein coronas in solution, which could provide insight into the stabilization effect. Additional purification methods could also be explored, such as applying a sucrose density gradient to centrifugation methods or size exclusion chromatography.^{99,100} In addition to model helical structures, sulfur-containing peptides and proteins (i.e., cysteine and methionine) have the ability to interact strongly with gold/silver colloids, which could be further investigated.^{101,102}

4.6 References

- (1) Khan, I. et al. Nanoparticles: Properties, Applications and Toxicities. *Arab. J. Chem.*, **2019**, 12 (7), 908–931.
- (2) Albanese, A. et al. The Effect of Nanoparticle Size, Shape, and Surface Chemistry on Biological Systems. *Annu. Rev. Biomed. Eng.*, **2012**, 14, 1–16.
- (3) Jeevanandam, J. et al. Review on Nanoparticles and Nanostructured Materials: History, Sources, Toxicity and Regulations. *Beilstein J. Nanotechnol.*, **2018**, 9 (1), 1050–1074.
- (4) Heo, J. H. et al. Ultrastable-Stealth Large Gold Nanoparticles with DNA Directed Biological Functionality. *Langmuir*, **2015**, 31 (51), 13773–13782.

- (5) Wang, T. Y. et al. Multicolor Functional Carbon Dots via One-Step Refluxing Synthesis. *ACS Sensors*, **2017**, 2 (3), 354–363.
- (6) Dondapati, S. K. et al. Label-Free Biosensing Based on Single Gold Nanostars as Plasmonic Transducers. *ACS Nano*, **2010**, 4 (11), 6318–6322.
- (7) Tan, S. F. et al. Molecular Coatings for Stabilizing Silver and Gold Nanocubes under Electron Beam Irradiation. *Langmuir*, **2017**, 33 (5), 1189–1196.
- (8) Zhou, O. et al. Materials Science of Carbon Nanotubes: Fabrication, Integration, and Properties of Macroscopic Structures of Carbon Nanotubes. *Acc. Chem. Res.*, **2002**, 35 (12), 1045–1053.
- (9) Sperling, R. A. and Parak, W. J. Surface Modification, Functionalization and Bioconjugation of Colloidal Inorganic Nanoparticles. *Philos. Trans. R. Soc. A Math. Phys. Eng. Sci.*, **2010**, 368 (1915), 1333–1383.
- (10) Akbarzadeh, A. et al. Liposome: Classification, Preparation, and Applications. *Nanoscale Res. Lett.*, **2013**, 8 (1), 1–9.
- (11) Bailey, R. E. and Nie, S. Alloyed Semiconductor Quantum Dots: Tuning the Optical Properties without Changing the Particle Size. *J. Am. Chem. Soc.*, **2003**, 125 (23), 7100–7106.
- (12) Giri, J. et al. Interactions of Poly(Amidoamine) Dendrimers with Human Serum Albumin: Binding Constants and Mechanisms. *ACS Nano* **2011**, 5 (5), 3456–3468.
- (13) Mahtab, R. et al. Temperature- and Salt-Dependent Binding of Long DNA to Protein-Sized Quantum Dots: Thermodynamics of “Inorganic Protein” - DNA Interactions. *J. Am. Chem. Soc.*, **2000**, 122 (1), 14–17.
- (14) Lin, Y. Z. and Chang, P. L. Colorimetric Determination of DNA Methylation Based on the Strength of the Hydrophobic Interactions between DNA and Gold Nanoparticles. *ACS Appl. Mater. Interfaces*, **2013**, 5 (22), 12045–12051.
- (15) Kumar, S. et al. Structure and Interaction of Nanoparticle-Protein Complexes. *Langmuir*, **2018**, 34 (20), 5679–5695.
- (16) Shang, L. et al. Engineered Nanoparticles Interacting with Cells: Size Matters. *J. Nanobiotechnology*, **2014**, 12 (1), 1–11.
- (17) Wan, S. et al. The “Sweet” Side of the Protein Corona: Effects of Glycosylation on Nanoparticle-Cell Interactions. *ACS Nano*, **2015**, 9 (2), 2157–2166.
- (18) Wegner, K. D. and Hildebrandt, N. Quantum Dots: Bright and Versatile in Vitro and in Vivo Fluorescence Imaging Biosensors. *Chem. Soc. Rev.*, **2015**, 44 (14), 4792–4834.
- (19) Guo, Q. et al. In Situ Real-Time Tracing of Hierarchical Targeting Nanostructures in Drug Resistant Tumors Using Diffuse Fluorescence Tomography. *Chem. Sci.*, **2019**, 10 (34), 7878–7886.
- (20) Powell, A. E. et al. A Single Immunization with Spike-Functionalized Ferritin Vaccines Elicits Neutralizing Antibody Responses against SARS-CoV-2 in Mice. *ACS Cent. Sci.*, **2021**, 7 (1), 183–199.
- (21) Tenchov, R. et al. Lipid Nanoparticles—From Liposomes to mRNA Vaccine Delivery, a Landscape of Research Diversity and Advancement. *ACS Nano*, **2021**, 15 (11), 16982–17015.

- (22) Rejeeth, C. et al. A Novel Magnetic Drug Delivery Nanocomplex with a Cisplatin-Conjugated Fe₃O₄ Core and a PEG-Functionalized Mesoporous Silica Shell for Enhancing Cancer Drug Delivery Efficiency. *RSC Adv.*, **2015**, 5 (115), 94534–94538.
- (23) Behrouzi, K. and Lin, L. Biosensors and Bioelectronics Gold Nanoparticle Based Plasmonic Sensing for the Detection of SARS-CoV-2 Nucleocapsid Proteins. *Biosens. Bioelectron.*, **2022**, 195, 1–10.
- (24) Peterson, V. M. et al. Orthogonal Amplification of Nanoparticles for Improved Diagnostic Sensing. *ACS Nano*, **2012**, 6 (4), 3506–3513.
- (25) Mu, Q. et al. Chemical Basis of Interactions between Engineered Nanoparticles and Biological Systems. *Chem. Rev.*, **2014**, 114 (15), 7740–7781.
- (26) Zhao, Y. et al. Biological Molecules-Governed Plasmonic Nanoparticle Dimers with Tailored Optical Behaviors. *J. Phys. Chem. Lett.*, **2017**, 8 (22), 5633–5642.
- (27) Gerken, L. R. H. et al. Lanthanide-Doped Hafnia Nanoparticles for Multimodal Theranostics: Tailoring the Physicochemical Properties and Interactions with Biological Entities. *ACS Appl. Mater. Interfaces*, **2019**, 11 (1), 437–448.
- (28) Pershina, A. G. et al. Magnetic Nanoparticles – DNA Interactions: Design and Applications of Nanobiohybrid Systems. *Russ. Chem. Rev.*, **2014**, 83 (4), 299–322.
- (29) Nikitin, A. A. Magnetic Nanoparticles as a Tool for Remote DNA Manipulations at a Single-Molecule Level. *ACS Appl. Mater. Interfaces*, **2021**, 13 (12), 14458–14469.
- (30) Ruiz-Hernández, E. et al. Smart Drug Delivery through DNA/Magnetic Nanoparticle Gates. *ACS Nano*, **2011**, 5 (2), 1259–1266.
- (31) Wiogo, H. T. R. et al. Insight into Serum Protein Interactions with Functionalized Magnetic Nanoparticles in Biological Media. *Langmuir*, **2012**, 28 (9), 4346–4356.
- (32) Fornara, A. et al. Tailored Magnetic Nanoparticles for Direct and Sensitive Detection of Biomolecules in Biological Samples. *Nano Lett.*, **2008**, 8 (10), 3423–3428.
- (33) De Souza Castilho, M. et al. Magneto Immunoassays for Plasmodium Falciparum Histidine-Rich Protein 2 Related to Malaria Based on Magnetic Nanoparticles. *Anal. Chem.*, **2011**, 83 (14), 5570–5577.
- (34) Zhang, J. et al. Long-Circulating Heparin-Functionalized Magnetic Nanoparticles for Potential Application as a Protein Drug Delivery Platform. *Mol. Pharm.*, **2013**, 10 (10), 3892–3902.
- (35) Ranalli, A. et al. Peptide-Based Stealth Nanoparticles for Targeted and pH-Triggered Delivery. *Bioconjug. Chem.*, **2017**, 28 (2), 627–635.
- (36) Xue, Y. et al. θ -Solvent-Mediated Double-Shell Polyethylene Glycol Brushes on Nanoparticles for Improved Stealth Properties and Delivery Efficiency. *J. Phys. Chem. Lett.*, **2021**, 12 (22), 5363–5370.
- (37) Cheng, L. et al. Organic Stealth Nanoparticles for Highly Effective in Vivo Near-Infrared Photothermal Therapy of Cancer. *ACS Nano*, **2012**, 6 (6), 5605–5613.
- (38) Liu, K. et al. Physiology, Pathology and the Biomolecular Corona: The Confounding Factors in Nanomedicine Design. *Nanoscale*, **2022**, 14, 2136–2154.

- (39) Ju, Y. et al. Person-Specific Biomolecular Coronas Modulate Nanoparticle Interactions with Immune Cells in Human Blood. *ACS Nano*, **2020**, 14 (11), 15723–15737.
- (40) Wang, F. et al. The Biomolecular Corona Is Retained during Nanoparticle Uptake and Protects the Cells from the Damage Induced by Cationic Nanoparticles until Degraded in the Lysosomes. *Nanomedicine Nanotech. Biol. Med.*, **2013**, 9 (8), 1159–1168.
- (41) Leeman, M. et al. Proteins and Antibodies in Serum, Plasma, and Whole Blood—Size Characterization Using Asymmetrical Flow Field-Flow Fractionation (AF4). *Anal. Bioanal. Chem.*, **2018**, 410 (20), 4867–4873.
- (42) Gudjonsson, A. et al. A Genome-Wide Association Study of Serum Proteins Reveals Shared Loci with Common Diseases. *Nat. Commun.*, **2022**, 13 (1), 1–13.
- (43) Fleischer, C. C. and Payne, C. K. Secondary Structure of Corona Proteins Determines the Cell Surface Receptors Used by Nanoparticles. *J. Phys. Chem. B*, **2014**, 118 (49), 14017–14026.
- (44) Fleischer, C. C. and Payne, C. K. Nanoparticle-Cell Interactions: Molecular Structure of the Protein Corona and Cellular Outcomes. *Acc. Chem. Res.*, **2014**, 47 (8), 2651–2659.
- (45) Zhang, Y. et al. An Analysis of the Binding Function and Structural Organization of the Protein Corona. *J. Am. Chem. Soc.*, **2020**, 142 (19), 8827–8836.
- (46) Park, S. J. Protein – Nanoparticle Interaction: Corona Formation and Conformational Changes in Proteins on Nanoparticles. *Int. J. Nanomed.*, **2020**, 15, 5783–5802.
- (47) Huang, R. et al. Effects of Surface Compositional and Structural Heterogeneity on Nanoparticle–Protein Interactions: Different Protein Configurations. *ACS Nano*, **2014**, 6, 5402–5412.
- (48) Deng, Z. J. et al. Nanoparticle-Induced Unfolding of Fibrinogen Promotes Mac-1 Receptor Activation and Inflammation. *Nat. Nanotech.*, **2011**, 6, 4–9.
- (49) Wang, L. et al. Revealing the Binding Structure of the Protein Corona on Gold Nanorods Using Synchrotron Radiation-Based Techniques: Understanding the Reduced Damage in Cell Membranes. *J. Am. Chem. Soc.*, **2013**, 135, 17359–17368.
- (50) Jayaram, D. T. et al. Protein Corona in Response to Flow: Effect on Protein Concentration and Structure. *Biophys. J.*, **2018**, 115 (2), 209–216.
- (51) Wu, X. et al. Characterization of Secondary and Tertiary Conformational Changes of β -Lactoglobulin Adsorbed on Silica Nanoparticle Surfaces. *Langmuir*, **2008**, 24, 4989–4998.
- (52) Cukalevski, R. et al. Structural Changes in Apolipoproteins Bound to Nanoparticles. *Langmuir*, **2011**, 27, 14360–14369.
- (53) Garcia-Leis, A. and Sanchez-Cortes, S. Label-Free Detection and Self-Aggregation of Amyloid β -Peptides Based on Plasmonic Effects Induced by Ag Nanoparticles: Implications in Alzheimer’s Disease Diagnosis. *ACS Appl. Nano Mater.*, **2021**, 4, 3565–3575.
- (54) Xu, Z. and Grassian, V. H. Bovine Serum Albumin Adsorption on TiO₂ Nanoparticle Surfaces: Effects of pH and Coadsorption of Phosphate on Protein–Surface Interactions and Protein Structure. *J. Phys. Chem. C*, **2017**, 121, 21763–21771.
- (55) Kim, Y. S. et al. Two-Dimensional Infrared Spectra of Isotopically Diluted Amyloid Fibrils from A β 40. *Proc. Natl. Acad. Sci. U. S. A.*, **2008**, 105 (22), 7720–7725.

- (56) Woys, A. M. et al. 2D IR Line Shapes Probe Ovispirin Peptide Conformation and Depth in Lipid Bilayers. *J. Am. Chem. Soc.*, **2010**, 132 (8), 2832–2838.
- (57) Moran, S. D. et al. Two-Dimensional IR Spectroscopy and Segmental ¹³C Labeling Reveals the Domain Structure of Human Gamma γ -Crystallin Amyloid Fibrils. *Proc. Natl. Acad. Sci.*, **2012**, 109 (9), 3329–3334.
- (58) Remorino, A. et al. Residue-Specific Vibrational Echoes Yield 3D Structures of a Transmembrane Helix Dimer. *Science*, **2011**, 332, 1206–1210.
- (59) Middleton, C. T. et al. Residue-Specific Structural Kinetics of Proteins through the Union of Isotope Labeling, Mid-IR Pulse Shaping, and Coherent 2D IR Spectroscopy. *Methods*, **2010**, 52 (1), 12–22.
- (60) Muona, A. M. et al. Segmental Isotopic Labeling of Multi-Domain and Fusion Proteins by Protein Trans-Splicing in Vivo and in Vitro. *Nat. Protoc.*, **2010**, 5 (3), 574–587.
- (61) Huber, C. J. et al. 2D-IR Spectroscopy of Porous Silica Nanoparticles: Measuring the Distance Sensitivity of Spectral Diffusion. *J. Phys. Chem. C*, **2015**, 119, 25135–25144.
- (62) Díaz-Visurraga, J. et al. Study on Antibacterial Alginate-Stabilized Copper Nanoparticles by FT-IR and 2D-IR Correlation Spectroscopy. *Int. J. Nanomed.*, **2012**, 7, 3597–3613.
- (63) Tom, R. T. et al. Hemoprotein Bioconjugates of Gold and Silver Nanoparticles and Gold Nanorods: Structure-Function Correlations. *Langmuir*, **2007**, 17, 1320–1325.
- (64) Chakraborty, S. et al. Contrasting Effect of Gold Nanoparticles and Nanorods with Different Surface Modifications on the Structure and Activity of Bovine Serum Albumin. *Langmuir*, **2011**, 27, 7722–7731.
- (65) Ghosh, A. et al. Two-Dimensional Infrared Spectroscopy Reveals Molecular Self-Assembly on the Surface of Silver Nanoparticles. *J. Phys. Chem. Lett.*, **2019**, 10, 2481–2486.
- (66) Basu, A. et al. Glutathione Self-Assembles into a Shell of Hydrogen-Bonded Intermolecular Aggregates on “Naked” Silver Nanoparticles. *J. Phys. Chem. B*, **2021**, 125, 895–906.
- (67) Mandal, H. S. and Kraatz, H. Effect of the Surface Curvature on the Secondary Structure of Peptides Adsorbed on Nanoparticles. *J. Am. Chem. Soc.*, **2007**, 129, 6356–6357.
- (68) Kondo, A. and Mihara, J. Comparison of Adsorption and Conformation of Hemoglobin and Myoglobin on Various Inorganic Ultrafine Particles. *J. Coll. Inter. Sci.*, **1996**, 177, 214–221.
- (69) Mollmann, S. H. et al. Interfacial Adsorption of Insulin Conformational Changes and Reversibility of Adsorption. *Eur. J. Pharm. Sci.*, **2006**, 27, 194–204.
- (70) Brandes, N. et al. Adsorption-Induced Conformational Changes of Proteins onto Ceramic Particles: Differential Scanning Calorimetry and FTIR Analysis. *J. Coll. Int. Sci.*, **2006**, 299, 56–69.
- (71) Mishra, V. and Heath, R. J. Structural and Biochemical Features of Human Serum Albumin Essential for Eukaryotic Cell Culture. *Int. J. Mol. Sci.*, **2021**, 22, 1–16.
- (72) Mosesson, M. W. Fibrinogen and Fibrin Structure and Functions. *J. Thromb. Haemost.*, **2005**, 3, 1894–1904.
- (73) Marqusee, S. and Baldwin, R. L. Helix Stabilization by Glu⁻ ... Lys⁺ Salt Bridges in Short Peptides of de Novo Design. *Proc. Natl. Acad. Sci. U. S. A.*, **1987**, 84, 8898–8902.

- (74) Sa, G. et al. Influence of the Global Charge of the Protein on the Stability of Lysozyme – AuNP Bioconjugates. *J. Phys. Chem. C*, **2014**, 118, 22274–22283.
- (75) Ghosh, S. Structure of Soft and Hard Protein Corona around Polystyrene Nanoplastics — Particle Size and Protein Types. *Biointerphases*, **2021**, 15 (5), 1–9.
- (76) Danial, M. et al. Complex Coacervate Core Micelles with a Lysozyme-Modified Corona. *Langmuir*, **2007**, 23, 8003–8009.
- (77) Dong, Z. et al. Protein Corona-Mediated Transport of Nanoplastics in Seawater-Saturated Porous Media. *Water Res.* **2020**, 182, 1–9.
- (78) Sarker, P. et al. Protein Corona on Gold Nanoparticles Studied with Coarse-Grained Simulations. *Langmuir*, **2020**, 36, 13356–13363.
- (79) Anthis, N. J. and Clore, G. M. Sequence-Specific Determination of Protein and Peptide Concentrations by Absorbance at 205 nm. *Protein Sci.*, **2013**, 22, 851–858.
- (80) Bast, N. G. et al. Kinetically Controlled Seeded Growth Synthesis of Citrate-Stabilized Gold Nanoparticles of up to 200 nm: Size Focusing versus Ostwald Ripening. *Langmuir*, **2011**, 27, 11098–11105.
- (81) Yonezawa, T. et al. Direct Preparation and Size Control of Palladium Nanoparticle Hydrosols by Water-Soluble Isocyanide Ligands. *Langmuir*, **2001**, 17, 4701–4703.
- (82) Dwyer, C. O. and Holmes, J. D. Comparing Thermal and Chemical Removal of Nanoparticle Stabilizing Ligands: Effect on Catalytic Activity and Stability. *ACS Appl. Nano Mater.*, **2018**, 1, 7129–7138.
- (83) Chew, A. K. et al. The Interplay of Ligand Properties and Core Size Dictates the Hydrophobicity of Monolayer-Protected Gold Nanoparticles. *ACS Nano*, **2021**, 15, 4534–4545.
- (84) Vargas, K. M. et al. Isolated Effects of Surface Ligand Density on the Catalytic Activity and Selectivity of Palladium Nanoparticles. *ACS Appl. Nano Mater.*, **2019**, 2, 7188–7196.
- (85) Van Lehn, R. C. and Alexander-Katz, A. Fusion of Ligand-Coated Nanoparticles with Lipid Bilayers: Effect of Ligand Flexibility. *J. Phys. Chem. A*, **2014**, 118, 5848–5856.
- (86) Behafarid, F. et al. Structural and Electronic Properties of Micellar Au Nanoparticles: Size and Ligand Effects. *ACS Nano*, **2014**, 8 (7), 6671–6681.
- (87) Stankus, D. P. et al. Interactions between Natural Organic Matter and Gold Nanoparticles Stabilized with Different Organic Capping Agents. *Environ. Sci. Technol.*, **2011**, 45, 3238–3244.
- (88) El Badawy, A. M. et al. Impact of Environmental Conditions (pH, Ionic Strength, and Electrolyte Type) on the Surface Charge and Aggregation of Silver Nanoparticles Suspensions. *Environ. Sci. Technol.*, **2010**, 44 (4), 1260–1266.
- (89) Greenfield, N. J. Using Circular Dichroism Spectra to Estimate Protein Secondary Structure. *Nat. Protocols*, **2007**, 1 (6), 2876–2890.
- (90) Scholtz, J. M. et al. Parameters of Helix-Coil Transition Theory for Alanine-Based Peptides of Varying Chain Lengths in Water*. *Biopolymers*, **1991**, 31, 1463–1470
- (91) Runa, S. et al. TiO₂ Nanoparticles Alter the Expression of Peroxiredoxin Antioxidant Genes. *J. Phys. Chem. C*, **2016**, 120, 20736–20742.

- (92) Cedervall, T. et al. Detailed Identification of Plasma Proteins Adsorbed on Copolymer Nanoparticles. *Angew. Chemie Int. Ed.*, **2007**, 46, 5754–5756.
- (93) Casals, E. et al. Time Evolution of the Nanoparticle Protein Corona. *ACS Nano*, **2010**, 4 (7), 3623–3632.
- (94) Maiolo, D. et al. Surfactant Titration of Nanoparticle – Protein Corona. *Anal. Chem.*, **2014**, 86, 12055–12063.
- (95) Stathopoulos, P. B. et al. Sonication of Proteins Causes Formation of Aggregates That Resemble Amyloid. *Protein Sci.*, **2004**, 13, 3017–3027.
- (96) Zhu, Z. et al. Effects of Sonication on the Physicochemical and Functional Properties of Walnut Protein Isolate. *Food Res. Int.*, **2018**, 106, 853–861.
- (97) Tian, R. et al. Ultrasound Driven Conformational and Physicochemical Changes of Soy Protein Hydrolysates. *Ultrason.–Sonochemistry*, **2020**, 68, 1–8.
- (98) Kaur, K. and Forrest, J. A. Influence of Particle Size on the Binding Activity of Proteins Adsorbed onto Gold Nanoparticles. *Langmuir*, **2012**, 28, 2736–2744.
- (99) Plantevin, S. et al. Protein Corona Formation for Nanomaterials and Proteins of a Similar Size: Hard or Soft Corona? *Nanoscale*, **2013**, 5, 1658–1668.
- (100) Potti, A. P. et al. In Depth Characterisation of the Biomolecular Coronas of Polymer Coated Inorganic Nanoparticles with Differential Centrifugal Sedimentation. *Sci. Rep.*, **2021**, 11, 1–12.
- (101) Vallee, A. et al. Peptide Interactions with Metal and Oxide Surfaces. *Acc. Chem. Res.*, **2010**, 43 (10), 1297–1306.
- (102) Wang, W. et al. Inhibition of Amyloid Peptide Fibril Formation by Gold – Sulfur Complexes. *J. Inorg. Biochem.*, **2017**, 171, 1–9.

Chapter 5: Environmental changes in the Influenza A M2 proton channel revealed by 2D IR spectroscopy

5.1 Abstract

Here, we have utilized 2D IR spectroscopy with isotope labeling to study the native transmembrane region of the influenza A matrix 2 protein (AM2TM). Distinctive spectral features in AM2TM were observed as a function of detergent type, revealing a conformational change in the highly-selective proton channel. A characteristic mode at $\sim 1630\text{ cm}^{-1}$ was observed in the inward closed state of the tetramer, which was assigned to an alkene (C=C) ring stretch. This vibrational signature likely arises from enhanced vibrational coupling between His37 and/or Trp44 residues in the closed conformation of the tetramer. Future studies will examine M2 mutants (H37G and W44Y) to ultimately identify this distinctive vibrational mode. This unique feature was not observed at low pH, suggesting a conformational change to the inward open state. Addition of amantadine to the inward open state of M2 resulted in channel closing, revealed by the presence of the $\sim 1630\text{ cm}^{-1}$ feature and more homogeneous lineshapes. Initial water dynamic studies of M2 (wild type and isotopologues) were investigated through 2D IR waiting time measurements under previously established conditions. While dynamic changes were observed in the M2 isotopologues, the underlying aspartic acid residues (Asp24 and Asp44) also exhibited some time-dependent fluctuations, complicating spectral interpretation. A ^{13}C -labeled AM2TM variant was also examined to determine if this label could avoid overlapping sidechain interferences, but was ineffective. Future studies will isotope edit aspartic acid sidechains and individual backbone carbonyls (Val27*, Ala30*, and Gly34*), which should decouple features in this spectral window.

Additionally, 2D IR waiting time studies of individually labeled aspartic acid residues (Asp24* and Asp44*) may provide further insight into water dynamics at the AM2 channel termini.

5.2 Introduction

Influenza viral infections can induce severe illnesses in humans and is the ninth leading cause of death among U.S. adults.¹ Influenza A is a common RNA virus that causes disease in many mammals and is responsible for annual flu epidemics within the human population.^{2,3} The influenza A matrix 2 (AM2) protein is located in the viral envelope and is an essential for maintaining homeostasis and viral replication.^{4,5} This 97-residue protein embedded in the viral membrane is a common target for antiviral medications, including small molecule inhibitors amantadine and rimantadine.^{6,7} The selectivity of the AM2 ion channel arises from the highly-conserved residues in the transmembrane region (22–46, SSDPLVVAASIIGILHLILWILDRL).^{8,9} The 25-residue AM2 transmembrane (AM2TM) peptide forms a homotetramer, which is ultimately responsible for moving protons across the membrane in a selective, pH-dependent manner.^{10–13} Structural studies of the AM2 protein have shown under mildly acidic conditions (~5), protonation of the His37 sidechain induces an “open” conformation in the tetramer, promoting conductance.^{10,14–16} At neutral pH (7.0), His37 deprotonation results in a conformational change to the “closed” state, which limits proton transport through the channel.^{10,14–16} These pH-dependent configurations of the M2 protein have been extensively characterized by X-ray diffraction and NMR spectroscopy.^{10,15,17,18} However, these conformations are highly sensitive to variations in experimental conditions, such as sequence mutations and certain membrane mimetics.^{18–20} Additionally, small molecule channel inhibitors, like amantadine and rimantadine, are largely ineffective due to growing antiviral resistance.^{21,22} Therefore, there

has been extensive research focused on elucidating the mechanism of proton conduction spanning all residues of the transmembrane M2 ion channel.

Ion channels accommodate water molecules, which play key roles in protein function.²³⁻²⁶ Substrate and ion transportation is mediated by water ordering, dynamics, and hydrogen bonding as it flows through the channel.²⁷⁻²⁹ Several methods have been proposed for water-mediated conductance mechanism(s) in influenza M2 proton channels.^{10,15,17,26,30} One proposed method of proton movement is by transiently hopping along chains of hydrogen-bonded water molecules, or water “wires”, from the N-terminus to the His37 tetrad and into the viral interior.^{9,31} Another potential mechanism is through proton shuttling by His37/Trp41 gating, triggered by a conformational switch.^{17,30} However, details of water structure and dynamics in the M2 proton channel are not completely understood. Other residues in the pore could be vital to support water’s hydrogen bonding network around His37 tetrad. Additionally, the water dynamics at various pore-lining residues could differ between the open and closed states. Water molecules also influence interactions between antiviral drugs and the target residues in the tetramer. Thus, revealing water orientation and movement along the transmembrane region is essential for a better understanding of ion channels and antiviral resistance in the AM2 protein.

In this chapter, I have outlined a collaboration between our group and the DeGrado Group at the University of California San Francisco (UCSF) to investigate water dynamics in the AM2TM channel using 2D IR spectroscopy. 2D IR spectroscopy has been previously used to characterize ultrafast events within ion channels, which is possible due to its inherent subpicosecond temporal sensitivity.^{19,20,32} Previously, the DeGrado group demonstrated structural control of the AM2TM tetrad through the use of different detergents.¹⁸ For this study, we chose decyl maltose neopentyl glycol (DMNG) and dodecylphosphocholine (DPC) detergents to

stabilize the inward closed and inward open conformations of AM2TM, respectively. Here, we characterized AM2TM stabilized in these two distinct conformations through 2D IR measurements, which revealed a novel spectral feature in the inward closed state. Additionally, this previous study by the DeGrado group demonstrated that adding amantadine to the AM2TM-DPC mixture induced a change from the inward open to inward closed state.¹⁸ Here, we also characterized spectral features before and after addition of amantadine to the inward open state, which confirmed channel closure. To probe water dynamics throughout the transmembrane channel, a single $^{13}\text{C}^{18}\text{O}$ label was incorporated into AM2TM at pore-lining residues Val27*, Ala30*, and Gly34* (where * denotes isotope location). Spectral dynamics at each labeled position were probed through waiting time studies under the two distinct conformations. Underlying sidechain features, likely arising from Asp24 and Asp44, interfered with the isotopic spectral signatures, which is discussed in detail below.

5.3 Materials and Methods

Wild type and isotope-edited M2 samples were synthesized and purified by Dr. Huong Tran Kratochvil in the DeGrado Group at UCSF. The lyophilized peptides, detergents, and amantadine (Sigma Aldrich) were shipped to Vanderbilt, where I prepared the sample solutions and performed 2D IR experiments. A total solution volume of 50 μL and a 1-to-50 mM peptide to detergent ratio were used for all 2D IR experiments. First, an excess ($\sim 500 \mu\text{L}$) of $\sim 50 \text{ mM}$ detergent stock solution was dissolved in deuterated methanol (CDOD_3 , Millipore Sigma) under $\text{N}_2(\text{g})$ flow. For the DMNG detergent (949.08 g/mol), this corresponds to ~ 23.73 grams in 500 μL of methanol-d4. For the DPC detergent (351.50 g/mol), ~ 8.76 grams were dissolved in $\sim 500 \mu\text{L}$ of methanol-d4. The detergent solution was sealed with Parafilm to prevent evaporation and

incubated at room temperature for an hour. An appropriate volume of the detergent stock was aliquoted into individual microfuge tubes such that resuspension in 50 μL of solvent resulted in a final detergent concentration of 50 mM. Excess D_2O (at least $\sim 3\text{x}$ by volume) was added to the microfuge tube to help successfully freeze and lyophilize the detergent solution. The detergent samples were sealed with Parafilm and incubated for at least an hour at room temperature. The detergent solutions were lyophilized overnight into a dry, white powder.

AM2TM peptides (wild type M2, molecular weight 2769 g/mol, and $^{13}\text{C}^{18}\text{O}$ -labeled M2, molecular weight 2772 g/mol) were quantified at A280 using the Nanodrop instrument in the pedestal mode ($\epsilon_{\text{AM2TM}} = 5500 \text{ M}^{-1}\text{cm}^{-1}$ or $A_{280} = 2.016$ for 1 mM of AM2TM). The stock M2 samples were dissolved in methanol- d_4 . Diluted samples were prepared in a 1:3 ratio of stock M2 to D_2O (e.g., 5 μL stock and 15 μL D_2O) and quantified at 280 nm. After confirming the stock concentration, an appropriate volume of M2 stock was added to the lyophilized detergent to result in a 1 mM final peptide concentration. Again, excess D_2O was added to the mixture to ensure the solution could be frozen with N_2 (l) and lyophilized. Before freezing, the mixtures were sealed with Parafilm and incubated at room temperature for an hour. The peptide-detergent mixtures were dried overnight by lyophilization. For M2 drug-binding studies with amantadine, a concentrated (~ 50 or 100 mM) amantadine (151.25 g/mol) stock was prepared in D_2O . An appropriate volume of amantadine stock was added to the peptide-detergent sample to result in a 4 mM final drug concentration. If necessary, the peptide-detergent-drug sample was further diluted with excess D_2O , sealed with Parafilm, and incubated for ~ 1 hour at room temperature. The sample was frozen with N_2 (l) and lyophilized overnight.

The final M2 samples were resuspended in 50 μL of deuterated sodium phosphate buffer (0.1 M, pH 7.5) under a constant flow of N_2 (g). The final peptide to detergent ratio was 1-to-50

mM. For amantadine studies, the final solution composition was 1 mM peptide, 50 mM detergent, and 4 mM amantadine in 50 μ L of solution. The final M2 samples were sealed with Parafilm and incubated at room temperature for an hour. After incubation, \sim 5 μ L of final M2 sample were sandwiched between two CaF₂ windows with a 50- μ m Teflon spacer under N₂ (g) flow. 2D IR measurements were collected and analyzed as described in Chapter 2 (Section 2.4). For waiting time studies, the time delay between the second and third pulses were programmed in the PhaseTech software, which controlled the motorized stage in the pump beamline. The final 2D IR spectra were analyzed with a custom MATLAB script and further processed in Adobe Illustrator.

5.4 Results and Discussion

5.4.1 AM2TM exhibits unique spectral feature in the inward closed state

2D IR spectra of wild type (WT) AM2TM in each detergent (1-to-50 mM peptide-to-detergent ratio) were collected to establish baseline spectral features (Figure 5.1). The DMNG and DPC detergents stabilize the M2 tetramer in the inward closed and open states, respectively, at neutral pH.¹⁸ The detergent-solubilized peptides both exhibited a strong amide I' transition centered near \sim 1659 cm⁻¹, indicative of a transmembrane α -helix. Additionally, a weak sidechain absorption was observed around \sim 1594 cm⁻¹ for both conformations, likely arising from two underlying aspartic acid residues. The high frequency peak at \sim 1680 cm⁻¹ present in both spectra is from trifluoroacetic acid (TFA), the counterion used during peptide purification. Spectral differences were observed between the two detergent samples. M2 in DMNG exhibits a more homogeneous (i.e., more rounded) amide I' lineshape (Figure 5.1C) compared to the peptide in DPC detergent (Figure 5.1D). The more homogeneous amide I' lineshape in the DMNG detergent indicates less water exposure in the inward closed state compared to the inward open state,

respectively. Another interesting difference in each 2D IR spectrum is the feature at $\sim 1630\text{ cm}^{-1}$. In the DPC sample, this region appeared as broadened shoulder. This peak is unique to the inward closed state, and could arise from enhanced vibrational coupling between alkene ($\text{C}=\text{C}$) ring stretches.³³ This absorption feature could signify enhanced vibrational coupling between His37 and/or Trp44 residues near the C-terminal end of the channel, which would be stronger in the inward closed state compared to the inward open state.

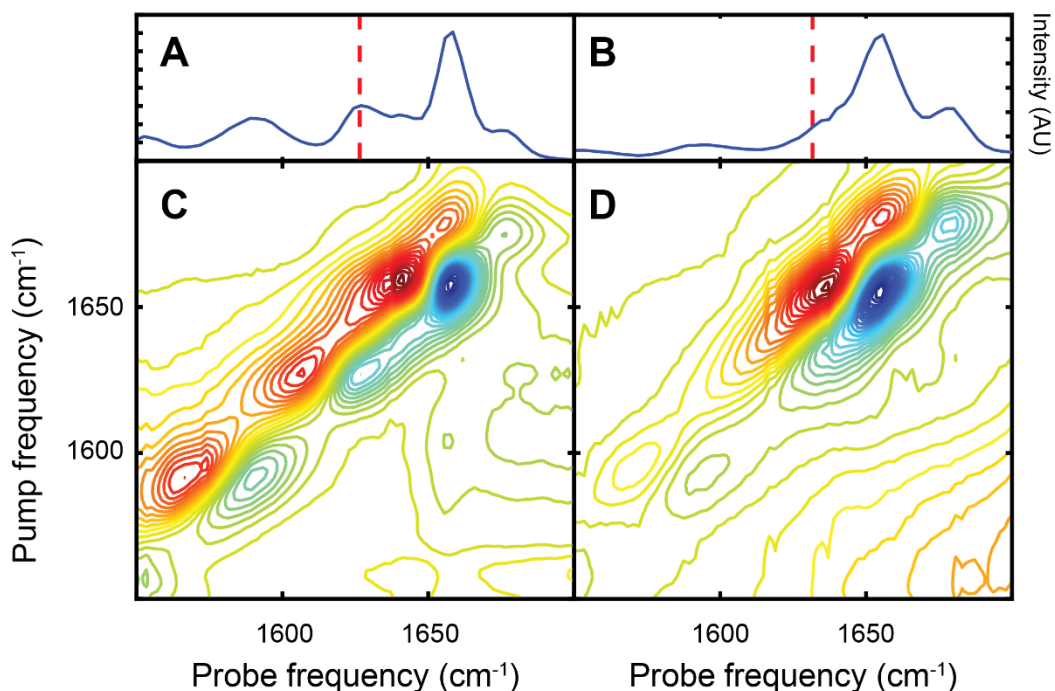


Figure 5.1 AM2TM exhibits prominent spectral signature in DMNG detergent. 2D IR spectra and linear trace along the fundamental mode (blue contours) of wild type AM2TM in (A, C) DMNG and (B, D) DPC detergent. Dashed red line denotes feature at $\sim 1630\text{ cm}^{-1}$ in the DMNG sample.

Additionally, 2D IR spectra of wild type M2 peptide in the DMNG detergent at low pH was also collected to further probe the sensitivity of this feature (Figure 5.2). At low pH, the histidine sidechains in the tetramer are fully protonated ($\text{pK}_a \sim 6.0$). As the solution pH was

lowered (~ 1.86), this absorption feature transformed into a broadened shoulder (Figure 5.2, B and D). Additionally, the mode at $\sim 1590 \text{ cm}^{-1}$ was not detected at the low pH condition, likely due to protonation of the aspartic acid sidechains ($\text{pK}_a \sim 4.0$). The vibrational signatures of M2 in DMNG at low pH (Figure 5.2, B and D) parallels those of M2 solubilized in DPC detergent at neutral pH (Figure 5.1, B and D). As the pH is lowered for M2 in DMNG detergent, the amide I' mode reflects more inhomogeneity, indicative of increased solvent exposure. This observation supports that a conformation change to the inward open state occurs upon protonation of the His37 tetrad. Protonation of His37 residues likely destabilizes the helix-helix packing and induces a conformational switch to the inward open conformation, promoting proton flow through the channel. In summary, this unique feature detects M2 stabilized in the inward closed state. However, future work examining M2 mutants (H37G and W44Y) under matched experimental conditions will be necessary to definitively assign this novel feature.

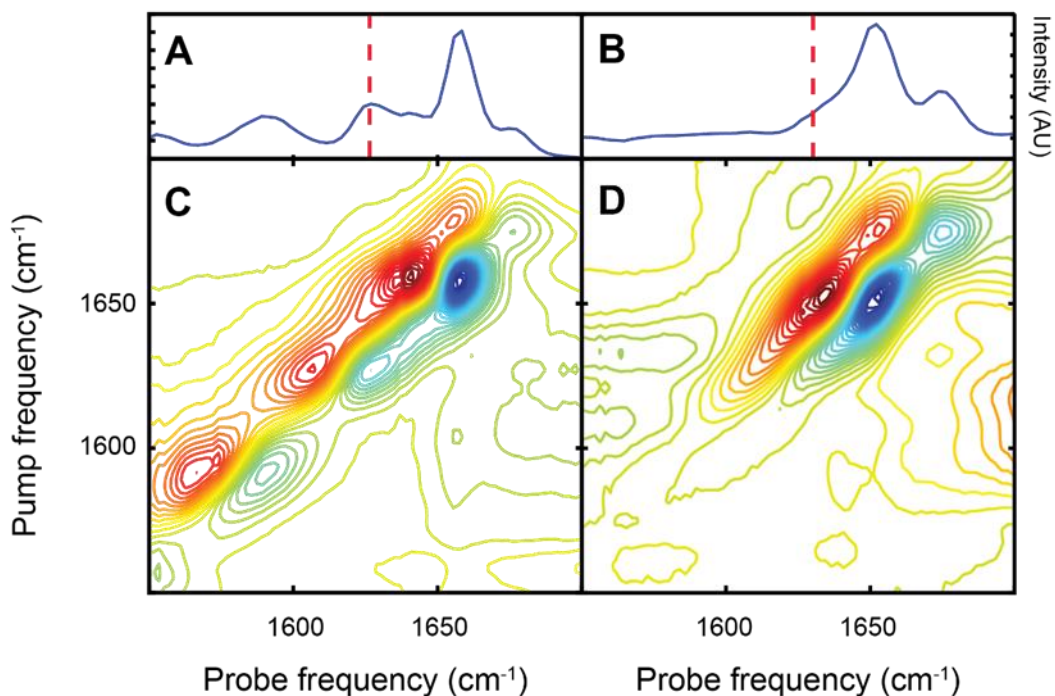


Figure 5.2 Characteristic M2 feature is not present at low pH in DMNG detergent. 2D IR spectra and diagonal trace along the $0 \rightarrow 1$ transition (blue contours) of wild type AM2TM in DMNG detergent at (A, C) neutral pH (7.50) and (B, D) low pH (1.86). M2 exhibits a broadened shoulder near $\sim 1630 \text{ cm}^{-1}$ at low pH. At neutral pH, the $\sim 1630 \text{ cm}^{-1}$ mode appears as an isolated transition.

5.4.2 Amantadine induces a conformational change in AM2TM

Amantadine is a small molecule with an adamantane backbone (Figure 5.3A) that can block and induce conformational changes in the AM2 proton channel.^{34,35} To probe if amantadine induced any conformational changes in the channel, 2D IR spectra were collected before and after addition of amantadine (4 mM) to wild type AM2TM in DPC (1 mM to 50 mM peptide to detergent ratio). Introducing amantadine to the M2 tetramer in the inward open state resulted in a more homogeneous amide I' lineshape (Figure 5.3). Additionally, the reappearance of the $\sim 1630 \text{ cm}^{-1}$ mode verifies the amantadine-induced conformational change (Figure 5.3, C and E).

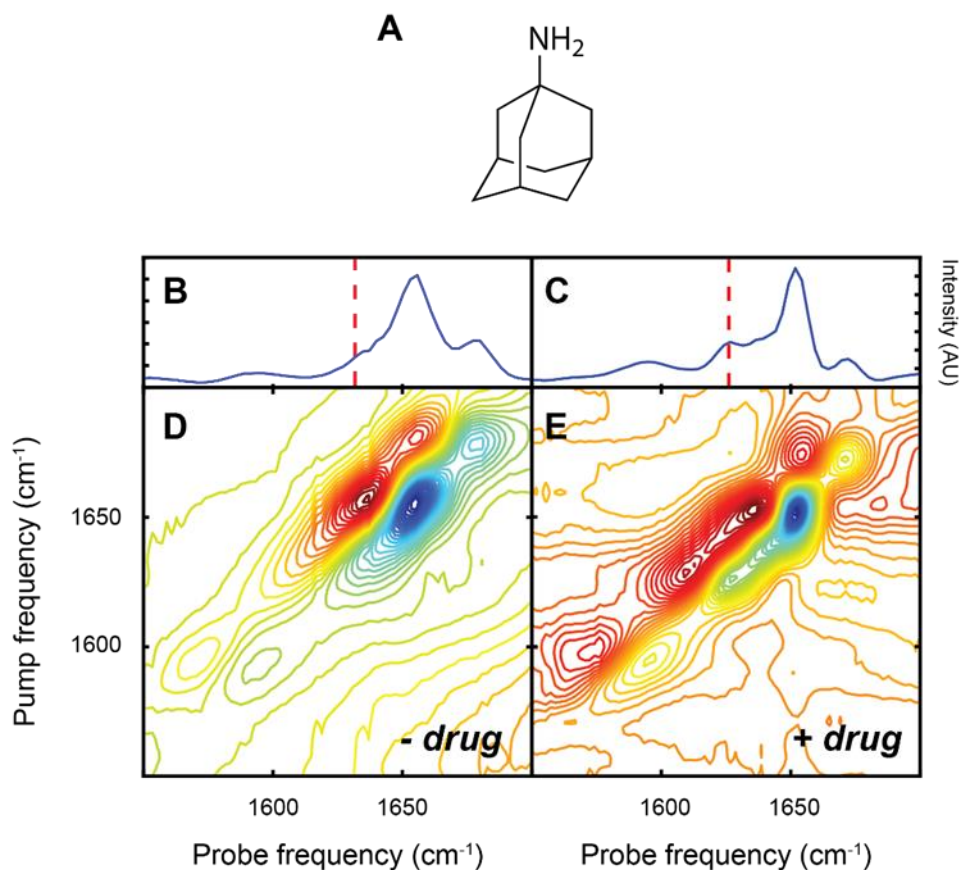


Figure 5.3 Amantadine alters AM2TM tetramer conformation. (A) Chemical structure of small molecule adamantane. 2D IR spectra of wild type AM2TM (B, D) without and (C, E) with amantadine (4 mM). M2 with added drug exhibits spectral features attributed to the inward closed state.

5.4.3 Isotopic lineshapes suggest differences in local water environment

To probe local water dynamics in the AM2 proton channel, 2D IR spectra of the M2 isotopologues (Val27*, Ala30*, and Gly34*) were measured at various waiting times. By varying delay between the pump and probe pulses in a 2D IR experiment, subpicosecond fluctuations are revealed. Spectral variations on this timescale are caused by electrostatic changes of the vibrational mode, which are heavily influenced by the surrounding water molecules.^{19,20} These vibrational fluctuations induce a change in the 2D lineshape. For example, a static lineshape indicates no relative electrostatic changes on the measured timescale (i.e., the pumped and probed frequencies

are the same). Variations in the 2D lineshape signify an altered environment on the timescale measured (i.e., the pumped and probed frequencies are not equivalent). A prominent example of this is hydrogen bond formation and breaking. When a carbonyl and water molecule are hydrogen bonded, the observed carbonyl frequency is lowered. Likewise, when the hydrogen bond is broken, the carbonyl frequency increases. More hydrogen bonding variations are accompanied by more homogeneous lineshapes (i.e., rounder peak pairs) as a function of increasing the pump-probe delay. Therefore, 2D IR waiting time studies are sensitive to the amount and mobility of water.

Static 2D IR measurements (i.e., 0 fs pump-probe delay) of M2 isotopomers in the inward closed and open states were collected to establish the baseline features. Upon visual inspection, Val27* and Ala30* AM2TM have similar lineshapes in both conformations (Figure 5.4, A–D). The Gly34* signature appears to have a slightly more homogeneous lineshape in the inward open state (Figure 5.4, E and F). Since all isotope-edited positions examined in this study are pore-lining, this static measurement could indicate an increase in water ordering surrounding the Gly34* backbone in the inward open state.

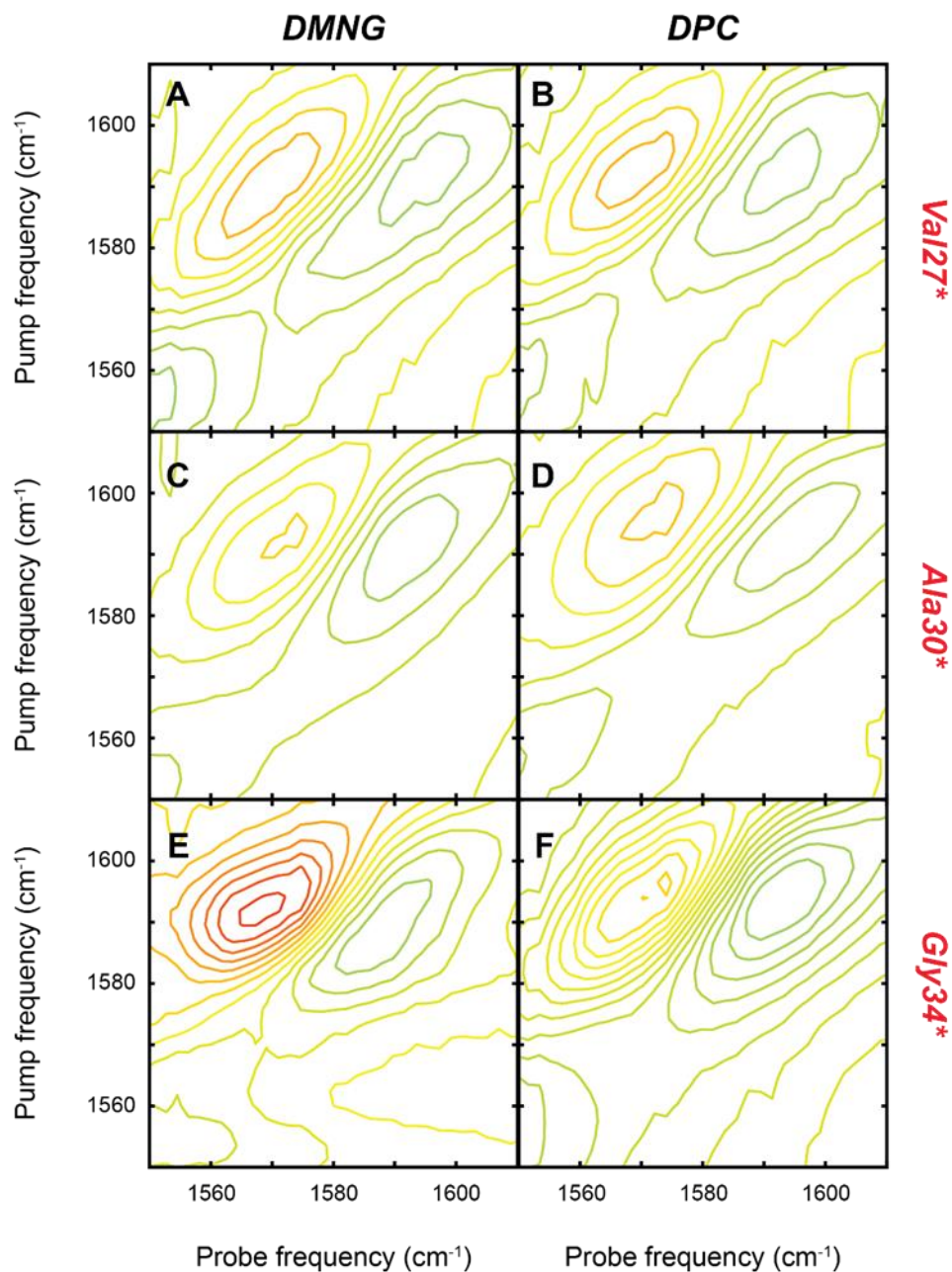


Figure 5.4 Static 2D IR measurements of AM2TM isotopologues. 2D IR spectra of (A, B) Val27*, (C, D) Ala30*, and (E, F) Gly34* in DMNG and DPC detergents, respectively. These measurements were collected with a standard 0-fs delay between the pump and probe pulses.

Next, time-dependent 2D IR spectra of the M2 isotopologues in both states were measured to examine the local water dynamics. Figure 5.5 displays the labeled region of AM2TM in the inward closed state (i.e., DMNG detergent samples) after a 500-fs pump-probe delay. The

signatures of Val27* and Gly34* are similar after the delay time, indicating the water dynamics are unaltered near these residues on this timescale. However, Ala30* exhibits a change in lineshape after the delay, reporting on a local fluctuation. This time-dependent feature suggests water molecules surround Ala30* residues in the inward closed conformation of AM2TM.

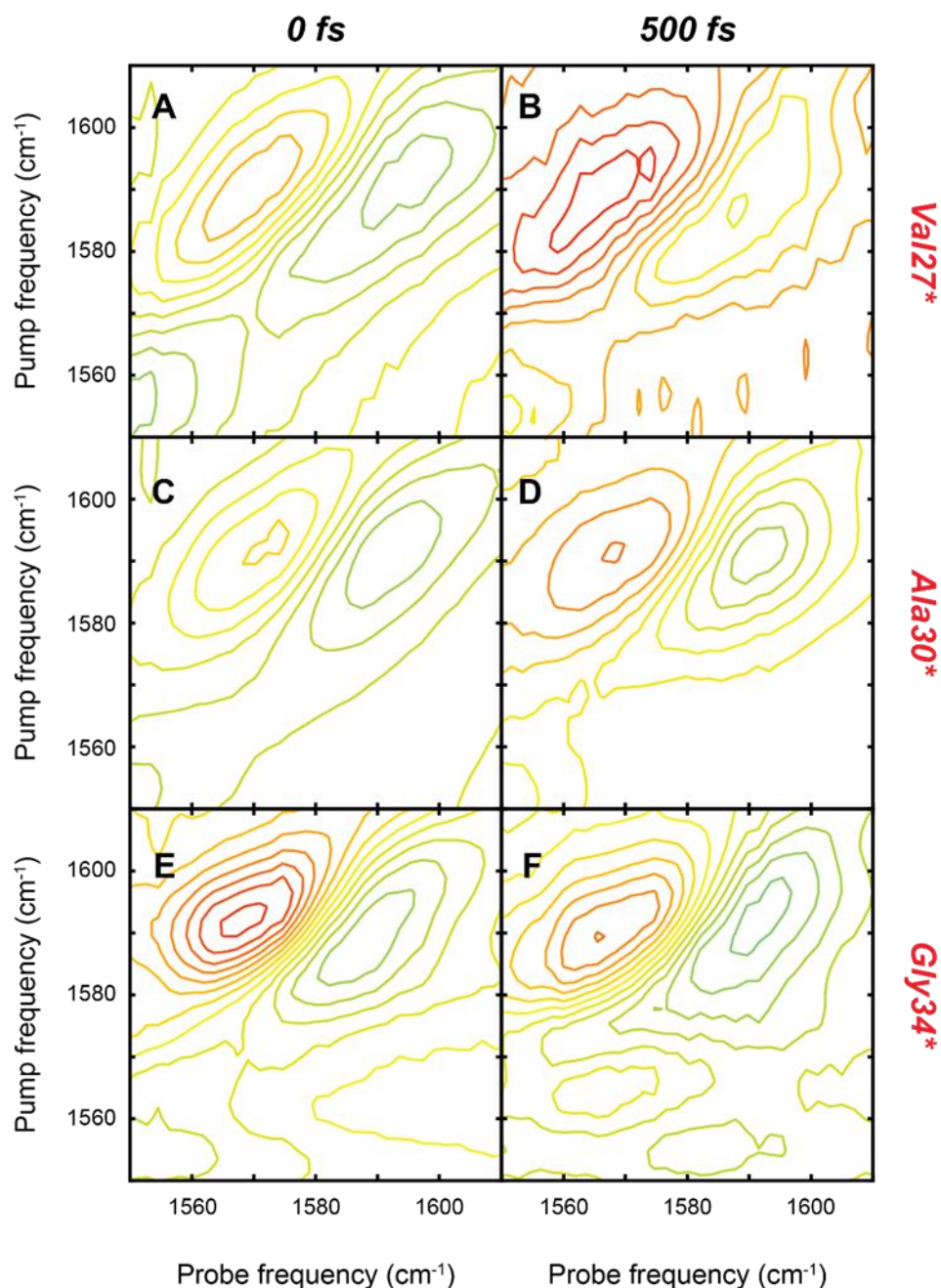


Figure 5.5 Isotopic signatures of AM2TM in the inward closed conformation. Time-dependent 2D IR spectra of AM2TM labeled at positions (A, B) Val27*, (C, D) Ala30*, and (E, F) Gly34* before (left column) and after (right column) a 500-fs delay.

Waiting-time measurements were also collected in the inward open state to reveal local water motions. 2D IR spectra of M2 isotopologues were collected after a 500-fs pump-probe delay and compared to the baseline spectra collected with no waiting time (Figure 5.6). Val27* does not

display any notable variations with an increased time delay (Figure 5.6, A and B). This result suggests proximal water is immobilized around Val27 on this timescale. A more homogeneous lineshape was observed for Ala30* after 500 fs, indicative of mobile water (Figure 5.6, C and D). Likewise, Gly34* exhibits a slightly more homogeneous lineshape after the delay (Figure 5.6, E and F). These initial 2D IR measurements suggest mobile water around Ala30* and Gly34* in the inward open state of the M2 channel.

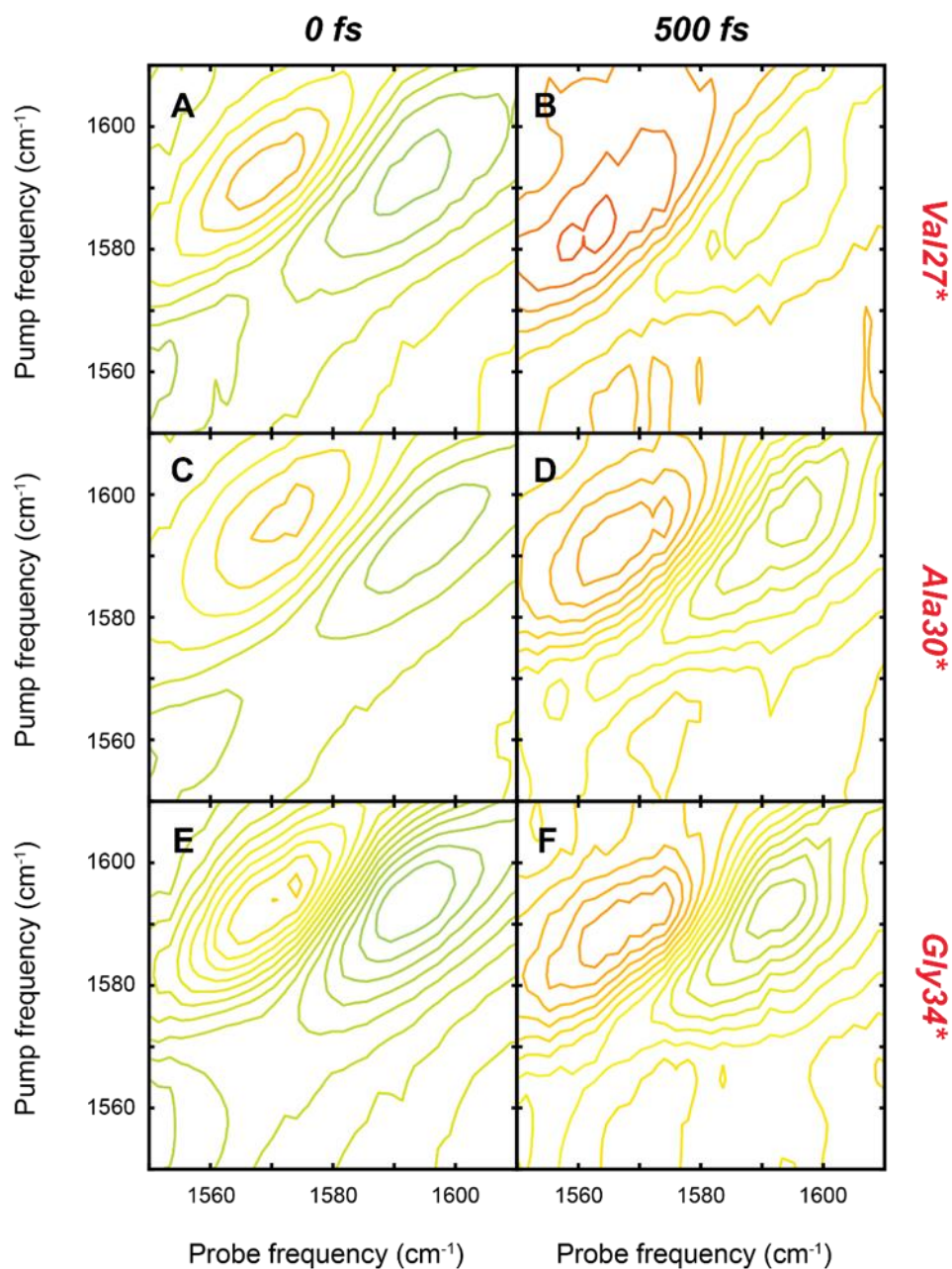


Figure 5.6 Isotopic features of AM2TM in the inward open state. 2D IR spectra of AM2TM isotope-edited at positions (A, B) Val27*, (C, D) Ala30*, and (E, F) Gly34* before (left column) and after (right column) a 500-fs time delay between the pump and probe pulses.

While there are distinct time-dependent features in the 2D IR spectra of isotope-edited M2 samples, it is important to acknowledge the underlying sidechain features arising from Asp24 and Asp44 in the AM2TM sequence. The aspartic acid residues are located at the N-terminal and C-

terminal ends of the transmembrane domain, and are likely critical for assisting proton conduction through the channel. Additionally, this sidechain mode in M2 spectra typically appears more intense in the closed state, which may arise due to their proximity. The time-dependence of the aspartic acid vibrations in wild type AM2TM peptide were also probed through 2D IR waiting time studies (Figure 5.7). After 500 fs, the aspartate lineshape becomes more homogeneous, indicative of solvent fluctuation in the inward closed state (Figure 5.7, A and B). However, the sidechain mode remains more inhomogeneous in the inward open configuration, suggesting a more constant water environment on this timescale (Figure 5.7, C and D). These features strongly suggest Asp24 and/or Asp44 associate with water in the inward closed state.

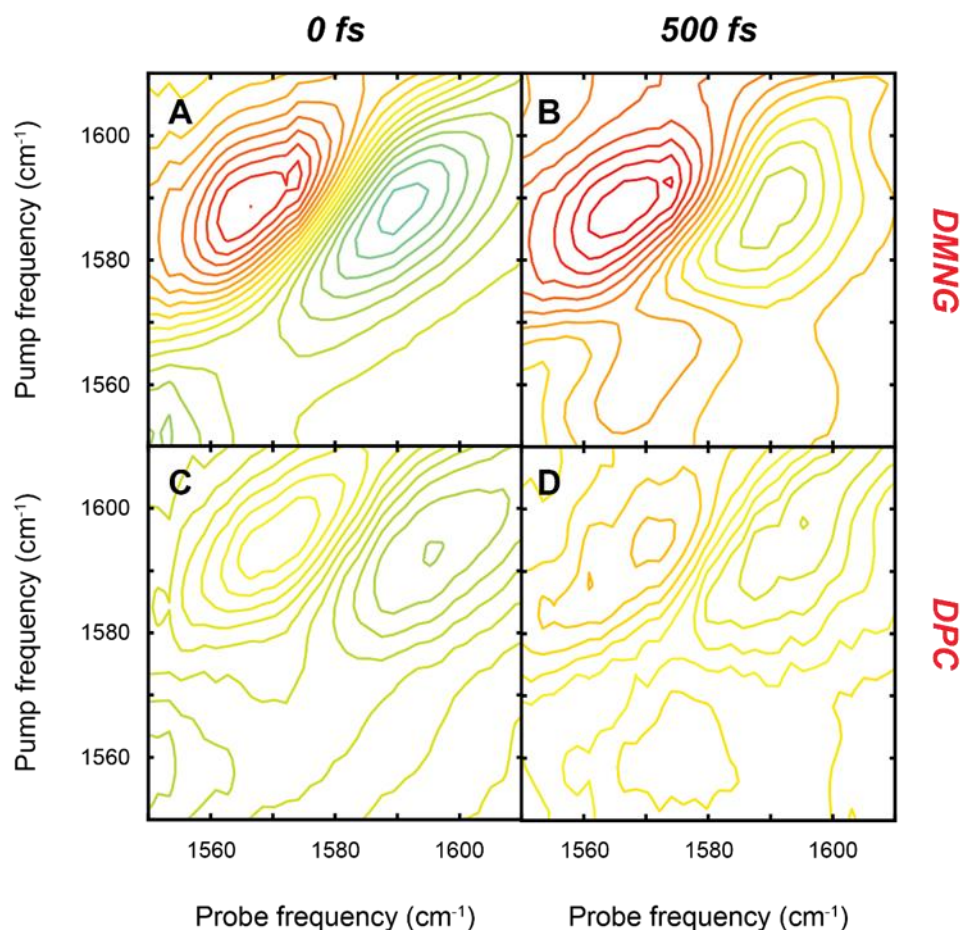


Figure 5.7 Sidechain exhibits time-dependent feature in inward closed state. 2D IR waiting time spectra of wild type AM2TM peptide stabilized in (A, B) DMNG and (C, D) DPC detergent before (left column) and after (right column) 500-fs delay. The aspartate mode is more homogeneous at 500 fs in DMNG. After the same waiting time, this mode is largely unchanged in the opposite detergent.

It is clear that $^{13}\text{C}^{18}\text{O}$ -edited amide I' residues and aspartic acid sidechains have similar vibrational frequencies, which complicates spectral assignments in native M2. To circumvent overlapping vibrations, while avoiding mutations that alter the channel's native conformation and activity (e.g., D44N)¹⁹, we investigated whether a single ^{13}C label was suitable for this system. Incorporating a single ^{13}C label is traditionally less ideal than $^{13}\text{C}^{18}\text{O}$ for longer peptide sequences due to the higher natural abundance of ^{13}C (~1.1%). However, for wild type AM2TM, this spectral region appears less congested in the 2D IR spectrum (Figure 5.1, C and D). Incorporating a ^{13}C

isotope should induce a $\sim 35\text{--}40\text{ cm}^{-1}$ redshift in the amide I' transition, theoretically allowing this mode to be more isolated compared to $^{13}\text{C}^{18}\text{O}$. However, no distinct isotopic feature was observed in the 2D IR spectra for the ^{13}C -labeled Ala30* sample (Figure 5.8), rendering the ^{13}C probe uninformative.

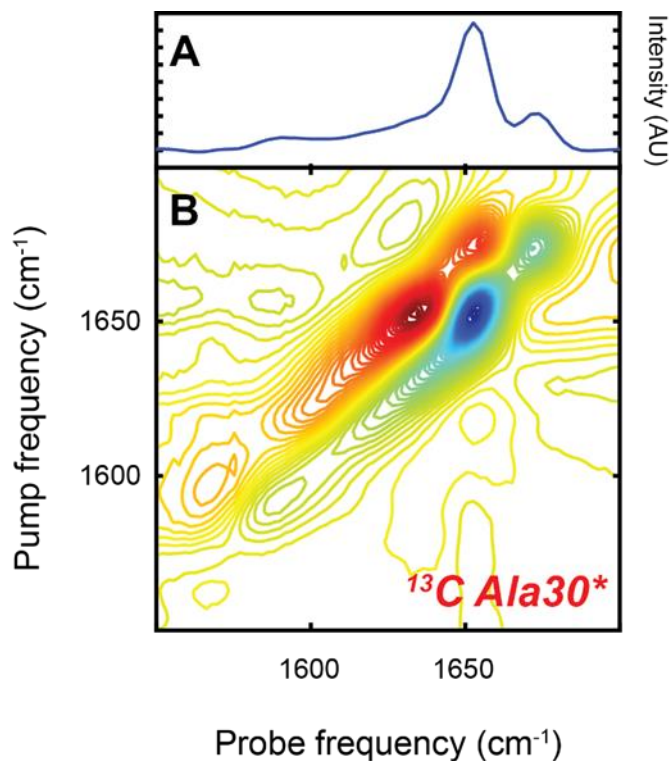


Figure 5.8 ^{13}C is not a feasible vibrational probe for AM2TM. Diagonal trace (A) and 2D IR spectrum (B) of ^{13}C -labeled AM2TM at residue Ala30* in DPC detergent. The ^{13}C isotope is not well-resolved in the anticipated spectral region ($\sim 1610\text{--}1620\text{ cm}^{-1}$).

5.5 Conclusions

In this chapter, the native influenza A M2 proton channel was characterized with 2D IR spectroscopy in collaboration with the DeGrado Group at UCSF. Here, we examined the wild type M2 transmembrane region (residues 22–46, SSDPLVVAASIIGILHLILWILDRL) along with

several isotopologues ($^{13}\text{C}^{18}\text{O}$ -labeled Val27*, Ala30*, Gly34*, and ^{13}C -edited Ala30*). The tetramer conformation (inward closed vs. open) was stabilized by different detergents, previously demonstrated in an NMR study of the S31N AM2 variant.¹⁸ Wild type AM2TM exhibited different 2D IR vibrational signatures in the inward closed and open states (Figure 5.1). In the inward closed configuration, the M2 tetramer exhibited a prominent feature at $\sim 1630\text{ cm}^{-1}$ (Figure 5.1B). This mode likely arises from the asymmetric alkene (C=C) ring stretch, perhaps due to stronger vibrational coupling between the His37 and/or Trp44 tetrad in the closed state. In the open state of the M2 tetramer, the $\sim 1630\text{ cm}^{-1}$ feature does not appear as an isolated transition (Figure 5.1D), reflecting an environmental change. Additionally, this unique feature exhibited pH-dependent behavior (Figure 5.2). At low pH (~ 2) in DMNG detergent (i.e., inward closed state), the $\sim 1630\text{ cm}^{-1}$ mode was not detected. Instead, the 2D IR spectrum strongly resembled the AM2 tetramer in DPC detergent (Figure 5.1D), confirming a pH-induced conformational switch to the inward open state. Additionally, introducing amantadine to the inward open state of AM2TM resulted in channel closure. This was revealed by changes in the amide I' lineshapes and the reappearance of the $\sim 1630\text{ cm}^{-1}$ feature (Figure 5.3). In summary, 2D IR spectroscopy detected conformational changes in the wild type AM2 transmembrane domain induced by differences in detergent, pH, and a small-molecule M2 inhibitor. Additional characterization of specific M2 mutants (H37G and W44Y) will be necessary to conclusively assign this novel, conformational-dependent feature in 2D IR spectra.

Initial waiting time experiments reported on water dynamics in the closed and opened AM2 tetramer surrounding Val27*, Ala30*, and Gly34*. Static measurements (i.e., 0 fs delay) suggested Gly34* exhibited a more homogeneous lineshape in the inward open state compared to the inward closed conformation (Figure 5.4, E and F). In the inward closed state, Ala30* displayed a more

homogeneous lineshape after 500 fs (Figure 5.5, C and D), which may indicate mobile water around this residue. In the inward open state, both Ala30* and Gly34* variants displayed lineshape changes, revealing subpicosecond water motions (Figure 5.6, C–F). Interestingly, the Val27* lineshape remained largely unchanged in both the inward closed and open states on the timescale measured (i.e., 500 fs). In summary, this 2D IR waiting time study detected transient (500 fs) water motions localized around Ala30* (in both states) and Gly34* (inward open state only).

The underlying aspartic acid residues, which cooperatively absorb in the isotope region, were also examined with 2D IR waiting time studies. Wild type AM2TM revealed a transition to a more homogeneous lineshape in the inward closed state after a 500-fs delay (Figure 5.7, A and B). However, no major time-dependent spectral changes were observed in the sidechain mode in the inward open conformation (Figure 5.7, C and D). Spectral interference from aspartic acid residues complicates the interpretation for the M2 isotopologues. While spectral subtraction can be applied to examine underlying features, we were not able to isolate the isotopes using this method in this study. However, the aspartic acid signatures are still quite useful because they provide additional information about water movement in the channel. 2D IR spectra suggests water is mobile on this timescale surrounding the aspartic acid residues in the inward closed state, but remains largely unchanged in the open state. This could indicate these terminal residues play essential roles regulating water in the closed state, whereas transient (500 fs) water interactions are likely facilitated by other internal residues in the inward open state. However, since we were primarily focused on the isotope-variants for this study, we attempted to circumvent the overlapping Asp/¹³C¹⁸O-edited amide I' absorptions by utilizing a ¹³C isotopic probe instead. Unfortunately, the ¹³C isotope was not visualized in the 2D IR spectrum of ¹³C-edited Ala30* AM2TM (Figure 5.8), indicating it was not a suitable vibrational probe for this system.

In addition to the previously discussed mutation studies, future work will incorporate $^{13}\text{C}^{18}\text{O}$ labels into Asp24 and Asp44. Sidechain isotope labeling will redshift their absorptions $\sim 60\text{ cm}^{-1}$, which is beneficial for many reasons. First, systematically labeling the Val27*, Ala30*, and Gly34* peptide backbones and both aspartic acid residues should avoid overlapping absorptions. After confirming this approach eliminates sidechain interferences near $\sim 1590\text{ cm}^{-1}$, the water dynamics will be systematically investigated for Val27*, Ala30*, and Gly34* M2 isotopologues under the previously established conditions. Additionally, individual isotopic editing of Asp24* or Asp44* could uncover critical water interactions at both ends of the M2 proton channel. Water movement around these residues initialize and finalize proton conduction at the transmembrane termini, which likely exhibit a conformational dependence. In conclusion, conformational differences and subpicosecond water fluctuations in the highly-selective AM2TM proton channel were revealed by 2D IR spectroscopy and isotope labeling. The foundational work outlined here can be expanded to examine more detailed structural and dynamic changes in this proton channel and other ion channels.

5.6 Acknowledgements

We would like to thank our collaborator, Dr. Huong T. Kratochvil, for preparation of all M2 samples and for her expert advice on these 2D IR studies. Additionally, we would like to thank the DeGrado Group, especially Dr. William F. DeGrado, for supporting this collaboration.

5.7 References

- (1) Centers for Disease Control and Prevention. Influenza Fast Stats. [cdc.gov/nchs/fastats/flu](https://www.cdc.gov/nchs/fastats/flu). Accessed February 15, 2022.
- (2) Centers for Disease Control and Prevention. Types of Influenza Viruses. [cdc.gov/flu/about/viruses/types](https://www.cdc.gov/flu/about/viruses/types). Accessed February 15, 2022.

- (3) Manzoor, R. et al. Influenza A Virus M2 Protein: Roles from Ingress to Egress. *Int. J. Mol. Sci.*, **2017**, 18 (12), 1–16.
- (4) Pinto, L. H. and Lamb, R. A. The M2 Proton Channels of Influenza A and B Viruses. *J. Biol. Chem.*, **2006**, 281 (14), 8997–9000.
- (5) Wang, J. et al. Structural and Dynamic Mechanisms for the Function and Inhibition of the M2 Proton Channel from Influenza A Virus. *Curr. Opin. Struct. Biol.*, **2011**, 21 (1), 68–80.
- (6) Cady, S. D. et al. Structure of the Amantadine Binding Site of Influenza M2 Proton Channels in Lipid Bilayers. *Nature*, **2010**, 463 (7281), 689–692.
- (7) Pielak, R. M.; Oxenoid, K.; Chou, J. J. Structural Investigation of Rimantadine Inhibition of the AM2-BM2 Chimera Channel of Influenza Viruses. *Structure*, **2011**, 19 (11), 1655–1663.
- (8) Wang, C. et al. Ion Channel Activity of Influenza A Virus M2 Protein: Characterization of the Amantadine Block. *J. Virol.*, **1993**, 67 (9), 5585–5594.
- (9) Luo, W. et al. Immobilization of the Influenza A M2 Transmembrane Peptide in Virus-Envelope Mimetic Lipid Membranes: A Solid-State NMR Investigation. *Biochemistry*, **2009**, 48 (27), 6361–6368.
- (10) Hu, J. et al. Histidines, Heart of the Hydrogen Ion Channel from Influenza A Virus: Toward an Understanding of Conductance and Proton Selectivity. *Proc. Natl. Acad. Sci. U. S. A.*, **2006**, 103 (18), 6865–6870.
- (11) Yi, M. et al. Conformational Heterogeneity of The M2 Proton Channel and a Structural Model for Channel Activation. *Proc. Nat. Acad. Sci. U. S. A.*, **2009**, 106 (32), 13311–13316.
- (12) Hong, M. and DeGrado, W. F. Structural Basis for Proton Conduction and Inhibition by the Influenza M2 Protein. *Protein Sci.*, **2012**, 21 (11), 1620–1633.
- (13) Cross, T. A. et al. M2 Protein from Influenza A: From Multiple Structures to Biophysical and Functional Insights. *Curr. Opin. Virol.*, **2012**, 2 (2), 128–133.
- (14) Moffat, J. C. et al. Proton Transport through Influenza A Virus M2 Protein Reconstituted in Vesicles. *Biophys. J.*, **2008**, 94 (2), 434–445.
- (15) Schnell, J. R. and Chou, J. J. Structure and Mechanism of the M2 Proton Channel of Influenza A Virus. *Nature*, **2008**, 451 (7178), 591–595.
- (16) Torabifard, H. et al. M2 Amphipathic Helices Facilitate pH-Dependent Conformational Transition in Influenza A Virus. *Proc. Natl. Acad. Sci. U. S. A.*, **2020**, 117 (7), 3583–3591.
- (17) Acharya, R. et al. Structure and Mechanism of Proton Transport through the Transmembrane Tetrameric M2 Protein Bundle of the Influenza A Virus. *Proc. Natl. Acad. Sci. U. S. A.*, **2010**, 107 (34), 15075–15080.
- (18) Thomaston, J. L. et al. X-Ray Crystal Structure of the Influenza A M2 Proton Channel S31N Mutant in Two Conformational States: An Open and Shut Case. *J. Am. Chem. Soc.*, **2019**, 141 (29), 11481–11488.
- (19) Ghosh, A. et al. Tidal Surge in the M2 Proton Channel, Sensed by 2D IR Spectroscopy. *Proc. Natl. Acad. Sci.*, **2011**, 108 (15), 6115–6120.
- (20) Ghosh, A. et al. 2D IR Spectroscopy Reveals the Role of Water in the Binding of Channel-Blocking Drugs to the Influenza M2 Channel. *J. Chem. Phys.*, **2014**, 235105 (140), 1–9.

- (21) Suzuki, H. et al. Emergence of Amantadine-Resistant Influenza A Viruses: Epidemiological Study. *J. Infect. Chemother.*, **2003**, 9 (3), 195–200.
- (22) Deyde, V. M. et al. Detection of Molecular Markers of Antiviral Resistance in Influenza A (H5N1) Viruses Using a Pyrosequencing Method. *Antimicrob. Agents Chemother.*, **2009**, 53 (3), 1039–1047.
- (23) Sansom, M. S. P. et al. Water in Channel-Like Cavities: Structure and Dynamics. *Biophys. J.*, **1996**, 70 (2), 693–702.
- (24) Sagnella, D. E. and Voth, G. A. Structure and Dynamics of Hydronium in the Ion Channel Gramicidin A. *Biophys. J.* **1996**, 70 (5), 2043–2051.
- (25) Rao, S. et al. Water and Hydrophobic Gates in Ion Channels and Nanopores. *Faraday Discuss.*, **2018**, 209, 231–247.
- (26) Gelenter, M. D. et al. Water Orientation and Dynamics in the Closed and Open Influenza B Virus M2 Proton Channels. *Commun. Biol.*, **2021**, 4 (1), 1–14.
- (27) Ulmschneider, M. B. et al. Molecular Dynamics of Ion Transport through the Open Conformation of a Bacterial Voltage-Gated Sodium Channel. *Proc. Nat. Acad. Sci.*, **2013**, 110 (16), 2–7.
- (28) Wang, Y. et al. Structural Mechanism of Plant Aquaporin Gating. *Nature*, **2006**, 439 (9), 688–694.
- (29) Kariev, A. M. and Green, M. E. Voltage Gated Ion Channel Function: Gating, Conduction, and the Role of Water and Protons. *Int. J. Mol. Sci.*, **2012**, 13, 1680–1709.
- (30) Wei, C. and Pohorille, A. Activation and Proton Transport Mechanism in Influenza A M2 Channel. *Biophys. J.*, 2013, 105 (9), 2036–2045.
- (31) Schweighofer, K. J. and Pohorille, A. Computer Simulation of Ion Channel Gating: The M2 Channel of Influenza A Virus in a Lipid Bilayer. *Biophys. J.*, **2000**, 78 (1), 150–163.
- (32) Kratochvil, H. et al. Instantaneous Ion Configurations in the K⁺ Ion Channel Selectivity Filter Revealed by 2D IR Spectroscopy. *Science*, **2016**, 353 (6303), 1040–1044.
- (33) Barth, A. The Infrared Absorption of Amino Acid Side Chains. *Prog. Biophys. Mol. Biol.*, **2000**, 74 (3–5), 141–173.
- (34) Hu, J. et al. The Chemical and Dynamical Influence of the Anti-Viral Drug Amantadine on the M2 Proton Channel Transmembrane Domain. *Biophys. J.*, **2007**, 93 (1), 276–283.
- (35) Cady, S. D. and Hong, M. Amantadine-Induced Conformational and Dynamical Changes of the Influenza M2 Transmembrane Proton Channel. *Proc. Natl. Acad. Sci. U. S. A.*, **2008**, 105 (5), 1483–1488.

Chapter 6: Outlook and Future Work

6.1 Introduction

Two-dimensional infrared (2D IR) spectroscopy in combination with isotope labeling can extract detailed molecular information about protein structure and dynamics in real time.¹⁻⁵ During graduate school, I have had the unique opportunity to explore interesting questions in protein science with cutting-edge techniques. I have been fortunate to learn and develop proficiency in many different synthetic and analytical techniques, which are outlined in Chapter 2. In this final chapter, I will summarize my graduate work and discuss future directions each project may take.

6.2 Investigating α -helical structures with 2D IR and isotope labeling

The most challenging project I have worked on, along with several others in the group, is the α -helix isotope labeling project (Chapter 3). During my second year, I worked closely with Kayla Hess to troubleshoot and optimize the synthesis and purification methods for $^{13}\text{C}^{18}\text{O}$ -backbone-labeled alanine. We later expanded these experimental methods to label glycine and phenylalanine at the same position (C_α), which were effective. After we successfully prepared the isotope-labeled MAHP samples in 2019, I then experienced difficulties acquiring decent spectra from the laser system. Our first laser system had many issues, which was ultimately resolved when the company replaced most of its parts in the summer of 2020. After these repairs, I was able to successfully collect clean isotope-labeled peptide spectra.

While we did not observe any crosspeaks indicative of helix formation in the labeling schemes studied, we were able to track helicity changes through frequency/intensity changes in MAHP. In the predominantly α -helical condition, the $\sim 10\text{ cm}^{-1}$ redshift in the labeled amide I'

mode was attributed to hydrogen bonding interactions, while drastic intensity changes were determined to arise from coupling between $^{13}\text{C}^{18}\text{O}$ labels. Coupling allowed us to probe isotopic features, even in the presence of evident sidechain modes. However, MAHP is a small α -helical peptide with only a few interfering sidechains (aspartic acid, glutamic acid, and arginine).⁶ Larger peptides and proteins have dozens of sidechains (e.g., 7 Asp, 2 Glu, and 12 Arg in HEWL) that strongly absorb in the $^{13}\text{C}^{18}\text{O}$ -edited amide I' region, limiting the feasibility of double $^{13}\text{C}^{18}\text{O}$ labeling.^{7,8} For structural studies of larger helices, it may be useful to uniformly label the entire domain with a more cost-effective ^{13}C isotope, which has been achieved with γ -D crystalline.⁹ Sometimes, isotopic features can be examined in the presence of sidechains with careful spectral subtraction methods.⁵ However, the data set should be collected on the same day, if possible, to minimize variations in spectral artifacts and other spectrometer conditions.

Studying native sidechain vibrational modes with 2D IR spectroscopy could be of great interest moving forward. In MAHP, the vibrational mode observed near $\sim 1580\text{--}1590\text{ cm}^{-1}$ is likely attributed to aspartic acid, arising primarily from the asymmetric C=O stretch in carboxylate.⁸ Aspartic acid residues have titratable sidechains ($\text{pK}_a \sim 4.0$), which plays critical roles in enzymatic activities.^{10–12} In the MAHP sequence, Asp1 deprotonation is responsible for N-terminal helix stabilization through end capping.⁶ Examining this sidechain feature in unlabeled MAHP would provide a label-free method to examine molecular details regarding terminal helix stabilization. 2D IR waiting time studies would reveal vibrational lifetime and environmental differences in the N-terminus as a function of peptide helicity, which has yet to be determined. MAHP mutants should be compared under high helicity conditions to ensure other modes (i.e., glutamic acid and arginine) do not contribute. If multiple sidechains contribute to the signal, the sidechain of interest could be isotopically labeled to isolate its signature, although this approach is more expensive.

6.3 Elucidating nanoparticle-induced structural changes in peptides and proteins with 2D IR spectroscopy

Here, I investigated the impact of gold colloids on a model α -helical peptide (EK-helix) and protein (hen egg white lysozyme, HEWL) with 2D IR spectroscopy. Different interactions were observed between the model peptide and protein in the presence of the same nanoparticle system. The model peptide associated strongly with the nanoparticles, indicated by a visual color change and a quantifiable redshift and decrease in the LSPR band. The model protein, however, did not appear to interact favorably with the gold colloids, as reflected by no visual color change or LSPR shift. Initial 2D IR measurements indicated the model peptide and protein retained their overall secondary structures in the presence of these nanoparticles. While this study demonstrated the capability of 2D IR to measure peptide/protein signals without interference from the gold nanoparticles, there are questions that remain unanswered and more avenues to explore. For example, how many peptides/proteins must coat nanoparticle surface to be detected with 2D IR? Can 2D IR examine different layers of the protein corona, or can it just detect changes in secondary structure within peptides/proteins with ambient nanoparticles in solution? Do certain nanoparticles (e.g., metal colloids) amplify the peptide/protein signal, allowing lower concentrations (below millimolar) to be detected? Can particular residues that directly interact with the nanoparticle surface be detected through isotope labeling? Can a chemical tag (e.g., cystine) be added to a stable model α -helix to facilitate metal nanoparticle interactions?

Different nanoparticle systems should be explored. However, it is critical that the nanoparticles do not absorb or scatter IR light in the amide I' region and can be solvent-matched. Gold colloids stabilized with citrate were a practical starting point because they did not absorb or

scatter IR light to a great extent. Additionally, the low concentration (0.1 mg/mL) of citrate stabilizer did not impact the protein signal or structure in 2D IR measurements (Chapter 4). The gold colloidal solution was also easy to exchange with a deuterated solvent system, which was required to eliminate overlapping water absorptions in the amide I' spectral window. Two rounds of centrifugation (~17,000g, 15 minutes, ~25 °C) was sufficient to replace the solvent with D₂O (with added citrate stabilizer), as water signals were not detected in 2D IR measurements. Centrifugation was the most straightforward technique for solvent exchange. Lyophilization was also examined, but this process caused irreversible nanoparticle degradation. Looking forward, the impact of charge on nanoparticle-peptide/protein interactions should be closely examined. Proteins and nanoparticles are both extremely sensitive to charged species, which influence the structure and stability of both species. I conducted my initial experiments at pH ~4 to closely match the pH of the colloidal suspension. The effect of pH and different ionic species on peptide/protein interactions with nanoparticles should be closely examined with 2D IR and complementary characterization methods.

Future experiments will be required to characterize underlying molecular interactions between peptides/proteins and gold colloids in solution. Dynamic light scattering (DLS) can be implemented to measure the hydrodynamic radii of peptide/protein-nanoparticle complexes in solution. CD spectroscopy can confirm that the helical structure is preserved upon introduction to nanoparticles, since the amide I' region is not as sensitive to these binary changes. Peptides and proteins with different secondary structures could be examined with these gold nanoparticles, which do not interfere with the amide I' signal under the conditions examined here. Specifically, peptides/proteins with sulfur-containing residues can covalently interact with gold atoms, which may induce unique interactions.¹³⁻¹⁵ Other noble metal nanoparticles, like silver and copper, could

also be examined, which share similar advantages and properties to the gold colloids used here. For example, 2D IR spectroscopy has been recently used to examine the self-assembly of glutathione, a thiol-containing peptide, on the surface of silver nanoparticles.¹⁶ The link between varying nanoparticle properties (size, shape, ligand, etc.) on peptide/protein structure could also be examined with the same peptide/protein.

6.4 Probing local water dynamics in the Influenza A M2 proton channel with 2D IR spectroscopy

In collaboration with the DeGrado Group at UCSF, we demonstrated the utility of 2D IR to extract molecular changes in the influenza A M2 proton channel. 2D IR revealed distinctive spectral features in the AM2 tetramer as it transitioned between the inward open and closed states, which was precisely controlled by the detergent type.¹⁷ In the inward closed state, M2 exhibited more homogeneous lineshapes, indicative of a more hydrophobic environment. Additionally, a unique feature at $\sim 1630\text{ cm}^{-1}$ was detected for M2 in the inward closed state. This mode was assigned to the asymmetric stretch of an alkene (C=C) ring, which would experience stronger vibrational coupling due to channel closure.⁸ This C=C stretch likely arises from the His37 proton sensor and/or Trp44 gate, although future mutation studies will be required to definitively assign this novel feature. Upon conformational switch to the inward open state, the AM2TM lineshapes were inhomogeneously broadened, likely due to water flow through the channel. The effect of pH and amantadine, a small-molecule channel inhibitor, on M2 conformation were also identified by these characteristic features in 2D IR spectra. 2D IR waiting time studies were employed to investigate water dynamics in wild type AM2TM and three isotopologues (Val27*, Ala30*, and Gly34*), where * indicates backbone labeling with a single $^{13}\text{C}^{18}\text{O}$. These experiments revealed subpicosecond and conformation-dependent water movement in specific residues of the AM2

proton channel, but definitive assignments were complicated by underlying aspartic acid modes (Asp24 and Asp44).

There are still many unanswered questions regarding proton conduction through AM2TM. For example, the origin of the novel feature at $\sim 1630\text{ cm}^{-1}$ is still not well understood. This likely arises from either the highly-conserved His37 proton sensor, Trp44 gate, or both. To address this question, future studies will mutate these residues systematically to examine if this feature persists. Since both residues are crucial for the proton conduction through the M2 channel, experimental conditions (i.e., detergent type, pH, etc.) will need to be reestablished to ensure the conformational dependence is retained. If these conditions hold, H37G and W44Y mutants will then be characterized with 2D IR and compared to our previous findings.

Additionally, it is still not well understood how water transiently and selectively moves throughout the M2 channel. It is well-established that water molecules accommodated in ion channels facilitate critical interactions.¹⁸⁻²⁰ Thus, transient water movement along the M2 channel is an essential piece of the puzzle to AM2TM's selectivity. Underlying sidechain absorptions from aspartic acid residues (Asp24 and Asp44) overlap significantly with the $^{13}\text{C}^{18}\text{O}$ -edited amide I' backbones, complicating spectral interpretation. Mutating these residues is an option, but these changes impart structural and functional differences from the wild type peptide. Therefore, future 2D IR experiments will utilize additional labeling procedures to separate the sidechain signatures from the critical pore-lining residues (Val27*, Ala30*, and Gly34*). The carboxylate groups of Asp24 and Asp44 will be isotopically labeled to shift their sidechains below 1550 cm^{-1} , leaving behind only the signatures from the individual backbone-labeled residues. 2D IR waiting time studies on the backbone- and sidechain-labeled M2 samples will be conducted to investigate local water dynamics in the inward open and closed states. The M2 channel with bound amantadine will

also be examined through 2D IR waiting time experiments to reveal how the drug alters local water interactions. Future 2D IR studies will compare these findings to the S31N mutant, which is amantadine-resistant. Additionally, different combinations of isotopes (^{13}C , ^{18}O , ^{15}N) can be incorporated into single aspartic acid residues to simultaneously investigate the transitory water dynamics at the pore termini, which has yet to be illuminated.

6.5 Acknowledgements

I have worked alongside many great individuals over the past five years. In particular, the α -helix project was a result of many individuals' hard work and dedication, including Kayla Hess, Kathryn Segner, Alisa Schmidt, and Ian Gile. Additionally, the collaborative M2 work was made possible by Dr. Huong T. Kratochvil. I have been very fortunate to collaborate with her during my time in the group, and I look forward to the directions the M2 work takes in the future. Lastly, I am especially grateful for my wonderful colleagues who have provided helpful scientific advice and feedback over the past few years, including Amanda Cao, Dr. Lindsey Miller, Dr. Carson Moore, and Dr. Jenna DeSousa.

6.6 References

- (1) Ghosh, A. et al. Tidal Surge in the M2 Proton Channel, Sensed by 2D IR Spectroscopy. *Proc. Natl. Acad. Sci.*, **2011**, 108 (15), 6115–6120.
- (2) Kim, Y. S. et al. Two-Dimensional Infrared Spectra of Isotopically Diluted Amyloid Fibrils from A β 40. *Proc. Natl. Acad. Sci.*, **2008**, 105 (22), 7720–7725.
- (3) Buchanan, L. E. et al. Mechanism of IAPP Amyloid Fibril Formation Involves an Intermediate with a Transient β -Sheet. *Proc. Natl. Acad. Sci. U. S. A.*, **2013**, 110 (48), 19285–19290.
- (4) Woys, A. M. et al. 2D IR Line Shapes Probe Ovispirin Peptide Conformation and Depth in Lipid Bilayers. *J. Am. Chem. Soc.*, **2010**, 132 (8), 2832–2838.
- (5) Kratochvil, H. T. et al. Probing the Effects of Gating on the Ion Occupancy of the K $^{+}$ Channel Selectivity Filter Using Two-Dimensional Infrared Spectroscopy. *J. Am. Chem. Soc.*, **2017**, 139 (26), 8837–8845.

- (6) Forood, B. et al. Stabilization of α -Helical Structure in Short Peptides via End Capping. *Proc. Natl. Acad. Sci. U. S. A.*, **1993**, 90, 838–842.
- (7) Weiss, M. S. et al. Crystallization, Structure Solution and Refinement of Hen Egg-White Lysozyme at pH 8.0 in the Presence of MPD. *Acta Crystallogr. Sect. D Biol. Crystallogr.*, **2000**, 56, 952–958.
- (8) Barth, A. The Infrared Absorption of Amino Acid Side Chains. *Prog. Biophys. Mol. Biol.*, **2000**, 74 (3–5), 141–173.
- (9) Moran, S. D. et al. Two-Dimensional IR Spectroscopy and Segmental ^{13}C Labeling Reveals the Domain Structure of Human γD -Crystallin Amyloid Fibrils. *Proc. Natl. Acad. Sci.*, **2012**, 109 (9), 3329–3334.
- (10) Van Den Bergh, C. J. et al. The Role of Asp-49 and Other Conserved Amino Acids in Phospholipases A2 and Their Importance for Enzymatic Activity. *J. Cell. Biochem.*, **1989**, 39, 379–390.
- (11) Craik, C. S. et al. The Catalytic Role of the Active Site Aspartic Acid in Serine Proteases. *Science*, **1987**, 237 (4817), 909–913.
- (12) Goto, Y. et al. Aspartic Acid 221 Is Critical in the Calcium-Induced Modulation of the Enzymatic Activity of Human Aminopeptidase A*. *J. Biol. Chem.*, **2007**, 282 (51), 37074–37081.
- (13) Xue, Y. et al. Quantifying Thiol-Gold Interactions towards the Efficient Strength Control. *Nat. Commun.*, **2014**, 5 (4348), 1–9.
- (14) Pensa, E. et al. The Chemistry of the Sulfur-Gold Interface: In Search of a Unified Model. *Acc. Chem. Res.*, **2012**, 45 (8), 1183–1192.
- (15) Wang, W. et al. Inhibition of Amyloid Peptide Fibril Formation by Gold–Sulfur Complexes. *J. Inorg. Biochem.*, **2017**, 171, 1–9.
- (16) Basu, A. et al. Glutathione Self-Assembles into a Shell of Hydrogen-Bonded Intermolecular Aggregates on “Naked” Silver Nanoparticles. *J. Phys. Chem. B*, **2021**, 125, 895–906.
- (17) Thomaston, J. L. et al. X-Ray Crystal Structure of the Influenza A M2 Proton Channel S31N Mutant in Two Conformational States: An Open and Shut Case. *J. Am. Chem. Soc.*, **2019**, 141 (29), 11481–11488.
- (18) Ulmschneider, M. B. et al. Molecular Dynamics of Ion Transport through the Open Conformation of a Bacterial Voltage-Gated Sodium Channel. *Proc. Natl. Acad. Sci.*, **2013**, 110 (16), 6364–6369.
- (19) Tornroth-Horsefield, S. et al. Structural Mechanism of Plant Aquaporin Gating. *Nature*, **2006**, 439 (9), 688–694.
- (20) Kariev, A. M. and Green, M. E. Voltage Gated Ion Channel Function: Gating, Conduction, and the Role of Water and Protons. *Int. J. Mol. Sci.*, **2012**, 13, 1680–1709.

Appendix 1. Supporting Information for Chapter 3

A1.1 Materials and Experimental Methods

A1.1.1 General information

All reagents were used as purchased, excluding the modifications made to L-alanine and L-glycine (1-¹³C), as described in the 9-fluorenylmethoxycarbonyl (Fmoc) protection and ¹⁸O-exchange reaction sections. Fmoc-protected amino acids, Oxyma, and Rink Amide ProTide resin (high-loading, 0.70 meq/g) were purchased from CEM. Isotope reagents, including L-alanine (1-¹³C, 99%), L-glycine (1-¹³C), and ¹⁸O-H₂O (98% enriched), were purchased from Cambridge Isotope Laboratories. Piperazine and *N*-Methylacetamide (NMA) were purchased from Alfa Aesar. *N,N'*-Diisopropylcarbodiimide (DIC), *N*-Methyl-2-pyrrolidone (NMP), and *N*-(9-Fluorenylmethoxycarbonyloxy)succinimide (Fmoc-Osu) were purchased from Oakwood Chemical. Sodium deuterioxide (NaOD, 30 wt. %), deuterium chloride (DCl, 20 wt. %), triisopropyl silane (TIPS), and 2,2,2-trifluoroethanol (TFE, 99.8% extra pure) were purchased from Acros Organics. Sodium bicarbonate (NaHCO₃), potassium bisulfate (KHSO₄), dimethylformamide (DMF), diethyl ether, acetone, acetonitrile, hydrochloric acid (12.1 N), and methanol were purchased from Fisher. All other reagents were purchased from Sigma Aldrich.

A1.1.2 Peptide synthesis and purification

The 12-residue model α -helical peptide (MAHP, DPAEAAKAAAGR-NH₂) was synthesized on a CEM Liberty Blue automated microwave peptide synthesizer using conventional 9-fluorenylmethoxycarbonyl (Fmoc) solid-phase peptide synthesis (SPPS) with piperazine deprotection and DIC/Oxyma activation. Rink Amide ProTide resin was used as a solid support to

produce an amidated C-terminus. MAHP was cleaved from the resin and side-chain protecting groups were removed using a cleavage cocktail of 95% trifluoroacetic acid (TFA), 2.5% triisopropylsilane (TIPS), and 2.5% water for 3 hours. The peptide was filtered from the resin and the solvent was removed. The crude peptide was precipitated in ice-cold diethyl ether and further purified via high-performance liquid chromatography (HPLC) using an XBridge C18 preparative column coupled with a UV detector (215 nm). A binary solvent system of water (Solvent A) and 90% acetonitrile in water (Solvent B) with 0.045% HCl as the counterion was used for all HPLC methods. A gradient of 0% Solvent A to 40% Solvent B (2% per minute) was sufficient to elute the peptide (~11 minutes, Figure 2A). Fractions were collected, lyophilized, and stored at -20 °C for short-term use. Isotope-labeled peptides were synthesized and purified in the same manner as previously described, using isotope-labeled alanine (^{13}C and $^{13}\text{C}^{18}\text{O}$) labeled at the C1 position during SPPS. L-Alanine ($1\text{-}^{13}\text{C}$, 99%) was modified using the Fmoc-protection (Figure A1.1) and ^{18}O -exchange procedures (Figure A1.2) prior to solid-phase peptide synthesis.

A1.1.3 Fmoc protection reaction with ^{13}C -enriched amino acids

The Fmoc protecting group was added to L-alanine- $1\text{-}^{13}\text{C}$ before peptide synthesis (Figure 1). This reaction was carried out on a 1-gram (10 mmol) scale using equimolar amounts of amino acid, Fmoc-OSu, and NaHCO_3 . The starting materials were combined in a 100-mL round-bottom (RB) flask and dissolved in 30 mL of 1:1 water/acetone mixture. The reaction stirred for 24 hours at room temperature, followed by quenching with 2 M KHSO_4 until the solution reached pH 2 (~3 mL). The white precipitate was washed with ~50 mL of ice-cold deionized water, collected via vacuum filtration, and dried via lyophilization. These washes were repeated at least 3 times to remove salts. The purity of the Fmoc- ^{13}C -alanine was confirmed via electrospray-ionization mass spectrometry (ESI-MS). Fmoc- ^{13}C -glycine was prepared in the same manner.

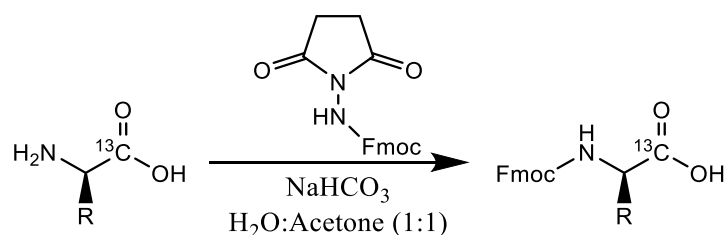


Figure A1.1 Fmoc protection of a generic ^{13}C -C₁-L-amino acid for solid-phase peptide synthesis. R group = CH₃ for alanine and H for glycine.

A1.1.4 Acid-catalyzed ^{18}O -exchange with Fmoc-protected ^{13}C -edited amino acids

For $^{13}\text{C}^{18}\text{O}$ -labeled peptides, an acid-catalyzed ^{18}O -exchange was performed with the Fmoc-protected ^{13}C -alanine. This reaction was performed on a 1-gram scale using the Fmoc-protected ^{13}C alanine in dioxane/4 M HCl in dioxane and ^{18}O -enriched water (Figure 2). All glassware was flame dried under vacuum before adding Fmoc- ^{13}C -alanine. The amino acid was quickly added to a 50-mL round-bottom (RB) flask and the glassware was flame dried again to remove residual water. The amino acid was dissolved in dioxane (8 mL) and 4 M HCl in dioxane (4 mL) under an atmosphere of nitrogen. The reaction mixture was heated to reflux at 150 °C (bright yellow solution) for ~30 minutes before injecting 1 mL of ^{18}O -enriched water. The mixture refluxed for 4 hours at 150 °C. After 4 hours, the solvent was removed by lyophilization. This procedure was repeated twice more (3 times in total) to ensure the labeling efficiency was >90% (determined by ESI-MS, Equation 1). ^{18}O -enriched glycine was prepared in the same manner.

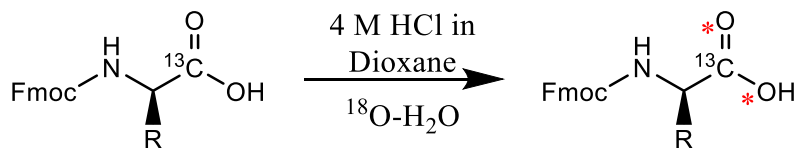


Figure A1.2. HCl-catalyzed ^{18}O -exchange with generic Fmoc- ^{13}C -C $_1$ -L-amino acid. Red asterisks denote ^{18}O isotopes. Both ^{16}O -oxygens were exchanged with ^{18}O , as they are chemically-equivalent during solid-phase peptide synthesis. R = CH_3 for alanine and H for glycine.

% enrichment

$$= \frac{\text{Intensity}(^{13}\text{C } ^{18}\text{O } ^{18}\text{O}) + \frac{1}{2} * \text{Intensity}(^{13}\text{C } ^{18}\text{O } ^{16}\text{O})}{\text{Intensity}(^{13}\text{C } ^{18}\text{O } ^{18}\text{O}) + \text{Intensity}(^{13}\text{C } ^{18}\text{O } ^{16}\text{O}) + \text{Intensity}(^{13}\text{C } ^{16}\text{O } ^{16}\text{O})} \quad (1)$$

Fmoc- $^{13}\text{C}^{18}\text{O}^{18}\text{O}$ -alanine was purified by precipitation with dry, ice-cold diethyl ether. The first wash yielded a dark orange supernatant with a small amount of precipitate. The precipitate was likely an unwanted side product of acid-catalyzed ^{18}O -exchange (Figure 2) and was discarded. The dark orange supernatant was dried with compressed air and resuspended in ~10 mL of dry diethyl ether to precipitate the amino acid. The mixture was centrifuged at 5000 rpm for 5 minutes. This wash yielded a substantial amount of off-white precipitate and a yellow-orange supernatant. The supernatant was removed and dried with compressed air/nitrogen. The washes were repeated until a reasonable yield (>70%) of amino acid was achieved (4 washes total).

A1.1.5 Sample preparation for ESI-MS characterization

All peptides and isotope-labeled amino acids were characterized using ESI-MS on a ThermoFisher Scientific LTQ XL linear ion trap mass spectrometer using direct infusion mode. HPLC/Optima grade solvents were used to make all solutions for MS analysis. For peptide samples, 1 mg/mL stock solutions were prepared by dissolving the lyophilized peptide in a 70/30

methanol/water mixture. 10 $\mu\text{g}/\text{mL}$ dilutions were made from the stock solution and the same solvent mixture. Fmoc- ^{13}C -alanine and glycine solutions were prepared following the same procedure. Fmoc- $^{13}\text{C}^{18}\text{O}^{18}\text{O}$ alanine and glycine were dissolved in 100% acetonitrile instead of an organic/aqueous mixture to avoid significant back exchange with the ^{18}O -enriched oxygens.

A1.1.6 Sample preparation for 2D IR and circular dichroism experiments

Lyophilized MAHP was dissolved in D_2O to make a ~ 10 mM stock solution. The stock solution was quantified on a Nanodrop One-C spectrometer (ThermoFisher Scientific, MA, USA). 5 mM MAHP dilutions were prepared in D_2O and TFE (if applicable) for 2D IR and CD measurements. The following three solvent conditions were prepared: (1) low pH (~ 2) without TFE, (2) high pH (~ 10) without TFE, and (3) high pH (~ 10) with 40% TFE (v/v). The solution pH was adjusted using small aliquots (~ 0.20 μL) of NaOD and/or DCl stocks. For the high helicity condition (high pH with 40% TFE by volume), the pH of the peptide solution was adjusted, 40% TFE (v/v) was added, and the pH was measured again to ensure the acid did not cause a significant (<1 unit) drop in pH.

The peptide solutions were gently vortexed and incubated at room temperature for at least an hour before 2D IR and CD measurements. For 2D IR experiments, a small aliquot (~ 10 μL or less) of peptide solution was placed between two CaF_2 windows (Crystran, UK) separated by a 50- μm Teflon spacer. The sample cell was placed in the spectrometer box purged with dry, compressed air to avoid hydrogen exchange from ambient water vapor. For CD experiments, ~ 40 μL of the stock solution was placed between two 0.1-mm quartz windows (Starna Cells, CA, USA).

A1.1.7 Peptide quantification

All peptide solutions were quantified using a NanoDrop One-C spectrophotometer (ThermoFisher Scientific, MA, USA). All peptides were quantified at 205 nm. The molar extinction coefficient of MAHP at 205 nm was estimated by accounting for backbone residues and sidechains that absorb ultraviolet radiation at this wavelength (for a 1-cm pathlength at 205 nm, $\epsilon=31,930 \text{ M}^{-1}\text{cm}^{-1}$ or 28.36 mg/mL).¹ Peptide solutions were quantified in triplicate and the average concentration was recorded.

A1.1.8 2D IR measurements

A detailed description of 2D IR data collection and processing methods are described elsewhere.² Briefly, 800-nm pulses (7 mJ, 1 kHz, 60 fs) were generated by a Ti:sapphire oscillator and amplified with a neodymium-doped yttrium orthovanadate (Nd:YVO₄)-pumped regenerative amplifier (Solstice Ace, Spectra Physics, CA, USA). The 800-nm pulses were directed into a 50/50 beam splitter, where half the beam was sent into an optical parametric amplifier (TOPAS-Prime, Spectra Physics, CA, USA) coupled with difference frequency generation (DFG) to produce 6- μm pulses (30 μJ , 1 kHz, 70 fs). The mid-IR light was directed into a commercial 2D IR spectrometer (2DQuick IR, PhaseTech Spectroscopy Inc., WI, USA) and split into pump (90%) and probe (10%) lines. The pump line was passed through a germanium acousto-optic modulator (Ge AOM) pulse-shaper to generate pairs of pump pulses with varying time delays between them. The pump and probe pulses were overlapped at the sample to generate the signal. The signal was directed into a monochromator and dispersed onto a mercury cadmium telluride (MCT) array detector (Princeton Instruments, NJ, USA). The data was collected using QuickControl Software (PhaseTech

Spectroscopy Inc., WI, USA) and further processed using a custom MATLAB script. Adobe Illustrator software was used to process final 2D IR spectra.

Prior to 2D IR measurements, the MCT array was calibrated with a 4-nitrobenzaldehyde (4NBA, 500 mM in toluene) standard. 4NBA (~300 mM in toluene) absorbs IR radiation at 1535 cm^{-1} , 1605 cm^{-1} , and 1711 cm^{-1} , which spans the isotope and amide I' spectral regions. The probe spectrum of the calibrant was collected and the pixels were matched to the absorption minima. Calibration with small molecules standards like 4NBA minimizes variations in the data collected over various months. Additionally, while ambient water vapor can also be used to calibrate the detector, small-molecule calibrants are more robust because they are invariant to ambient humidity variations.

A1.1.9 Circular dichroism measurements

All CD measurements were collected on a J-810CD spectropolarimeter (Jasco, MD, USA). The instrument was purged with $\text{N}_2(\text{g})$ to prevent damage to the optics. Spectra were collected from 190–260 nm in 1-nm increments. All measurements were collected at 24 °C, 100 mdeg sensitivity, and a scan rate of 100 nm per minute. Three spectra were collected for each sample and solvent blank, which were averaged and smoothed in Microsoft Excel. Additional post-processing was completed with MATLAB and Adobe Illustrator software. The CD signal was converted from millidegrees to mean residue ellipticity (Equation 2) and compared to the theoretical value of a perfectly helical peptide (Equations 3 and 4).^{3,4}

$$[\theta] \left(\frac{\text{deg} * \text{cm}^2}{\text{dmol}} \right) = \frac{\theta \text{ (mdeg)}}{l(\text{cm}) * C \left(\frac{\text{mol}}{L} \right) * N(\#)} \quad (2)$$

$$[\theta]_H = -40,000 * \left(1 - \frac{2.5}{N}\right) + 100 * T \quad (3)$$

$$\% \text{ helicity} = \frac{[\theta]}{[\theta]_H} * 100 \quad (4)$$

A1.2 Supplementary Data

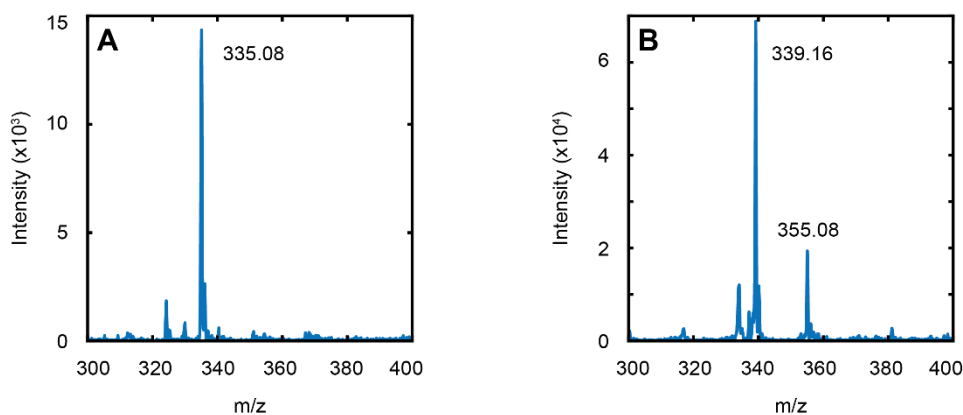


Figure A1.3. Characterization of ¹³C and ¹³C¹⁸O¹⁸O-labeled alanine. Mass spectrum of (A) Fmoc-¹³C-alanine, where m/z 335.08 corresponds to the Na⁺ adduct, and (B) Fmoc-¹³C¹⁸O¹⁸O-alanine, where m/z 339.16 and 355.08 correspond to the Na⁺ and K⁺ adducts, respectively.

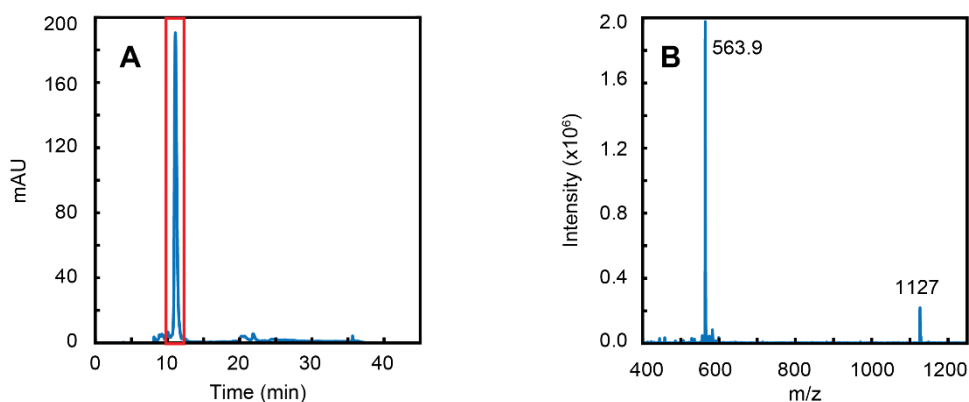


Figure A1.4. Purification and characterization of unlabeled model peptide. Chromatogram (A) and corresponding mass spectrum (B) for unlabeled MAHP (molecular weight = 1126 g/mol). The peaks at m/z 1127 and 563.9 corresponds to the 1⁺ and 2⁺ protonated charge states of MAHP, respectively.

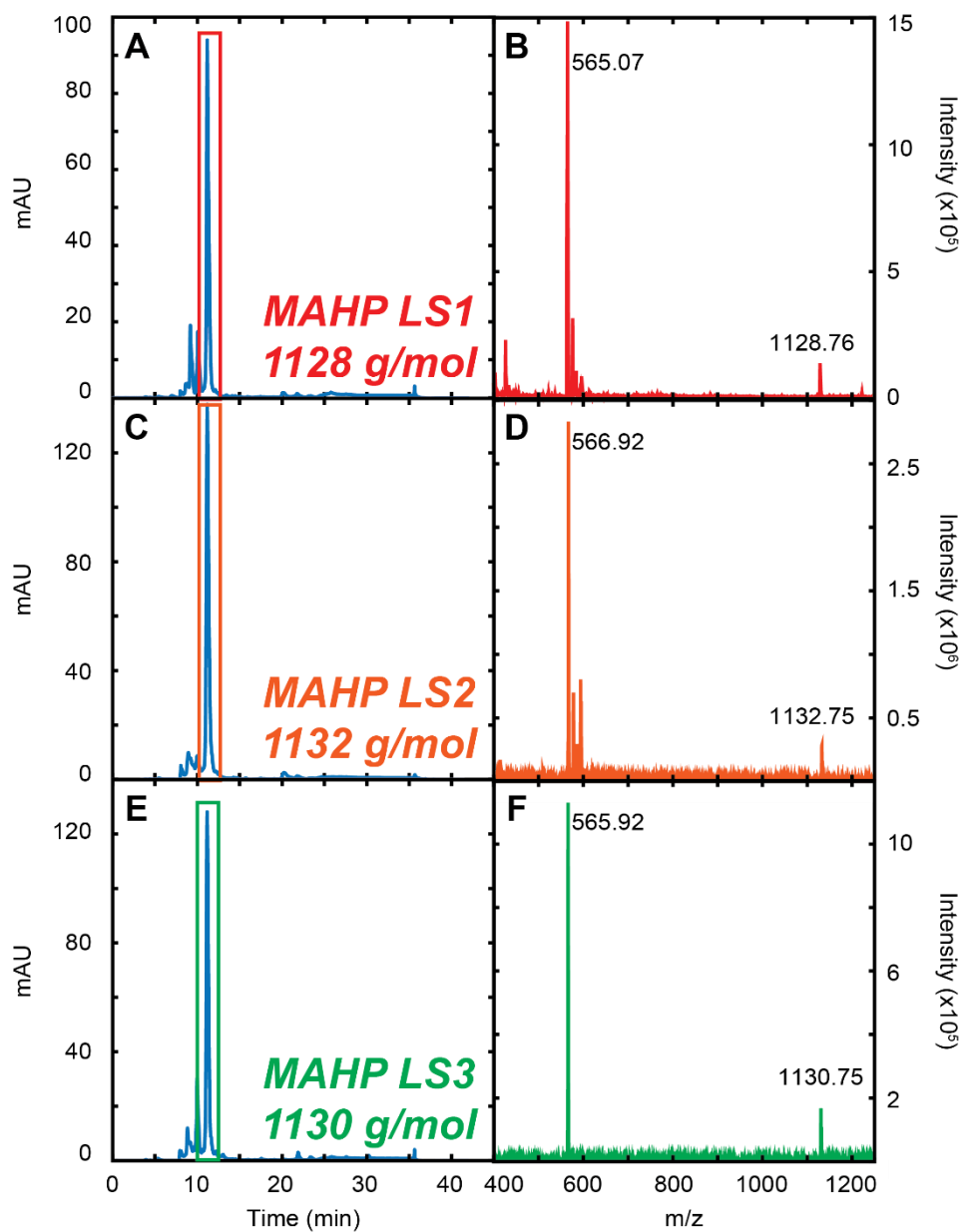


Figure A1.5. Purification and characterization of MAHP isotopologues. Chromatograms (A, C, and E) and corresponding mass spectra (B, D, and F) for labeled peptides (LS1, LS2, and LS3, respectively). All peptides eluted at ~10 minutes after they were injected onto the C18 column. The 1⁺ and 2⁺ protonated charge states were observed for all labeled peptides corresponding to the correct molecular weight.

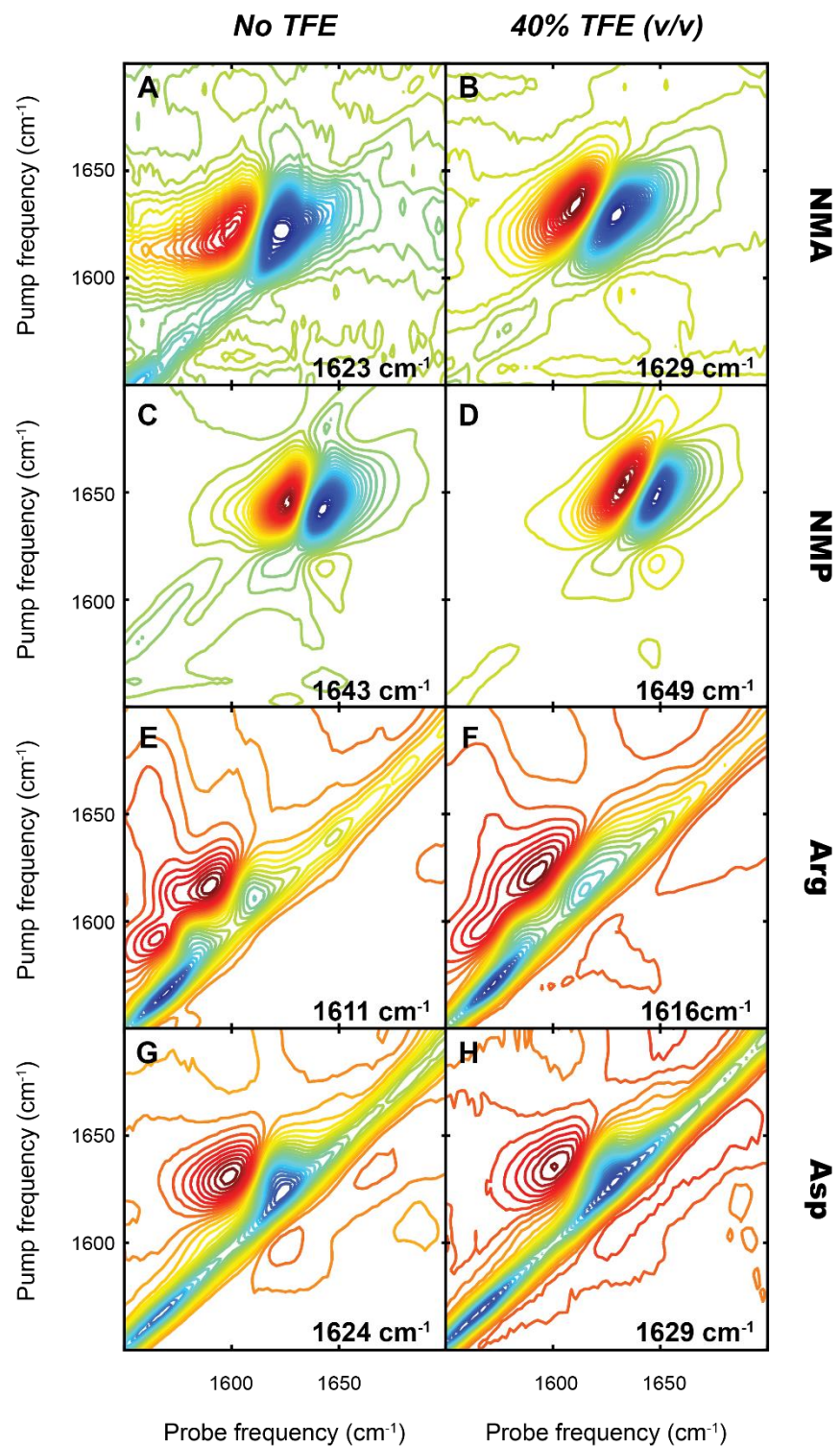


Figure A1.6. Supplementary 2D IR spectra for small-molecule solvatochromism study with TFE. Model compounds (A, B) NMA, (C, D) NMP, (E, F) Arg, and (G, H) Asp without and with 40% TFE (v/v) added. Diagonal frequency shifts $\sim 5\text{--}6\text{ cm}^{-1}$ in the presence of TFE.

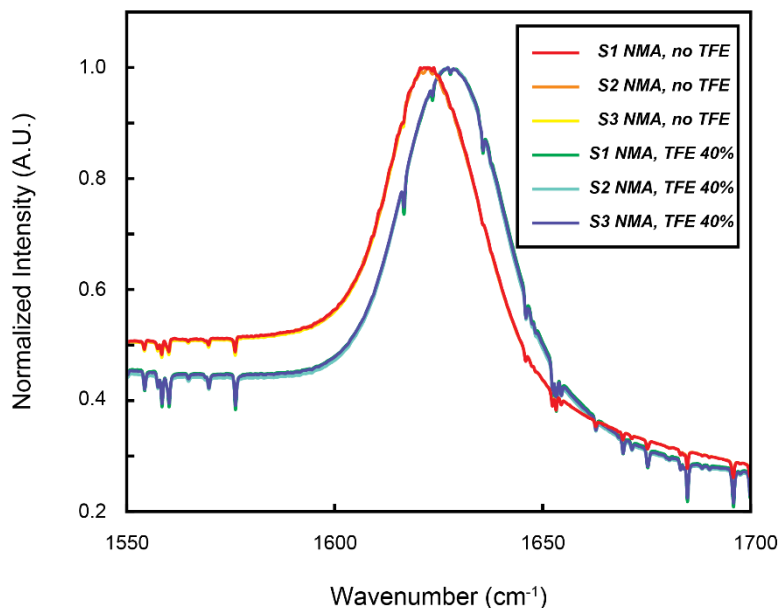


Figure A1.7. FTIR measurements corroborate TFE-induced blueshift in NMA frequency. FTIR spectra of neat NMA in D₂O (68 mM) exhibits an amide transition centered at 1623 cm⁻¹ (red, orange, and yellow traces). A blueshift in NMA's frequency to 1629 cm⁻¹ was observed upon addition of 40% TFE (v/v) (green, blue, and purple traces).

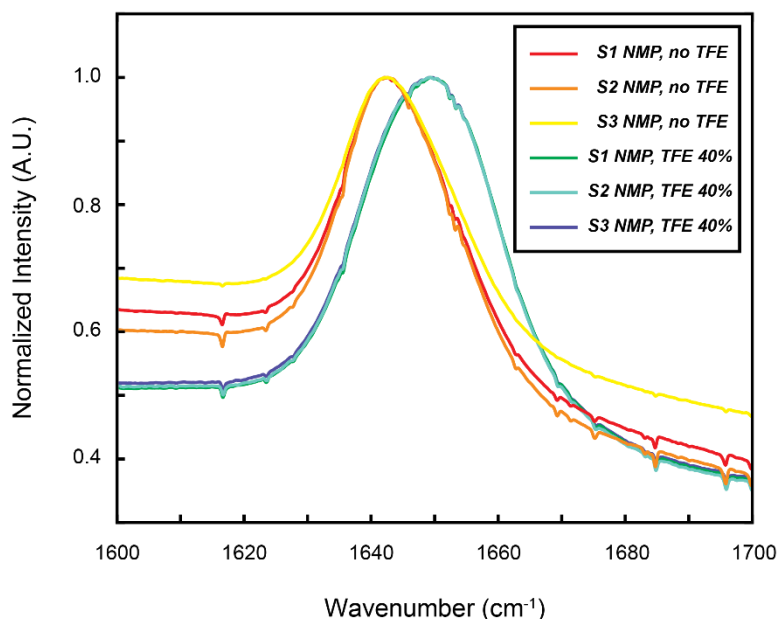


Figure A1.8. FTIR measurements verify cosolvent-induced blueshift in NMP frequency. FTIR spectra of neat NMP in D₂O (60 mM) exhibits consistent transition centered at 1643 cm⁻¹ (red, orange, and yellow traces). A blueshift in NMP's frequency to 1649 cm⁻¹ was observed upon addition of 40% TFE (v/v) (green, blue, and purple traces).

Table A1.1 Solvatochromatic effects of TFE on model peptide-like compounds			
<i>Model Compound</i>	<i>% TFE (by volume)</i>	<i>Average Frequency (cm⁻¹)</i>	<i>Average Shift (cm⁻¹)</i>
NMA	0	1623	+6
	40	1629	
NMP	0	1643	+6
	40	1649	
Arginine	0	1624	+6
	40	1630	
Aspartic Acid	0	1611	+5
	40	1616	

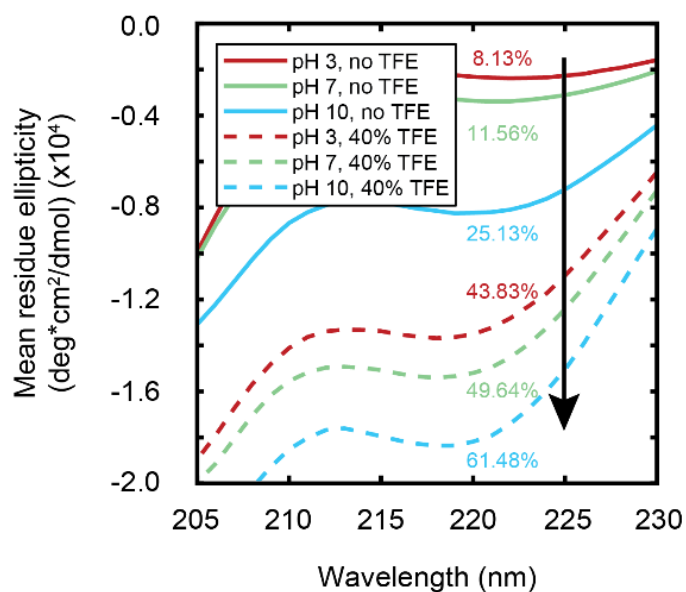


Figure A1.9. Quantifying peptide α -helicity as a function of solvent conditions. Unlabeled MAHP helicity increases with pH and the addition of TFE according to CD spectroscopy. An increase in pH from 3–10 resulted in an increase in peptide helicity (solid lines, 8.13%–25.13%). The addition of 40% TFE (by volume) further enhanced the peptide’s helicity with increasing pH (dashed lines, 43.83%–61.48%). *Equivalent to Figure 3.2 in the main text.

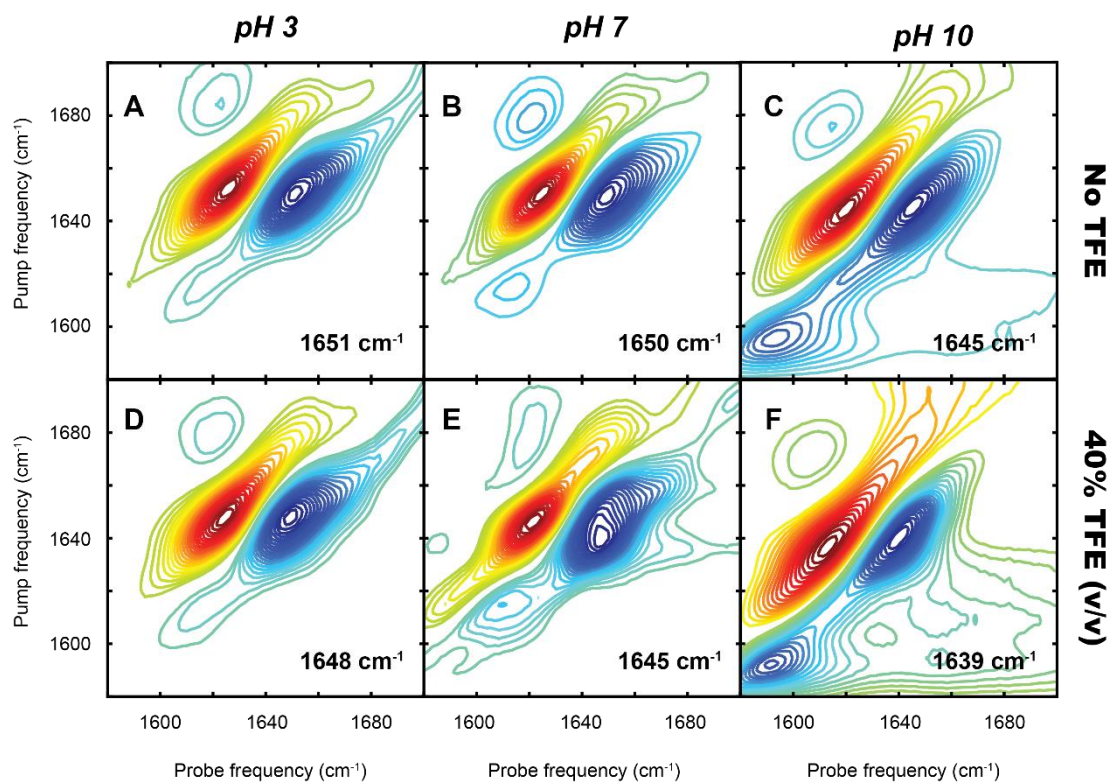


Figure A1.10. Monitoring structural changes induced by pH and 40% TFE (v/v) through 2D IR frequency shifts. A redshift in the amide I' frequency is observed as the pH increased (A–C). The addition of 40% TFE (by volume) induces a larger redshift in the amide I' mode (D–F). The solvatochromic effect of TFE is discussed in detail in the main text.

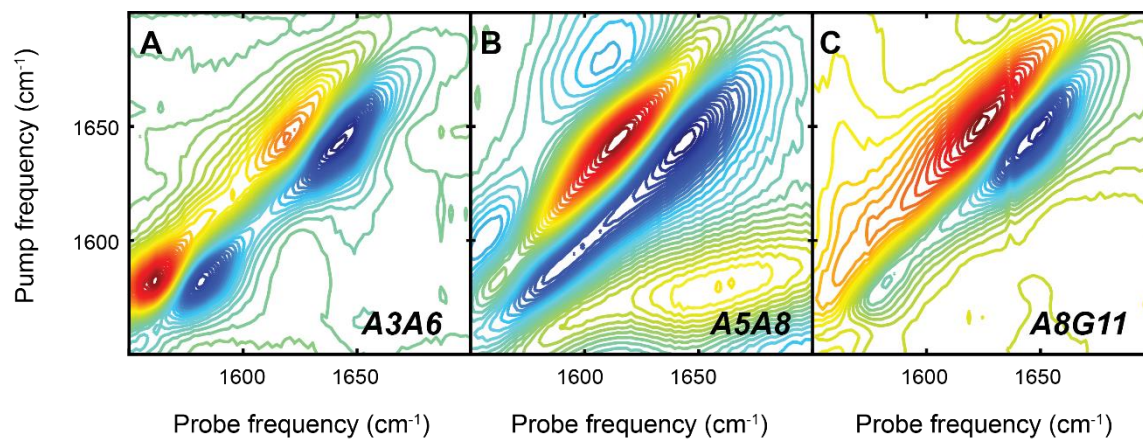


Figure A1.11. Perpendicular 2D IR spectra of double $^{13}\text{C}^{18}\text{O}$ -edited peptides at high helicity condition. MAHP labeled with $^{13}\text{C}^{18}\text{O}$ probe pairs at residues (A) A3A6, (B) A5A8, and (C) A8G11. In each spectrum, no crosspeaks were observed between the labeled and main amide I' mode.

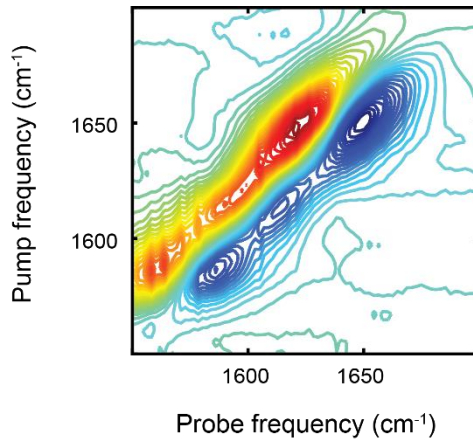


Figure A1.12. Perpendicular 2D IR spectrum of MAHP LS3 (mixed ^{13}C and $^{13}\text{C}^{18}\text{O}$) at intermediate helicity condition. No crosspeaks were detected between the two labeled isotopic transitions at the intermediate helicity condition.

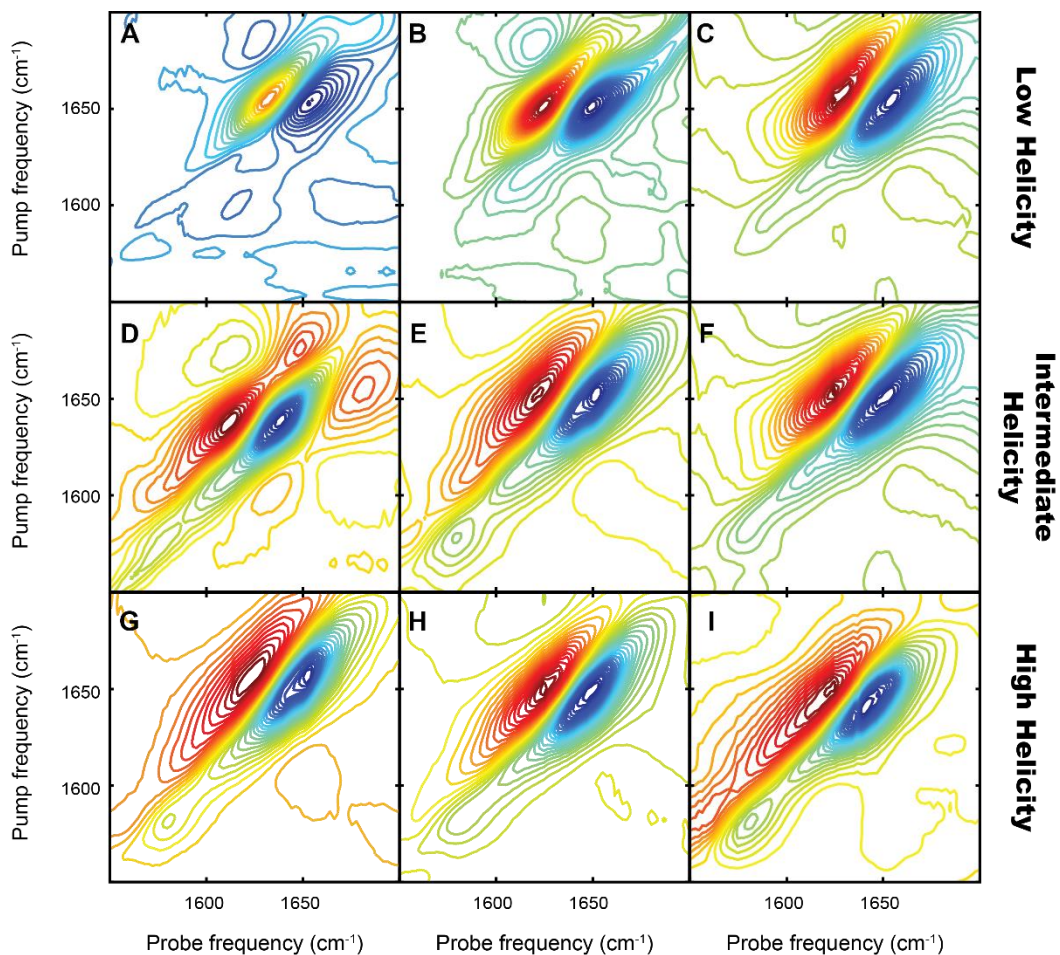


Figure A1.13. Comprehensive 2D IR spectra of unlabeled MAHP under each solvent condition used for intensity ratio calculations. MAHP under (A–C) low, (D–F) intermediate, and (G–I) high helicity solvent conditions. Minimum intensity values used in calculations are listed in Table A1.2.

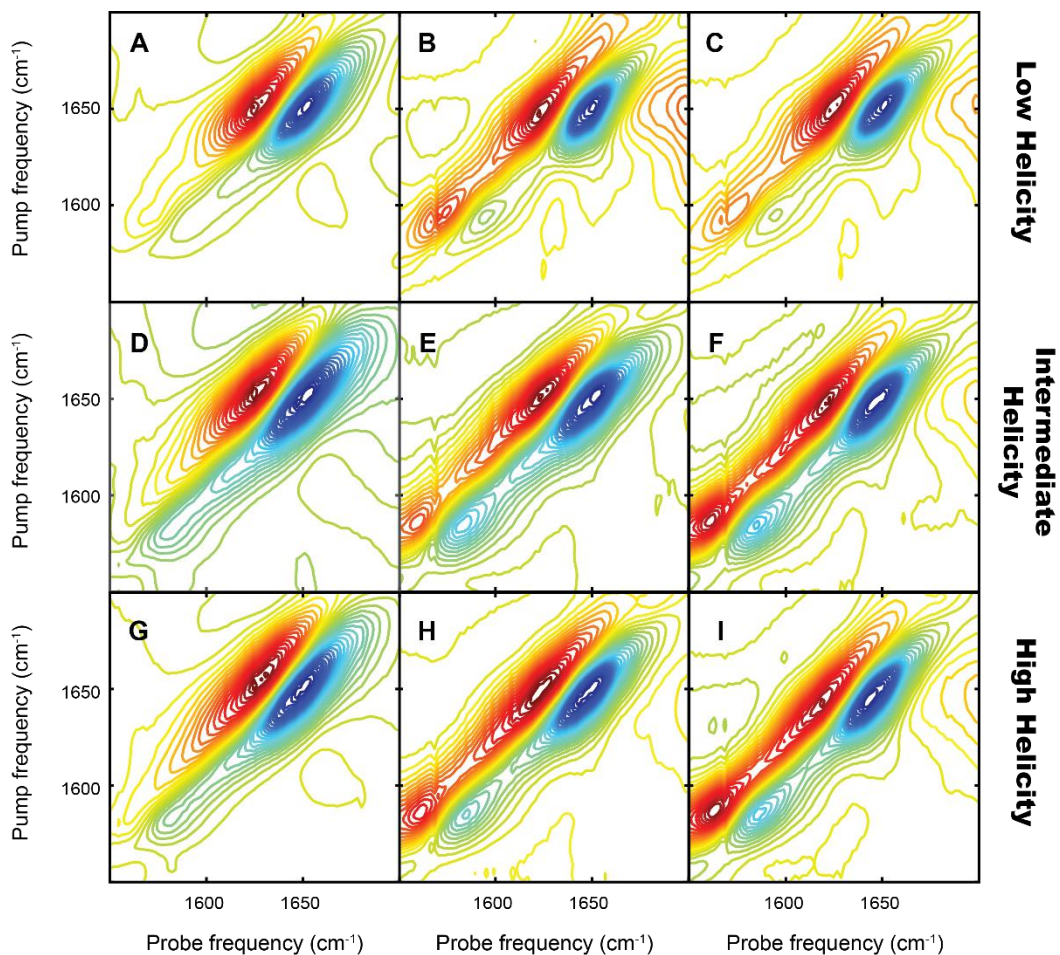


Figure A1.14. Comprehensive 2D IR spectra of single-labeled A5 MAHP under each solvent condition used for intensity ratio calculations. A5 MAHP under (A–C) low, (D–F) intermediate, and (G–I) high helicity solvent conditions. Corresponding intensity values are listed in Table A1.3.

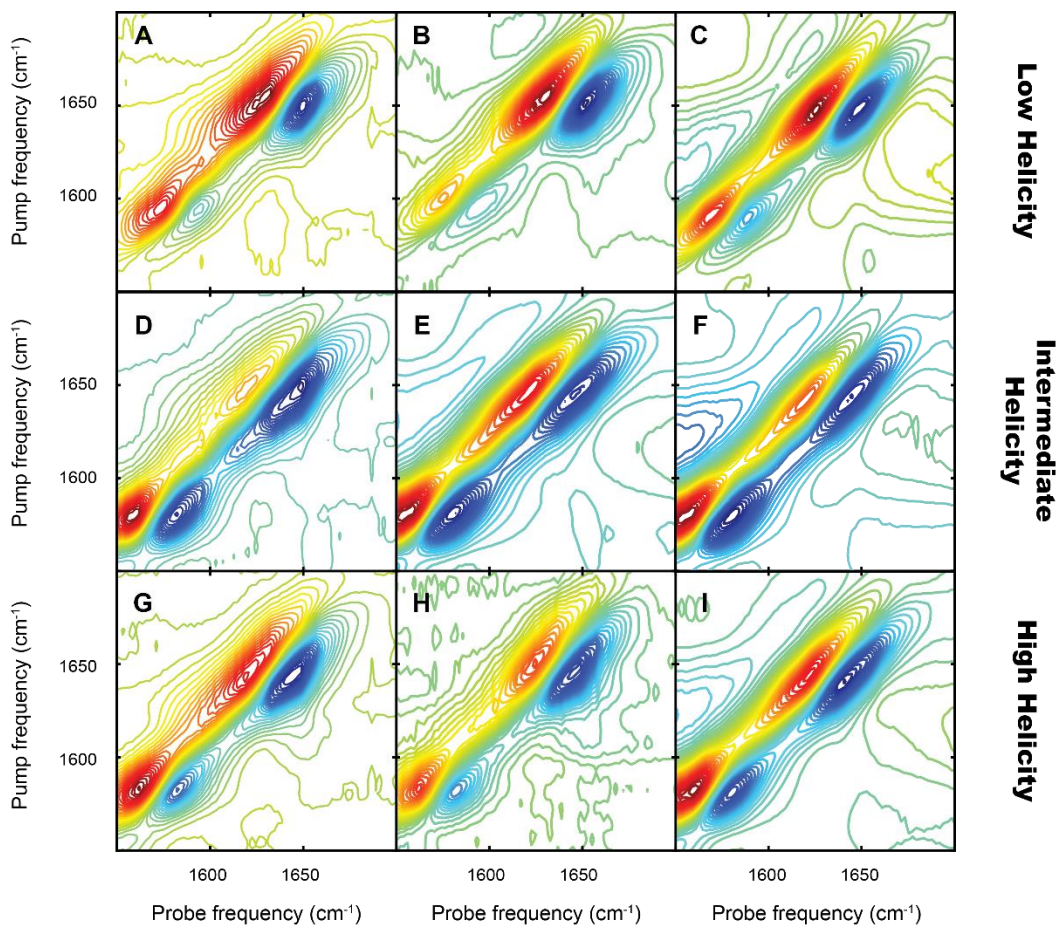


Figure A1.15. 2D IR spectra of double $^{13}\text{C}^{18}\text{O}$ -labeled A3A6 MAHP under each solvent condition used for intensity ratio calculations. A3A6 MAHP under (A–C) low, (D–F) intermediate, and (G–I) high helicity solvent conditions. Corresponding intensity values are listed in Table A1.4.

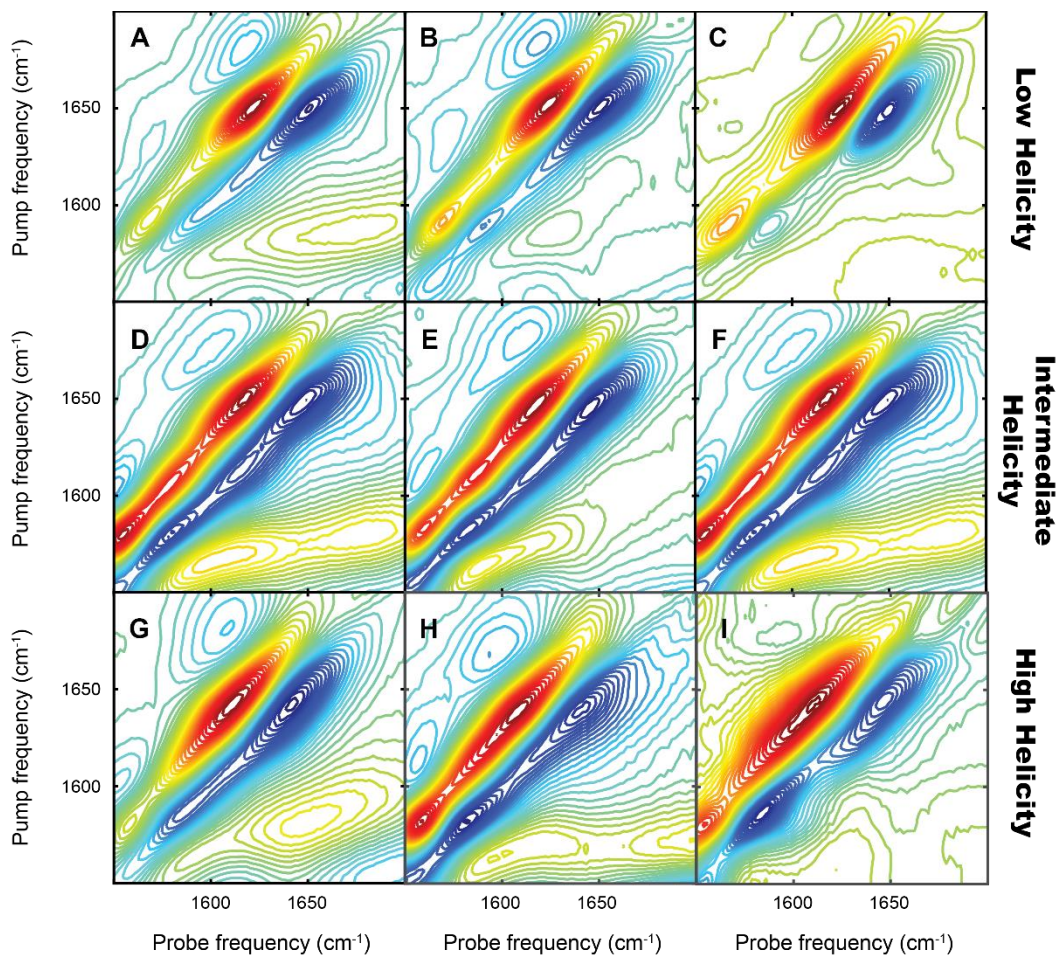


Figure A1.16. Comprehensive 2D IR spectra of double $^{13}\text{C}^{18}\text{O}$ -edited A5A8 MAHP under optimized solvent conditions used for intensity ratio comparisons. MAHP A5A8 isotopomer at (A–C) low, (D–F) intermediate, and (G–I) high helicity solvent conditions. Corresponding intensity values are listed in Table A1.5.

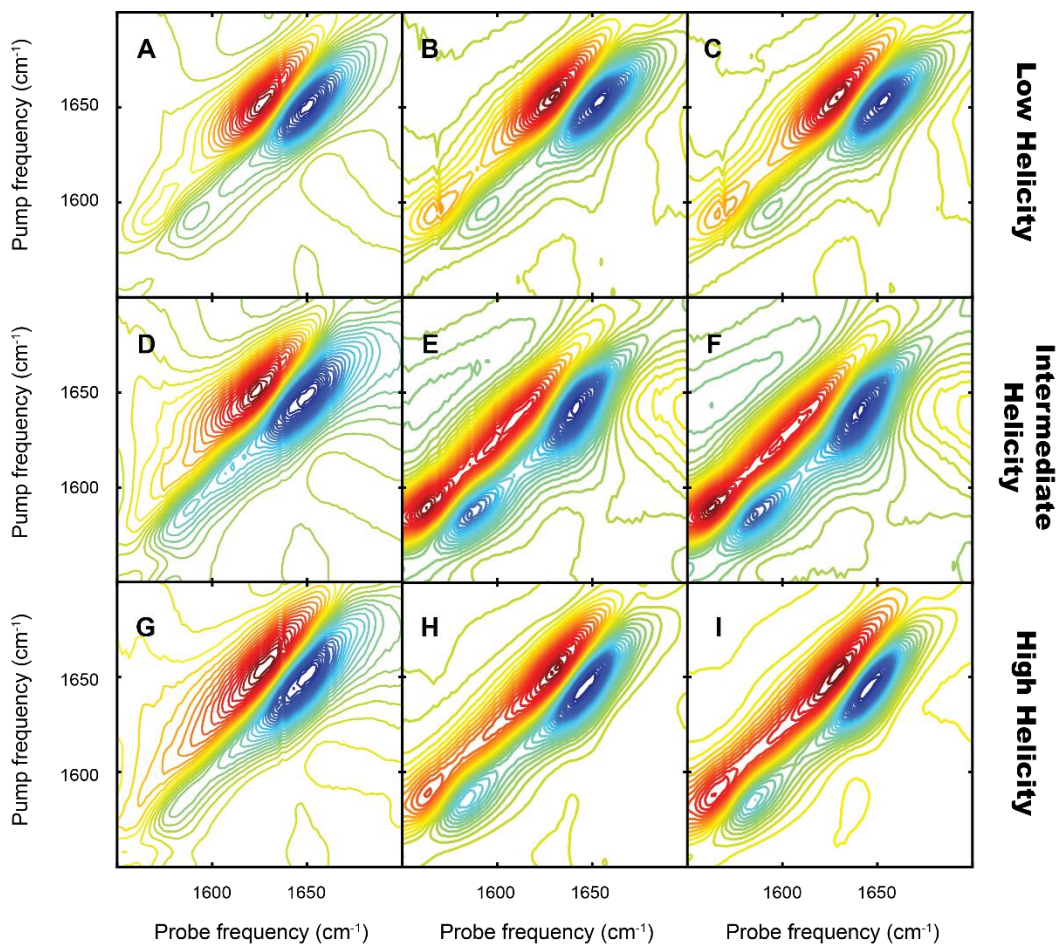


Figure A1.17. All 2D IR spectra of double $^{13}\text{C}^{18}\text{O}$ -labeled A8G11 MAHP under each solvent condition used for intensity ratio calculations. A8G11 MAHP under (A–C) low, (D–F) intermediate, and (G–I) high helicity solvent conditions. Corresponding intensity values are listed in Table A1.6.

Table A1.2 Signal strength comparison of sidechain to amide I' mode for unlabeled MAHP					
<i>Solvent Condition</i>	<i>Reference Spectrum</i>	<i>Amide I' Intensity</i>	<i>SC / IL Intensity</i>	<i>Intensity Ratio (%)</i>	<i>Average Intensity Ratio (%)</i>
Low pH, no TFE	A1.13, A	-0.0409765	-0.00333121	8.1	7.0 ± 1.4
	A1.13, B	-0.0419162	-0.00227966	5.4	
	A1.13, C	-0.102823	-0.00752702	7.3	
High pH, no TFE	A1.13, D	-0.0257806	-0.00417583	16.2	15.8 ± 3.2
	A1.13, E	-0.0556773	-0.0104532	18.8	
	A1.13, F	-0.0805287	-0.00969614	12.0	
High pH, 40% TFE (v/v)	A1.13, G	-0.061468	-0.0103226	16.8	18.2 ± 5.2
	A1.13, H	-0.112093	-0.015577	13.9	
	A1.13, I	-0.110395	-0.0264468	24.0	

Table A1.3 Signal strength comparison of low-frequency to amide I' mode for A5 MAHP					
<i>Solvent Condition</i>	<i>Reference Spectrum</i>	<i>Amide I' Intensity</i>	<i>SC / IL Intensity</i>	<i>Intensity Ratio (%)</i>	<i>Average Intensity Ratio (%)</i>
Low pH, no TFE	A1.14, A	-0.104994	-0.0103601	9.9	15.1 ± 4.3
	A1.14, B	-0.039532	-0.00804571	20.4	
	A1.14, C	-0.0500183	-0.0075983	15.2	
High pH, no TFE	A1.14, D	-0.0895657	-0.0186268	20.8	37.0 ± 11.8
	A1.14, E	-0.0447408	-0.0184542	41.2	
	A1.14, F	-0.0375706	-0.0183449	48.8	
High pH, 40% TFE (v/v)	A1.14, G	-0.136546	-0.0277935	20.4	34.7 ± 11.1
	A1.14, H	-0.0499752	-0.0182188	36.5	
	A1.14, I	-0.0457998	-0.021667	47.3	

Table A1.4 Signal strength comparison of low-frequency to amide I' mode for A3A6 MAHP					
<i>Solvent Condition</i>	<i>Reference Spectrum</i>	<i>Amide I' Intensity</i>	<i>SC / IL Intensity</i>	<i>Intensity Ratio (%)</i>	<i>Average Intensity Ratio (%)</i>
Low pH, no TFE	A1.15, A	-0.0306391	-0.00986792	32.2	33.6 ± 9.4
	A1.15, B	-0.0601529	-0.0137586	22.9	
	A1.15, C	-0.0558441	-0.0255479	45.7	
High pH, no TFE	A1.15, D	-0.0185848	-0.0161305	86.8	103.4 ± 11.7
	A1.15, E	-0.0475488	-0.053132	111.7	
	A1.15, F	-0.0460252	-0.0513296	111.5	
High pH, 40% TFE (v/v)	A1.15, G	-0.0437578	-0.0279592	63.9	66.4 ± 9.5
	A1.15, H	-0.0252376	-0.0142072	56.3	
	A1.15, I	-0.0658208	-0.0520858	79.1	

Table A1.5 Signal strength comparison of low-frequency to amide I' mode for A5A8 MAHP					
<i>Solvent Condition</i>	<i>Reference Spectrum</i>	<i>Amide I' Intensity</i>	<i>SC / IL Intensity</i>	<i>Intensity Ratio (%)</i>	<i>Average Intensity Ratio (%)</i>
Low pH, no TFE	A1.16, A	-0.0272617	-0.00997091	36.6	34.3 ± 3.1
	A1.16, B	-0.0232173	-0.00842695	36.3	
	A1.16, C	-0.0512339	-0.01533512	30.0	
High pH, no TFE	A1.16, D	-0.0216698	-0.0184578	85.2	79.1 ± 7.7
	A1.16, E	-0.0183814	-0.0154162	83.9	
	A1.16, F	-0.0382742	-0.0261437	68.3	
High pH, 40% TFE (v/v)	A1.16, G	-0.0390891*	-0.021818*	55.8*	116.2 ± 2.9
	A1.16, H	-0.0164337	-0.0186122	113.3	
	A1.16, I	-0.0346594	-0.0412963	119.1	
<i>*Asterisk denotes outlier (Grubb's test) and was omitted from average ratio calculation.</i>					

Table A1.6 Signal strength comparison of low-frequency to amide I' mode for A8G11 MAHP					
<i>Solvent Condition</i>	<i>Reference Spectrum</i>	<i>Amide I' Intensity</i>	<i>SC / IL Intensity</i>	<i>Intensity Ratio (%)</i>	<i>Average Intensity Ratio (%)</i>
Low pH, no TFE	A1.17, A	-0.0699669	-0.011792	16.9	18.9 ± 1.5
	A1.17, B	-0.0332828	-0.00678339	20.4	
	A1.17, C	-0.0352358	-0.00690865	19.6	
High pH, no TFE	A1.17, D	-0.0573457	-0.016404	28.6	51.2 ± 16.1
	A1.17, E	-0.0347388	-0.0209255	60.2	
	A1.17, F	-0.0348736	-0.022595	64.8	
High pH, 40% TFE (v/v)	A1.17, G	-0.0556688	-0.0120884	21.7	35.9 ± 10.1
	A1.17, H	-0.306972	-0.13148	42.8	
	A1.17, I	-0.307934	-0.133335	43.3	

A1.3 References

- (1) Anthis, N. J. and Clore, G. M. Sequence-specific determination of protein and peptide concentrations by absorbance at 205 nm. *Protein Sci.*, **2013**, 22 (1), 851–858.
- (2) Middleton, C. T. et al. Residue-Specific Structural Kinetics of Proteins through the Union of Isotope Labeling, Mid-IR Pulse Shaping, and Coherent 2D IR Spectroscopy. *Methods* **2010**, 52 (1), 12–22.
- (3) Forood, B. et al. Stabilization of α -helical structures in short peptides via end capping. *Proc. Natl. Acad. Sci.*, **1993**, 90 (1), 838–842.
- (4) Scholtz, J. M. et al. Parameters of Helix-Coil Transition Theory for Alanine-Based Peptides of Varying Chain Lengths in Water*. *Biopolymers*, **1991**, 31, 1463–1470.

Curriculum Vitae for Kelsey R. Webb

EDUCATION

Vanderbilt University Nashville, TN
Doctor of Philosophy in Chemistry June 2017–May 2022

- GPA: 3.930/4.000
- Dissertation: Examining peptide and protein structure and dynamics with 2D IR spectroscopy
- Research Advisor: Lauren Buchanan, Ph.D.

The University of Virginia's College at Wise Wise, VA
Bachelor of Science in Chemistry, Minors in Mathematics and Physics August 2013–May 2017

- GPA: 3.908/4.000 (*Summa cum laude*)
- Research Advisor: Floyd Beckford, Ph.D.

Honors and Awards

- National Science Foundation (NSF) Graduate Research Fellow June 2018–June 2021
- Warren Fellow Summer 2017
- Chancellor's Medal for Undergraduate Research April 2017
- American Institute of Chemists Award April 2017
- NSF Research Experience for Undergraduates Fellow Summer 2016
- Fellowship in Natural Sciences Awards Summers 2014 and 2015
- CRC Freshman in Chemistry Award April 2013
- Chemistry Alumni Scholarship August 2013–May 2017 (All Semesters)
- Dean's List of Distinguished Students August 2013–May 2017 (All Semesters)

RESEARCH EXPERIENCE

Vanderbilt University Nashville, TN
Graduate Research Fellow June 2017–Current

- Independently funded 3 years of my graduate career with a highly-competitive NSF fellowship (\$138k total)
- Synthesized and characterized peptide samples containing sensitive isotopic probes (^{13}C , $^{13}\text{C}^{18}\text{O}$, and ^{15}N)
- 5 years' experience with procurement, operation, calibration, troubleshooting, and maintenance of various analytical instruments, including an HPLC system, peptide synthesizer, and ultrafast mid-IR spectrometer
- Direct experience with building, aligning, and product testing a commercial 2D IR spectrometer during a week-long internship at PhaseTech Spectroscopy, Inc. in Madison, Wisconsin (March 2020)
- Communicated my research findings through presentations on campus and at regional/national conferences

University of Tennessee Knoxville, TN
National Science Foundation Research Experience for Undergraduates (NSF REU) Fellow Summer 2016

- Awarded prestigious NSF grant (\$5k) providing 10 weeks of scientific research funding at an R1 institution
- Aided in the development of a noninvasive spectroscopic technique to detect neurochemicals behind the skull, which resulted in a co-authored publication in *Analytical Chemistry*
- Shared my research findings through poster and oral presentations at various REU symposia on campus

The University of Virginia's College at Wise Wise, VA
Undergraduate Fellow in Natural Sciences Summers 2014 and 2015

- Received two competitive Fellowship in Natural Sciences awards (\$10k total) based upon strength of grant proposals and academic record to fund undergraduate research endeavors
- Synthesized and characterized the initial biophysical activity of novel copper and ruthenium complexes with biologically-active ligands
- Presented my research to scientific and non-scientific audiences at 5 regional and national conferences

PUBLICATIONS

4. Huong T. Kratochvil*, **Kelsey R. Webb***, William F. DeGrado, and Lauren E. Buchanan. "2D IR reveals conformational changes in the influenza A M2 proton channel." *In preparation*. *Denotes co-first authorship.
3. **Kelsey R. Webb**, Kayla A. Hess, Alisa Schmidt, Kathryn D. Segner, and Lauren E. Buchanan. "Detailed structural changes in a model α -helix revealed by 2D IR spectroscopy and isotope labeling." *In preparation*.
2. Amber S. Moody, Peymon C. Baghernejad, **Kelsey R. Webb**, and Bhavya Sharma. "Surface Enhanced Spatially Offset Raman Spectroscopy Detection of Neurochemicals Through the Skull." *Analytical Chemistry* 2017, 89 (11), 5688-5692.
1. Floyd A. Beckford and **Kelsey R. Webb**. "Copper complexes containing thiosemicarbazones derived from 6-nitropiperonal: Antimicrobial and biophysical properties." *Spectrochimica Acta Part A: Molecular and Biomolecular Spectroscopy* 2017, 183, 158-171.

SELECTED PRESENTATIONS

8. **Kelsey Webb** and Lauren Buchanan. "Examining interactions between model alpha-helical peptides and proteins with nanoparticles with 2D IR spectroscopy." Poster presentation scheduled for the Vibrational Spectroscopy Gordon Research Conference, which was cancelled due to COVID-19 in July 2020.
7. **Kelsey Webb** and Lauren Buchanan. "Probing structural changes in nanoparticle-bound proteins with 2D IR spectroscopy and isotope labeling." Poster presentation scheduled for 260th National Meeting of the American Chemical Society. Poster presentation was withdrawn due to virtual format due COVID-19 restrictions in August 2020.
6. **Kelsey Webb**, Kathryn Segner, and Lauren Buchanan. "Designing isotope-labeling schemes for protein 2D IR spectroscopy." Poster presentation at the 257th National Meeting of the American Chemical Society. Orlando, Florida. April 1, 2019 (Poster highlighted at the Sci-Mix session) and April 3, 2019 (Physical Chemistry Division). Paper ID: PHYS 361.
5. **Kelsey Webb**, Kathryn Segner, and Lauren Buchanan. "Designing an isotope-labeling scheme for protein 2D IR." Poster presentation at the 70th Southeastern Regional Meeting of the American Chemical Society (SERMACS). Augusta, Georgia. November 1, 2018. Paper ID: 418.
4. **Kelsey Webb**, Amber Moody, and Bhavya Sharma. "Surface-Enhanced Spatially Offset Raman Spectroscopy for Neuroscience." Oral presentation (July 28, 2016) and poster presentation (July 15, 2016) at the University of Tennessee. Knoxville, Tennessee. July 28, 2016.
3. Floyd Beckford and **Kelsey Webb**. "Synthesis, Characterization, and DNA Reactivity of Half-Sandwich Ruthenium Complexes Containing Curcuminoid Ligands." Oral presentation at the 30th Annual National Conference on Undergraduate Research, Asheville, North Carolina. April 7, 2016.
2. Floyd Beckford and **Kelsey Webb**. "Synthesis, characterization, and DNA reactivity of half-sandwich ruthenium complexes containing ferrocene curcuminoid ligands." Poster presentation at the 250th National Meeting of the American Chemical Society. San Diego, California. March 2016. Paper ID: CHED 1044.
1. Floyd Beckford, **Kelsey Webb**, and Bailey Helbert. "Synthesis and characterization of copper-thiosemicarbazone complexes: Interaction with DNA and anti-oxidant behavior." Poster presentation at the 249th National Meeting of the American Chemical Society. Denver, Colorado. March 2015. Paper ID: CHED 839.

LEADERSHIP & MENTORSHIP ROLES

- Directly procured and negotiated costs with scientific vendors for essential scientific supplies and equipment (totaling ~\$15k)
- Solely responsible for ordering nitrogen (gas and liquid) and keeping detailed records (number of tanks, monitoring gas/liquid levels, evaluating monthly costs, etc.) within my graduate research group
- Mentored 9 highly-motivated undergraduate and graduate students throughout my graduate tenure
- Designed creative content for Vanderbilt Chemistry's recruitment events (posters, presentations, Slack channels, videos, and Spotify playlists) and served as a graduate student host for prospective Ph.D. students
- Instructed and upheld strict safety protocols throughout 9 different teaching assistant roles throughout graduate and undergraduate careers

PROFESSIONAL AFFILIATIONS

- American Chemical Society, *Member* June 2017–Present
- Warren Committee, *Member* August 2018–May 2020
- Sigma Zeta Math and Science Honor Society (Alpha Xi Chapter) April 2015–May 2017
 - President* (2016–2017)
 - Member*
- Darden Honor Society April 2015–May 2017
 - Vice President* (2016–2017)
 - Member*

ADDITIONAL SKILLS & INTERESTS

Skills: Microsoft Office Products, MATLAB, Adobe Illustrator, ChemDraw, experimental spectroscopies

Interests: Nanomedicine, ultrafast spectroscopy, chemical recycling and upcycling, scientific communication and outreach, traveling, baking, photography, reading